INTERACTIVE SPACECRAFT TRAJECTORY DESIGN STRATEGIES FEATURING POINCARÉ MAP TOPOLOGY

A Dissertation

Submitted to the Faculty

of

Purdue University

by

Wayne R. Schlei

In Partial Fulfillment of the

Requirements for the Degree

of

Doctorate of Philosophy in Aeronautics and Astronautics

May 2017

Purdue University

West Lafayette, Indiana

Dedicated to my wife Brittany, my family, and the Lord.

"We also have joy with our troubles, because we know that these troubles produce patience. And patience produces character, and character produces hope. And this hope will never disappoint us, because God has poured out his love to fill our hearts. He gave us his love through the Holy Spirit, whom God has given to us." –*Romans 5:3-5*

ACKNOWLEDGMENTS

Firstly, I am grateful to Visualization Sciences Group (VSG, which is now an FEI company) and their truly marvelous software Avizo®. I applaud all of the people responsible for constructing and maintaining this software. I would like to thank all of the support staff at FEI for assistance in building the utilities and programs specific to this work. Also, I extend my thanks to the Purdue Envision Center for help in establishing immersive 3D visualization software and equipment. I am also appreciative of the opportunity to work in the Eliasen Visualization Laboratory.

I owe my deepest gratitude to my advisers – Professor Kathleen Howell (Aeronautics and Astronautics) and Professor Xavier Tricoche (Computer Science). I am quite fortunate to have the opportunity to work with Professor Howell. She has invaluable guidance, a vast knowledge base, and unparalleled patience. I can't thank her enough for the priceless edits throughout this work. Working with Professor Tricoche has also been a tremendous blessing. His assistance with funding this work as well as programming assistance when I had no clue what to do helped make this work exist. I would also like to thank my other committee members, Professor James Longuski and Professor Tom Shih, for the excellent courses that I took with them, their advice in problem solving and analysis, and for reviewing my dissertation. And my gratitude is extended to Purdue University as well for an excellent Aeronautics and Astronautics department and for letting me be a part of it.

Many members of my research group deserve credit for the assistance and advice they have provided. I would like to thank Dr. Martin Ozimek and Dr. Daniel Grebow for my first opportunities to employ visual analysis to research problems and for demonstrating some of my visualizations to the astrodynamics community. Thank you Dr. Zubin Olikara, Todd Brown, Chris Patterson, and Dr. Cody Short (the other "Viz Guys") for generating some of the foundations that this work is built on. Dr. Thomas Pavlak and Dr. Jeffery Stuart also have my gratitude for their generous answers to my numerous questions and key assistance in times of personal struggles. Similarly, Ted Wahl deserves credit for helping me see a calmer view on the challenges of graduate school. I would also like to thank Chris

Spreen for always providing an exuberant greeting when I arrived at the office. And finally, I am grateful to every member of the research group for the challenging conversations and intriguing suggestions that are freely shared as well as the uncanny advice for handling graduate studies.

Also, I must thank my family for their unconditional support and love. My parents, Randy and Deb, were always there when I needed support and believed in me when I doubted myself. My grandparents, Gerald and Darlene, deserve a lot of credit for this degree as they introduced me to planetary visualizations by giving me a book about space when I was five years old (I still keep that book on my desk). To my Uncle Shawn, thanks for visiting me once every fall for a Purdue football game. Every member of my family provided the support I needed to keep going, so I will always be grateful for them and love them always. Most of all my family, I must thank my wonderful wife, Brittany. She was there for me when times were rough, always giving me a kick in the pants to keep going. It's remarkable how we squeezed a wedding in while trying to complete this work, but we did it!

Most importantly, thank you Lord for the wisdom, perseverance, and patience that You have given me. It has been a long and difficult journey to complete this degree, and I reached the end because of the blessings You placed in my life. Without You, this degree could not have been finished. Lord, You are my rock; anything can be accomplished through faith in You!

TABLE OF CONTENTS

LIST OF TABLES

LIST OF FIGURES

ABSTRACT

Schlei, Wayne R. Ph.D., Purdue University, May 2017. INTERACTIVE SPACECRAFT TRAJECTORY DESIGN STRATEGIES FEATURING POINCARÉ MAP TOPOLOGY. Major Professors: Kathleen C. Howell and Xavier M. Tricoche.

Space exploration efforts are shifting towards inexpensive and more versatile vehicles. Versatility regarding spacecraft trajectories refers to the agility to correct deviations from an intended path or even the ability to adapt the future path to a new destination – all with limited spaceflight resources (i.e., small ΔV budgets). This versatile, low-ΔV design paradigm requires the exploitation of *Poincaré map topology*, or the interconnected web of dynamical structures, existing within the chaotic dynamics of multi-body gravitational models. This investigation outlines an autonomous procedure to extract the periodic orbits (topology nodes) and correlated asymptotic flow structures (or the invariant manifolds representing topology links). The autonomous procedure presented in this investigation (termed PMATE) overcomes discontinuities on the Poincaré section that arise in the applied multi-body model (the planar circular restricted three-body problem) and detects a wide variety of novel periodic orbits. New interactive capabilities construct a visual analytics foundation for versatile spaceflight design, especially for initial guess generation and manipulation. Such interactive strategies include the selection of states and arcs from Poincaré section visualizations and the capabilities to draw and drag trajectories to remove dependency on initial state input. Furthermore, immersive selection is expanded to cull invariant manifold structure, yielding low-ΔV or even ΔV-free transfers between periodic orbits. The application of interactive design strategies featuring a dense extraction of Poincaré map topology is demonstrated for agile spaceflight with a simple spacecraft rerouting scenario incorporating a very limited ΔV budget. In the Earth-Moon system, a low-ΔV transfer from low Earth orbit (LEO) to the distant retrograde orbit (DRO) vicinity is derived with interactive topology-based design tactics. Finally, Poincaré map topology is exploited in the Saturn-Enceladus system to explore a possible ballistic capture scenario around Enceladus.

1. INTRODUCTION

The era of billion-dollar flagship missions is passing as space-mission efforts shift towards inexpensive and more versatile vehicles. Regarding spacecraft trajectories, the versatility of a space vehicle refers to the capability of simultaneously addressing many mission objectives, preferably with agile transfers to multiple destinations (celestial bodies or man-made orbital structures). In the event of an unanticipated perturbation, agile vehicles adapt the future path by employing a small correction (via a maneuver that creates a change in spacecraft velocity or ΔV) that exploits the existing dynamics to naturally flow back to the intended target or even modify the strategy to achieve the design goal. An astute knowledge of the dynamical structures within a multi-body gravitational model, one that includes chaotic behavior, is fundamental to delivering this form of spacecraft versatility. Technology governing human-computer interaction establishes useful design precedents for creating and modifying graphical assets within the entertainment, medical, and structural-design industries. Akin to the enabling technologies in human-computer interaction, flexible trajectory design architecture is also contingent upon the ability to quickly modify the current assembly of information. Innovative adaptation of the trajectory-planning paradigm is accomplished through the exploitation of the fundamental dynamical structures that exist even considering the chaos inherent in multi-body regimes and creative approaches for rapid arc-construction within a visual environment.

Initiating preliminary trajectory design via visual environments and employing interactive and rapid modifications are tasks well-suited for *visual analytics*–a science that merges the intuition of humans with scientific visualization and immersive environments. The goal of a visual analytics application is an insight or innovation concerning a particular problem or data set; a visual analytics approach employs scientific visualization techniques and analytical abstractions via user interfaces [1, 2]. Spacecraft trajectory design relates to the creation of pathways through space to accomplish mission objectives, leading to an interactive design philosophy. Recent toolkits such as Adaptive Trajectory Design (ATD, see Haapala et al. [3]) and other computational frameworks (e.g., Museth, Barr and Lo [4],

Haapala and Howell [5], and Schlei [2]) demonstrate the powerful ability to interactively construct designs through selection utilizing various visualizations and adjustable parameters. These toolkits also offer a graphical user interface (GUI) to modify refinement criteria and immediately apply differential corrections for a continuous result. Path-planning for space-based assets through an interactive visual framework, where a trajectory itinerary is defined 'on-the-fly' based on knowledge of the underlying orbital structures, fulfills the flexible design paradigm for preliminary studies and delivers spacecraft versatility during real-time operations.

A rich understanding of the influential dynamical behavior is necessary for a visual analytics design ideology for flexible destinations and versatile spacecraft. Within the context of multi-body dynamics, researchers demonstrate that observing trajectory patterns from a global or macroscopic perspective highlights the potential ΔV-free pathways between different orbits [5–8]. The *Poincaré map*, or first-return map, supplies insight by portraying a global snapshot of all trajectories (i.e., a *Poincaré section*) at the crossing of a user-defined hyperplane. It is the *Poincaré map topology*, or the inter-connectivity of map components, that frequently supplies the vital pieces for effective design strategies in a dynamical system of interest. Periodic orbits, or fixed points on the surface of section, stand in as nodes on the map with topological behavior consistent with centers (stable orbits) and saddles (unstable orbits). Invariant manifolds–asymptotic flow structures that exist as another base element of the topological structure associated with unstable fixed points–frequently exist as near-optimal options for maneuvering into and out of periodic orbits [6,9]. Utilizing the invariant manifolds present on a Poincaré section as part of a pre-existing design catalog then allows a trajectory designer to construct flyby sequences and initiate strategies to design low-cost transfers between a variety of orbital structures [7–10]. The key to unlocking the potential ΔV-savings of multi-body gravitational models is then reflected in the Poincaré map topology. Thus, it is imperative to develop new metrics for identifying previously unknown fixed points and companion structures so the full extent of multi-body dynamics principles are available in an immersive design setting.

The standard computational and visualization methods for employing Poincaré maps possess several drawbacks. Commonly regarded as the standard approach for displaying maps and the associated topology in multi-body gravity models, the *puncture plot* is a

representation of the Poincaré map as points indicating the trajectory returns to (or punctures of) a specified hyperplane. These returns are revealed by numerically simulating a set of initial states over a substantial duration while detecting the crossing points of a particular surface of section. For an adequate description of the dynamical behavior, the puncture plot approach requires the solution to a large number of initial value problems. The resulting point-set visualization of the Poincaré map conveys the general distinction between quasi-periodic regions and chaos; however, visualizing a topological construct in the puncture plot is only accomplished through significant post-processing analysis. Even locating the periodic orbits in a given puncture plot entails an iterative user-input process without the guarantee that the surrounding relevant structures will be revealed. Thus, an autonomous topology extraction method is required to design with Poincaré map topology. This investigation seeks to enhance the visualization of Poincaré maps and exploit topology-based methods to extract topological frameworks for multi-body design applications. Interactive approaches specific to astrodynamics applications are also explored to support the construction of trajectory itineraries.

1.1 Research Objectives

The over-arching goal of this investigation is the development of a visual analytics foundation for designing more complex spacecraft trajectories than previously available to fully exploit multi-body dynamics and the natural orbital topology. Specifically, this visual analytics application focuses on transfers between periodic orbits; Poincaré map topology delivers connections between periodic orbits by exposing the inherent pathways (i.e., invariant manifolds of unstable orbits). If sufficient orbital structures emerge, then the low-cost, interconnected pathways between orbital structures become available, leading to a "roadmap" for designing transfers (at least in area-preserving systems at the current development level). The evolution of visual design with Poincaré map topology originates with the advancement of interactive procedures relevant to trajectory design and Poincaré maps. Improving the display techniques for Poincaré sections is also of paramount importance. In conjunction with small maneuvers that support low-ΔV connections, interactive design

concepts bridge the network of design options and forge a novel design philosophy based on the fundamental dynamics. The following research objectives summarize the requirements:

1. Expand human-computer interaction for visual analytics trajectory design scenarios.
2. Enhance visualization of Poincaré sections for easier recognition of dynamical structures.
3. Develop and employ an autonomous Poincaré map topology extraction protocol to highlight periodic orbits and invariant manifold structures relevant to a given design problem.
4. Establish fundamental interaction principles with Poincaré maps and associated topology to construct sophisticated itineraries (e.g., tour-designs) that exploit natural dynamical structures.

Completing these objectives grants trajectory designers not only a rapid and immersive visual analytics design capabilities but also allows access to complex trajectory itineraries that fully exploit multi-body dynamics. The proposed immersive design framework broadens readily available options for trajectory designers and facilitates the interaction with the scientists.

1.2 Related Contributions

Interactive visual design techniques are recognized with only a limited history in the trajectory design community but are gaining ground in recent years. Visual design efforts are channeled into commercial software packages such as Satellite Tool-Kit® (STK® by Analytical Graphics, Inc.) that stress the importance of higher-fidelity modeling and visualization for mission support; however, the design components in STK® and similar software packages are initial-state based GUIs with little immersive capabilities for astrodynamics and initial guess generation. As a more immersive application, point-and-click options for constructing initial guesses within a GUI framework are demonstrated by Haapala and Howell [5] where selecting a glyph representing higher-dimensional Poincaré map data populates an orbit-to-orbit transfer option in the full circular restricted three-body problem (CRTBP). The

result can subsequently be transitioned to a higher-fidelity model. Museth, Barr and Lo [4] introduce a similar immersive visual design concept employing arc selection within a 3D immersive environment (e.g., a 3D Workbench) by assisting guess generation through visual cues, leading to the interactive selection of a stable manifold arc emanating from a desired CRTBP halo orbit in backwards time. The concept of selection and simple manipulation within a virtual environment is demonstrated for a visual analytics design philosophy by Schlei [2] as a visualization software add-on and furthered by Haapala et al. [3] with the Matlab-based GUI package ATD. These interactive packages simplify trajectory formulation in multi-body dynamics and offer general access to dynamical structures in support of low-cost trajectory designs.

Methodologies that employ topology for analyzing scalar fields, vector fields, and dynamical systems are a leading research topic in the scientific visualization community. Many vector-field visualization methods exploit flow topology to assist in computing important flow structures, and the underlying concepts are also applicable to Poincaré maps. One such example is a software package developed by Yip that combines geometric and graph theory criteria to automatically recognize topological structures in maps defined by analytical expressions [11]. In addition, Sanderson et al. describe an approach to link points in a puncture plot that reside on the same quasi-periodic tori to assist in the approximation of periodic orbits on the Poincaré map [12]. Several published papers in the literature present methods for computing invariant manifolds for topological consideration. Most relevant to the current work is a 1D continuation method that employs subsequent boundary-value problems (BVPs) to advect manifolds on the map in a manner similar to streamline propagation. England et al. [13] formalize the BVP manifold advection method by applying criteria for downstream 'smoothness' to adapt step-sizing. Finally, Tricoche et al. offer a robust and computationally efficient algorithm for extracting topological structures from Poincaré sections in area-preserving Hamiltonian systems with periodic domains; examples include the Chirikov-Taylor Map (or Standard Map) as well as maps that model plasma confinement in the Tokamak fusion reactor [14]. The investigation by Tricoche et al. demonstrates that a Poincaré map computation over a relatively sparse grid supplies sufficient information to autonomously extract topological features in a Poincaré section without significant user input [14].

End-to-end trajectory design techniques related to tour-design applications possess a long-standing history in the two-body model, but current multi-body equivalents only partially contribute to tour-design solutions. Tour-design problems are typically centered around an *endgame solution*–constructing a low-cost orbit-insertion maneuver at the desired science orbit as part of a robotic spacecraft mission [15]. The standard solution technique employs patched-conics (i.e., an isolated two-body gravitational model within designated spheres of influence). A popular patched-conics technique – dubbed V_∞*-leveraging* by Longuski and first documented by Williams [16] – utilizes a series of small maneuvers (called V_∞-leveraging maneuvers or VILMs) [16, 17]. The VILMs are designed in concert with gravity assists through a Tisserand graph (comparison of two-body orbit parameters linked by constant values from Tisserand's criterion) to establish transitions between relevant resonant orbits [15, 18]. As Strange, Campagnola, and Russell [18] demonstrate, the V_∞-leveraging design approach, in conjunction with a sequence of multiple moon flybys, can significantly reduce science-orbit insertion costs at bodies of high scientific interest (e.g., Enceladus in the Saturnian system) without exceptionally long flight times. One suggested multi-body version of the VILM approach is offered by Campagnola and Russell [19] where Tisserand's criterion mixes with Poincaré sections to create a Tisserand-Poincaré (T-P) graph for design selection, one that utilizes two-body design ideals in the higher-fidelity CRTBP [16, 17]. In contrast, while examining two-body flyby trajectories and the transition between resonant orbits, Lo et al. [6] as well as Anderson and Lo [7] discovered that the trajectories from low-cost patched-conic designs are almost identical to utilizing an unstable to stable invariant manifold transition from the corresponding CRTBP resonant orbits. In addition, various publications, including Koon et al. [20], Ross et al. [21], Gómez et al. [8], and Vaquero and Howell [22], indicate that invariant manifolds of unstable orbits residing in the CRTBP model are the driving elements for low-cost transfer design. The T-P graph, though, neglects invariant manifold structure, so Gawlik et al. [23] and Lantoine, Russell, and Campagnola [24] generate a multi-body tour-design approach combining selections from the T-P graph with the natural dynamics via the Keplerian map (a quick, pseudo-analytic Poincaré map relating changes to conic orbital elements [25]). The endgame solution is then established by defining an initial path that links unstable resonant orbits (the topological saddles of the Keplerian map) and targeting a final contin-

uous solution [23, 24]. Yet, even the Keplerian map omits much of the possible structure available in multi-body regimes since it is focused on the transition link between two-body and multi-body resonant orbits. As demonstrated by Anderson and Lo [7] and Vaquero and Howell [9, 10, 22], configuration-space Poincaré sections in the CRTBP reveal efficient transfer pathways employing basic orbital structures. In fact, maneuver-free transfer options exist in the form of heteroclinic manifold connections [20], which are not acknowledged in patched-conic tour-design techniques. Clearly, understanding the inter-connected orbit topology in CRTBP Poincaré sections augments the standard tour-design knowledge base and provides a guiding natural dynamics framework for design procedures.

Spacecraft trajectory construction techniques that employ the associated Poincaré map topology framework within an immersive environment are still emerging, yet suggestions for practical implementation are available in the literature. Ideally, transfer construction with Poincaré map topology closely follows invariant manifolds and heteroclinic (ΔV-free) connections [6, 20], but an important drawback with such design practice is the extended time of flight required for inexpensive transfers [24]. Bollt and Meiss [26] reduce exceptionally long transfer times by targeting states of recurrence (i.e., states that return near the original location within a threshold distance at some downstream mapping) to bypass wait time. Another approach by Schroer and Ott [27] suggests a pass-targeting method to transfer between periodic orbits; the pass-targeting method propagates on-map control segments around departure and arrival orbits forward and backward in time, respectively, to identify an intermediate overlap location that suggests the fastest transfer [27]. Unfortunately, both recurrence-targeting and pass-targeting only approximate invariant manifolds as individual techniques without actually exploiting the true dynamical structure. Directly employing the Poincaré map topology skeleton, though, facilitates the selection of shorter, low-cost transfers since the available catalog of nearby structure is visually apparent on the map. The base elements of such a design concept are demonstrated by Scott and Spencer [28] where initial guesses for Earth-launch to Sun-Earth CRTBP orbits are selected utilizing locations where Earth-collision states intersect the Poincaré section, specifically near stable manifolds corresponding to desired destination orbits. Similarly, Vaquero and Howell [9, 10] indicate that transfers from low-Earth orbits (LEOs) to various periodic orbits can be constructed employing invariant manifolds of numerous resonant orbits selected

from a meaningful Poincaré section. Vaquero and Howell also convey a design template on Poincaré sections that produces low-cost transfer options with relatively fast flight times relying on invariant manifolds of known resonant and libration point orbits [10]. Autonomous Poincaré map topology extraction may supply the missing structure to fully incorporate multi-body dynamics as a viable foundation for tour-design procedures.

1.3 Current Work

The primary focus of the current work is to merge Poincaré map topology from multi-body regimes with an immersive design framework for interactive application to versatile transfer-design and tour-design problems. The current investigation reviews astrodynamics theory and design methods in parallel with the synopsis of Poincaré map topology design elements in the following order.

- Chapter 2:

  The fundamental gravitational models to support trajectory computations are developed. The equations of motion in the time-invariant CRTBP model are derived, and equilibrium solutions are obtained. The concept of zero-velocity surfaces offers a preliminary examination of dynamical behavior in the CRTBP.

- Chapter 3:

  Linear variational analysis and targeting schemes are critical techniques for generating solutions to trajectory design problems. Targeting algorithms are employed to compute two-dimensional (2D) and three-dimensional (3D) periodic orbits through various formulations. A multiple-option shooting algorithm for a real-time design implementation with a graphical user interface is presented.

- Chapter 4:

  The concept of Poincaré sections is introduced for a planar examination of the CRTBP. Analysis concerning the stability of periodic orbits reveals the existence and definition of invariant manifolds. The application of Poincaré maps and invariant manifold theory is discussed.

- Chapter 5:

  A novel approach for displaying dynamical behavior on a Poincaré section is presented through a texture processing technique termed *orbit convolution*. The constructed images provide a clear depiction that is vital to the selection of relevant domains.

- Chapter 6:

  Computer graphics fundamentals are presented to build a foundation for interactive design technologies. Several interactive design strategies are developed for application with Poincaré maps and preliminary trajectory design scenarios.

- Chapter 7:

  An autonomous Poincaré map topology extraction algorithm is designed specifically for computing periodic orbits and flow structures in the planar CRTBP model. The many facets of the numerical extraction process are described in detail.

- Chapter 8:

  Interaction principles with autonomously extracted Poincaré map topology data are established. The framework to construct designs featuring Poincaré map topology data is also outlined.

- Chapter 9:

  Periodic orbits are autonomously extracted and analyzed in various systems and energy levels. Also, transfer possibilities are explored for various orbit-to-orbit scenarios to demonstrate spaceflight versatility available through Poincaré map topology data. And finally, the endgame problem is investigated for a possible destination orbit about Enceladus that permits a nearly-ballistic capture solution.

- Chapter 10:

  The extent of this work is summarized, and future adjustments to the autonomous Poincaré map topology extraction procedure are suggested. Several add-ons to the current work are offered for future research.

With the included chapters, this study illustrates the effectiveness of Poincaré map topology information and interactive trajectory construction techniques towards versatile spaceflight design scenarios.

2. FOUNDATIONS FOR TRAJECTORY COMPUTATION IN MULTI-BODY REGIMES

Prediction of spacecraft motion, or the motion of a similarly small body, under the influence of multiple gravitational fields is a challenging problem. Developing an understanding of the underlying dynamics of such behavior is essential to the trajectory design process. In fact, new scientific objectives for spacecraft missions can be realized by blending recent advancements in mathematics with the latest computational methods. However, an understanding of the basic laws of orbital mechanics and the correct formulation of multi-body gravitational models are essential for successful design.

2.1 The N-Body Model

As celestial bodies move throughout the universe, each body applies an attracting gravitational force to every other body. If the celestial bodies are represented as point masses, the distance between each pair determines the magnitude of each gravitational force. Confining the system to N gravitational point masses (each a particle P_j with mass m_j), a body of interest P_i, relative to an inertially fixed point, is illustrated as seen in Figure 2.1. The other $N-1$ point masses exert forces on the body of interest that are directly proportional to the mass of each perturbing body and inversely proportional to the distance between the pair of bodies. This model is consistent with Newton's inverse-square gravitational law.

The total gravitational force on the body of interest is the resultant due to the gravitational forces from all the other bodies in the system. From Newton's Second Law of Motion, the set of second-order vector differential equations that govern the motion of a particle P_i with respect to an inertial observer is written

$$m_i \boldsymbol{r}_i'' = -G \sum_{\substack{j=1 \\ j \neq i}}^{N} \frac{m_i m_j}{r_{ji}^3} \boldsymbol{r}_{ji}. \tag{2.1}$$

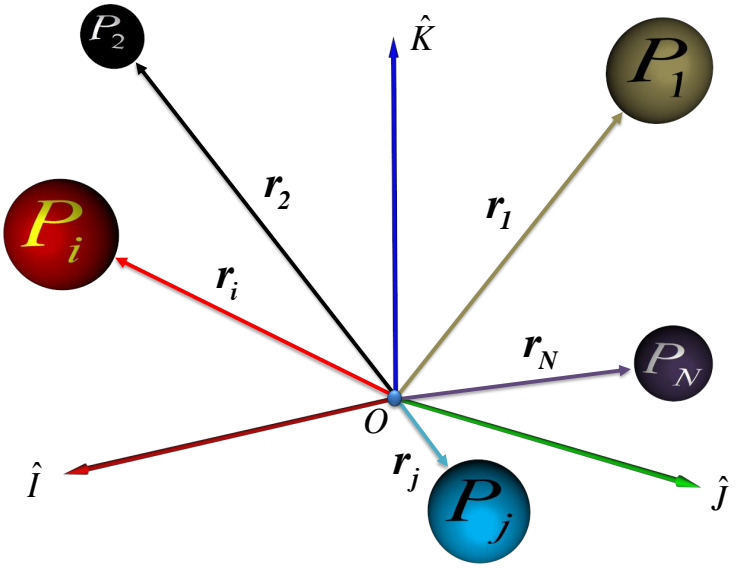

Figure 2.1. N-body system with the locations defined relative to an inertially fixed point O.

The prime notation indicates derivatives with respect to dimensional time. Note that $\boldsymbol{r}_{ji}$ represents the vector directed from particle P_j to particle P_i and is evaluated from the vector relationship $\boldsymbol{r}_{ji} = \boldsymbol{r}_i - \boldsymbol{r}_j$ [29].

Identifying an inertially fixed point in space is challenging since all the bodies in the universe are constantly in motion. Thus, the relationship in Equation (2.1) is not particularly useful in trajectory design. Employing a formulation for the motion of particle P_i relative to another body removes the requirement for an inertially fixed base point. The expression

$$\boldsymbol{r}''_{ji} + G\frac{m_i + m_j}{r_{ji}^3}\boldsymbol{r}_{ji} = \sum_{\substack{k=1 \\ k\neq i,j}}^{N} Gm_k \left(\frac{\boldsymbol{r}_{ik}}{r_{ik}^3} - \frac{\boldsymbol{r}_{jk}}{r_{jk}^3} \right), \tag{2.2}$$

models the motion of P_i relative to particle P_j [29]. Terms on the left side of Equation (2.2) reflect the acceleration of P_i with respect to P_j as well as the gravitational force of P_j on P_i. Expressions on the right side, denoted perturbing accelerations, are separated into two

groups: direct terms that apply a gravitational force on P_i and indirect terms that subtract the gravitational forces applied on P_j.

Unfortunately, the differential equations in the N-body problem are difficult to solve. A total of $6N$ integrals of the motion are required to solve the system of equations analytically, but only 10 constants exist, originating with the laws of conservation [29]. Numerical solutions to the N-body problem incur high computational costs since N second-order differential equations are propagated simultaneously. Trajectory designers typically simplify the N-body model by reducing the number of particles to a minimum number that effectively represents a given scenario.

2.2 Two-Body Model

The simplest approach to modeling the motion of a celestial body is to assume only one body is applying a gravitational force. In the relative two-body model, Equation (2.2) reduces to

$$\boldsymbol{r}'' + \frac{\mu}{r^3}\boldsymbol{r} = \boldsymbol{0}, \tag{2.3}$$

representing the set of second-order differential equations with $N = 2$. In Equation (2.3), the primary mass of the system is selected to be P_1 with mass m_1, the mass parameter μ is defined as $G(m_1 + m_2)$, and the subscript i is neglected for the body of interest. Since only two bodies are involved in the model, the perturbing accelerations are zero.

The solution to the two-body problem is well documented. Johannes Kepler postulated that the planets followed elliptical orbits relative to the Sun, with the Sun at one focus; he also deduced other laws of planetary motion based on empirical observations. Later, Isaac Newton published his laws of motion and proposed a mathematical form for the gravitational force. Based on differential and integral calculus, Newtons's solution to the differential equations governing motion in the two-body problem confirmed Kepler's conclusions about planetary movement [30]. The closed-form solution in the two-body problem is the familiar set of conic sections.

In trajectory design, many physical problems are well represented by the two-body model. Satellites in low Earth orbits, for example, employ the two-body model during preliminary design and analysis phases [30]. Also, patched-conic techniques allow for the

approximation of spacecraft trajectories to the Moon or other planetary bodies within the context of the two-body problem [31]. Perturbations to conic motion can also be accommodated to improve the approximation. However, in recent years, investigation of motion under the simultaneous influence of multiple gravity fields has produced a wider range of trajectory types that do not exist within the context of the two-body problem. With the recent expansion of numerical capabilities, exploration of these newest possibilities for trajectory design are becoming a priority.

2.3 Circular Restricted Three-Body Model

Multi-body regimes offer an ever-expanding array of new solutions, but effective design requires the development of tailored strategies for analysis and trajectory planning. To explore the essential elements of a multi-body problem, the model is extended to multiple gravitational bodies. Increasing the number of bodies in the model from two to three bodies increases the complexity significantly, but introduces the fundamental features associated with multiple gravitational forces. For the three bodies in the system, let P_1 be defined as the body with the largest mass, P_2 as the intermediate body, and P_3 as the body with the smallest mass. The two largest bodies, P_1 and P_2, are then denoted as the primary bodies in the system. The relative motion of the body of interest, P_3, with respect to the primaries in an inertial frame of reference results through the simplification of Equation (2.2). The expression in the form

$$\boldsymbol{r}''_{j3} + G\frac{m_3 + m_j}{r_{j3}^3}\boldsymbol{r}_{j3} = Gm_k\left(\frac{\boldsymbol{r}_{3k}}{r_{3k}^3} - \frac{\boldsymbol{r}_{jk}}{r_{jk}^3}\right), \tag{2.4}$$

reflects the two relative vector equations of motion for P_3 in an inertial frame. The indexes j and k in Equation (2.4) are equal to 1 or 2, with $k \neq j$. The relative motion in the three-body system is fully described when the relative position vectors $\boldsymbol{r}_{13}$ and $\boldsymbol{r}_{23}$, as well as the corresponding time derivatives, are known. In general, P_3 influences the positions of P_1 and P_2. Thus, solving for the time history of the motion of P_3 analytically requires 12 integrals of motion, which would also include a solution for the relative positions of the primaries. But only 10 constants are available.

Simplification of the relative three-body model is achieved by imposing assumptions on the system. First, the mass of P_3 is assumed to be of negligible significance ($m_3 << m_1, m_2$), implying that the motion of P_3 no longer impacts the motion of primaries P_1 and P_2. As an isolated two-body system, the primaries orbit the center of mass of the system (the barycenter B) in closed conic orbits. Although it is not necessary, the closed conic path of the primaries is selected to be circular for simplicity in the analysis.

A more elegant approach to describe the motion exists by reformulating the equations of motion in a rotating frame rather than an inertial frame. As a consequence of Keplerian primary motion, P_1 and P_2 move about the barycenter, B, in circular orbits and remain in a fixed plane of motion. The inertial frame, I ($\hat{\boldsymbol{I}} - \hat{\boldsymbol{J}} - \hat{\boldsymbol{K}}$), is then defined with the origin at B and the $\hat{\boldsymbol{K}}$ axis oriented parallel to the orbital angular momentum vector of the primaries. At some arbitrary epoch, the $\hat{\boldsymbol{I}}$ axis rests on the line adjoining P_1 and P_2, directed from B to P_2. The right-handed triad that represents the inertial frame is completed by defining $\hat{\boldsymbol{J}}$ as the cross product of $\hat{\boldsymbol{K}}$ and $\hat{\boldsymbol{I}}$. The inertial frame is displayed in Figure 2.2 for an arbitrary $P_1 - P_2$ system as a set of black axes with the origin at B. Note that the $\hat{\boldsymbol{K}}$ axis is directed out of the page. The rotating coordinate frame, R ($\hat{\boldsymbol{x}} - \hat{\boldsymbol{y}} - \hat{\boldsymbol{z}}$), possesses the same origin as the inertial frame (B); however, the $\hat{\boldsymbol{x}}$ axis rotates with the primaries such that $\hat{\boldsymbol{x}}$ is always directed from B to P_2. The $\hat{\boldsymbol{z}}$ axis is coincident with the $\hat{\boldsymbol{K}}$ axis and is the axis of rotation between the two frames. The $\hat{\boldsymbol{y}}$ axis is perpendicular to $\hat{\boldsymbol{x}}$, while in the primary plane of motion, and completes the right-handed triad. Red, green, and blue vectors represent the $\hat{\boldsymbol{x}}$, $\hat{\boldsymbol{y}}$, and $\hat{\boldsymbol{z}}$ axes of the rotating frame in Figure 2.2; the blue $\hat{\boldsymbol{z}}$ axis is directed out of the page.

The transformation between the inertial and rotating frames highlights the differences between the vector components associated with each set of unit vectors. If θ serves as the angle of rotation between the frames at some arbitrary time as illustrated in Figure 2.2, a vector expressed in terms of inertial frame coordinates is rewritten in rotating frame

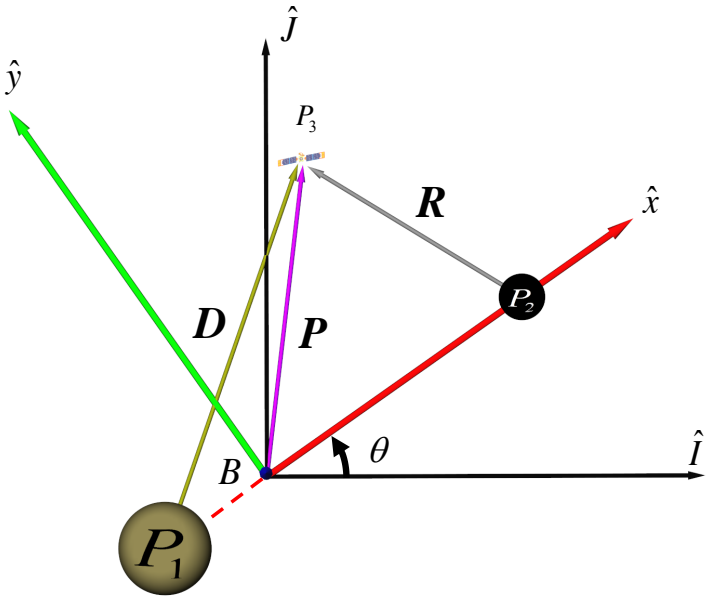

Figure 2.2. Inertial and rotating coordinate frames that serve as the framework for a mathematical formulation in the CRTBP.

coordinates through multiplication with the appropriate direction cosine matrix. The transformation of position coordinates from the inertial frame to the rotating frame appears as

$$\begin{Bmatrix} \hat{\boldsymbol{x}} \\ \hat{\boldsymbol{y}} \\ \hat{\boldsymbol{z}} \end{Bmatrix} = {}^{I}L^{R} \begin{Bmatrix} \hat{\boldsymbol{I}} \\ \hat{\boldsymbol{J}} \\ \hat{\boldsymbol{K}} \end{Bmatrix}. \tag{2.5}$$

The direction cosine matrix for the rotation from I to R is defined as

$${}^{I}L^{R} = \begin{bmatrix} \cos\theta & -\sin\theta & 0 \\ \sin\theta & \cos\theta & 0 \\ 0 & 0 & 1 \end{bmatrix}. \tag{2.6}$$

The inverse transformation results by multiplying Equation (2.5) by the transpose of ${}^{I}L^{R}$ from the left. Vector derivatives are, of course, impacted by the motion of frame R. Let ${}^{I}\boldsymbol{\omega}^{R}$ denote the angular velocity vector of the rotating frame relative to the inertial frame.

Since frame R is defined through a rotation of θ about the $\hat{\boldsymbol{K}}$ axis, ${}^{I}\boldsymbol{\omega}^{R}$ is determined as the time rate of change of θ, i.e.,

$$ {}^{I}\boldsymbol{\omega}^{R} = \frac{d\theta}{dt}\hat{\boldsymbol{K}} = \frac{d\theta}{dt}\hat{\boldsymbol{z}} = \theta'\hat{\boldsymbol{z}}. \tag{2.7} $$

Again, the prime notation indicates a derivative with respect to dimensional time. The basic kinematic equation (BKE) relates a derivative as viewed by two different observers. For this application, the BKE applied to some arbitrary vector $\boldsymbol{a}$ has the form

$$ \frac{{}^{I}d\boldsymbol{a}}{dt} = \frac{{}^{R}d\boldsymbol{a}}{dt} + {}^{I}\boldsymbol{\omega}^{R} \times \boldsymbol{a}. \tag{2.8} $$

Here, the time rate of change of $\boldsymbol{a}$ with respect to a rotating observer, $\frac{{}^{R}d\boldsymbol{a}}{dt}$, is transformed to a derivative with respect to an inertial observer, $\frac{{}^{I}d\boldsymbol{a}}{dt}$.

As determined by Euler in 1772 [32], the formulation of the equations of motion relative to a rotating frame uses the Keplerian motion of the primaries to produce the motion of P_3 with respect to the barycenter. Given the assumptions consistent with the CRTBP, only one second-order vector differential equation is required to model the motion of P_3. Incorporating the law of gravity to model the forces due to the primaries, the vector form of Newton's second law of motion yields the following

$$ \boldsymbol{P}'' = -\frac{Gm_1\boldsymbol{D}}{D^3} - \frac{Gm_2\boldsymbol{R}}{R^3}, \tag{2.9} $$

where $\boldsymbol{P}$ corresponds to the vector from B to P_3 [29,33,34]. The relative vectors $\boldsymbol{r}_{13}$ and $\boldsymbol{r}_{23}$ from Equation (2.4) are redefined as $\boldsymbol{D}$ and $\boldsymbol{R}$, respectively. The double-prime notation ($''$) represents the second-order derivative with respect to dimensional time. For convenience, the equations of motion are nondimensionalized such that the gravitational constant, G, becomes unity. Let the magnitude of the vector from B to P_1 be defined as $\|\overrightarrow{BP_1}\|$ and the magnitude of the vector from B to P_2 be $\|\overrightarrow{BP_2}\|$. The characteristic length (l^*), mass (m^*), and time (t^*) are then defined as follows:

$$ l^* = \|\overrightarrow{BP_1}\| + \|\overrightarrow{BP_2}\|, \tag{2.10} $$

$$m^* = m_1 + m_2, \tag{2.11}$$

$$t^* = \left[\frac{l^{*3}}{Gm^*}\right]^{\frac{1}{2}}. \tag{2.12}$$

The nondimensional mass parameter, μ, represents the nondimensional mass $\frac{m_2}{m^*}$, and the nondimensional mass $\frac{m_1}{m^*}$ is written $1-\mu$. If $\boldsymbol{\rho}$ is the nondimensional position vector of P_3 with respect to B, then it now appears as a nondimensional vector such that

$$\boldsymbol{\rho} = \frac{\boldsymbol{P}}{l^*} = x\hat{\boldsymbol{x}} + y\hat{\boldsymbol{y}} + z\hat{\boldsymbol{z}}, \tag{2.13}$$

where x, y, and z are the scalar components corresponding to the rotating frame. Then, the nondimensional representation of Equation (2.9) is rewritten as

$$\ddot{\boldsymbol{\rho}} = -\frac{(1-\mu)\,\boldsymbol{d}}{r_1^3} - \frac{\mu \boldsymbol{r}}{r_2^3}. \tag{2.14}$$

If nondimensional time is represented as

$$\tau = \frac{t}{t^*}, \tag{2.15}$$

then the dot notation symbolizes a derivative with respect to nondimensional time. The vectors $\boldsymbol{r}_1$ and $\boldsymbol{r}_2$ are the nondimensional counterparts of $\boldsymbol{D}$ and $\boldsymbol{R}$, respectively. The nondimensional vectors from the B to P_1 and P_2 are then

$$\frac{\overrightarrow{BP_1}}{l^*} = -\mu\hat{\boldsymbol{x}}, \tag{2.16}$$

$$\frac{\overrightarrow{BP_2}}{l^*} = (1-\mu)\,\hat{\boldsymbol{x}}. \tag{2.17}$$

With these relationships, vector addition constructs $\boldsymbol{d}$ and $\boldsymbol{r}$ such that

$$\boldsymbol{r}_1 = (x+\mu)\hat{\boldsymbol{x}} + y\hat{\boldsymbol{y}} + z\hat{\boldsymbol{z}}, \tag{2.18}$$

$$\boldsymbol{r}_2 = (x-1+\mu)\hat{\boldsymbol{x}} + y\hat{\boldsymbol{y}} + z\hat{\boldsymbol{z}}. \tag{2.19}$$

The right side of Equation (2.14) is available in terms of nondimensional rotating components.

The kinematic expansion of the left side of Equation (2.14) is required to deliver the scalar component form of the equations of motion. The acceleration, $\ddot{\boldsymbol{\rho}}$, is a second-order derivative with respect to an inertial observer, so the BKE is required. Since the primaries are assumed to be in circular motion, the rotational rate between the inertial and rotating frames is assumed to be a constant; it is evaluated simply as the nondimensional mean motion about the $\hat{\boldsymbol{z}}$ axis. For circular orbits, the nondimensional mean motion, n, is unity since,

$$n = Nt^* = \left[\frac{Gm^*}{l^{*3}}\right]^{\frac{1}{2}} \left[\frac{l^{*3}}{Gm^*}\right]^{\frac{1}{2}} = 1. \tag{2.20}$$

The BKE (Equation (2.8)) is applied twice such that

$$\dot{\boldsymbol{\rho}} = \frac{{}^I d\boldsymbol{\rho}}{d\tau} = \frac{{}^R d\boldsymbol{\rho}}{d\tau} + {}^I\boldsymbol{\omega}^R \times \boldsymbol{\rho}, \tag{2.21}$$

$$\ddot{\boldsymbol{\rho}} = \frac{{}^I d\dot{\boldsymbol{\rho}}}{d\tau} = \frac{{}^R d\dot{\boldsymbol{\rho}}}{d\tau} + {}^I\boldsymbol{\omega}^R \times \dot{\boldsymbol{\rho}}. \tag{2.22}$$

Thus, the kinematic expansion reflecting the acceleration of P_3 relative to B as viewed by an inertial observer is evaluated as

$$\ddot{\boldsymbol{\rho}} = (\ddot{x} - 2n\dot{y} - n^2 x)\hat{\boldsymbol{x}} + (\ddot{y} + 2n - n^2 y)\hat{\boldsymbol{y}} + \ddot{z}\hat{\boldsymbol{z}}. \tag{2.23}$$

The expression in Equation (2.23) is substituted into the vector equation of motion in Equation (2.14). Then, the scalar second-order differential equations governing the motion of P_3 are written as

$$\ddot{x} - 2n\dot{y} - n^2 x = -\frac{(1-\mu)(x+\mu)}{r_1^3} - \frac{\mu(x-1+\mu)}{r_2^3}, \tag{2.24}$$

$$\ddot{y} + 2n\dot{x} - n^2 y = -\frac{(1-\mu)y}{r_1^3} - \frac{\mu y}{r_2^3}, \tag{2.25}$$

$$\ddot{z} = -\frac{(1-\mu)z}{r_1^3} - \frac{\mu z}{r_2^3}, \tag{2.26}$$

where the nondimensional distances are

$$r_1 = \|\boldsymbol{r}_1\| = \sqrt{((x+\mu)^2 + y^2 + z^2)}, \tag{2.27}$$

$$r_2 = \|\boldsymbol{r}_2\| = \sqrt{((x-1+\mu)^2 + y^2 + z^2)}. \tag{2.28}$$

The expressions in Equations (2.24)–(2.26) constitute the dynamical model for the circular restricted three-body problem (CRTBP) [29, 33, 34].

The relative masses in some representative systems appear in Table 2.1. The Hénon system refers to an example where both primaries possess the same mass which is similar to a binary-star system. However, no dimensional units are associated with the Hénon system because an actual system with such a configuration does not exist. Characteristic quantities for the same systems are summarized in Table 2.2.

System	GM_1 (km^3/s^2)	GM_2 (km^3/s^2)	μ
Hénon	1 unit	1 unit	0.5
Earth-Moon	3.986004418×10^{5}	4.9027949×10^{3}	$1.2150571430596\times10^{-2}$
Sun-Earth	1.327122×10^{11}	3.986004418×10^{5}	$3.0034860744462\times10^{-6}$
Jupiter-Europa	1.26686535×10^{8}	3.202739×10^{3}	$2.5280177046369\times10^{-5}$
Saturn-Titan	3.7940585×10^{7}	8.9781382×10^{3}	$2.3658080508871\times10^{-4}$
Saturn-Enceladus	3.7940585×10^{7}	7.2027×10^{0}	$1.8984152807945\times10^{-7}$

Table 2.1 Characteristic masses for several CRTBP systems [35].

System	Abbr.	R_1 (km)	R_2 (km)	l^* (km)	t^* (days)
Hénon	H	N/A	N/A	1 dist. unit	1 time unit
Earth-Moon	EM	6378.1	1738.2	384388.2	4.34228
Sun-Earth	SE	695990.0	6378.1	149597886.0	58.13242
Jupiter-Europa	JE	71492.0	1560.8	671100.0	0.56532
Saturn-Titan	ST	60268.0	2574.7	1221865.0	2.53757
Saturn-Enceladus	SEnc	60268.0	252.1	238042.0	0.21823

Table 2.2 Abbreviations, characteristic quantities, and body radii (denoted R_1 and R_2 for P_1 and P_2, respectively) for several CRTBP systems [35].

2.4 The Pseudo-Potential Function

The equations of motion for the CRTBP (Equations (2.24)–(2.26)) can also be written in terms of a potential function. The nondimensional formulation for the gravity potential,

$$U = \frac{(1-\mu)}{r_1} + \frac{\mu}{r_2}, \tag{2.29}$$

does not apply to the equation of motion in Equation (2.14) for the CRTBP because the frame of reference is rotating. However, an augmented potential function, Υ, includes the original gravity potential yet accommodates the rotating elements. The pseudo-potential function, Υ, is defined as

$$\Upsilon = \frac{1-\mu}{r_1} + \frac{\mu}{r_2} + \frac{1}{2}n^2\left(x^2+y^2\right). \tag{2.30}$$

The third term in Equation (2.30) incorporates the Coriolis effect from the rotating frame [29]. The equations are then rewritten in the form

$$\ddot{x} - 2n\dot{y} = \frac{\partial \Upsilon}{\partial x}, \tag{2.31}$$

$$\ddot{y} + 2n\dot{x} = \frac{\partial \Upsilon}{\partial y}, \tag{2.32}$$

$$\ddot{z} = \frac{\partial \Upsilon}{\partial z}, \tag{2.33}$$

where the partials represent applications of the gradient ($\boldsymbol{\nabla}_i \Upsilon$) such that

$$\frac{\partial \Upsilon}{\partial x} = \Upsilon_x = x - \frac{(1-\mu)(x+\mu)}{r_1^3} - \frac{\mu(x-1+\mu)}{r_2^3}, \tag{2.34}$$

$$\frac{\partial \Upsilon}{\partial y} = \Upsilon_y = y - \frac{(1-\mu)y}{r_1^3} - \frac{\mu y}{r_2^3}, \tag{2.35}$$

$$\frac{\partial \Upsilon}{\partial z} = \Upsilon_z = -\frac{(1-\mu)z}{r_1^3} - \frac{\mu z}{r_2^3}. \tag{2.36}$$

Hence, Equations (2.31)–(2.33) summarize the equations of motion for the CRTBP written in terms of the pseudo-potential function.

2.5 Equilibrium Points

Investigation of the motion in the CRTBP is initiated by isolating equilibrium solutions. If the velocity and acceleration relative to the rotating frame is equal to zero in Equations (2.31)–(2.33), conditions for the equilibrium solutions result, i.e.,

$$\Upsilon_x = \Upsilon_y = \Upsilon_z = 0. \tag{2.37}$$

The roots of Equation (2.37) determine the equilibrium points. Dynamically, the equilibrium solutions in the CRTBP represent locations where gravitational and centrifugal forces balance such that a spacecraft at the exact equilibrium location, with no velocity or acceleration relative to the rotating frame, is fixed indefinitely. The equilibrium points are sometimes labeled the libration or Lagrange points.

A total of five equilibrium points exist in the CRTBP, as determined by Lagrange in 1772 [33]. The solution for the z component in Equation (2.37) results in all of the equilibrium points being restricted to the xy plane. Three collinear points are located on the $\hat{x}$-axis with L_1 between P_1 and P_2, L_2 on the far side of P_2 ($+\hat{\boldsymbol{x}}$), and L_3 is located on the far side of P_1 ($-\hat{\boldsymbol{x}}$). The L_4 and L_5 points form equilateral triangles with the two primaries and the $\hat{x}$-axis. Figure 2.3 displays the general location of the five equilibrium points with respect to P_1 and P_2.

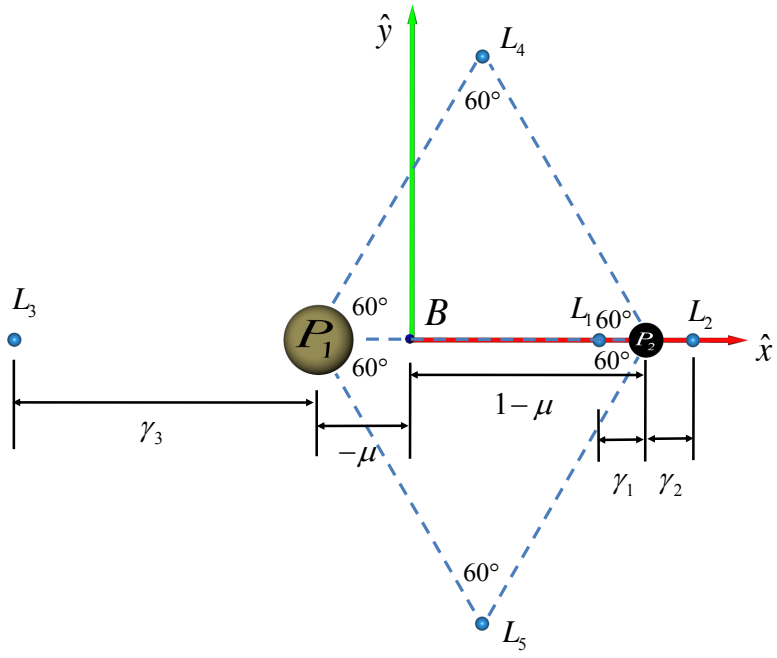

Figure 2.3. Positions and characteristic distances for the Lagrange points of a generic system.

Numerical analysis is required to compute the actual x values corresponding to the collinear points. The collinear points are described mathematically in terms of the distance

from the closest primary, labeled γ_i with $i = 1, 2, 3$ as indicated in Figure 2.3. Assuming $y = 0$ to produce $\Upsilon_y = 0$, expansion and rearrangement of the first expression in Equation (2.37) leads to the function

$$f(x) = \Upsilon_x = x - \frac{(1-\mu)(x+\mu)}{|x+\mu|^3} - \frac{\mu(x-1+\mu)}{|x-1+\mu|^3} = 0, \tag{2.38}$$

for the collinear points ($y = z = 0$, $n = 1$). The absolute values in Equation (2.38) are added since the denominators are strictly distances. If γ_1 denotes the distance from P_2 to L_1, then the value of x_{L_1} is equal to the quantity $1 - \mu - \gamma_1$. This value enters Equation (2.38) to produce

$$(1 - \mu - \gamma_1) = \frac{(1-\mu)}{(1-\gamma_1)^2} - \frac{\mu}{\gamma_1^2}. \tag{2.39}$$

In a similar manner, defining x_{L_2} as $1 - \mu + \gamma_2$ leads to a function for the determination of the L_2 position, that is,

$$(1 - \mu + \gamma_2) = \frac{(1-\mu)}{(1+\gamma_2)^2} + \frac{\mu}{\gamma_2^2}, \tag{2.40}$$

and the L_3 position is determined from x_{L_3} expressed as $-(\mu + \gamma_3)$, which yields

$$(\mu + \gamma_3) = \frac{(1-\mu)}{\gamma_3^2} + \frac{\mu}{(1+\gamma_3)^2}. \tag{2.41}$$

A numerical root-finding algorithm, such as a Newton-Rhapson, bisection, or regula falsi procedure, is applied to Equation (2.39) and isolates the Lagrange point positions in terms of the values of γ_i [36]. The values of γ_i for four different systems are listed in Table 2.3. In addition, the x_{L_i} counterparts of γ_i are displayed in Table 2.4. Given the functional form of Equations (2.39)–(2.41), the mass parameter of the system clearly influences the location of the collinear points. As μ increases, L_1 and L_2 move away from P_2 while L_3 shifts closer to both primaries. As a general trend, for smaller μ values (such as values less than that for the Earth-Moon system), L_1 and L_2 remain fairly close to P_2, and L_3 is positioned on the opposite side of P_1 at relatively the same distance as P_2 from P_1.

The locations for the L_4 and L_5 Lagrange points are available analytically. Considering Equation (2.35) with a non-zero y component, the relationship

$$1 - \frac{(1-\mu)}{r_1^3} - \frac{\mu}{r_2^3} = 0, \tag{2.42}$$

	NonDimensional		
System	γ_1	γ_2	γ_3
Hénon	0.5	0.6984061	0.6984061
Earth-Moon	0.1509342	0.1678327	0.9929121
Sun-Earth	0.0099704	0.0100371	0.9999982
Jupiter-Europa	0.0202106	0.0204867	0.9999853
Saturn-Titan	0.0422638	0.0434894	0.9998620
Saturn-Enceladus	0.0039797	0.0039902	0.9999999
	Dimensional (km)		
Hénon	N/A	N/A	N/A
Earth-Moon	5.801733×10^4	6.451290×10^4	3.816637×10^5
Sun-Earth	1.491552×10^6	1.501533×10^6	1.495976×10^8
Jupiter-Europa	1.356334×10^4	1.374860×10^4	6.710901×10^5
Saturn-Titan	5.164060×10^4	5.313821×10^4	1.221696×10^6
Saturn-Enceladus	9.473248×10^2	9.498448×10^2	2.380420×10^5

Table 2.3 Collinear Lagrange point distances from the primaries for various systems in the CRTBP.

	NonDimensional		
System	x_{L_1}	x_{L_2}	x_{L_3}
Hénon	0.0	1.1984061	-1.1984061
Earth-Moon	0.8369152	1.1556821	-1.0050626
Sun-Earth	0.9900266	1.0100341	-1.0000013
Jupiter-Europa	0.9797641	1.0204614	-1.0000105
Saturn-Titan	0.9574997	1.0432528	-1.0000986
Saturn-Enceladus	0.9960202	1.0039901	-1.0000001
	Dimensional (km)		
Hénon	N/A	N/A	N/A
Earth-Moon	3.217003×10^5	4.442305×10^5	-3.863341×10^5
Sun-Earth	1.481059×10^8	1.510990×10^8	-1.495981×10^8
Jupiter-Europa	6.575197×10^5	6.848316×10^5	-6.711071×10^5
Saturn-Titan	1.169935×10^6	1.274714×10^6	-1.221985×10^6
Saturn-Enceladus	2.370946×10^5	2.389918×10^5	-2.380420×10^5

Table 2.4 Collinear equilibrium point locations for various systems in the CRTBP.

must be satisfied. Only the condition $d = r = 1$ (in nondimensional units) fulfills Equation (2.42). Thus, L_4 and L_5 form equilateral triangles with the primaries and the $\hat{x}$-axis. With this fact, geometry dictates the x and y coordinates for the equilateral points to be

$$x_{L_{4,5}} = \frac{1}{2} - \mu, \tag{2.43}$$

$$y_{L_{4,5}} = \pm\frac{\sqrt{3}}{2}. \tag{2.44}$$

Note that, by convention, the L_5 point is the trailing point with $x_{L_5} = x_{L_4}$ and $y_{L_5} = -y_{L_4}$. The coordinates of the L_4 point for the various systems are summarized in Table 2.5. As is apparent in Equations (2.43) and (2.44), only the x coordinate of the equilateral points depends on μ, but both depend on the value of l^* in the dimensional case.

	NonDimensional	
System	x_{L_4}	y_{L_4}
Hénon	0.0	0.8660254
Earth-Moon	0.4878494	0.8660254
Sun-Earth	0.4999970	0.8660254
Jupiter-Europa	0.4999747	0.8660254
Saturn-Titan	0.4997634	0.8660254
Saturn-Enceladus	0.4999998	0.8660254
	Dimensional (km)	
Hénon	N/A	N/A
Earth-Moon	1.875236×10^5	3.328899×10^5
Sun-Earth	7.479849×10^7	1.295556×10^8
Jupiter-Europa	3.355330×10^5	5.811896×10^5
Saturn-Titan	6.106434×10^6	1.058166×10^6
Saturn-Enceladus	1.190210×10^5	2.061504×10^5

Table 2.5 Equilateral equilibrium point locations for various systems in the CRTBP.

2.6 The Jacobi Integral and Zero-Velocity Surfaces

Integrals of the motion reduce the dimensionality of dynamical systems and supply a basis for understanding the dynamical behavior. In the CRTBP, one integral of the motion exists as determined by Jacobi [33]. The Jacobi integral is isolated by computing the dot product between the equations of motion in terms of the pseudo-potential (Equations (2.34)-(2.36)) and the corresponding rotating frame velocity components, creating the result

$$\dot{x}\ddot{x} + \dot{y}\ddot{y} + \dot{z}\ddot{z} = \Upsilon_x\dot{x} + \Upsilon_y\dot{y} + \Upsilon_z\dot{z}. \tag{2.45}$$

Since Υ is strictly a function of position, the right side represents a total derivative of Υ. Thus, integration of Equation (2.45) with respect to nondimensional time, τ, results in the expression

$$\tfrac{1}{2}(\dot{x}^2 + \dot{y}^2 + \dot{z}^2) = \Upsilon - \frac{C}{2}, \tag{2.46}$$

where the third term is the integration constant expressed in a convenient form. If the magnitude of the relative velocity in the rotating frame, v, is defined as

$$v = \sqrt{\dot{x}^2 + \dot{y}^2 + \dot{z}^2}, \tag{2.47}$$

then the Jacobi integral is written as

$$v^2 = 2\Upsilon - C, \tag{2.48}$$

with the Jacobi constant, C, represented by

$$C = 2\Upsilon - v^2. \tag{2.49}$$

The Jacobi constant is similar to an energy expression since it is the difference between a term that reflects a kinetic energy (v^2) and a potential term (2Υ), but is associated with differential equations formulated in terms of a rotating frame. The six states ($\boldsymbol{x} = [x, y, z, \dot{x}, \dot{y}, \dot{z}]^T$) are essentially reduced to five by enforcing a specific value for the Jacobi

constant. Also, observing the Jacobi constant along a numerically integrated trajectory supplies a check on the accuracy of a numerical integration scheme.

The Jacobi constant clearly depends on the position and velocity states. The Jacobi constant is evaluated precisely at the Lagrange points with a velocity value in Equation (2.49) equal to 0 by definition. The values of Jacobi constant at each of the Lagrange points are summarized in Table 2.6 for various systems. The value of Jacobi constant

System	C_{L_1}	C_{L_2}	C_{L_3}	$C_{L_{4,5}}$
Hénon	4.000000	3.456796	3.456796	2.750000
Earth-Moon	3.188341	3.172160	3.012147	2.987997
Sun-Earth	3.000891	3.000887	3.000003	2.999997
Jupiter-Europa	3.003643	3.003609	3.000025	2.999975
Saturn-Titan	3.015765	3.015449	3.000237	2.999763
Saturn-Enceladus	3.000142	3.000142	3.000000	2.999999

Table 2.6 Jacobi constant comparisons for Lagrange points of different systems.

remains near 3.0 for the cases indicated, yet the range from L_1 to $L_{4,5}$ widens for larger values of μ. Note that the Jacobi constant for the L_4 and L_5 points are equal since the Jacobi constant depends on x^2 and y^2. As it is defined, the Jacobi constant decreases to access Lagrange points in an ascending order.

A powerful application of the Jacobi constant concept is realized in the formation of a surface that separates viable regions for the flow. If the relative velocity is zero, the Jacobi constant is a function of position only; more specifically,

$$C = x^2 + y^2 + \frac{2\,(1-\mu)}{r_1} + \frac{2\mu}{r_2}. \tag{2.50}$$

This relationship actually corresponds to the equation of a surface, historically denoted as the zero-velocity surface. Extraction of the zero-velocity surface for a specific value of Jacobi constant is achieved by solving an isovalue problem based on Equation (2.50). In many visualization algorithms, the isocontour is created using a marching-squares algorithm in a 2D application or a marching-cubes algorithm to produce a 3D surface [37]. A planar intersection of the zero-velocity surface in the Hénon system for $C = 3.75$ appears in Figure 2.4. In this figure, the two black curves represent the intersection of the zero-velocity surface and the xy plane (labeled the zero-velocity curve). The gray region between the black curves

is not available since the back-substitution of the position state and Jacobi constant value into the Jacobi integral expression (Equation (2.48)) yields a complex value of velocity in this region. This region that cannot be reached via a 'real' value of velocity is frequently denoted the "forbidden region." Thus, zero-velocity curves, as well as the zero-velocity surfaces, represent a boundary for possible motion at the given C value. In Figure 2.4, all initial states within the interior, peanut-shaped zero-velocity curve remain in the vicinity of the primaries; any initial conditions beyond the outer, near-circular zero-velocity curve remain exterior to the system.

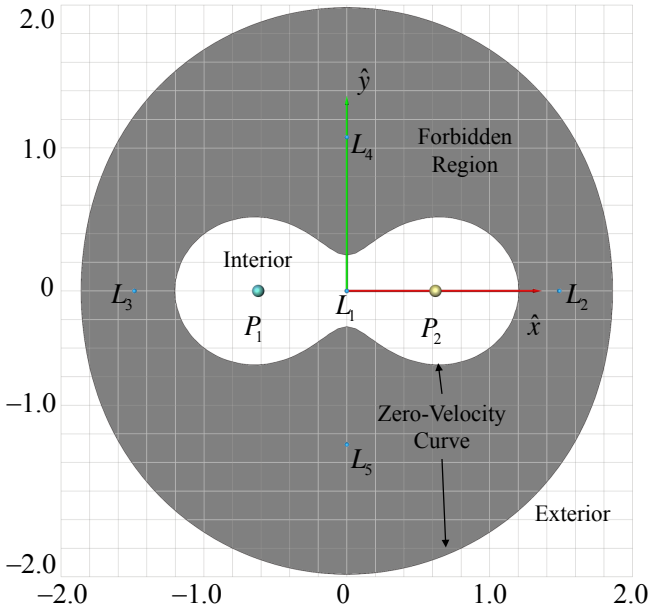

Figure 2.4. Regions of motion bounded by the zero-velocity curve in the xy plane as computed for the Hénon system at $C = 3.75$.

Multiple isocontours of the zero-velocity surface that bisect the xy plane demonstrate the evolution of the zero-velocity curve as the Jacobi constant value declines. In Figure 2.5, several zero-velocity curves in both the Hénon and Earth-Moon systems are plotted and colored by the value of Jacobi constant. These xy planar intersections reflect the fact that the zero-velocity surfaces change shape as the Jacobi constant, as well as the system parameter, vary. In the Hénon system, the zero-velocity surface initially appears as two

ovoids surrounding the primaries with a boundary encircling the perimeter for a Jacobi constant value that is relatively high ($C > C_{L_1} = 4.0$). As the value of Jacobi constant descends to C_{L_1}, the interior ovoids expand outwards and both collapse toward the L_1 point. The extruding pieces of the interior regions connect and open up when the Jacobi constant passes through the value corresponding to L_1, C_{L_1}. The Jacobi constant is then representative of the region $C_{L_{2,3}} < C < C_{L_1}$. The open connection represents a gateway between the P_1 and P_2 vicinities, that is, flow between the primaries is possible for the values in this range of Jacobi constant. While the interior regions connect and expand outwards in this range, the exterior bounding curve contracts and elongates in the $\hat{\boldsymbol{y}}$ direction. The interior and exterior curves meet at the L_2 and L_3 points when $C = C_{L_{2,3}}$ and separate as C decreases further. In the region $C_{L_{4,5}} < C < C_{L_{2,3}}$, new gateways form between the interior and exterior regions in the vicinity of the L_2 and L_3 points, allowing flow from the interior to exterior regions or vice versa. The zero-velocity curves eventually collapse towards the L_4 and L_5 as the Jacobi constant approaches $C_{L_{4,5}}$ and actually disappear from the xy plane when $C < C_{L_{4,5}}$.

The xy planar intersections, i.e., the zero-velocity curves, in the Earth-Moon system (Figure 2.5(b)) behave in a manner similar to the Hénon system with some visually apparent differences. Since the μ value in the Earth-Moon system is significantly lower than that of the Hénon system, the impact of P_1 (Earth) on the zero-velocity surface is much more significant than in the Hénon case. The zero-velocity surface shifts with the Lagrange points toward the P_2 vicinity. This decrease in μ also adds a transition region that clarifies the behavior of the zero-velocity surfaces in the L_3 region as $C_{L_3} \neq C_{L_2}$ when $\mu \neq 0.5$. Thus, a gateway near L_3 opens at $C = C_{L_3}$ and expands as the Jacobi constant approaches $C_{L_{4,5}}$.

Advances in scientific visualization allow a 3D display of the zero-velocity surface for a given value of Jacobi constant. The out-of-plane behavior of the surface is apparent when applying an isosurface extraction algorithm (e.g., marching cubes) on the scalar field of data that is represented by Equation (2.50). The images in Figures 2.6–2.8 are created from an isosurface extraction for a variety of Jacobi constants on a $200 \times 200 \times 200$ uniformly spaced grid in the Earth-Moon system. The range of grid points along the $\hat{\boldsymbol{x}}$, $\hat{\boldsymbol{y}}$, and $\hat{\boldsymbol{z}}$ axes are all in the closed interval $[-1.5, 1.5]$ in nondimensional units or $[-576582.261, 576582.261]$ km. The Earth and Moon models are scaled by a factor of 4 for easier visual acquisition.

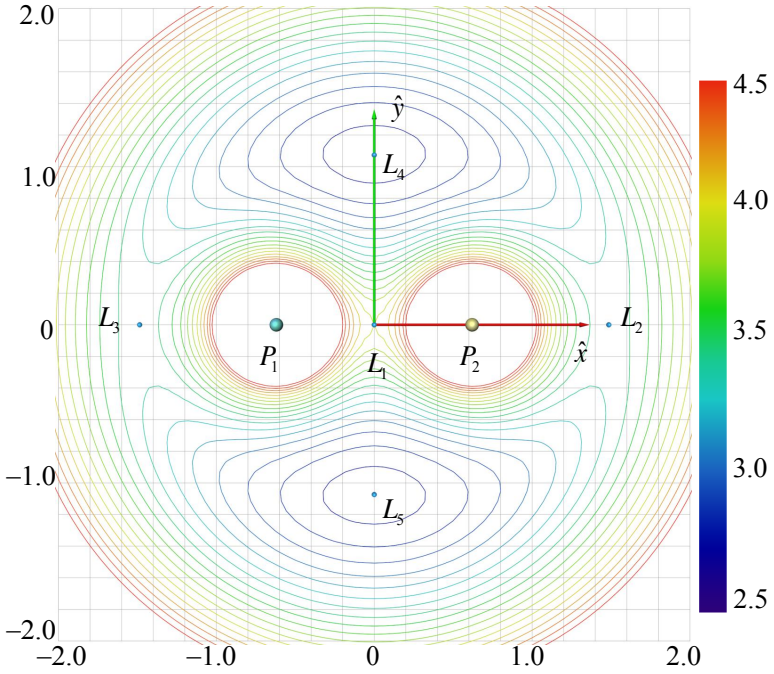

(a) Hénon System

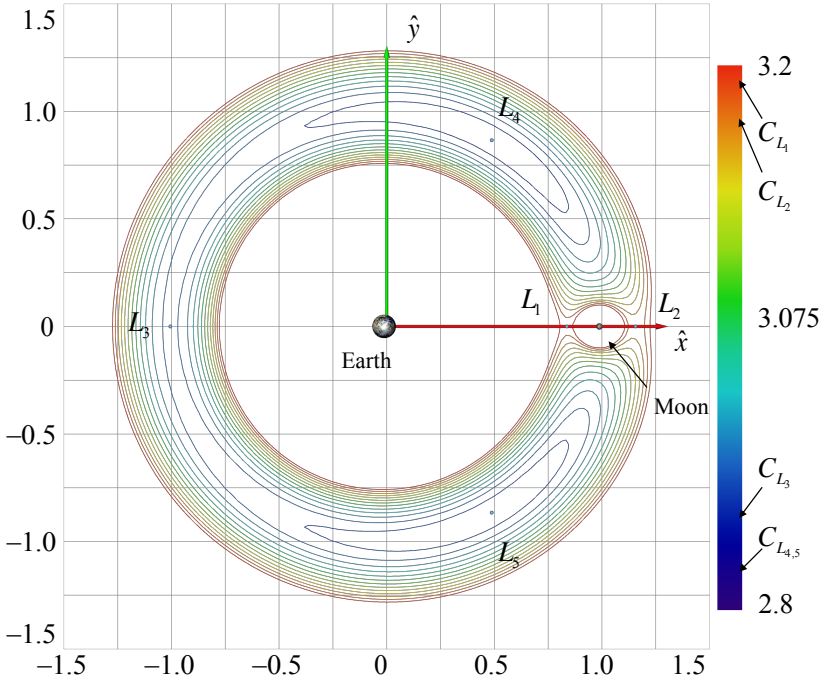

(b) Earth-Moon System (Nondimensional Units)

Figure 2.5. Multiple zero-velocity curves in the xy plane for two systems, colored by Jacobi constant.

The evolution of the zero-velocity surfaces is consistent with the previous projections, but new information is available from the 3D perspective. For Jacobi constants greater than C_{L_1}, the zero-velocity surface consists of two near-ellipsoids that isolate the allowable motion to remain near the primaries and an exterior cylindrical surface that forbids entry into the system. As the Jacobi constant decreases through C_{L_1} to C_{L_2}, the perspective views in Figure 2.6 display the fact that the L_1 gateway expands in 3D space, exposing potential transfer access between P_1 and P_2 that exists above and below the xy plane. Note that the outer boundary of the zero-velocity surface dips towards the L_2 point and intersects the inner surface as C drops to C_{L_2} (Figure 2.6(d)). Reducing the Jacobi constant to a value between C_{L_1} and C_{L_2} creates a tunnel from the interior region to the exterior region as is evident in Figure 2.7. Although no actual flow is demonstrated, this tunnel reveals that three-body dynamics can be employed to deliver spacecraft to locations beyond the Earth-Moon confines and return them to Earth via close lunar encounters. The evolution of the zero-velocity surfaces for a range of Jacobi constant values $C_{L_{4,5}} < C < C_{L_3}$ is demonstrated in Figure 2.8. A gateway opens at L_3 that is relatively wide in the $\hat{\boldsymbol{y}}$ direction but narrow in the $\hat{\boldsymbol{z}}$ direction as the Jacobi value falls through C_{L_3} towards $C_{L_{4,5}}$ (Figure 2.8(a)). The gateway openings widen towards the L_4 and L_5 points as the Jacobi constant continues to decrease; however, the expansion in the $\hat{\boldsymbol{z}}$ direction is smaller than the growth in other directions. For $C < C_{L_{4,5}}$, the zero-velocity surface begins to detach from the xy plane and expands in the $\hat{\boldsymbol{z}}$ direction. Trajectory motion is allowed throughout the xy plane, yet locations above and below the xy plane are still excluded. With these 3D representations, the zero-velocity surface helps indicate the available behavior of trajectories at a specific value of Jacobi constant.

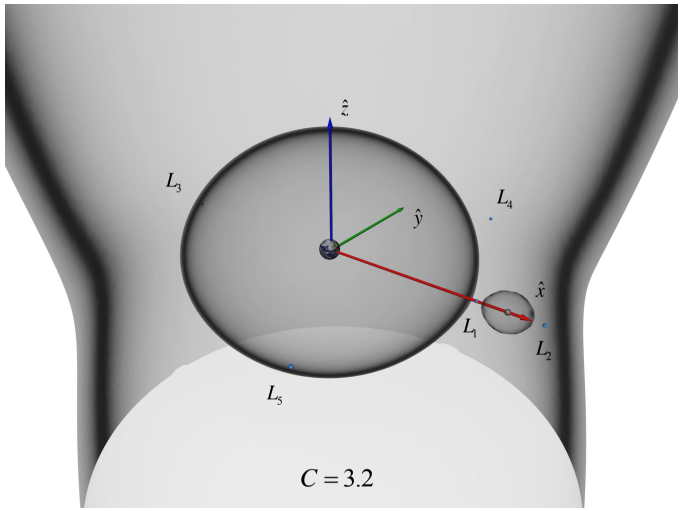

(a) $C > C_{L_1}$

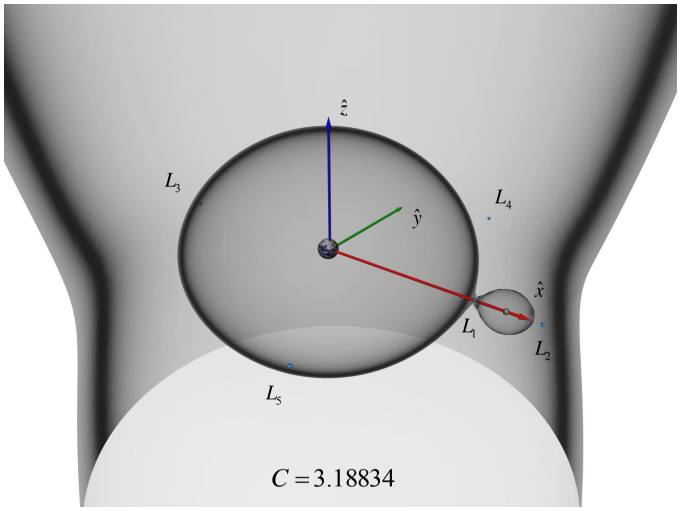

(b) $C = C_{L_1}$

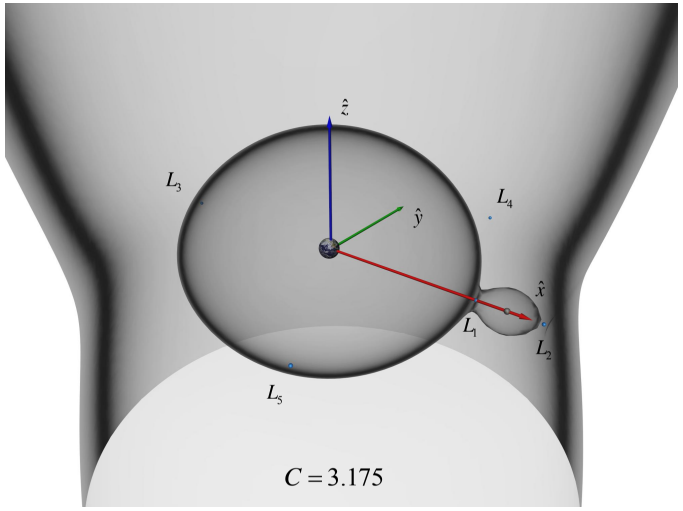

(c) $C_{L_2} < C < C_{L_1}$

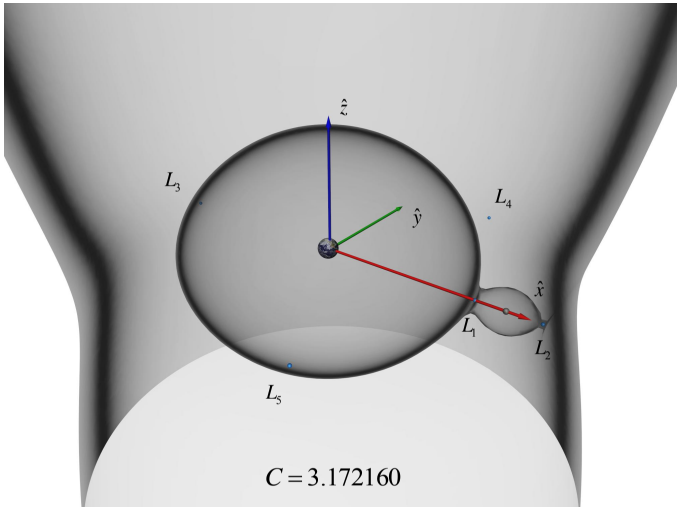

(d) $C = C_{L_2}$

Figure 2.6. Zero-velocity surfaces in the Earth-Moon system without access to the exterior region.

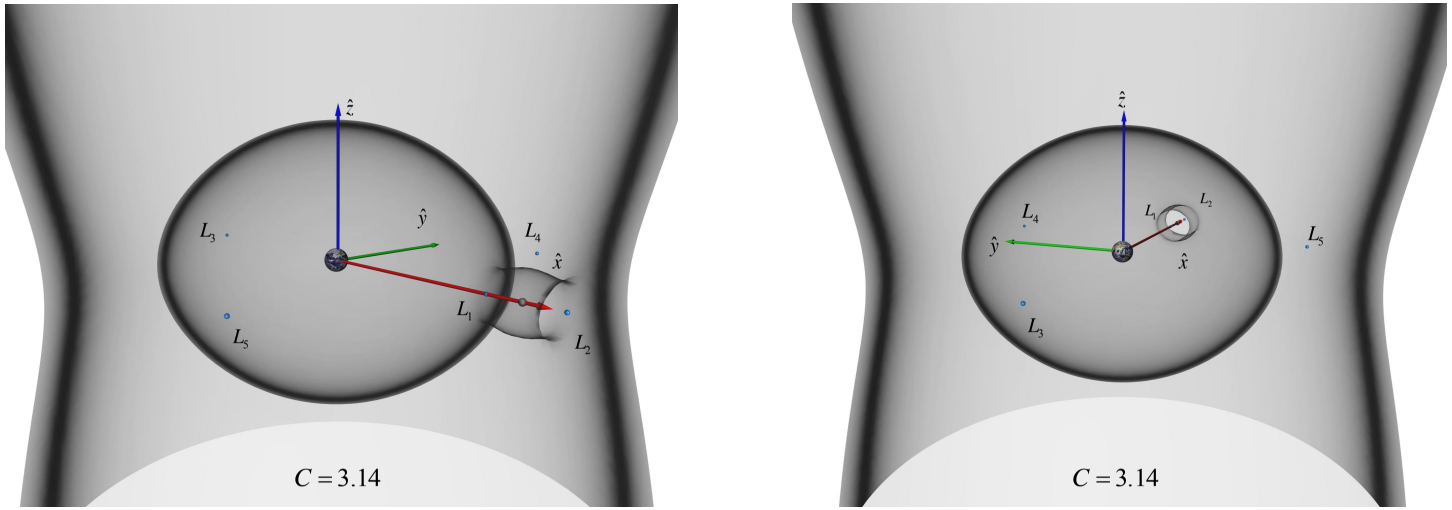

(a) (b)

Figure 2.7. Two views of a zero-velocity surface in the Earth-Moon system for a Jacobi constant value within the range $C_{L_3} < C < C_{L_2}$.

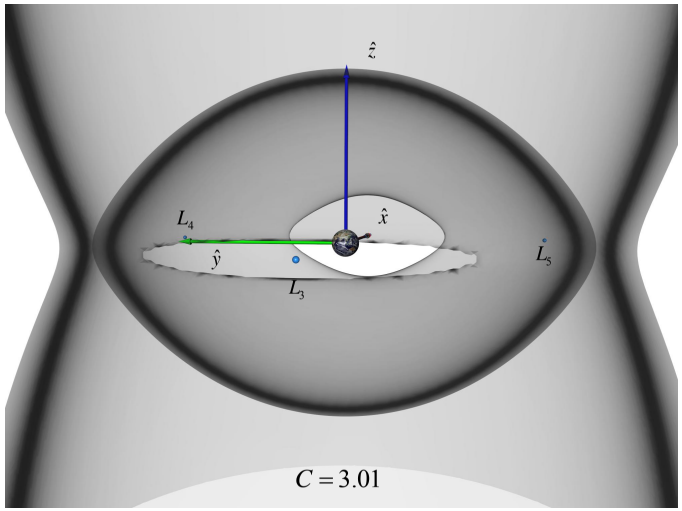

(a) $C_{L_{4,5}} < C < C_{L_3}$

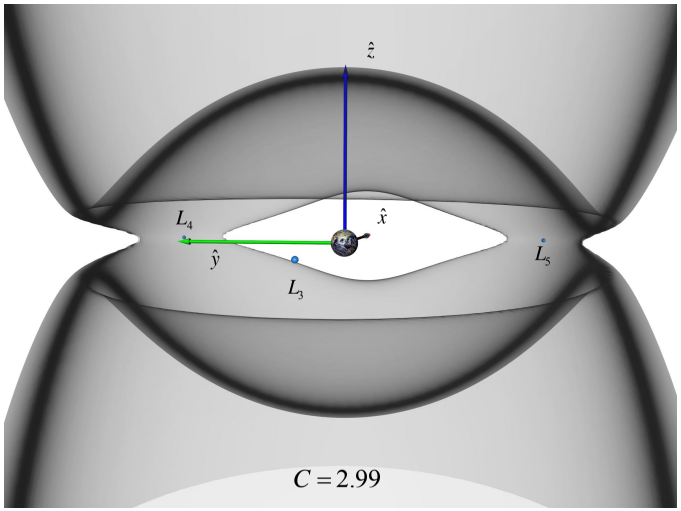

(b) $C_{L_{4,5}} < C < C_{L_3}$

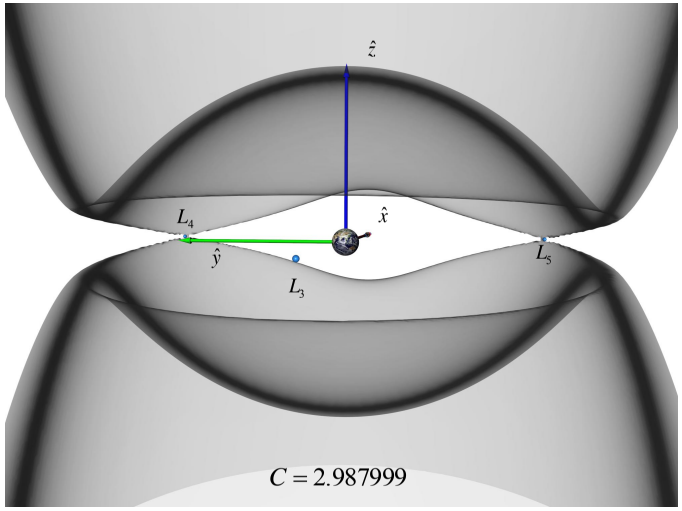

(c) $C = C_{L_{4,5}}$

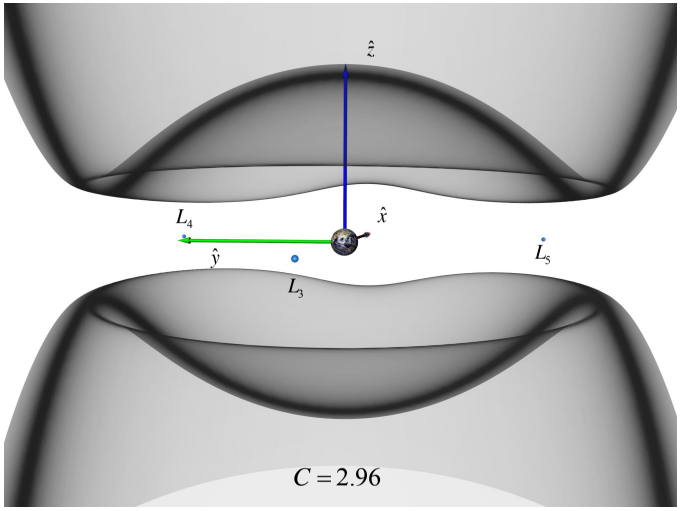

(d) $C < C_{L_{4,5}}$

Figure 2.8. Zero-velocity surfaces with exterior access in the Earth-Moon system.

3. DIFFERENTIAL CORRECTIONS WITH SHOOTING

Mission design frequently involves the task of computing trajectories that satisfy a set of mission constraints. Such constraints range in complexity from simply delivering a continuous trajectory with no maneuvers to advanced scenarios that incorporate many potentially competing constraints (e.g., maneuver costs below a specified threshold while maintaining path-specific and timing boundaries). The design of an acceptable trajectory typically relies on a differential corrections process that solves two-point boundary value problems (TPBVPs).

3.1 Fundamentals of Variational Analysis

Variational analysis resides at the core of any targeting procedure. Small changes in an upstream state result in a variety of downstream effects, for example, a slight modification that enables an asymptotic approach to a periodic orbit or forces chaotic motion. Thus, a small variation from a prescribed trajectory can be advantageous or detrimental to a particular mission depending on the size, type, and timing of the deviation. Quantification of sensitivity information, combined with a differential corrections procedure, allows mission designers to bias a trajectory to a set of preferred conditions [38–40]. Mathematical representations of sensitivity information exist through the variational equations and the state transition matrix.

3.1.1 State Transition Matrix

In a dynamical system such as the CRTBP, the state transition matrix (STM) is determined by first considering the variational equations. With the state elements defined in

terms of rotating coordinates as $\boldsymbol{x} = [x, y, z, \dot{x}, \dot{y}, \dot{z}]^T$, the CRTBP equations of motion are expressed as a set of first-order differential equations through the simple expression

$$\dot{\boldsymbol{x}} = \boldsymbol{\phi}(\boldsymbol{x}, \tau), \tag{3.1}$$

where $\boldsymbol{\phi}(\boldsymbol{x}, \tau)$ represents the flow map governed by Equations (2.24) – (2.26) and the nondimensional time parameter is denoted by τ. The six-dimensional (6D) state vector, $\boldsymbol{x}$, is modeled in terms of a nearby reference, $\boldsymbol{x}_0$, and a small variation from the reference state vector, $\delta\boldsymbol{x}$, that is,

$$\boldsymbol{x} = \boldsymbol{x}_0 + \delta\boldsymbol{x}. \tag{3.2}$$

If the variation is isochronous, then substituting Equation (3.2) into Equation (3.1) results in the expression

$$\dot{\boldsymbol{x}} + \delta\dot{\boldsymbol{x}} = \boldsymbol{\phi}(\boldsymbol{x} + \delta\boldsymbol{x}, \tau). \tag{3.3}$$

A Taylor series expansion of the right side of Equation (3.3) about the reference is truncated to first order and yields a linear relationship for the time rate of change of the variation, i.e., $\delta\dot{\boldsymbol{x}}$, in terms of the variation, $\delta\boldsymbol{x}$, written as

$$\delta\dot{\boldsymbol{x}} = \left.\frac{\partial\boldsymbol{\phi}}{\partial\boldsymbol{x}}\right|_{\boldsymbol{x}_0} \delta\boldsymbol{x} = A(\tau)\delta\boldsymbol{x}. \tag{3.4}$$

The symbol $A(\tau)$ reflects the matrix of the spatial derivatives of $\boldsymbol{\phi}(\boldsymbol{x}, \tau)$ in the form of

$$A(\tau) = \begin{pmatrix} \mathbf{0}_{3\times3} & I_{3\times3} \\ \Upsilon_{ij} & 2\Omega \end{pmatrix}, \tag{3.5}$$

where Υ_{ij} represents the 3×3 submatrix of second-order partial derivatives of the pseudo-potential, Υ, such that

$$\Upsilon_{ij} = \frac{\partial^2\Upsilon}{\partial i \partial j}. \tag{3.6}$$

The i and j indexes are evaluated over the position components x, y, and z. The constant Ω submatrix is defind as

$$\Omega = \begin{pmatrix} 0 & 1 & 0 \\ -1 & 0 & 0 \\ 0 & 0 & 0 \end{pmatrix}, \tag{3.7}$$

and incorporates the effects of the rotational rate of the system. The $A(\tau)$ matrix is a time-varying map since the elements are evaluated along the reference solution $\boldsymbol{x}_0$. If the reference solution is periodic, then $A(\tau)$ is also periodic. However, the $A(\tau)$ matrix is constant when the reference solution is constant such as an equilibrium point.

Solving the variational equations yields the definition of the STM. The general solution to the variational equations in Equation (3.4) possesses the form

$$\delta\boldsymbol{x}(\tau) = \Phi(\tau, \tau_0)\delta\boldsymbol{x}(\tau_0). \tag{3.8}$$

Here, the STM, $\Phi(\tau, \tau_0)$, is essentially a linear map relating the variation in the initial condition to the variations downstream that are associated with the final state based on a numerical simulation from τ_0 to τ. Thus, the STM is expressed as

$$\Phi(\tau, \tau_0) = \frac{\delta\boldsymbol{x}(\tau)}{\delta\boldsymbol{x}(\tau_0)} = \begin{pmatrix} \frac{\partial x}{\partial x_0} & \frac{\partial x}{\partial y_0} & \frac{\partial x}{\partial z_0} & \frac{\partial x}{\partial \dot{x}_0} & \frac{\partial x}{\partial \dot{y}_0} & \frac{\partial x}{\partial \dot{z}_0} \\ \frac{\partial y}{\partial x_0} & \frac{\partial y}{\partial y_0} & \frac{\partial y}{\partial z_0} & \frac{\partial y}{\partial \dot{x}_0} & \frac{\partial y}{\partial \dot{y}_0} & \frac{\partial y}{\partial \dot{z}_0} \\ \frac{\partial z}{\partial x_0} & \frac{\partial z}{\partial y_0} & \frac{\partial z}{\partial z_0} & \frac{\partial z}{\partial \dot{x}_0} & \frac{\partial z}{\partial \dot{y}_0} & \frac{\partial z}{\partial \dot{z}_0} \\ \frac{\partial \dot{x}}{\partial x_0} & \frac{\partial \dot{x}}{\partial y_0} & \frac{\partial \dot{x}}{\partial z_0} & \frac{\partial \dot{x}}{\partial \dot{x}_0} & \frac{\partial \dot{x}}{\partial \dot{y}_0} & \frac{\partial \dot{x}}{\partial \dot{z}_0} \\ \frac{\partial \dot{y}}{\partial x_0} & \frac{\partial \dot{y}}{\partial y_0} & \frac{\partial \dot{y}}{\partial z_0} & \frac{\partial \dot{y}}{\partial \dot{x}_0} & \frac{\partial \dot{y}}{\partial \dot{y}_0} & \frac{\partial \dot{y}}{\partial \dot{z}_0} \\ \frac{\partial \dot{z}}{\partial x_0} & \frac{\partial \dot{z}}{\partial y_0} & \frac{\partial \dot{z}}{\partial z_0} & \frac{\partial \dot{z}}{\partial \dot{x}_0} & \frac{\partial \dot{z}}{\partial \dot{y}_0} & \frac{\partial \dot{z}}{\partial \dot{z}_0} \end{pmatrix}. \tag{3.9}$$

The elements of $\Phi(\tau, \tau_0)$ approximate the change in a downstream state component due to the variations or perturbations in an upstream component.

The state sensitivities are dependent upon the initial positions and velocities as well as the length of the simulation. Thus, the STM depends on the initial state and time.

Differentiation of Equation (3.8), followed by substitution into Equation (3.4), produces the linear set of equations in a matrix form,

$$\dot{\Phi}(\tau, \tau_0) = A(\tau)\Phi(\tau, \tau_0), \tag{3.10}$$

that controls the progression of the STM. The initial condition associated with Equation (3.10) enforces the fact that the initial STM possesses no cross-component effect, or,

$$\Phi(\tau_0, \tau_0) = I_{6\times 6}. \tag{3.11}$$

Equation (3.10) is actually comprised of 36 first-order scalar differential equations that are numerically integrated to evaluate the STM at some time downstream. In a numerical integration process, these 36 differential equations are solved simultaneously with the six first-order equations of motion, resulting in a state vector with 42 elements.

3.1.2 Contemporaneous and Non-Contemporaneous Variation

Two types of state variations form the basis of many targeting techniques used in mission design: contemporaneous and non-contemporaneous variations. Consider a dynamical system with a reference path and a neighboring trajectory arc that is sufficiently close to the reference such that linear approximations are valid. A contemporaneous variation is defined by a vector, $\delta\boldsymbol{x}$, from a state on the reference path and the isochronous state on the nearby arc. Alternatively, the vector difference between a state on the reference path and another state on the nearby arc that is offset by a small, temporal variation, $\delta\tau$, is defined as the non-contemporaneous variation, $\delta\boldsymbol{q}$. A visual representation (see Figure 3.1) highlights the correspondence between the two types of variations. For a state on the reference arc at some arbitrary time, $\boldsymbol{x}_0(\tau)$, the contemporaneous variation, $\delta\boldsymbol{x}(\tau)$, appears as the red vector in Figure 3.1 directed towards the isochronous state on the nearby trajectory, $\boldsymbol{x}(\tau)$. Incorporating a small variation in time, $\delta\tau$, the non-contemporaneous variation, $\delta\boldsymbol{q}(\tau)$, is indicated by the purple vector in Figure 3.1.

The relationship between the two types of variations aids in predicting future deviations along a numerically integrated path. Let $\boldsymbol{\psi}$ represent the mapping function for a numerical

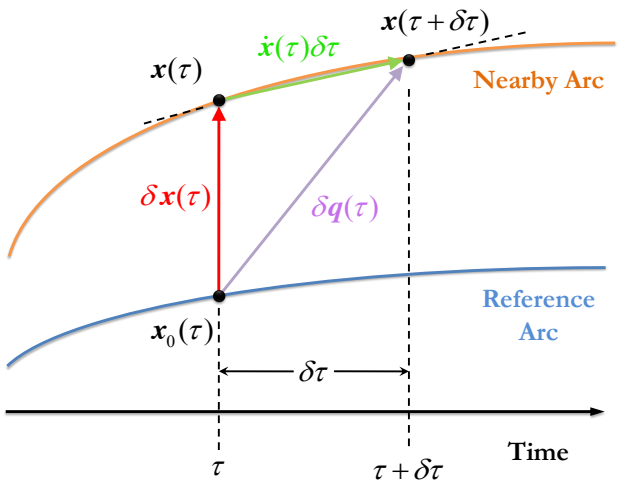

Figure 3.1. Schematic highlighting correspondence between types of variation [40].

integration procedure. A state along the reference arc is evaluated from the numerical integration process as

$$\boldsymbol{x}_0(\tau) = \boldsymbol{\psi}(\boldsymbol{x}_0(0), \tau), \tag{3.12}$$

where the initial state, $\boldsymbol{x}_0(0)$, is integrated forward from 0 to τ. If the small variations $\delta\boldsymbol{x}_0(0)$ and $\delta\tau$ are applied to the initial state on the reference arc as well as the integration time, respectively, then numerical integration results in a state on the nearby arc, i.e.,

$$\boldsymbol{x}(\tau+\delta\tau) = \boldsymbol{\psi}(\boldsymbol{x}_0(0) + \delta\boldsymbol{x}_0(0), \tau+\delta\tau). \tag{3.13}$$

The final state along the nearby trajectory is also represented as

$$\boldsymbol{x}(\tau+\delta\tau) = \boldsymbol{x}_0(\tau) + \delta\boldsymbol{q}(\tau). \tag{3.14}$$

Expanding Equation (3.13) in a Taylor series about the null variation and truncating the first-order terms produces the expression

$$\boldsymbol{x}(\tau+\delta\tau) = \boldsymbol{\psi}(\boldsymbol{x}_0, \tau) + \left.\frac{\partial\boldsymbol{\psi}}{\partial\boldsymbol{x}_0(0)}\right|_{\boldsymbol{x}_0(\tau)} \delta\boldsymbol{x}_0(0) + \left.\frac{\partial\boldsymbol{\psi}}{\partial\tau}\right|_{\boldsymbol{x}_0(\tau)} \delta\tau. \tag{3.15}$$

Recall Equation (3.9) and the STM, $\Phi_{\boldsymbol{x}_0(0)}(\tau, 0)$, evaluated as a set of partials. Given the initial condition along the reference, the state vectors are evaluated from 0 to τ and are approximated via the STM as follows

$$\Phi_{\boldsymbol{x}_0(0)}(\tau, 0) = \left.\frac{\partial \boldsymbol{\psi}}{\partial \boldsymbol{x}_0(0)}\right|_{\boldsymbol{x}_0(\tau)}. \tag{3.16}$$

In addition, the first-order derivative of the mapping function with respect to τ, evaluated at $\boldsymbol{x}_0(\tau)$, corresponds to the derivative of the reference state evaluated at τ, $\dot{\boldsymbol{x}}_0(\tau)$, through the expression

$$\dot{\boldsymbol{x}}_0(\tau) = \left.\frac{\partial \boldsymbol{\psi}}{\partial \tau}\right|_{\boldsymbol{x}_0(\tau)}. \tag{3.17}$$

Substituting Equations (3.8) and (3.14) into Equation (3.15) yeilds the relationship between the two types of variations, i.e.,

$$\delta \boldsymbol{q}(\tau) = \delta \boldsymbol{x}(\tau) + \dot{\boldsymbol{x}}(\tau)\delta\tau. \tag{3.18}$$

Equation (3.18) is consistent with the visual depiction in Figure 3.1. In summary, the contemporaneous variation (red vector) is added to the product of the state derivative evaluated on the nearby arc and the temporal variation (green vector) to approximate the non-contemporaneous variation (purple vector). Thus, future variations of both types are computed using linear approximations and an understanding of the sensitivity of a numerically generated result to small perturbations in the initial state as well as the time of integration.

3.2 Shooting Schemes

One approach to produce a solution in a TPBVP is a shooting scheme. Such a process is based on the same principles as throwing darts at a bullseye. Released at an initial position and velocity, a dart lands at some location on the dart board. If the dart does not hit the desired target (bullseye), the distance on the dart board from the final location to the target is used to approximate changes in the initial position and velocity such that the next throw hits the target. Thus, a shooting method systematically improves the "aim" of the

next throw [36]. The mission design equivalent to this dart-throwing process requires much more accuracy and autonomy, but the concept is similar.

3.2.1 Foundations of Any Shooting Scheme

Shooting approaches are typically based on linear variational analysis to numerically solve TPBVPs. In the dart board example, adjustments to the "aim" of subsequent throws are determined by observing the landing error of the current throw (the distance from the final location to the target) and computing the adjustment that is required to reduce the landing error. In a trajectory design problem, this "aim" adjustment is computed systematically by measuring the miss distance at a desired target and solving for the design variables that eliminate the error. The error relative to a target is considered a *constraint* on the TPBVP, that is, the problem is formulated to iterate until the design variables satisfy the constraint – the error at the target is zero. The design quantities, or *free variables*, are updated throughout the corrections process to reach targeted values. The relationship between the constraints and the free variables is assessed through a combination of Equation eqrefeq:varRelation and Equation (3.8). The downstream noncontemporaneous variation, $\delta\boldsymbol{x}(\tau+\delta\tau)$, is then approximated mathematically as

$$\delta\boldsymbol{x}(\tau+\delta\tau) = \begin{bmatrix} \Phi(\tau,\tau_0) & \dot{\boldsymbol{x}}(\tau) \end{bmatrix}_{\boldsymbol{x}(\tau_0)} \begin{Bmatrix} \delta\boldsymbol{x}(\tau_0) \\ \delta\tau \end{Bmatrix}. \tag{3.19}$$

The state transition matrix, $\Phi(\tau,\tau_0)$, and the derivative of the state vector, $\dot{\boldsymbol{x}}(\tau)$, are evaluated after the propagation originating from $\boldsymbol{x}(\tau_0)$, the initial condition, and integrating over the interval $\tau-\tau_0$ [40,41]. Since $\delta\boldsymbol{x}(\tau+\delta\tau)$ represents the measured error relative to the target, inverting Equation (3.19) to solve for the variation in the initial state vector, $\delta\boldsymbol{x}(\tau_0)$, and the change in integration length, $\delta\tau$, is the basic goal of any differential corrections scheme. In a "pure" shooting algorithm, conditions at the end of a simulation are matched to targeted values by modifying the initial conditions with the inversion of Equation (3.19), locating all the design, or free, variables at the initial state and all the constraints at the end state [36]. However, most TPBVPs possess free variables and constraints at both the initial and final states. Therefore, the computation of free variables in these adapted

problems requires modifications to Equation (3.19). Nevertheless, the goal in any differential corrections scheme is, ultimately, to drive the constraints to zero by computing iterative adjustments to the set of free variables with linear variational analysis.

Differential corrections strategies are often classified in terms of the integration time. More explicitly, an option exists to include integration time as a free variable or to fix the time and maintain the original value throughout all the iterations. A variable-time scheme incorporates the non-contemporaneous variations since the propagation time is included as a free variable. Hence, the implementation of Equation (3.19) as a differential corrections process is then defined as a variable-time update scheme. In the fixed-time alternative formulation, the integration time is equal to a specified value to incorporate only contemporaneous variations. Thus, the integration time is not considered a free-variable, reducing Equation (3.19) to Equation (3.8). In general, variable-time schemes allow a larger number of constraints since there are more free variables, but fixed-time formulations are more straightforward. However, the selection of a specific approach for implementation is problem-specific.

A visual design methodology depends on the selection of an adequate differential corrections strategy. Many very specific targeting algorithms are formulated for solving TPBVPs in trajectory design, each with a variety of implementation methods. Shooting schemes, in particular, are easily generalized for a wide array of TPBVPs, and the algorithm structure is well-suited to an object-oriented programming approach. Thus, shooting schemes are an appropriate choice for a visual analytics design philosophy.

3.2.2 Implementation of Shooting Schemes

The first step towards implementation of any shooting process consists of the appropriate definitions for the free variables and the constraints that apply to a particular problem. The

free-variable vector, $\boldsymbol{X}$, contains n state elements or other pertinent quantities on either boundary in the form

$$\boldsymbol{X} = \left\{ \begin{array}{c} X_1 \\ X_2 \\ \vdots \\ X_n \end{array} \right\}. \tag{3.20}$$

For targeting in trajectory design, the n elements of $\boldsymbol{X}$ are typically selected as controllable quantities, e.g., initial position components (that can be controlled by an *a priori* maneuver) or velocity components at either boundary (that can be translated into ΔV data). The constraint or error vector, $\boldsymbol{F}(\boldsymbol{X})$, collects the m constraint functions, $F_g(\boldsymbol{X})$ with $g = 1, ..., m$, into the vector

$$\boldsymbol{F}(\boldsymbol{X}) = \left\{ \begin{array}{c} F_1(\boldsymbol{X}) \\ F_2(\boldsymbol{X}) \\ \vdots \\ F_m(\boldsymbol{X}) \end{array} \right\}. \tag{3.21}$$

The constraint functions are formulated to correlate with the conditions at each boundary such that $\boldsymbol{F}(\boldsymbol{X}^*) = \boldsymbol{0}$, where $\boldsymbol{X}^*$ is the set of free variables that solves the TPBVP [36]. For reference, typical constraints in a mission design scenario include position or velocity states that are specified and, subsequently, fixed, ΔV values at specific locations, and payload or propellant masses. With the definitions of $\boldsymbol{X}$ and $\boldsymbol{F}(\boldsymbol{X})$, the TPBVP is defined with n free variables that are subject to m constraints.

The determination of a solution $\boldsymbol{X}^*$ that satisfies $\boldsymbol{F}(\boldsymbol{X}^*) = \boldsymbol{0}$ transforms into a multi-dimensional root-finding problem due to the formulation in terms of the free variables and constraints. Linear approximations simplify the corrections process, but are applied iteratively to solve a nonlinear system of equations. Consider a free-variable vector, $\boldsymbol{X}^j$, at the j^{th} iteration where the solution of the TPBVP is not yet attained ($\boldsymbol{F}(\boldsymbol{X}^j) \neq \boldsymbol{0}$). The constraint vector corresponding to the next iteration, $\boldsymbol{F}(\boldsymbol{X}^{j+1})$, is approximated with a first-order Taylor series expansion about the previous free-variable vector, $\boldsymbol{X}^j$. The resulting expansion,

$$\boldsymbol{F}(\boldsymbol{X}^{j+1}) = \boldsymbol{F}(\boldsymbol{X}^j) + D\boldsymbol{F}(\boldsymbol{X}^j)(\boldsymbol{X}^{j+1} - \boldsymbol{X}^j) = \boldsymbol{0}, \tag{3.22}$$

isolates the next guess, that is, the updated free-variable vector, $\boldsymbol{X}^{j+1}$. The term $D\boldsymbol{F}(\boldsymbol{X}^j)$ in Equation (3.22) represents the $m \times n$ Jacobian matrix, evaluated using the current free-variable vector, $\boldsymbol{X}^j$, such that

$$D\boldsymbol{F}(\boldsymbol{X}) = \frac{\partial \boldsymbol{F}}{\partial \boldsymbol{X}} = \begin{bmatrix} \frac{\partial F_1}{\partial x_1} & \frac{\partial F_1}{\partial x_2} & \cdots & \frac{\partial F_1}{\partial x_n} \\ \frac{\partial F_2}{\partial x_1} & \frac{\partial F_2}{\partial x_2} & \cdots & \frac{\partial F_2}{\partial x_n} \\ \vdots & \vdots & \ddots & \vdots \\ \frac{\partial F_m}{\partial x_1} & \frac{\partial F_m}{\partial x_2} & \cdots & \frac{\partial F_m}{\partial x_n} \end{bmatrix}. \tag{3.23}$$

Derivatives of the elements that comprise the Jacobian matrix are evaluated (i) analytically by computing the appropriate partial derivatives, or (ii) numerically through a finite-differencing scheme [36]. In trajectory design problems, elements of $D\boldsymbol{F}(\boldsymbol{X})$ frequently reflect elements of the STM (Equation (3.9)) since the design variables and constraints are usually state elements at either boundary [40, 41]. A multi-dimensional Newton-Rhapson scheme generates an update to the free-variable vector, $\boldsymbol{X}^{j+1}$, if $D\boldsymbol{F}(\boldsymbol{X}^j)$ is square and non-singular ($n = m$, and the problem is properly posed) [36, 42, 43]. Thus, the locally convergent approach to computing the solution, $\boldsymbol{X}^*$, that satisfies $\boldsymbol{F}(\boldsymbol{X}^*) = \boldsymbol{0}$ is the iterative application of the expression

$$\boldsymbol{X}^{j+1} = \boldsymbol{X}^j - D\boldsymbol{F}(\boldsymbol{X}^j)^{-1}\boldsymbol{F}(\boldsymbol{X}^j). \tag{3.24}$$

If the problem is well-posed but $n > m$, then the solution is determined iteratively using a minimum-norm algorithm [36, 43], i.e.,

$$\boldsymbol{X}^{j+1} = \boldsymbol{X}^j - D\boldsymbol{F}(\boldsymbol{X}^j)^T \left[D\boldsymbol{F}(\boldsymbol{X}^j)D\boldsymbol{F}(\boldsymbol{X}^j)^T\right]^{-1} \boldsymbol{F}(\boldsymbol{X}^j). \tag{3.25}$$

An infinite number of solutions exist to Equation (3.22), so the minimum-norm algorithm utilizes a projection onto the solution space to isolate the adjusted vector $\boldsymbol{X}^{j+1}$ that is closest to $\boldsymbol{X}^j$. The iterative updates in Equations (3.24) and (3.25) are applied until the magnitude of the constraint vector reaches zero, within some specified tolerance. When $n < m$, the problem is over-constrained and possesses no solution. A least-squares algorithm may be applied to obtain an approximation to a solution that minimizes the error, but the

solution is infeasible ($\boldsymbol{F}(\boldsymbol{X}^*) \neq \boldsymbol{0}$). Therefore, only the viable trajectory solutions from the problems formulated to be consistent with $n = m$ and $n > m$ are considered.

3.2.3 Fixed-Time Single Shooting Method

For a single shooting scheme with a fixed integration time in a mission design problem, a single trajectory segment is considered while defining constraints and free variables. The free variable vector, $\boldsymbol{X}$, is populated with components from either the initial state or the ending condition. The constraint functions are typically the desired elements at the end state, but constraints may also be other useful quantities, e.g., the Jacobi constant. If the Jacobi constant that is evaluated at the initial state, $\boldsymbol{x}_0$, is constrained at a target value C_D, then the corresponding constraint equation is constructed in the form $F_g(\boldsymbol{X}) = C(\boldsymbol{x}_0) - C_D$ where $C(\boldsymbol{x}_0)$ is the evaluation of Equation (2.49) using the state elements in $\boldsymbol{x}_0$. The Jacobian matrix is then generated with Equation (3.23) employing the chain rule where necessary. Trajectory design problems are then solved with the iterative application of the appropriate linear update equation.

A simple visual example demonstrates the application of the single-shooting method. The schematic in Figure 3.2 represents a sample iteration history in an arbitrary single-shooting problem. The free-variable vector is selected to be the starting state on the left, and the target condition on the right reflects the desired characteristics at the final time. After the selection of a target condition, the specified initial guess, $\boldsymbol{X}^0$ is propagated via numerical integration along the initial arc (blue) to a state downstream that misses the target by the error vector $\boldsymbol{F}(\boldsymbol{X}^0)$. Using Equation (3.24) or (3.25) depending on the dimensions of the problem, the error vector corresponding to the initial arc determines the next guess for the free variables, $\boldsymbol{X}^j$. With the updated design variables, the intermediate arc (red) is propagated downstream but yields an offset relative to the target condition; the offset is reflected in the nonzero vector constraint, $\boldsymbol{F}(\boldsymbol{X}^j)$. A second application of Equation (3.24) or (3.25) produces the modifications to the design variables which, in this example, results in $\boldsymbol{X}^*$. The desired arc (green) is then achieved since the numerical integration of the ideal free-variable vector, $\boldsymbol{X}^*$, produced a downstream result of $\boldsymbol{F}(\boldsymbol{X}^*) = \boldsymbol{0}$ (within some

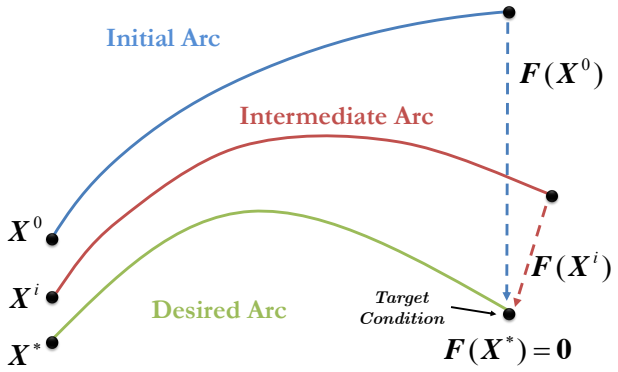

Figure 3.2. Shooting arcs that demonstrate the potential paths toward the desired solution in a single-shooting scheme.

tolerance). Thus, in this simple example, the single-shooting approach converged on the target trajectory with the desired characteristics in just two iterations.

3.2.4 Variable-Time Single Shooting Method

Incorporating a variable integration time into a single-shooting scheme introduces an additional layer of complexity. A fixed-time single-shooting method exploits contemporaneous variations to iteratively determine the solution to $\boldsymbol{F}(\boldsymbol{X}) = \boldsymbol{0}$; however, the variable-time version bases the targeting algorithm on non-contemporaneous variations. The integration time, t, is now included as a free-variable and appended to $\boldsymbol{X}$ as

$$\boldsymbol{X} = \begin{Bmatrix} X_1 \\ X_2 \\ \vdots \\ X_{n-1} \\ t \end{Bmatrix}. \tag{3.26}$$

The size of $\boldsymbol{X}$ is still denoted as n even though the variable-time version of $\boldsymbol{X}$ holds one more component than the fixed-time version of $\boldsymbol{X}$ (Equation (3.20)). The constraint

vector, $\boldsymbol{F}(\boldsymbol{X})$, remains the same as in Equation (3.21) with dimension m, but the constraint functions may now depend on t. The $m \times n$ Jacobian matrix in the variable-time single-shooting method appears as

$$D\boldsymbol{F}(\boldsymbol{X}) = \frac{\partial \boldsymbol{F}}{\partial \boldsymbol{X}} = \begin{bmatrix} \frac{\partial F_1}{\partial X_1} & \frac{\partial F_1}{\partial X_2} & \cdots & \frac{\partial F_1}{\partial X_{n-1}} & \frac{\partial F_1}{\partial t} \\ \frac{\partial F_2}{\partial X_1} & \frac{\partial F_2}{\partial X_2} & \cdots & \frac{\partial F_2}{\partial X_{n-1}} & \frac{\partial F_1}{\partial t} \\ \vdots & \vdots & \ddots & \vdots & \vdots \\ \frac{\partial F_m}{\partial X_1} & \frac{\partial F_m}{\partial X_2} & \cdots & \frac{\partial F_m}{\partial X_{n-1}} & \frac{\partial F_m}{\partial t} \end{bmatrix}. \tag{3.27}$$

The form of Equation (3.27) is the same as the fixed-time counterpart (Equation (3.23)), but the final column of $D\boldsymbol{F}(\boldsymbol{X})$ contains time-dependent derivatives evaluated at the end of the integration step. In the trajectory design application, the final column of the Jacobian matrix is typically comprised of state derivatives. Construction of a solution remains consistent with the iterative application of Equation (3.24) for $n = m$ or Equation (3.25) for $n > m$. The basin of convergence in the variable-time formulation is expanded in comparison to the fixed-time application [42, 43]. Thus, the inclusion of the integration time as a design variable increases the likelihood of obtaining a a solution and may slightly decrease a dependency on the initial guess.

3.2.5 Fixed-Time Multiple Shooting Method

Although single-shooting algorithms are useful for many applications, some problems are numerically challenging to solve with a single-shooting strategy. Some problems include trajectory arcs that pass through dynamically sensitive regions. In the CRTBP , such arcs include those that pass close to either primary [39, 41]. As a consequence, a relatively minor adjustment to the initial conditions during the iterative update (Equation (3.24) or (3.25)) may produce very large changes downstream, which causes convergence difficulties. As an alternative, a multiple-shooting approach decomposes a trajectory into smaller arcs to create a more tractable problem.

Denoted as parallel-shooting by Keller [42,44], a multiple-shooting algorithm essentially splits the variables and constraints into components. The first set of components represents a series of single-shooting problems, each of shorter length, and continuity is required from

segment to segment. The origin and terminal points along each segment are denoted as *patch points*. All of the remaining free variables and constraints are collected into the second group of components. Thus, the free-variable vector, $\boldsymbol{X}$, splits into a set of k full 6D state vectors, each identifying one of the patch points, that must satisfy continuity, as well as a set of l additional free variables. The form of $\boldsymbol{X}$ is then organized as

$$\boldsymbol{X} = \left\{ \begin{array}{c} \boldsymbol{X}_k \\ \boldsymbol{X}_l \end{array} \right\}, \tag{3.28}$$

where

$$\boldsymbol{X}_k = \left\{ \begin{array}{c} \boldsymbol{x}_1 \\ \boldsymbol{x}_2 \\ \vdots \\ \boldsymbol{x}_k \end{array} \right\} \text{ and } \boldsymbol{X}_l = \left\{ \begin{array}{c} X_1 \\ X_2 \\ \vdots \\ X_l \end{array} \right\}.$$

If the algorithm is a fixed-time application, the integration time between patch points, t, is fixed as a specified value. In the CRTBP , each patch point is defined by the six scalar state variables that are expressed in terms of rotating frame coordinates, so the dimension of $\boldsymbol{X}$ is $n = 6k + l$. The full constraint vector, $\boldsymbol{F}(\boldsymbol{X})$, includes the continuity constraints, $\boldsymbol{F}_k(\boldsymbol{X})$ as well as any additional constraint functions, $\boldsymbol{F}_c(\boldsymbol{X})$, i.e.,

$$\boldsymbol{F}(\boldsymbol{X}) = \left\{ \begin{array}{c} \boldsymbol{F}_k(\boldsymbol{X}) \\ \boldsymbol{F}_c(\boldsymbol{X}) \end{array} \right\}. \tag{3.29}$$

Internal patch point continuity is ensured if the mapping of a patch point, $\boldsymbol{x}_i$, via numerical integration in time, successfully arrives at the next patch point, $\boldsymbol{x}_{i+1}$. If $\boldsymbol{x}_{i+1}(\boldsymbol{x}_i, t)$ symbolizes the mapping of $\boldsymbol{x}_i$ over the integration time t, then the continuity constraints are collected as

$$\boldsymbol{F}_k(\boldsymbol{X}) = \left\{ \begin{array}{c} \boldsymbol{x}_2(\boldsymbol{x}_1, t) - \boldsymbol{x}_2 \\ \boldsymbol{x}_3(\boldsymbol{x}_2, t) - \boldsymbol{x}_3 \\ \vdots \\ \boldsymbol{x}_k(\boldsymbol{x}_{k-1}, t) - \boldsymbol{x}_k \end{array} \right\}. \tag{3.30}$$

Note that the final patch point, $\boldsymbol{x}_k$, is constrained only through $\boldsymbol{F}_c(\boldsymbol{X})$. The total dimension of $\boldsymbol{F}(\boldsymbol{X})$ is then $m = 6(k-1)+c$ since there are $6(k-1)$ continuity constraints and c additional constraints.

A schematic of the multiple-shooting concept aids in the formulation of the modified TPBVP. A multiple-shooting formulation to iteratively solve a TPBVP similar to the example in the previous section is displayed in Figure 3.3. The desired objective is that the solution, $\boldsymbol{x}_1^*$, reaches the target state after a specified time. The initial guess is comprised of four initial trajectory segments that correspond to four initial patch points, $\boldsymbol{x}_i$, where $i = 1, ..., 4$. Note that the four patch points plus the target point bracket the four segments. The initial patch points are selected such that the states reside close to the desired solution but typically do not form a continuous arc. Numerical integrations originating at each patch point $\boldsymbol{x}_i$, over the integration times t_i, are accomplished in parallel and yield the downstream mappings of the patch points, $\boldsymbol{x}_i(\boldsymbol{x}_{i-1}, t_i)$. In the fixed-time formulation, all of the t_i values are equal. The resulting mappings 'miss' the subsequent patch points and the 'miss' distance is represented by the continuity error vectors determined from Equation (3.30). The corrections algorithm then iteratively shifts the 6D patch points until reaching the desired solutions, $\boldsymbol{x}_i^*$, that form a continuous trajectory and reaches the target condition downstream.

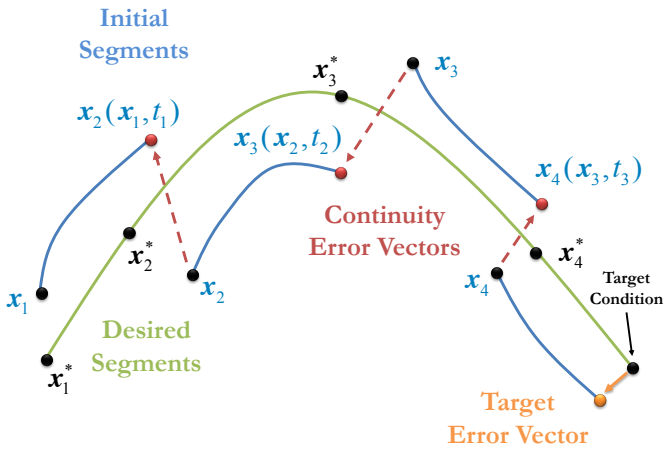

Figure 3.3. Segmented shooting arcs applied in the multiple-shooting approach.

With the separation of the $\boldsymbol{X}$ and $\boldsymbol{F}(\boldsymbol{X})$ vectors into components, the Jacobian matrix, $D\boldsymbol{F}(\boldsymbol{X})$, is also modified into a new form. Four submatrices comprise the $m \times n$ Jacobian matrix as

$$D\boldsymbol{F}(\boldsymbol{X}) = \begin{bmatrix} D\boldsymbol{F}_k(\boldsymbol{X}_k) & D\boldsymbol{F}_k(\boldsymbol{X}_l) \\ D\boldsymbol{F}_c(\boldsymbol{X}_k) & D\boldsymbol{F}_c(\boldsymbol{X}_l) \end{bmatrix} = \begin{bmatrix} \dfrac{\partial \boldsymbol{F}_k}{\partial \boldsymbol{X}_k} & \dfrac{\partial \boldsymbol{F}_k}{\partial \boldsymbol{X}_l} \\ \dfrac{\partial \boldsymbol{F}_c}{\partial \boldsymbol{X}_k} & \dfrac{\partial \boldsymbol{F}_c}{\partial \boldsymbol{X}_l} \end{bmatrix}, \tag{3.31}$$

in lieu of Equations (3.28) and (3.29). The upper left submatrix of the Jacobian matrix, the sensitivity of the continuity constraints to the patch points, $D\boldsymbol{F}_k(\boldsymbol{X}_k)$, is a banded-diagonal matrix with dimensions $6(k-1) \times 6k$ based on the spatial derivatives, i.e.,

$$D\boldsymbol{F}_k(\boldsymbol{X}_k) = \frac{\partial \boldsymbol{F}_k}{\partial \boldsymbol{X}_k} = \begin{bmatrix} \frac{\partial \boldsymbol{x}_2(\boldsymbol{x}_1,t)}{\partial \boldsymbol{x}_1} & -I & 0 & 0 & 0 \\ 0 & \frac{\partial \boldsymbol{x}_3(\boldsymbol{x}_2,t)}{\partial \boldsymbol{x}_2} & -I & 0 & 0 \\ & & \ddots & \ddots & \\ 0 & 0 & 0 & \frac{\partial \boldsymbol{x}_k(\boldsymbol{x}_{k-1},t)}{\partial \boldsymbol{x}_{k-1}} & -I \end{bmatrix}. \tag{3.32}$$

The I notation represents a 6×6 identity matrix. As evident in Equation (3.9), entries along the main diagonal, $\frac{\partial \boldsymbol{x}_{i+1}(\boldsymbol{x}_i,t)}{\partial \boldsymbol{x}_i}$, are the state transition matrices, $\Phi_i(t,0)$ integrated from the point $\boldsymbol{x}_i$ to the next point downstream $\boldsymbol{x}_{i+1}$, over the fixed time interval t. Using this fact, Equation (3.32) is rewritten as

$$D\boldsymbol{F}_k(\boldsymbol{X}_k) = \frac{\partial \boldsymbol{F}_k}{\partial \boldsymbol{X}_k} = \begin{bmatrix} \Phi_2(t,0) & -I & 0 & 0 & 0 \\ 0 & \Phi_3(t,0) & -I & 0 & 0 \\ & & \ddots & \ddots & \\ 0 & 0 & 0 & \Phi_k(t,0) & -I \end{bmatrix}. \tag{3.33}$$

Thus, the elements of the Jacobian matrix linked to continuity are computed at the same time as the continuity constraints since the STM is included as part of the numerical integration process. The solution to the TPBVP in the multiple-shooting formulation again depends on the iterative application of a Newtonian inverse (Equation (3.24)) or a minimum-norm algorithm (Equation (3.25)). Also notable is the fact that $D\boldsymbol{F}(\boldsymbol{X})$ contains many zero-elements due to the formulation of the multiple-shooting method. Thus, sparse-matrix solution algorithms are exploited to apply the iterative updates in Equations (3.24) and (3.25).

3.2.6 Variable-Time Multiple Shooting Method

Time-varying approaches exist in the multiple-shooting formulation as well. Allowing the integration time between patch points to vary implies that the integration times are also incorporated in the free-variable vector. If the integration times are collected into the vector $\boldsymbol{T}_q$ where q is the number of elements in $\boldsymbol{T}_q$, then the free-variable vector is arranged as

$$\boldsymbol{X} = \begin{Bmatrix} \boldsymbol{X}_k \\ \boldsymbol{T}_q \\ \boldsymbol{X}_l \end{Bmatrix}. \tag{3.34}$$

Here, the dimension of $\boldsymbol{X}$ is $n = 6k + q + l$ where k and l are the number of patch points and the additional free variables, respectively. The constraint vector in the variable-time formulation, $\boldsymbol{F}(\boldsymbol{X})$, possesses a form that is similar to that in the fixed-time algorithm (Equation (3.29)), but the continuity and additional constraints also depend on the vector of integration times, $\boldsymbol{T}_q$. Thus, the Jacobian matrix contains an additional set of submatrices. With m constraints and n free variables, the $m \times n$ Jacobian matrix appears as

$$D\boldsymbol{F}(\boldsymbol{X}) = \begin{bmatrix} D\boldsymbol{F}_k(\boldsymbol{X}_k) & D\boldsymbol{F}_k(\boldsymbol{T}_q) & D\boldsymbol{F}_k(\boldsymbol{X}_l) \\ D\boldsymbol{F}_c(\boldsymbol{X}_k) & D\boldsymbol{F}_c(\boldsymbol{T}_q) & D\boldsymbol{F}_c(\boldsymbol{X}_l) \end{bmatrix}, \tag{3.35}$$

in the variable-time formulation. The solution approach involves the same update formulas (Equations (3.24) and (3.25)) as the other multiple-shooting approaches depending on the dimensions of $D\boldsymbol{F}(\boldsymbol{X})$.

Different implementations to incorporate non-contemporaneous variations are available in variable-time multiple shooting methods. One possible approach is the population of $\boldsymbol{T}_q$ with the integration times corresponding to each internal segment. Thus, the variable-time portion of the free-variable vector is comprised of the integration times, t_i for $i = 1, ..., k$, in the form

$$\boldsymbol{T}_q = \begin{Bmatrix} t_1 \\ t_2 \\ \vdots \\ t_k \end{Bmatrix}. \tag{3.36}$$

Since there are k integration segments, the dimension of $\boldsymbol{T}_q$ is then $q = k$, such that the total dimension of $\boldsymbol{X}$ is $n = 7k + l$. The continuity portion of the Jacobian matrix is modified from the fixed-time equivalent (Equation (3.33)) to

$$D\boldsymbol{F}_k(\boldsymbol{X}_k) = \frac{\partial \boldsymbol{F}_k}{\partial \boldsymbol{X}_k} = \begin{bmatrix} \Phi_2(t_1,0) & -I & 0 & 0 & 0 \\ 0 & \Phi_3(t_2,0) & -I & 0 & 0 \\ & & \ddots & \ddots & \\ 0 & 0 & 0 & \Phi_k(t_{k-1},0) & -I \end{bmatrix}, \tag{3.37}$$

where the integration times for each STM are equal to the corresponding components of $\boldsymbol{T}_q$. The continuity constraints are impacted by a variation in the integration time, so the top center submatrix of $D\boldsymbol{F}(\boldsymbol{X})$ possesses the form

$$D\boldsymbol{F}_k(\boldsymbol{T}_q) = \frac{\partial \boldsymbol{F}_k}{\partial \boldsymbol{T}_q} = \begin{bmatrix} \frac{\partial \boldsymbol{x}_2(\boldsymbol{x}_1,t_1)}{\partial t_1} & 0 & 0 & 0 & 0 \\ 0 & \frac{\partial \boldsymbol{x}_3(\boldsymbol{x}_2,t_2)}{\partial t_2} & 0 & 0 & 0 \\ & & \ddots & & \\ 0 & 0 & 0 & \frac{\partial \boldsymbol{x}_k(\boldsymbol{x}_{k-1},t_{k-1})}{\partial t_{k-1}} & 0 \end{bmatrix}. \tag{3.38}$$

with a column of zero elements since there is no continuity constraint on the last patch point. Applying Equation (3.17), each partial derivative in $D\boldsymbol{F}_k(\boldsymbol{T}_q)$ is replaced by state derivatives evaluated at the end of the integration time, i.e.,

$$D\boldsymbol{F}_k(\boldsymbol{T}_q) = \frac{\partial \boldsymbol{F}_k}{\partial \boldsymbol{T}_q} = \begin{bmatrix} \dot{\boldsymbol{x}}_2(\boldsymbol{x}_1,t_1) & 0 & 0 & 0 & 0 \\ 0 & \dot{\boldsymbol{x}}_3(\boldsymbol{x}_2,t_2) & 0 & 0 & 0 \\ & & \ddots & & \\ 0 & 0 & 0 & \dot{\boldsymbol{x}}_k(\boldsymbol{x}_{k-1},t_{k-1}) & 0 \end{bmatrix}. \tag{3.39}$$

Referring to the general multiple-shooting schematic in Figure 3.3, the variable-time formulation appears similar to the fixed-time multiple shooting method with one exception. Each segment is now also determined by changes in the integration times, t_i where $i = 1, ..., 4$. For the example, $k = 4$ as the number of patch points in $\boldsymbol{X}_k$, the dimension of $\boldsymbol{T}_q$ is $q = k = 4$, and the total size of $\boldsymbol{X}$ equals $n = 7k + l = 28 + l$ (l is selected via constraints applied at the target condition).

A second technique for implementation of a variable-time multiple shooting strategy is the incorporation of the total integration time as the time-varying component. In this approach, the total integration time, T, represents the sole variable in $\boldsymbol{T}_q$, i.e.,

$$\boldsymbol{T}_q = \{T\}\,. \tag{3.40}$$

Thus, the dimension of $\boldsymbol{T}_q$ is now $q = 1$. With this definition of $\boldsymbol{T}_q$, each integration time is an equal portion of T (e.g., if $k = 4$ then the integration time for each segment is $t_i = \frac{T}{k} = \frac{T}{4}$). The submatrix linked to continuity, $D\boldsymbol{F}_k(\boldsymbol{X}_k)$, is then adjusted to the form

$$D\boldsymbol{F}_k(\boldsymbol{X}_k) = \frac{\partial \boldsymbol{F}_k}{\partial \boldsymbol{X}_k} = \begin{bmatrix} \Phi_2(T/k,0) & -I & 0 & 0 & 0 \\ 0 & \Phi_3(T/k,0) & -I & 0 & 0 \\ & & \ddots & \ddots & \\ 0 & 0 & 0 & \Phi_k(T/k,0) & -I \end{bmatrix}, \tag{3.41}$$

and the sensitivity of the continuity constraints with respect to the total integration time reduces to the single column

$$D\boldsymbol{F}_k(\boldsymbol{T}_q) = \frac{\partial \boldsymbol{F}_k}{\partial \boldsymbol{T}_q} = \frac{1}{k}\begin{bmatrix} \dot{\boldsymbol{x}}_2(\boldsymbol{x}_1, \frac{T}{k}) \\ \dot{\boldsymbol{x}}_3(\boldsymbol{x}_2, \frac{T}{k}) \\ \vdots \\ \dot{\boldsymbol{x}}_k(\boldsymbol{x}_{k-1}, \frac{T}{k}) \end{bmatrix}. \tag{3.42}$$

The factor $\frac{1}{k}$ appears in $D\boldsymbol{F}_k(\boldsymbol{T}_q)$ due to the chain rule.

Generating a solution to TPBVPs with a variable-time multiple shooting scheme is again based on the iterative application of the appropriate update equation. Variable-time formulations tend to possess more free variables than their fixed-time counterparts; therefore, implementation of the minimum-norm update (Equation (3.25)) is more likely for variable-time multiple shooting applications. But, with the additional design variables available in a variable-time scheme, more constraints can be applied to enhance flexibility in creating trajectory design solutions.

3.3 Application of Shooting Methods to Trajectory Design Problems

In a trajectory design problem, shooting methods are applied in a specific order to yield a desired continuous solution to a TPBVP. Let ε represent the pre-specified convergence tolerance in evaluation of the constraint equation $\boldsymbol{F}(\boldsymbol{X}) = \boldsymbol{0}$. For spacecraft mission analysis, the steps for generating a continuous trajectory that solves a particular TPBVP (within the tolerance ε) are summarized in the following procedural sequence:

1. Select a numerical model appropriate to the mission.
2. Select a shooting scheme: fixed-time or variable-time approach in a single shooting or multiple shooting application.
3. Identify the free variables, $\boldsymbol{X}$.
4. Formulate the constraint vector, $\boldsymbol{F}(\boldsymbol{X})$.
5. Derive the partial derivative expressions in the Jacobian matrix, $D\boldsymbol{F}(\boldsymbol{X})$, or select an applicable numerical differentiation technique.
6. Generate an estimated solution by applying theoretical approximations or propagating initial conditions.
7. Define the initial guess vector, $\boldsymbol{X}^j$ with $j = 0$, by extracting information from the estimated solution in Step 6 – either the state variables for a single-shooting scheme or patch points for multiple-shooting.
8. Iterate to produce a feasible solution ($\|\boldsymbol{F}(\boldsymbol{X}^j)\| < \varepsilon$):
   (a) Numerically integrate the current states in the design variable vector, $\boldsymbol{X}^j$.
   (b) Compute the constraint vector, $\boldsymbol{F}(\boldsymbol{X}^j)$.
   (c) Evaluate $\|\boldsymbol{F}(\boldsymbol{X}^j)\|$ against the goal, $\|\boldsymbol{F}(\boldsymbol{X}^j)\| = 0$ within tolerance ε.
   (d) Compute the Jacobian matrix, $D\boldsymbol{F}(\boldsymbol{X}^j)$, analytically or numerically.
   (e) Evaluate and update the design variable vector, $\boldsymbol{X}^{j+1}$, using Equation (3.24) or Equation (3.25).
9. Evaluate the result and return to Step 2 as necessary.

At the conclusion of this process, the solution, $\boldsymbol{X}^*$, is comprised of the state variables or patch points that form a continuous trajectory, but an additional numerical simulation is required to generate the full trajectory that solves the TPBVP.

The particular approach to produce the initial guess may vary along each segment, but the strategy that is selected does substantially impact the result. For example, consider a trajectory design scenario such that a transfer arc from an Earth orbit to a Lunar orbit within the complex N-body model is desired. Since designing transfers in the N-body model is difficult due to the complex dynamical behavior, approximations with the two-body model generate initial guesses for the first and last segments, that is, likely orbits about the Earth and Moon, respectively. Initial guesses for the intermediate segments exploit the circular restricted three-body model for the Earth-Moon system because these intermediate segments are strongly influenced by both gravity fields. Then, a shooting process is employed with the initial guess segments to determine the actual transfer in the N-body model. In general, shooting algorithms produce trajectory arcs that can achieve the same objectives in different models. However, it is possible that an initial guess resides so distant from the desired trajectory that shooting approaches experience convergence difficulties. The selection of appropriate initial conditions can be critical.

3.4 Generating Periodic Orbits in the CRTBP

Computation of periodic orbits in the CRTBP serves as a straightforward application of shooting methods in trajectory design problems. Poincaré speculated that an infinite number of periodic orbits exist in the CRTBP [45,46], but the determination of such an orbit requires an effective targeting scheme and a reasonable initial guess. Symmetry properties in the CRTBP are exploited to compute planar periodic orbits in the vicinity of the collinear libration points.

3.4.1 Planar Lyapunov Orbits

Periodic libration point orbits in the CRTBP are constructed by first generating an initial guess. Szebehely derives the initial guess for a planar orbit about an equilibrium point from

a linear approximation relative to the equilibrium points in the CRTBP equations of motion in Equations (2.31), (2.32), and (2.33). Let $\boldsymbol{\xi} = [\xi, \eta, \zeta, \dot{\xi}, \dot{\eta}, \dot{\zeta}]^T$ represent a state vector with respect to a collinear equilibrium point L_i ($\boldsymbol{x}_{L_i} = [x_{L_i}, 0, 0, 0, 0, 0]^T$ where $i = 1, 2, 3$). The linear variational equations are derived and appear in the form

$$\dot{\boldsymbol{\xi}} = A_{L_i}\boldsymbol{\xi}, \tag{3.43}$$

where A_{L_i} is a 6×6 constant matrix evaluated at L_i. The matrix A_{L_i} possesses two real eigenvalues ($\lambda_{1,2}$) and four imaginary eigenvalues such that $\lambda_{3,4} = \pm\omega i$ and $\lambda_{5,6} = \pm\chi i$ [33]. The out-of-plane motion associated with the eigenvalues $\lambda_{5,6}$ decouples from the planar motion, and the real eigenvalues are suppressed to excited periodic motion corresponding to $\lambda_{3,4}$. Thus, the linear approximation for a planar orbit about a collinear point is sinusoidal, i.e.,

$$\xi(t) = \xi_0 \cos\omega t + (\eta_0/\beta_3)\sin\omega t, \tag{3.44}$$

$$\eta(t) = \eta_0 \cos\omega t - \xi_0\beta_3 \sin\omega t, \tag{3.45}$$

where

$$\beta_3 = \frac{\omega^2 + \Upsilon_{xx,L_i}}{2\omega}, \tag{3.46}$$

and Υ_{xx,L_i} is the pseudo-potential function evaluated at the collinear point [33]. A planar initial condition is then computed by selecting the position components ξ_0 and η_0 and computing the initial velocity states $\dot{\xi}_0$ and $\dot{\eta}_0$.

A variable-time, single shooting algorithm is employed to compute planar periodic orbits about the collinear points, i.e., the Lyapunov orbits. In this implementation, the corrections algorithm exploits the mirror configuration across the $\hat{\boldsymbol{x}}$ axis in the CRTBP. In a planar periodic orbit, the intersection with the plane $\Sigma : y = 0$ is perpendicular. The plane Σ is, therefore, used implicitly in the numerical integration process to terminate the propagation at the plane crossing. A schematic of the approach for computing planar Lyapunov orbits appears in Figure 3.4, where $\boldsymbol{x}_0$ indicates the initial state and $\boldsymbol{x}_\Sigma$ represents the termination of numerical propagation at the intersection of the plane Σ. The initial guess resides on the plane Σ with an arbitrary offset from L_i, i.e., ξ_0. Perpendicular departure from the $\hat{x}$ axis

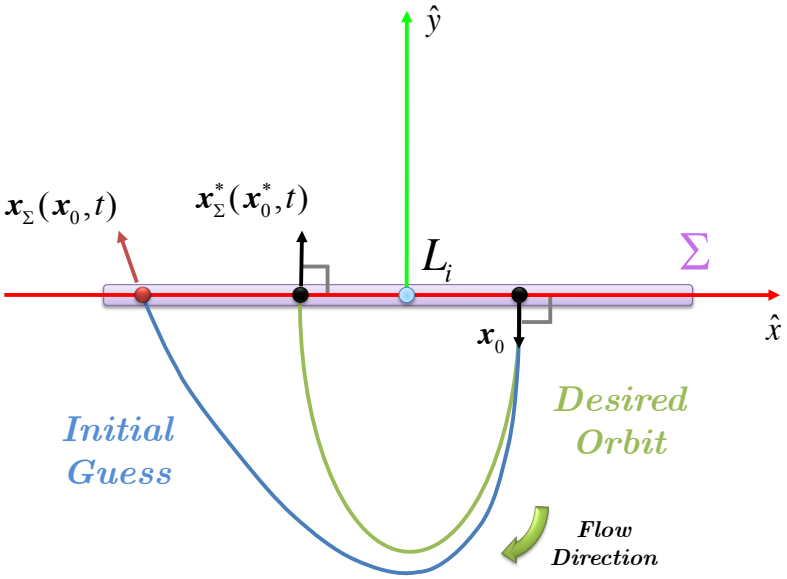

Figure 3.4. Implicit use of the hyperplane $\Sigma : y = 0$ in a variable-time single-shooting algorithm to target a periodic orbit about a collinear libration point.

is enforced through the initial conditions such that $\dot{\xi}_0 = \dot{x}_0 = 0$. The initial guess for the velocity $\dot{y}_0$ is deduced from the linear approximation in Equation (3.45). A periodic orbit is generated by updating this $\dot{y}_0$ value until the return to the plane Σ is perpendicular. Thus, the free-variable vector includes the initial velocity, $\dot{y}_0$, and the time of integration, t, i.e.,

$$\boldsymbol{X} = \left\{ \begin{array}{c} \dot{y}_0 \\ t \end{array} \right\}. \tag{3.47}$$

The constraint vector, $\boldsymbol{F}(\boldsymbol{X})$, enforces a perpendicular crossing of the plane Σ through the constraints

$$\boldsymbol{F}(\boldsymbol{X}) = \left\{ \begin{array}{c} \dot{x}_\Sigma(\dot{y}_0, t) \\ y_\Sigma(\dot{y}_0, t) \end{array} \right\} = \boldsymbol{0}. \tag{3.48}$$

Since there are two constraints and two free variables, $D\boldsymbol{F}(\boldsymbol{X})$ appears as the square matrix

$$D\boldsymbol{F}(\boldsymbol{X}) = \begin{bmatrix} \dfrac{\partial \dot{x}_\Sigma}{\partial \dot{y}_0} & \dfrac{\partial \dot{x}_\Sigma}{\partial t} \\ \dfrac{\partial y_\Sigma}{\partial \dot{y}_0} & \dfrac{\partial y_\Sigma}{\partial t} \end{bmatrix} = \begin{bmatrix} \Phi_{45}(t,0) & \ddot{x}_\Sigma \\ \Phi_{25}(t,0) & \dot{y}_\Sigma \end{bmatrix}, \tag{3.49}$$

where $\Phi_{45}(t,0)$ indicates the STM element representing the downstream effect of $\dot{y}_0$ on $\dot{x}_\Sigma$. The Newton-Rhapson update expression in Equation (3.24) is applied iteratively to compute the initial velocity $\dot{y}_0$ and the integration time, t, that produce a periodic Lyapunov orbit.

After the computation of a planar periodic orbit about a collinear point, the resulting initial state is employed again in a continuation algorithm to generate a subsequent orbit in the same vicinity. A *family* of periodic orbits characterize a set of orbits that are defined in terms of a specified parameter. If the parameter possesses physical significance, then the orbits in a family exhibit similar spatial characteristics. Families of Lyapunov orbits about the collinear libration points in the Earth-Moon CRTBP appear in Figure 3.5. The orbit families in the figure are generated using parameter continuation where a single parameter, such as x, is sequentially increased and the orbit is recomputed for each family member. As an alternative scheme, pseudo-arclength continuation generates a prediction for each subsequent family member that is tangent to the evolving family [40,41]. The orbit families in Figure 3.5 are terminated at an arbitrary energy level for each case even though larger members do, in fact, exist. The Lyapunov families are all plotted together in Figure 3.6. Energy levels corresponding to the various orbits are contrasted by coloring each orbit consistent with Jacobi constant. As evident from Figure 3.6(b), the L_3 Lyapunov family exists at a much lower Jacobi constant value than the trajectories in the L_1 and L_2 families.

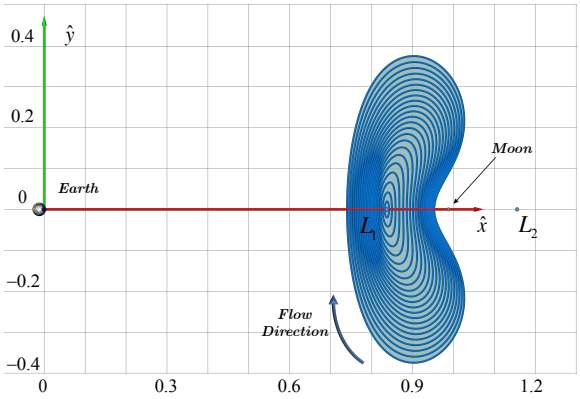

(a) The L_1 Lyapunov Family

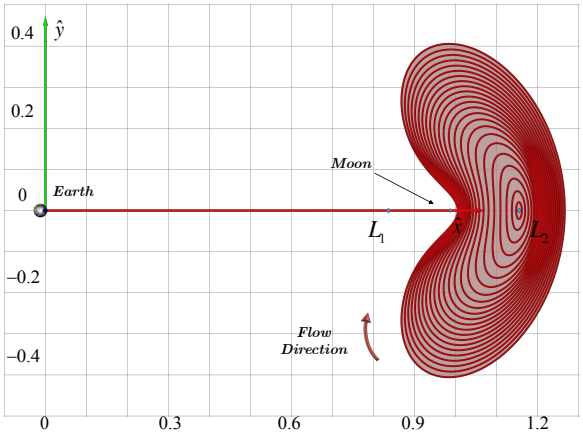

(b) The L_2 Lyapunov Family

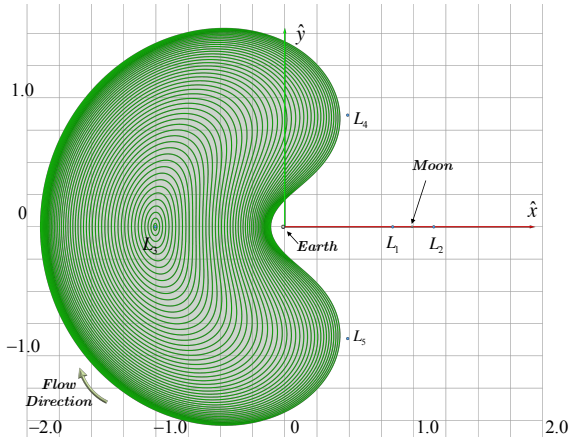

(c) The L_3 Lyapunov Family

Figure 3.5. Planar families of Lyapunov orbits around the collinear libration points in the Earth-Moon system. The units shown are nondimensional distances.

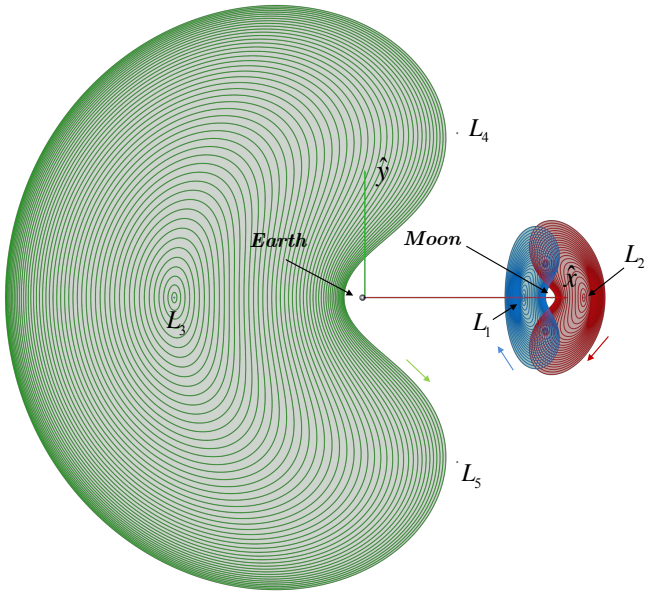

(a)

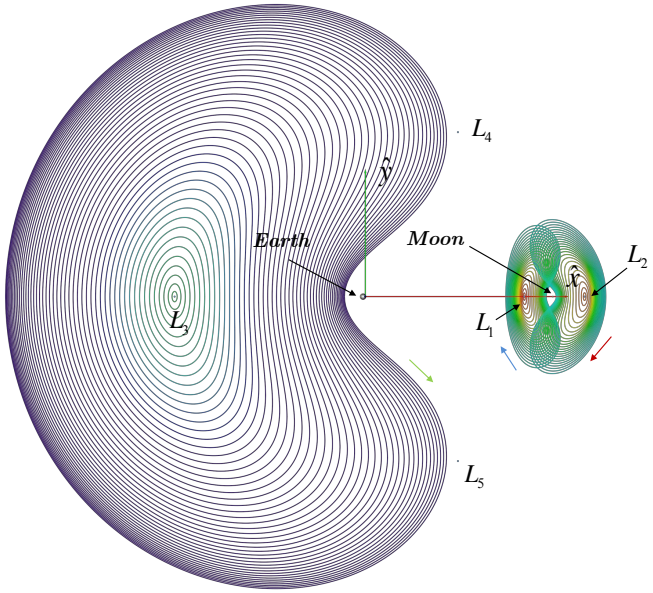

(b)

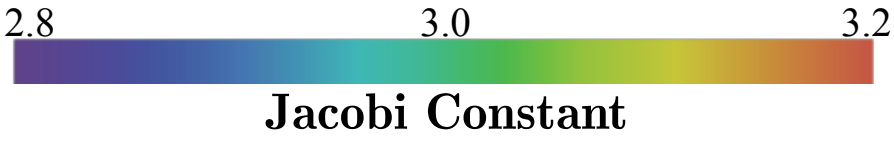

Figure 3.6. Lyapunov orbit families in the Earth-Moon system depicted together with an additional rendering that colors orbits corresponding to Jacobi constant values.

3.5 Generic Multiple Shooting Method for Targeting Periodic Orbits

A shooting algorithm with greater flexibility is required to compute periodic orbits possessing higher complexity, including 3D periodic solutions that better reflect the true ephemeris behavior of the gravitational bodies. Also, some periodic trajectories, especially orbits in the vicinity of L_4 and L_5, are not symmetric across an axis [47]. Unfortunately, the targeting approach applied in Section 3.4.1 is ineffective for seeking 3D and asymmetric periodic tracks. Thus, an alternative shooting strategy is employed to compute periodic orbits of various types.

A variable-time, multiple shooting approach with constraints to insure periodicity is formulated to expand the types of periodic orbits available. For application to any periodic orbit in the CRTBP, the algorithm must be able to compute orbits originating near any libration point or primary. Define the point H, with the position components (x_H, y_H, z_H), as the equilibrium point or primary associated with the proposed orbit. Assume that an initial guess for a periodic orbit in the vicinity of H is represented as a set of k patch points with each patch point state defined as $\boldsymbol{x}_i$ with $i = 0, ..., k-1$. A schematic diagram (Figure 3.7) displays four patch points that approximate an orbit about H. The desired periodic solution may possess 3D components and is not required to be symmetric. The period, T, is incorporated as the only component of $\boldsymbol{T}_q$ in the variable-time multiple shooting scheme; therefore, the integration time corresponding to each segment is T/k, which is $T/4$ in the diagram that appears in Figure 3.7. Continuity constraints are enforced for all internal patch points. However, computing a periodic orbit with a multiple shooting scheme requires an additional continuity constraint, or periodicity constraint, that equates $\boldsymbol{x}_0(\boldsymbol{x}_{k-1}, T/k)$, the downstream propagation of $\boldsymbol{x}_{k-1}$, to the initial patch point $\boldsymbol{x}_0$. Note that the initial patch point departs the line $y = y_H$ with a velocity such that $\dot{y}_0 < 0$, reflecting clockwise motion. Rather than fixing the initial y-component, i.e., $y_0(\boldsymbol{x}_{k-1}, T/k) = y_0$ as a constraint, the direction of motion is incorporated into the targeting algorithm by equating y_0 to the same value as the y-component corresponding to point H, y_H, and explicitly enforcing the direction $\dot{y}_0(\boldsymbol{x}_{k-1}, T/k) < 0$ with the constraint equation

$$\dot{y}_0(\boldsymbol{x}_{k-1}, T/k) + \beta^2 = 0, \tag{3.50}$$

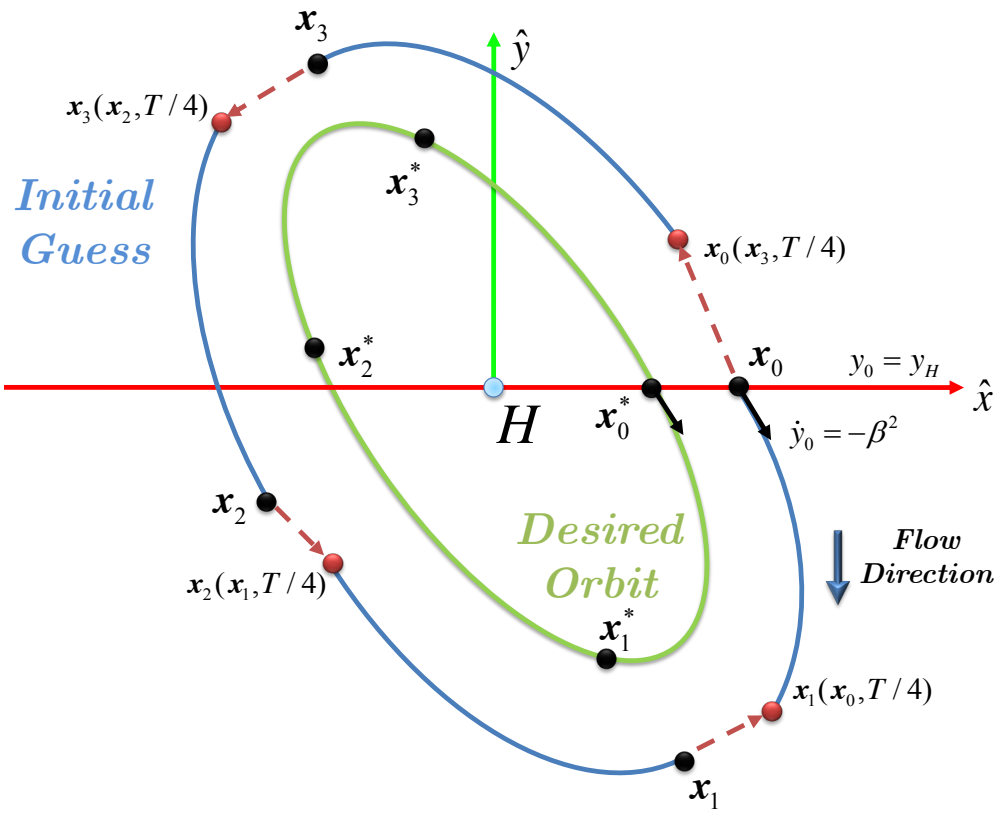

Figure 3.7. A schematic diagram of the initial guess and converged trajectory for a generic variable-time multiple shooting algorithm that isolates a periodic orbit about the arbitrary point H in the CRTBP. The approach accommodates an arbitrary number of k patch points, and $k = 4$ is illustrated in the figure.

where β is a slack variable that is introduced to replace an inequality with an equality constraint [40]. If an initial guess possesses counterclockwise motion about H (i.e., $\dot{y}_0(\boldsymbol{x}_{k-1}, T/k) > 0$), the sign of the β^2 term flips to accommodate the opposite inequality.

The free-variable vector and the constraint vector in a targeting algorithm to produce a periodic orbit are formulated to be consistent with the variable-time multiple shooting

method. The state vectors corresponding to the k patch points, the period T, and the slack variable β are collected to form the free-variable vector as

$$\boldsymbol{X} = \begin{Bmatrix} \boldsymbol{x}_0 \\ \boldsymbol{x}_1 \\ \vdots \\ \boldsymbol{x}_{k-1} \\ T \\ \beta \end{Bmatrix}, \tag{3.51}$$

where the dimension of $\boldsymbol{X}$ is now $n = 6k+p+l = 6k+2$. The constraint vector incorporates the standard continuity constraints, or $\boldsymbol{F}_k(\boldsymbol{X})$ from Equation (3.30), and seven additional constraints that comprise $\boldsymbol{F}_c(\boldsymbol{X})$ – one to maintain $y_0 = y_H$, five for periodicity, and one additional constraint to insure the specified direction for $y_0(\boldsymbol{x}_{k-1}, T/k)$. Overall, the dimension of the constraint vector, $\boldsymbol{F}(\boldsymbol{X})$, is $m = 6(k-1)+c = 6k+1$, and the constraint vector appears in the form

$$\boldsymbol{F}(\boldsymbol{X}) = \begin{Bmatrix} \boldsymbol{x}_1(\boldsymbol{x}_0, T/k) - \boldsymbol{x}_1 \\ \boldsymbol{x}_2(\boldsymbol{x}_1, T/k) - \boldsymbol{x}_2 \\ \vdots \\ \boldsymbol{x}_{k-1}(\boldsymbol{x}_{k-2}, T/k) - \boldsymbol{x}_{k-1} \\ x_0(\boldsymbol{x}_{k-1}, T/k) - x_0 \\ y_0(\boldsymbol{x}_{k-1}, T/k) - y_0 \\ z_0(\boldsymbol{x}_{k-1}, T/k) - z_0 \\ \dot{x}_0(\boldsymbol{x}_{k-1}, T/k) - \dot{x}_0 \\ \dot{y}_0(\boldsymbol{x}_{k-1}, T/k) \pm \beta^2 \\ \dot{z}_0(\boldsymbol{x}_{k-1}, T/k) - \dot{z}_0 \\ y_0 - y_H \end{Bmatrix}. \tag{3.52}$$

The "+" sign on the β^2 term is employed for clockwise motion about H whereas counterclockwise motion incorporates the "−" sign. The Jacobian matrix is then evaluated as

$$D\boldsymbol{F}(\boldsymbol{X}) = \begin{bmatrix} \frac{\partial \boldsymbol{x}_1(\boldsymbol{x}_0, T/4)}{\partial \boldsymbol{x}_0} & -I & & & \frac{\dot{\boldsymbol{x}}_1(\boldsymbol{x}_0, T/k)}{k} & \\ & \frac{\partial \boldsymbol{x}_2(\boldsymbol{x}_1, T/4)}{\partial \boldsymbol{x}_1} & -I & & \frac{\dot{\boldsymbol{x}}_2(\boldsymbol{x}_1, T/k)}{k} & \\ & & \ddots & \ddots & \vdots & \\ \Psi_1 & & & \frac{\partial \boldsymbol{x}_0(\boldsymbol{x}_{k-1}, T/k)}{\partial \boldsymbol{x}_{k-1}} & \frac{\dot{\boldsymbol{x}}_0(\boldsymbol{x}_3, T/k)}{k} & \Psi_2 \\ \Psi_3 & & & & & \end{bmatrix}, \tag{3.53}$$

with Ψ_1, Ψ_2, and Ψ_3 representing special submatrices. The missing entries in the $D\boldsymbol{F}(\boldsymbol{X})$ matrix are zero elements, and the indicated special submatrices appear in the forms

$$\Psi_1 = \begin{bmatrix} -1 & 0 & 0 & 0 & 0 & 0 \\ 0 & -1 & 0 & 0 & 0 & 0 \\ 0 & 0 & -1 & 0 & 0 & 0 \\ 0 & 0 & 0 & -1 & 0 & 0 \\ 0 & 0 & 0 & 0 & 0 & 0 \\ 0 & 0 & 0 & 0 & 0 & -1 \end{bmatrix}, \Psi_2 = \begin{bmatrix} 0 \\ 0 \\ 0 \\ 0 \\ \pm 2\beta \\ 0 \end{bmatrix}, \text{ and } \Psi_3 = \begin{bmatrix} 0 & 1 & 0 & 0 & 0 & 0 \end{bmatrix}.$$

Again, clockwise motion indicates the use of the "+" sign in Ψ_2. The size of the Jacobian matrix is $m \times n$, or $6k+1 \times 6k+2$. Since $n > m$ for this general periodic orbit targeting method, the minimum-norm update relationship (Equation (3.25)) is applied iteratively to evaluate a periodic orbit based on an initial guess.

3.5.1 Three-Dimensional Halo Orbits

Halo orbits in the Earth-Moon system are computed utilizing the general periodicity targeting algorithm. Members of the planar Lyapunov families in the vicinity of each collinear libration point exhibit deviations in certain characteristics [40,47]. Changes in the stability characteristics of an orbit are observed in the eigenvalues of the *monodromy matrix*, that is, the STM associated with a periodic orbit that is evaluated after exactly one period ($\Phi(T, 0)$). A change in the type of eigenvalues (e.g., a switch from real values to complex

values), identifies a bifurcation. At such locations, certain types of eigenvalues may suggest that new families exist and may intersect the current family [40, 48]. In the CRTBP, the intersection orbit between the halo family and the Lyapunov family occurs at the Lyapunov orbit associated with the first bifurcation as the family evolves outward from L_i [47]. (See Perko [48] for more information on bifurcation theory; refer to Grebow [40] and Doedel et al. [47] for additional details on bifurcation analysis applied to periodic orbit generation.) If the point H is defined as a collinear point (L_1,L_2, or L_3), the initial guess for an out-of-plane halo orbit is then created by extracting a set of patch points from the Lyapunov orbit. The patch points are equally distributed in time; the state where $y_H = 0$ and $\dot{y}_0 < 0$ is selected as the initial patch point. The initial patch point includes a small z component that triggers the out-of-plane behavior. Because of the symmetry property in the CRTBP across the xy plane [40], the direction of the out-of-plane perturbation determines an orbit that is either (i) a northern halo orbit, where a majority of the orbit exists above the xy plane, or (ii) a member of the southern halo family. A northern halo orbit is computed in the vicinity of each collinear point utilizing the generic periodicity targeting algorithm, and a continuation scheme is applied to generate a range of halo orbits in a family defined for each collinear point. Representative periodic orbits are displayed in Figure 3.8 with various views where the blue, red, and green colors correspond to the L_1, L_2, and L_3 northern halo orbit families, respectively. The orbit closest to the xy plane in each halo family is very similar in appearance to the associated Lyapunov orbits in Figure 3.5 but is twisted slightly out-of-plane. As the halo families are extended using continuation, the resulting trajectories evolve into vastly different shapes with significant out-of-plane components. As evident in Figure 3.9, rendering the northern halo families with a colormap that reflects the value of the Jacobi constant associated with each orbit. Each orbit with an increasing value of z-amplitude requires a velocity magnitude that also increases since the Jacobi constant value recedes as z-amplitude grows. Also notable, the L_3 halo family exists at much lower Jacobi constant values than the L_1 and L_2 halo families.

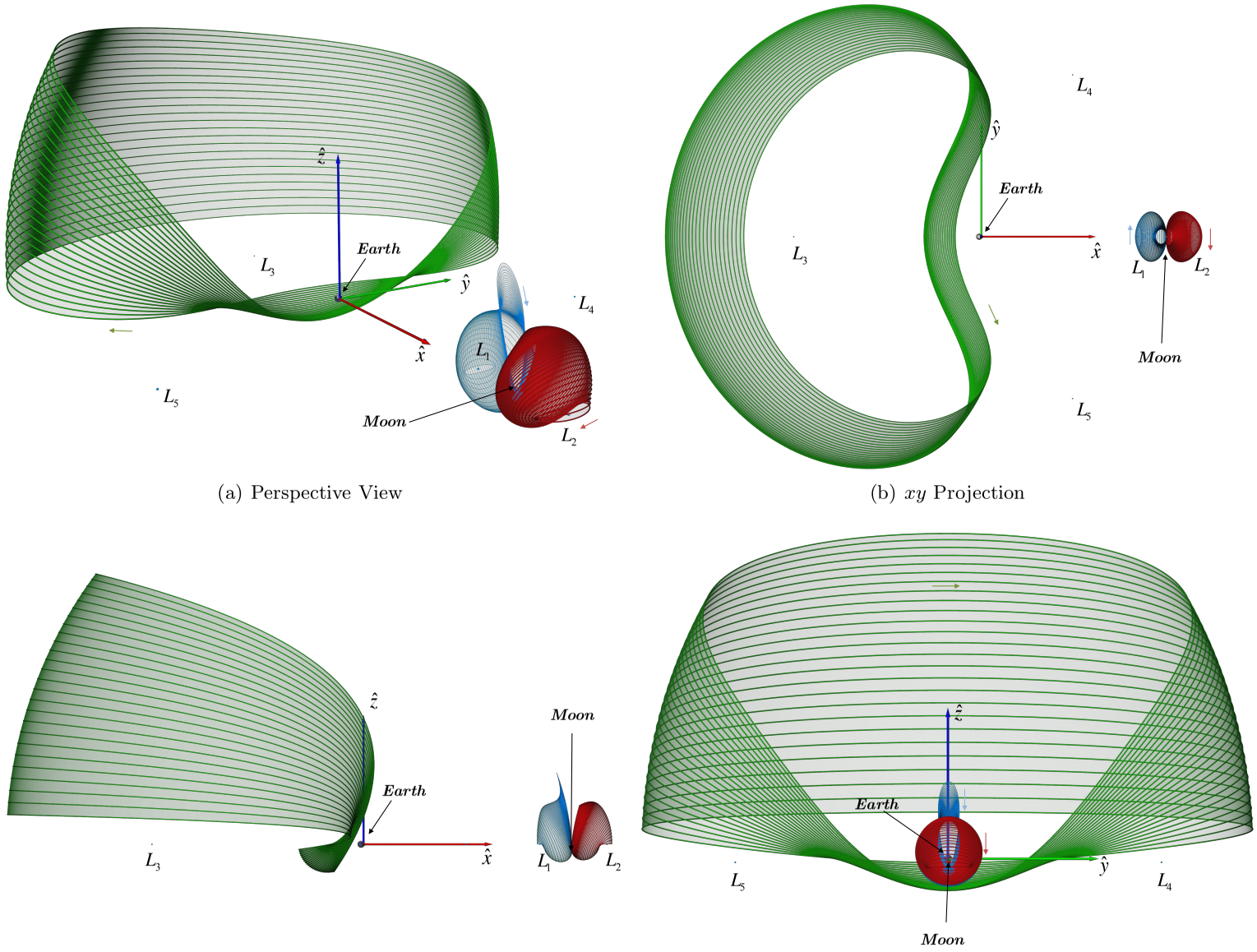

(a) Perspective View

(b) xy Projection

(c) xz Projection

(d) yz Projection

Figure 3.8. Halo orbit families (northern) about the collinear libration points in the Earth-Moon system.

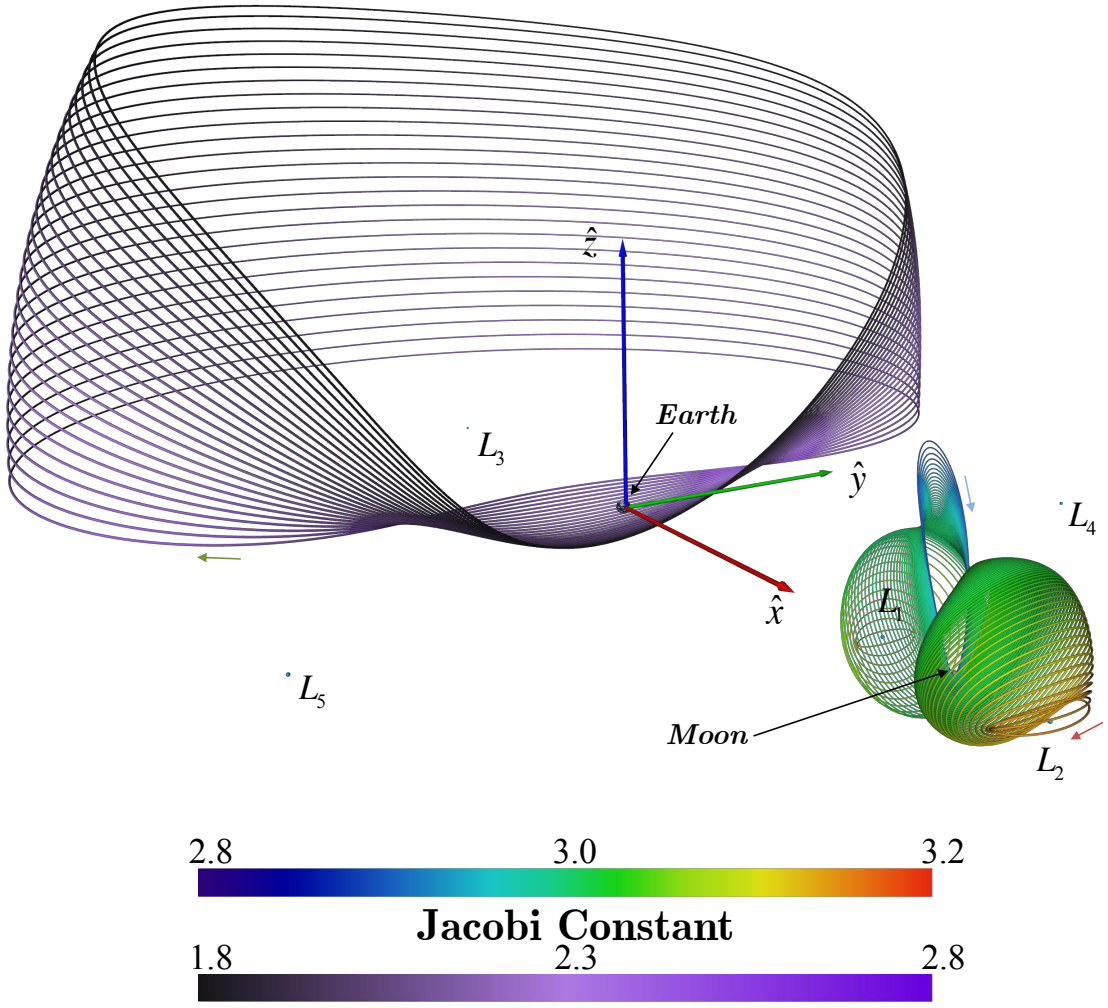

Figure 3.9. Halo orbit families (northern) about the collinear libration points colored by the value of the Jacobi constant associated with each orbit in the Earth-Moon system.

3.5.2 Asymmetric, Short-Period L_4 and L_5 Orbits

The general periodicity targeting algorithm is also used to compute asymmetric periodic solutions such as the orbits in the vicinity of L_4 and L_5. For this new application, however, the initial guess for such orbits must be generated first. The initial guess for periodic motion near the equilateral point also originates from Szebehely [33]. The equations of motion in the CRTBP are linearized about an equilateral libration point L_i, where $i = 4, 5$, to form the linear system

$$\dot{\boldsymbol{\xi}} = A_{L_i}\boldsymbol{\xi}, \tag{3.54}$$

where $\boldsymbol{\xi} = [\xi, \eta, \zeta, \dot{\xi}, \dot{\eta}, \dot{\zeta}]^T$ again represents the deviation from $\boldsymbol{x}_{L_i} = [x_{L_i}, y_{L_i}, 0, 0, 0, 0]^T$, and A_{L_i} is a 6×6 constant matrix evaluated at L_i. For the equilateral points, the characteristic roots of A_{L_i} consist of three imaginary pairs represented as $\lambda_{1,2} = \pm s_1 i$, $\lambda_{3,4} = \pm s_2 i$, and $\lambda_{5,6} = \pm\chi i$ [33]. Again, the out-of-plane motion, which is associated with $\lambda_{5,6}$, is decoupled from the planar motion, so the out-of-plane motion is fixed as $\zeta = \dot{\zeta} = 0$. The resulting linear xy planar motion is then governed by the remaining two oscillatory modes such that

$$s_1 = \frac{\sqrt{2}}{2}\left(1 - [1 - 27\mu(1-\mu)]^{\frac{1}{2}}\right)^{\frac{1}{2}}, \tag{3.55}$$

and

$$s_2 = \frac{\sqrt{2}}{2}\left(1 + [1 - 27\mu(1-\mu)]^{\frac{1}{2}}\right)^{\frac{1}{2}}, \tag{3.56}$$

where μ is the mass fraction in the CRTBP [33]. The solution to the linear problem then appears as

$$\xi(t) = C_1\cos s_1 t + S_1 \sin s_1 t + C_2 \cos s_2 t + S_2 \sin s_2 t, \tag{3.57}$$

$$\eta(t) = \bar{C}_1\cos s_1 t + \bar{S}_1 \sin s_1 t + \bar{C}_2 \cos s_2 t + \bar{S}_2 \sin s_2 t, \tag{3.58}$$

but the coefficients $\bar{C}_j$ and $\bar{S}_j$ are tied to C_j and S_j through the expressions

$$\bar{C}_j = \alpha_j(2s_j S_j - \Upsilon_{xy,L_i} C_j), \tag{3.59}$$

$$\bar{S}_j = \alpha_j(2s_j C_j + \Upsilon_{xy,L_i} S_j), \tag{3.60}$$

with

$$\alpha_j = \frac{1}{s_j^2 + \Upsilon_{yy,L_i}}, \tag{3.61}$$

for $j = 1, 2$ [33]. Since $s_1 < s_2$, the oscillatory modes are denoted as either (i) the "long-period" motion corresponding to behavior dominated by s_1 or (ii) the "short-period" motion where s_2 supplies most of the dynamical influence. The long-period behavior is eliminated by selecting $C_1 = S_1 = \bar{C}_1 = \bar{S}_1 = 0$. The initial velocities $\dot{\xi}_0$ and $\dot{\eta}_0$ associated with only the short-period behavior are then

$$\dot{\xi}_0 = \frac{1}{2}\left(\Upsilon_{xy,L_i}\xi_0 + \frac{\eta_0}{\alpha_2}\right), \tag{3.62}$$

$$\dot{\eta}_0 = -\alpha_2\left(\Upsilon_{xy,L_i}\dot{\xi}_0 + 2s_2^2\xi_0\right), \tag{3.63}$$

where ξ_0 and η_0 are pre-specified initial positions from L_i [33]. The expressions

$$\xi(t) = \xi_0 \cos s_2 t + \frac{\dot{\xi}_0}{s_2}\sin s_2 t, \tag{3.64}$$

$$\eta(t) = \eta_0 \cos s_2 t + \frac{\dot{\eta}_0}{s_2}\sin s_2 t, \tag{3.65}$$

then constitute the linear approximation to a short-period orbit with pre-specified initial values ξ_0 and η_0 [33]. The initial guess for the generic periodicity targeting scheme is then created by selecting a suitable ξ_0 and η_0. If the "center" point H is selected as L_4 or L_5, then $\xi_0 = 0.01$ and $\eta_0 = 0$ is employed to seed the guess for the first orbit. A set of k patch points are evaluated as $\boldsymbol{x}(t) = \boldsymbol{\xi}(t) + \boldsymbol{x}_{L_i}$ with values of t that are equally spaced in time such that the integration time for each segment is T/k and $T = \frac{2\pi}{s_2}$ from the short-period approximation.

The generic periodicity variable-time multiple shooting scheme generates a family of short-period, asymmetric orbits about L_4 and L_5. For both the L_4 and L_5 computations of short-period orbits, a linear guess is introduced in the Earth-Moon CRTBP with four patch points. An initial solution is generated that remains close in proximity to the L_4 and L_5 equilateral points. The initial orbits, the orbits closest to the equilateral points in Figure 3.10(a), appear as "tilted" elliptical shapes with clockwise motion about the equilateral points. A pseudo-arclength continuation method is implemented to extend the initial orbits

into the short-period orbit families in the vicinity of L_4 (purple) and L_5 (orange) as displayed in Figure 3.10(a). As the families evolves outward from the equilateral points, the orbits also evolve in appearance and eventually reach the vicinity of L_3. A rendering colored with the corresponding values of the Jacobi constant on each orbit (Figure 3.10(b)) indicates that the short period orbits around the equilateral libration points do not exist until the zero-velocity surface leaves the xy plane ($C_{L_{4,5}} = 2.987997$ in the Earth-Moon system).

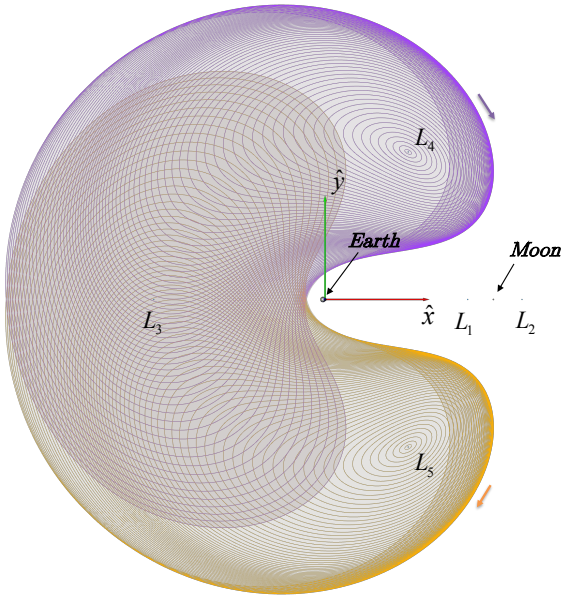

(a) Purple L_4 Orbits and Orange L_5 Orbits

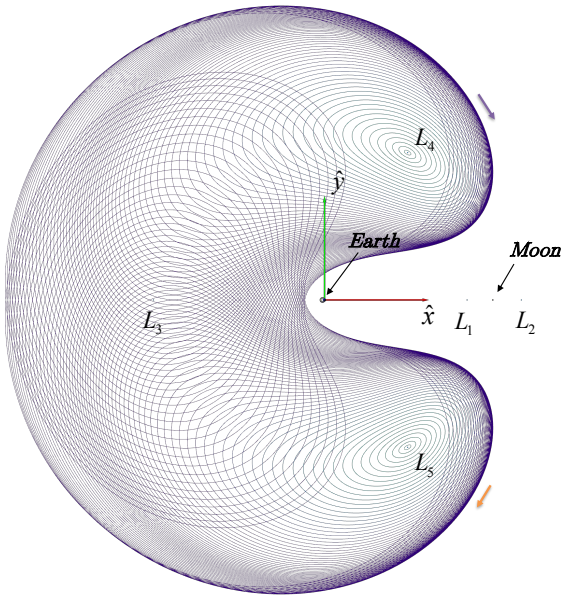

(b) Orbits Colored by Jacobi Constant

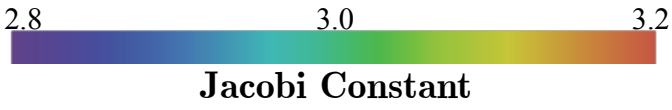

Figure 3.10. Families of planar periodic orbits encircling the equilateral points; the families are generated from linear short-period approximations in the Earth-Moon system.

3.6 Generic Multiple Shooting Method for a Graphical User Interface

A standard problem in design applications is the determination of a transfer trajectory with specific characteristics. The use of shooting schemes to solve these transfer problems insures numerous options; if one shooting approach, e.g., variable-time single shooting, proves inadequate for computing a transfer, another method, an alternative approach may be better-suited and the problem can be reformulated. However, construction of a targeting scheme for each problem slows down the concept creation speed, which is detrimental to an interactive design setting. Thus, a generic multiple shooting method is implemented with various targeting options that are controlled by a graphical user interface (or GUI).

A set of multiple shooting algorithms that are all similar serve as the basis for the analysis in a general targeting problem. Multiple options exist for implementation, so the available targeting options are focused on a smaller set of options that specifically involve multiple shooting approaches. The first option represents a choice between a variable-time or a fixed-time multiple shooting scheme. In either formulation, continuity constraints are enforced on a set of k patch points. Typically, generating a trajectory path must also include constraints on a starting point and/or a destination point. Thus, options to incorporate constraints on the first or last point along the trajectory arc are added as well. Let $\boldsymbol{r}_1 = [x_1, y_1, z_1]^T$ and $\boldsymbol{r}_k = [x_k, y_k, z_k]^T$ represent the position vectors corresponding to the first and last state vectors, respectively. The target conditions on the first and last position states are defined as $\boldsymbol{r}_0 = [x_0, y_0, z_0]^T$ and $\boldsymbol{r}_f = [x_f, y_f, z_f]^T$, respectively. The constraint options available are then summarized:

1. Continuity only.
2. Continuity with the first position constraint $\boldsymbol{r}_1 - \boldsymbol{r}_0 = \boldsymbol{0}$.
3. Continuity with the last position constraint $\boldsymbol{r}_k - \boldsymbol{r}_f = \boldsymbol{0}$.
4. Continuity with constrained first and last positions.

Overall, eight targeting algorithms are then available to solve a general targeting problem using multiple shooting. The algorithm permits four constraint options with either a fixed-time or variable-time approach.

Incorporating the eight different targeting schemes into the same GUI framework is accomplished by encoding Option 4 with a variable-time multiple shooting strategy. Assume that a set of k patch points $(\boldsymbol{x}_1, \boldsymbol{x}_2, ..., \boldsymbol{x}_k)$ with numerical propagation times along the segments $(t_1, t_2, ..., t_k)$ are available as the input guess. The free-variable vector, $\boldsymbol{X}$, for a variable-time multiple shooting scheme is constructed with the patch points and times as

$$\boldsymbol{X} = \left\{ \begin{array}{c} \boldsymbol{x}_1 \\ \boldsymbol{x}_2 \\ \vdots \\ \boldsymbol{x}_k \\ t_1 \\ t_2 \\ \vdots \\ t_k \end{array} \right\}. \tag{3.66}$$

The continuity constraints associated with linking the internal patch points are consistent with the definition of $\boldsymbol{F}_k(\boldsymbol{X})$ in Equation (3.30). Six additional constraints are added to ensure that the initial and final positions are driven to the desired values. The constraint vector for this generic algorithm is then expressed in the form

$$\boldsymbol{F}(\boldsymbol{X}) = \left\{ \begin{array}{c} \boldsymbol{F}_k(\boldsymbol{X}) \\ \boldsymbol{F}_{c0}(\boldsymbol{X}) \\ \boldsymbol{F}_{cf}(\boldsymbol{X}) \end{array} \right\}. \tag{3.67}$$

The initial position constraints are collected in the three-element vector

$$\boldsymbol{F}_{c0}(\boldsymbol{X}) = \left\{ \begin{array}{c} x_1 - x_0 \\ y_1 - y_0 \\ z_1 - z_0 \end{array} \right\}, \tag{3.68}$$

and another three-element vector,

$$\boldsymbol{F}_{cf}(\boldsymbol{X}) = \left\{ \begin{array}{c} x_k - x_f \\ y_k - y_f \\ z_k - z_f \end{array} \right\}, \tag{3.69}$$

represents the final position constraints. The Jacobian matrix is then separated into components pertaining to each type of free-variable and constraint as with Equation (3.35), i.e.,

$$D\boldsymbol{F}(\boldsymbol{X}) = \left[\begin{array}{cc} D\boldsymbol{F}_k(\boldsymbol{X}_k) & D\boldsymbol{F}_k(\boldsymbol{T}_p) \\ D\boldsymbol{F}_{c0}(\boldsymbol{X}_k) & D\boldsymbol{F}_{c0}(\boldsymbol{T}_p) \\ D\boldsymbol{F}_{cf}(\boldsymbol{X}_k) & D\boldsymbol{F}_{cf}(\boldsymbol{T}_p) \end{array} \right] \tag{3.70}$$

where $D\boldsymbol{F}_k(\boldsymbol{X}_k)$ and $D\boldsymbol{F}_k(\boldsymbol{T}_p)$ are consistent with the variable-time multiple shooting definitions in Equations (3.32) and (3.38). The submatrices $D\boldsymbol{F}_{c0}(\boldsymbol{T}_p)$ and $D\boldsymbol{F}_{cf}(\boldsymbol{T}_p)$ are zero matrices since the constraints on the initial and final positions do not depend on the integration times. The partial derivatives of the constraint equations with respect to the free variables are evaluated as

$$D\boldsymbol{F}_{c0}(\boldsymbol{X}_k) = \left[I_{3\times 6} \quad 0_{3\times 6(k-1)} \right] \tag{3.71}$$

and

$$D\boldsymbol{F}_{cf}(\boldsymbol{X}_k) = \left[0_{3\times 6(k-1)} \quad I_{3\times 6} \right]. \tag{3.72}$$

The seven other targeting algorithms are derived from this example by removing the appropriate components. Removing the constraint on the final position, for instance, is achieved by dropping $\boldsymbol{F}_{cf}(\boldsymbol{X})$ from the constraint vector and the subsequent portions of $D\boldsymbol{F}(\boldsymbol{X})$ (i.e., $D\boldsymbol{F}_{cf}(\boldsymbol{X}_k)$ and $D\boldsymbol{F}_{cf}(\boldsymbol{T}_p)$). Also, the switch to a fixed-time approach entails dropping the time elements, or terms referring to $\boldsymbol{T}_p$, from $\boldsymbol{X}$ and $D\boldsymbol{F}(\boldsymbol{X})$. The implementation of this generic targeting algorithm with a GUI environment allows users to quickly switch between the different eight targeting options presented.

3.7 Quasi-Newton Method

If a particular shooting method is experiencing hardship solving a TPBVP, a useful technique to improve convergence performance is the implementation of a scaled update step. Let the update step from Equation (3.24) for a square system ($m = n$) be defined as the *Newton step direction*, labeled $\delta \boldsymbol{X}^j$, as to set the next iteration free-variable vector, $\boldsymbol{X}^{j+1}$, given the current free-variable vector, $\boldsymbol{X}^j$, via the expression

$$\delta \boldsymbol{X}^j = -D\boldsymbol{F}(\boldsymbol{X}^j)^{-1}\boldsymbol{F}(\boldsymbol{X}^j). \tag{3.73}$$

Note that the Newton step for the minimum-norm solution in Equation (3.25) follows

$$\delta \boldsymbol{X}^j = -D\boldsymbol{F}(\boldsymbol{X}^j)^T \left[D\boldsymbol{F}(\boldsymbol{X}^j)D\boldsymbol{F}(\boldsymbol{X}^j)^T\right]^{-1} \boldsymbol{F}(\boldsymbol{X}^j). \tag{3.74}$$

The Newton step always offers a descent direction for a particular error or constraint vector, yet the amount to step along $\delta \boldsymbol{X}^j$ that ensures a decrease in error or constraint values remains uncertain. An attenuation factor, h, can assist with convergence utilizing the update equation

$$\boldsymbol{X}^{j+1} = \boldsymbol{X}^j + h\delta \boldsymbol{X}^j \tag{3.75}$$

where the attenuation factor ($0 < h \leq 1$) scales the Newton step to generate the next iteration of free-variables. For simplicity, let a scalar constraint function, $f(\boldsymbol{X})$, be defined as

$$f(\boldsymbol{X}) = \tfrac{1}{2}\boldsymbol{F}(\boldsymbol{X}) \cdot \boldsymbol{F}(\boldsymbol{X}) \tag{3.76}$$

where the coefficient is chosen arbitrarly. One could minimize the magnitude of the scalar constraint function with respect to the attenuation factor, but solving that optimization problem within the larger differential corrections problem is shown to be wasteful with unnecessary amounts of function evaluations [36]. Instead of minimizing, all that is required is a sufficient decrease in the overall constraint magnitude for the next iteration. This sufficient decrease condition satisfies

$$f(\boldsymbol{X}^{j+1}) = f(\boldsymbol{X}^j + h\delta \boldsymbol{X}^j) \leq f(\boldsymbol{X}^j) + \sigma \boldsymbol{\nabla} f(\boldsymbol{X}^j) \cdot \delta \boldsymbol{X}^j, \tag{3.77}$$

meaning that the error of the next iteration only needs to be a small factor less than the previous since $\boldsymbol{\nabla} f(\boldsymbol{X}^j) \cdot \delta \boldsymbol{X}^j < 0$ and σ is a small scaling factor (typically, $\sigma = 10^{-4}$) [36]. Next, the value of h is found by another numerical procedure including a line search for h along the $\boldsymbol{X}^j + h\delta \boldsymbol{X}^j$ line combined with a *backtrack* that applies the derived attenuation factor to form $\boldsymbol{X}^{j+1}$. Using data values associated with the initial step, the condition in Equation (3.77) is modeled as a polynomial with respect to h. Iteratively solving for the minimum of that polynomial delivers an appropriate h value while simultaneously preventing h from being too small to impede convergence (see Press et al. for further details [36]).

Employing the line search with backtracking during the differential corrections process represents a new method type–the *quasi-Newton method*. Given an existing scheme such as single shooting or multiple shooting, the quasi-Newton method places the line search and backtrack after the evaluation of the Newton step and applies the derived attenuation factor to update the free-variable vector for the next iteration. With the added search for an appropriate update, the quasi-Newton approach actually expands the basin of convergence compared to the original scheme as guesses can start further away from the desired solution [36]. Even though the quasi-Newton method is more robust than single-shooting or multiple-shooting alone, an important note about the quasi-Newton method is that the number of function evaluations increases drastically, and thus, the quasi-Newton method is often several factors slower regarding computational time. It is recommended to only employ the quasi-Newton method after the base method demonstrates convergence challenges.

4. DYNAMICAL SYSTEMS THEORY

The structure of a dynamical system guides the underlying flow behavior. Theory and principles related to time-invariant Hamiltonian systems (such as the CRTBP) harnesses the the available trajectories and flow patterns for versatile spaceflight applications. Differential corrections schemes supply a robust means of generating solutions to general trajectory design problems, but the success of such algorithms is still contingent upon the input guesses. Knowledge of the underlying dynamical behavior given a particular gravitational model greatly assists the formulation of initial guesses by exploiting special dynamical structures, namely periodic orbits and invariant manifolds emanating from unstable periodic orbits. These special structures also form the basis for the topological skeleton associated with Poincaré maps.

4.1 Poincaré Sections

One of the simplest yet a powerful tool for understanding periodic orbits and dynamical behavior is the Poincaré map. Let Γ represent a periodic orbit that is a solution to a set of differential equations, i.e.,

$$\dot{\boldsymbol{x}} = \boldsymbol{\phi}(\boldsymbol{x}, \tau), \tag{4.1}$$

that spans $\mathbb{R}^N$. Again, let $\boldsymbol{x}(\boldsymbol{x}_0, \tau)$ indicate the resulting state of numerically propagating the state $\boldsymbol{x}_0$ through the flow field $\boldsymbol{\phi}(\boldsymbol{x}, \tau)$for time τ. Assume that $\boldsymbol{x}^*$ is an initial state along the periodic solution Γ. When propagated with the system in Equation (4.1) over the period after one cycle, or T, the downstream propagation of $\boldsymbol{x}^*$, or $\boldsymbol{x}(\boldsymbol{x}^*, T)$, returns back to the initial state, i.e.,

$$\boldsymbol{x}(\boldsymbol{x}^*, T) = \boldsymbol{x}^*. \tag{4.2}$$

The hyperplane Σ is defined such that Σ intersects the curve Γ *transversally* at $\boldsymbol{x}^*$; the hyperplane Σ is selected as any hypersurface in $\mathbb{R}^{n-1}$ such that $\boldsymbol{x}^* \in \Sigma$ with *transversal* flow at the intersection. Given an initial state $\boldsymbol{x}$ on Σ, one that is assumed to be in the

neighborhood of a periodic orbit, the state $\boldsymbol{x}$ is propagated to the first return on Σ. From the initial $\boldsymbol{x}$, which originates near $\boldsymbol{x}^*$, the state that represents the return to Σ is then $\boldsymbol{\mathcal{P}}_\Sigma(\boldsymbol{x})$. Thus, the *Poincaré map*, or the first return map, is defined as the mapping

$$\boldsymbol{\mathcal{P}}_\Sigma(\boldsymbol{x}) := \boldsymbol{x} \longmapsto \boldsymbol{\mathcal{P}}_\Sigma(\boldsymbol{x}). \tag{4.3}$$

The Poincaré mapping performs a dimensional reduction, transporting $\mathbb{R}^N \mapsto \mathbb{R}^{N-1}$. The expected behavior on a Poincaré map for a near-integrable system is classified into four types–equilibrium, periodicity, quasi-periodicity, and chaos [49–51]. A periodic state, $\boldsymbol{x}^*$, returns to the same state through the Poincaré map, i.e.,

$$\boldsymbol{\mathcal{P}}^p(\boldsymbol{x}^*) = \boldsymbol{x}^*, \tag{4.4}$$

where p represents the number of returns required for a p-periodic trajectory to complete an orbit. Such periodic states on the surface of section are named *fixed points* since these points remain fixed when observing the Poincaré map. The schematic appearing in Figure 4.1 displays a periodic orbit Γ (blue) that intersects a green hyperplane Σ at $\boldsymbol{x}^*$. The state $\boldsymbol{x}_0$, which resides on Σ, generates the red trajectory when propagated forward until the return to Σ. The first return of $\boldsymbol{x}_0$ to Σ is then Poincaré map of $\boldsymbol{x}_0$, or $\boldsymbol{\mathcal{P}}_\Sigma(\boldsymbol{x}_0)$.

Incorporating Poincaré maps into a numerical process for trajectory computation requires some additional definitions. With numerical integration algorithms, event functions are employed to compute the returns of an initial state to the hyperplane Σ that defines a map. Return events are detected when some scalar function of the state variables, $f_\Sigma(\boldsymbol{x})$, crosses zero. Thus, the hyperplane is defined in terms of a scalar function such that

$$\Sigma := f_\Sigma(\boldsymbol{x}) = 0. \tag{4.5}$$

When computing a return, the scalar function may be increasing or decreasing through a zero-crossing. Thus, a one-sided Poincaré map is defined as either (i) $\boldsymbol{\mathcal{P}}_{+\Sigma}(\boldsymbol{x})$ corresponding to an increasing (or positive, $\dot{f}_\Sigma(\boldsymbol{x}) > 0$) return through Σ or (ii) $\boldsymbol{\mathcal{P}}_{-\Sigma}(\boldsymbol{x})$ where decreasing (or negative, $\dot{f}_\Sigma(\boldsymbol{x}) < 0$) zero-crossings of Σ are examined. The absence of a sign in the Poincaré map symbol, or $\boldsymbol{\mathcal{P}}_\Sigma(\boldsymbol{x})$, indicates an increasing one-sided map as that is the most

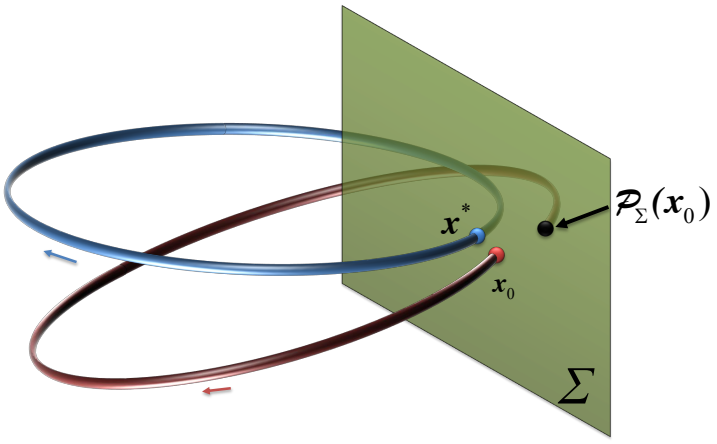

Figure 4.1. A schematic diagram of the Poincaré map.

common mapping throughout this work. A Poincaré map may also be two-sided, denoted $\mathcal{P}_{\pm\Sigma}(\boldsymbol{x})$, to capture both the positive and negative returns to Σ. Multiple crossings of a trajectory through a plane are also considered in many problems. Multiple iterates of the Poincaré map are computed by compounding the first return map, i.e.,

$$\mathcal{P}^p(\boldsymbol{x}_0) = \mathcal{P}_\Sigma(\mathcal{P}_\Sigma(\ldots\mathcal{P}_\Sigma(\boldsymbol{x}_0))), \tag{4.6}$$

where the map is evaluated for p returns to Σ. Both the initial state and first return to Σ appear as punctures of the green hyperplane in Figure 4.1. Generating a Poincaré section, or a collection of returns applied to a number of initial states, is accomplished by numerically propagating every initial state either forward or backward in time and computing the returns during the integration process.

Seeding a Poincaré section with an appropriate set of initial states is a crucial step to examine the dynamical behavior. Poincaré sections in the restricted three-body problem were demonstrated by Hénon in the 1960's, where Hénon focused his investigation of the

motion on the $\mu = 0.5$ system [52]. A sample Poincaré section in the Hénon system ($\mu = 0.5$), at a Jacobi constant value of $C = 3.75$, is explored in the rotating xy plane. The selection of an energy level, provided here with the selected C value, reduces the flow dimension again to now consider flow on $\mathbb{R}^{N-2}$. Given initial states in the plane, motion between the primaries is possible as evident from the zero-velocity curve for the $C = 3.75$ case provided in Figure 4.2, where the L_1 gateway is fully open. Because the response is limited to the xy plane, the 4-dimensional solution space exists and is modeled with the second-order differential equations consistent with the planar CRTBP (Equations (2.31) and (2.32)). The hyperplane Σ is selected as the $\hat{\boldsymbol{x}}$ axis, implying $\Sigma : f_\Sigma(\boldsymbol{x}) = y = 0$. Transverse flow to the hyperplane Σ is ensured by selecting initial states on Σ with a non-zero velocity component perpendicular to Σ ($\dot{y}_0 \neq 0$) and a zero in-plane velocity ($\dot{x}_0 = 0$). A two-sided Poincaré map, $\boldsymbol{\mathcal{P}}_{\pm\Sigma}(\boldsymbol{x})$, is then seeded with initial states along the $\hat{\boldsymbol{x}}$ axis ($y_0 = 0$) with various x_0 values. With C, y_0, and $\dot{x}_0$ specified for a seeding point at an arbitrary x_0 and a flow direction selected as $\dot{y}_0 > 0$, then $\dot{y}_0$ is fully determined through the Jacobi integral (Equation (2.48)). Therefore, the Poincaré map transports a $N = 4$ time-invariant Hamiltonian system into a 2-dimensional problem for analysis [49, 50]. The x_0 values for numerically generating $\boldsymbol{\mathcal{P}}_{\pm\Sigma}(\boldsymbol{x})$ are selected at arbitrary points that span the interior region as indicated in Figure 4.2.

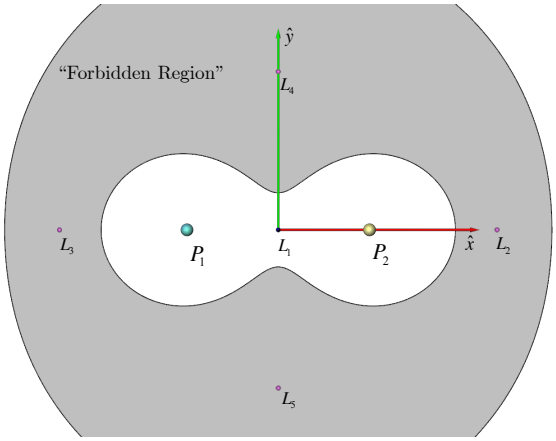

Figure 4.2. The viable region of motion in the Hénon system ($\mu = 0.5$) for a selected energy level ($C = 3.75$).

In the CRTBP, Poincaré sections are employed to characterize the global dynamical behavior by numerically integrating a set of initial states. The initial states seeding an example in the Hénon system are employed to generate a two-sided Poincaré section, $\boldsymbol{\mathcal{P}}_{\pm\Sigma}(\boldsymbol{x})$, for the first 200 returns to Σ. The resulting map is then visualized in a phase space (e.g., x-$\dot{x}$ space) as a discrete set of points at the phase space locations at the crossings. Such a depiction, known as a *puncture plot*, is demonstrated for the Hénon system in Figure 4.3. The returns in Figure 4.3 are colored such that each set of returns with the same color originates from the same initial state. The apparent behavior in the phase space projection is again classified into four different types: equilibrium, periodic orbits, quasi-periodic orbits, and chaotic trajectories. Critical points of the flow field stand as the equilibrium solutions (i.e., the Lagrange points). Fixed points, or periodic orbits, appear as crossing points that repeat the same returns, or $\boldsymbol{x}_i^*$, after p iterates ($\boldsymbol{\mathcal{P}}_{\pm\Sigma}^p(\boldsymbol{x}_i^*) = \boldsymbol{x}_i^*$ for $i = 0, \ldots, p-1$). Also in the phase space projection of the Poincaré section in Figure 4.3, some returns emanating from the same initial states encircle the fixed points. Since the returns in the cyclic shapes are not periodic but appear to trace a nearly repeating pattern, the behavior of the associated initial states is labeled *quasi-periodic*. The trajectories associated with quasi-periodic behavior form invariant tori in the full state space that approach a completely repeating pattern as the propagation time $t \to \infty$ [49,53]. A specific subset of quasi-periodic behavior collects returns into clusters that appear as a "chain of islands" as termed by Hénon [52]. Each "island" encircles a central point, and the collection of central points comprise another periodic orbit that resonates with the periodic orbit formed by $\boldsymbol{x}^*$ [52,54]. Another area in the phase space projection of the Poincaré section displays seemingly unordered behavior in which returns to the hyperplane Σ occur at unpredictable locations. Such behavior is known to be chaotic. In the CRTBP, chaos appears on Poincaré sections as "dusty" regions where chaotic trajectories visit the vicinity of both primaries in an unrecognizable configuration.

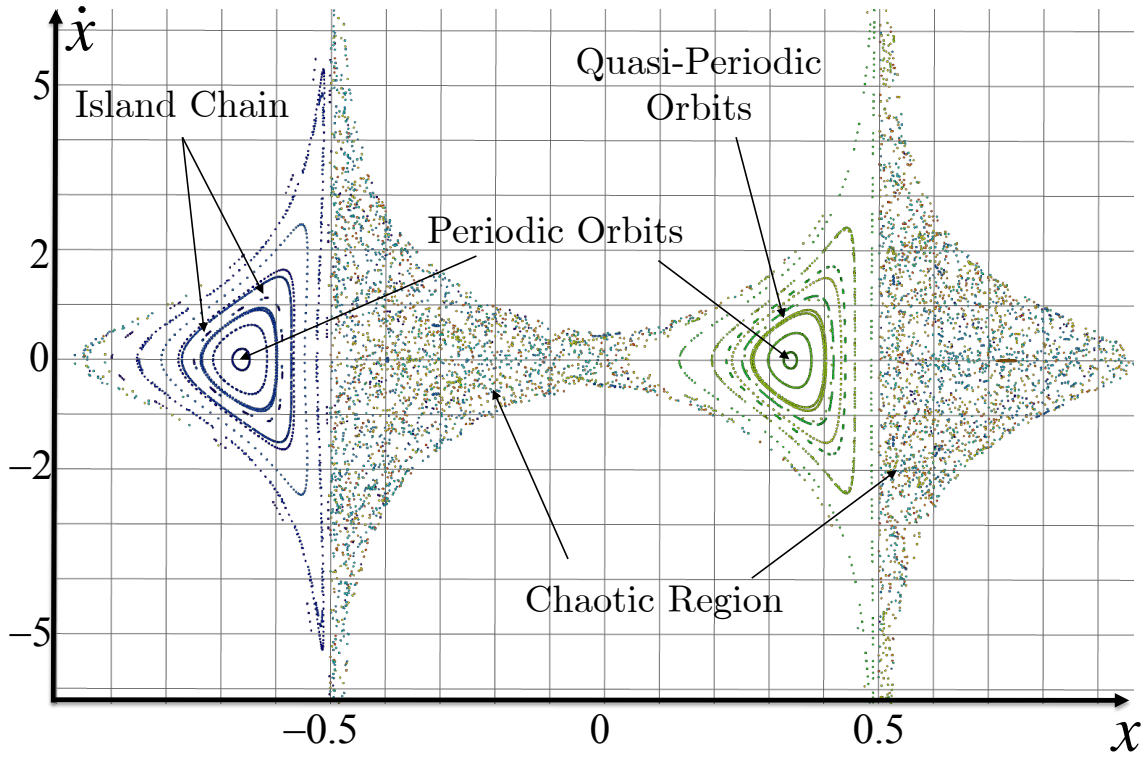

Figure 4.3. The Poincaré section projected into the x-$\dot{x}$ phase space for planar initial conditions originating on the $\hat{\boldsymbol{x}}$ axis with $\dot{y} > 0$ in the Hénon system ($\mu = 0.5$) for a selected energy level ($C = 3.75$).

4.2 Periodic Orbit Stability

Orbital stability is assessed by examining the characteristics of a fundamental matrix unique to periodic orbits. The *monodromy matrix* is defined as the state-transition matrix (or STM) associated with the fixed point $\boldsymbol{x}_0^*$ at time t_0 on a periodic orbit Γ and evaluated after one complete revolution along the orbit. Mathematically, the monodromy matrix, $\mathcal{M}$, is represented as

$$\mathcal{M} = \Phi(t_0 + T, t_0), \tag{4.7}$$

where T is the period of Γ. Stability characteristics of an orbit are then determined from the eigenvalues and eigenvectors of $\mathcal{M}$. In the stability analysis of a linear dynamical system, the solution space, $\mathbb{R}^N$, is segregated into three fundamental subspaces:

1. Stable Subspace $E^s \in \mathbb{R}^{n_s}$,
2. Unstable Subspace $E^u \in \mathbb{R}^{n_u}$,
3. Center Subspace $E^c \in \mathbb{R}^{n_c}$.

The total dimension of the solution space is then $N = n_s + n_u + n_c$. The eigenvectors associated with the stable, unstable, and center eigenvalues of the fundamental matrix in the linear system serve as the basis for the subspaces E^s, E^u, and E^c, respectively [48]. The monodromy matrix is the local linearization of the Poincaré map evaluated at the fixed point, and thus, the evolution of a small perturbation in the vicinity of $\boldsymbol{x}^*$ is governed by $\mathcal{M}$ via Equation (3.8). Perturbations that evolve towards $\boldsymbol{x}^*$ on the map represent an attracting or stable behavior; if a perturbation results drift away from $\boldsymbol{x}^*$, then this behavior is considered unstable with respect to the periodic orbit. Therefore, the eigenvalues of $\mathcal{M}$, i.e., λ_j where $j = 1, .., N$, are sorted into corresponding stability types by correlating the magnitudes, $|\lambda_j|$, with perturbation behavior, that is,

$$|\lambda_j| \begin{cases} < 1 & \text{Stable Eigenvalue,} \\ = 1 & \text{Center Eigenvalue,} \\ > 1 & \text{Unstable Eigenvalue.} \end{cases} \tag{4.8}$$

The eigenvalues of $\mathcal{M}$ are also known as the *characteristic (Floquet) multipliers* of the local discrete dynamical system formed by the Poincaré map [49, 50]. Floquet multipliers of a periodic orbit in a time-invariant Hamiltonian system appear in reciprocal pairs as the flow space is area-preserving (and volume-preserving) [50, 55]. Thus, if λ_j is an eigenvalue of $\mathcal{M}$, then λ_j^{-1} is also an eigenvalue of $\mathcal{M}$ [39, 50, 55]. Such a statement implies that a stable eigenvalue exists for $\mathcal{M}$ with a correlated unstable eigenvalue (or $n_u = n_s$). The classification of a periodic orbit as stable or unstable is then contingent upon this fact. An *unstable periodic orbit* is an orbit with a monodromy matrix possessing an unstable (and stable) subspace ($n_u = n_s > 1$). Conversely, a small perturbation relative to a *stable periodic*

orbit remains in the vicinity of that fixed point without attracting or repelling behavior ($n_u = n_s = 0$). Note, the center subspace always exists as a condition for periodicity, so $n_c \geq 2$ for all periodic orbits with the corresponding pair of Floquet multipliers at unity [48–50].

Stability characteristics are also classified with a stability index. Let the scalar metric, ν_{SI}, represent the stability index through the function

$$\nu_{SI} = \tfrac{1}{2}(\lambda + \lambda^{-1}), \tag{4.9}$$

with λ symbolizing a Floquet multiplier (commonly, the strongest unstable mode). The stability index now indicates unstable orbits when $|\nu_{SI}| > 1.0$ and stable orbits otherwise. Typically, this form of the stability index references the eigenvalues of the 4×4 *planar* (xy) monodromy matrix (or $\mathcal{M}_{xy}$). A useful application of the stability index is to separate planar behavior from the out-of-plane dynamics and characterize orbit stability for both in-plane and out-of-plane motion. The out-of-plane stability index is determined by utilizing properties of linear algebra. The trace of a matrix sums the entries along the main diagonal, but the trace also represents the sum of matrix eigenvalues. So, the trace of the monodromy matrix (6×6) is

$$\mathrm{tr}(\mathcal{M}) = \sum_j \lambda_j. \tag{4.10}$$

Note, one pair of eigenvalues of both $\mathcal{M}$ and $\mathcal{M}_{xy}$ are unity to represent periodicity [49,50]. Using this property and substituting in the planar stability index, ν_{SI}, and out-of-plane stability index, $\nu_{z,SI}$, the trace of $\mathcal{M}$ becomes

$$\mathrm{tr}(\mathcal{M}) = 2(1 + \nu_{SI} + \nu_{z,SI}) = \mathrm{tr}(\mathcal{M}_{xy}) + 2\nu_{z,SI}. \tag{4.11}$$

Note that the planar stability index is simply computed with

$$\nu_{SI} = \tfrac{1}{2}(\mathrm{tr}(\mathcal{M}_{xy}) - 2), \tag{4.12}$$

which is a very simple computation to determine stability characteristics that is more numerically reliable than a full eigenvalue analysis [36]. Rearranging Equation (4.11) decouples the z-directional motion from planar behavior in the stability index

$$\nu_{z,SI} = \tfrac{1}{2}(\mathrm{tr}(\mathcal{M}) - \mathrm{tr}(\mathcal{M}_{xy})) \tag{4.13}$$

Analogous to planar stability, the condition $|\nu_{z,SI}| > 1$ indicates a periodic orbit that is unstable to an out-of-plane perturbation; periodic orbits with $|\nu_{z,SI}| \leq 1.0$, on the other hand, demonstrate oscillatory motion about the orbit when perturbations in z are introduced. Negative values of ν_{SI} and $\nu_{z,SI}$ are possible and, in fact, signify special behavior related to the period-doubling bifurcation when $\nu_{SI} = -1$ or $\nu_{z,SI} = -1$ [49, 56, 57]. An even-odd instability occurs at this special condition where perturbations in a stable direction, for instance, approach $\boldsymbol{x}^*$ from *alternating* directions when mapped forward in time [58].

4.3 Invariant Manifolds Associated with Unstable Periodic Orbits

Invariant structures exist for an unstable periodic orbit that permit asymptotic arrival to and departure from the orbit. Stability analysis reveals that unstable periodic orbits possess both stable and unstable subspaces in the vicinity of a fixed point. An infinitesimal perturbation from the fixed point onto E^s or E^u identifies a trajectory that belongs to the corresponding nonlinear flow space. Since E^s and E^u are paired for unstable fixed points in time-invariant systems like the CRTBP [39,49], the flow behavior near the vicinity of the unstable fixed points appears topologically as a saddle [48–50]. This saddle-like behavior indicates that there are trajectories originating in the near-vicinity that freely flow either into the orbit or out of the orbit as $t \to \infty$. Although this apparent behavior emanates from one fixed point representing a periodic orbit, the same concept applies to every state along the periodic orbit since the eigenvalues of $\mathcal{M}$ are independent of the starting location along an orbit [39]. Thus, entire surfaces are comprised of trajectories exhibiting the same asymptotic behavior [48]. Such surfaces are then labeled the stable and unstable invariant manifolds associated with the unstable periodic orbit. In trajectory design problems, invariant manifolds offer trajectory options to asymptotically approach or leave a periodic orbit with only a small perturbation (e.g., a very small maneuver or ΔV).

Numerical computation of invariant manifolds is accomplished through the application of the linear mapping in the vicinity of the periodic orbit, i.e., the monodromy matrix. Local invariant manifolds that approach and depart the unstable orbits ($n_s = n_u \geq 1$) exist in the stable and unstable subspaces, respectively, and are defined in terms of the eigenvectors of $\mathcal{M}$. At the fixed point $\boldsymbol{x}^*$ corresponding to the periodic orbit Γ, the global stable and unstable invariant manifolds, $W^S(\Gamma)$ and $W^U(\Gamma)$, are tangent to the stable and unstable subspaces E^s and E^u of the monodromy matrix, respectively [39, 48]. Therefore, the eigenvectors associated with the stable and unstable eigenvalues of $\mathcal{M}$, written in component form as

$$\boldsymbol{v}_S = \begin{bmatrix} v_{x,S} \\ v_{y,S} \\ v_{z,S} \\ v_{\dot{x},S} \\ v_{\dot{y},S} \\ v_{\dot{z},S} \end{bmatrix} \text{ and } \boldsymbol{v}_U = \begin{bmatrix} v_{x,U} \\ v_{y,U} \\ v_{z,U} \\ v_{\dot{x},U} \\ v_{\dot{y},U} \\ v_{\dot{z},U} \end{bmatrix}, \tag{4.14}$$

are employed to approximate the global invariant manifolds with the local linear behavior in the fixed point vicinity.

Many methods exist to numerically generate invariant manifolds, but a majority of manifold computation methods focus on growing the structure from small initial perturbations throughout the saddle-type periodic orbit [13, 59, 60]. A standard approach to constructing manifolds in astrodynamics problems is called the *discrete geodesic evolution* (DGE) technique [59, 61]. In the DGE method, the geodesic is a closed curved along the streamsurface of an invariant manifold that is slightly perturbed from the periodic orbit Γ. A discrete set of states are sampled along this geodesic and evolved into a correlated group of trajectories to represent the specified invariant manifold [61]. The discrete states are selected by first examining a specified number of fixed points along an unstable periodic orbit. The eigenvectors associated with the most unstable (i.e., largest magnitude) eigenvalue and the reciprocal stable eigenvalue are collected to form a basis for E^u and E^s at each fixed point, respectively [39]. Eigenvectors are bidirectional by definition; thus, for convenience, the direction corresponding to $v_{x,S} > 0$ or $v_{x,U} > 0$ is considered the "+" direction, and the associated "+" eigenvector is denoted $\boldsymbol{v}_{S+}$ or $\boldsymbol{v}_{U+}$. As a visual demonstration, the sta-

ble and unstable eigenvectors from the monodromy matrices for a set of 30 fixed points constructed for an Earth-Moon L_1 halo orbit with $C = 3.17$ are computed. The result is rendered in Figure 4.4. A discrete geodesic is formed by perturbing the discrete set of fixed points in the direction of the eigenvectors to form approximate initial states on the stable and unstable invariant manifolds, $W^{S\pm}(\Gamma)$ and $W^{U\pm}(\Gamma)$, respectively. The eigenvectors are next normalized based on the position components, i.e.,

$$\boldsymbol{v}^{W^{S\pm}} = \frac{\boldsymbol{v}_{S\pm}}{(v_{x,S}^2 + v_{y,S}^2 + v_{z,S}^2)}, \tag{4.15}$$

$$\boldsymbol{v}^{W^{U\pm}} = \frac{\boldsymbol{v}_{U\pm}}{(v_{x,U}^2 + v_{y,U}^2 + v_{z,U}^2)}, \tag{4.16}$$

to control the magnitude of the perturbation from the corresponding $\boldsymbol{x}^*$ in terms of a distance. The initial states that along the discrete geodesic, $\boldsymbol{x}_{S\pm}$ and $\boldsymbol{x}_{U\pm}$, are then obtained through the expressions

$$\boldsymbol{x}_{S\pm} = \boldsymbol{x}^* + d_\rho \cdot \boldsymbol{v}^{W^{S\pm}}, \tag{4.17}$$

$$\boldsymbol{x}_{U\pm} = \boldsymbol{x}^* + d_\rho \cdot \boldsymbol{v}^{W^{U\pm}}, \tag{4.18}$$

where the d_ρ parameter is a specified distance that determines the magnitude of the perturbation related to position. Trajectories are then numerically evolved from initial states to form the DGE representation of the invariant manifold stream surfaces. Numerical integration of $\boldsymbol{x}_{U\pm}$ forward in time and $\boldsymbol{x}_{S\pm}$ backward in time for each specified fixed point generates the approximation of the unstable and stable invariant manifolds corresponding to the specified unstable periodic orbit [62]. The stable and unstable manifolds are also computed for the Earth-Moon L_1 halo orbit at $C = 3.17$, are projected into configuration space, and are then displayed in Figure 4.5. As is apparent for the Earth-Moon L_1 halo orbit, invariant manifolds corresponding to unstable 3D periodic orbits in the CRTBP appear as tube-like structures that fold and intersect themselves in numerous places in configuration space. All of the blue and cyan arcs representing W^S are potential trajectories that can be utilized to enter the underlying L_1 halo orbit asymptotically. Alternatively, a spacecraft in an Earth-Moon halo orbit, such as the orbit in Figure 4.5, could employ a very small maneuver to ride the unstable manifold back to Earth vicinity.

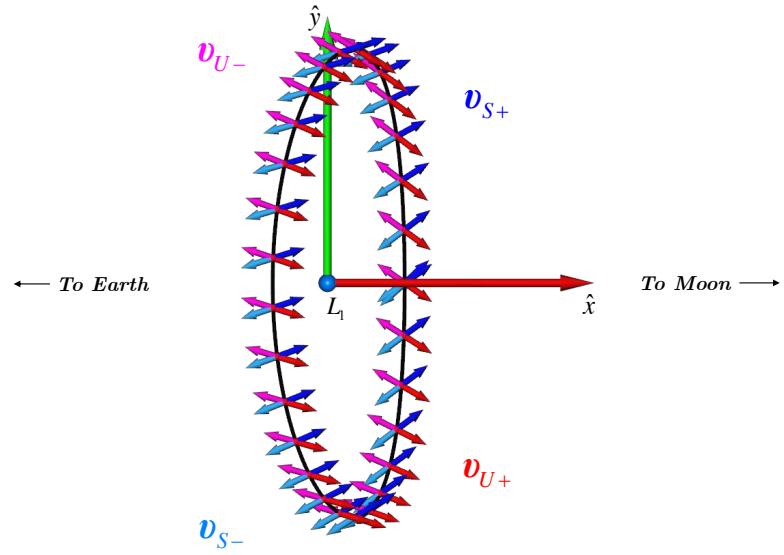

(a) Planar (xy) Projection

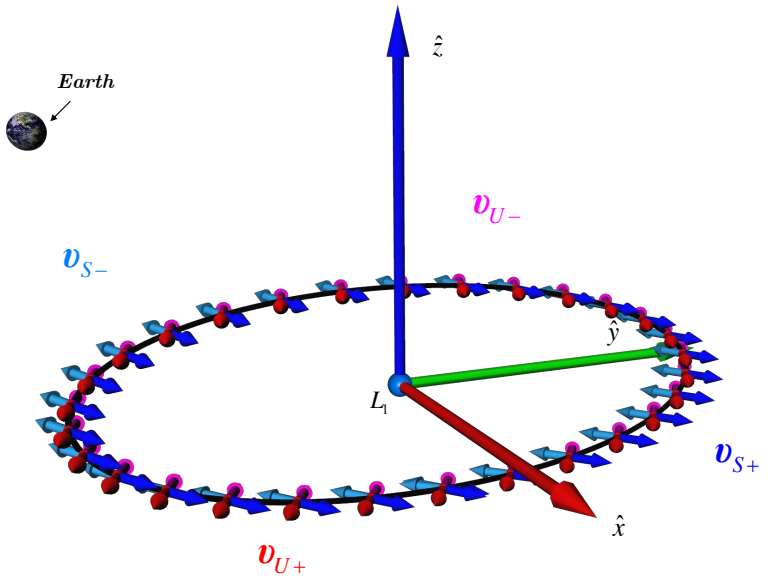

(b) Perspective View

Figure 4.4. Eigenvectors of the monodromy matrices for 30 fixed points on an L_1 halo orbit in the Earth-Moon system ($C = 3.17$).

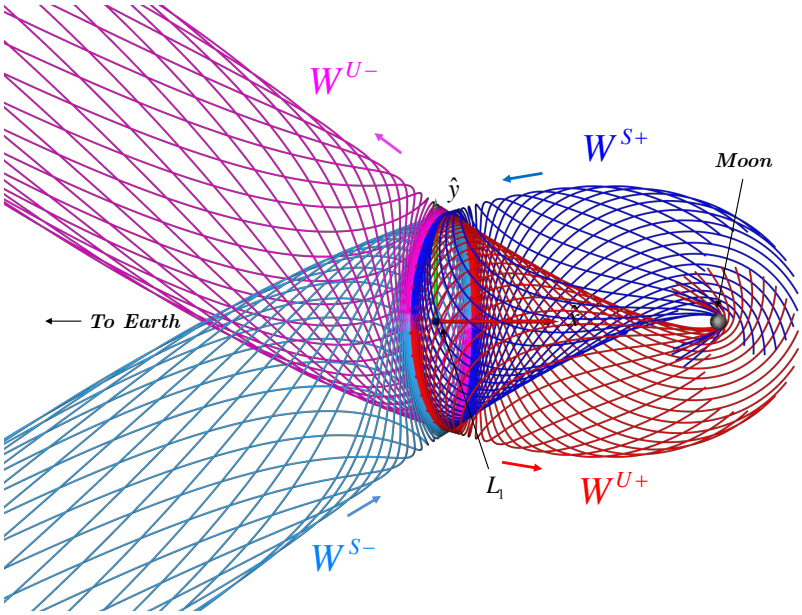

(a) Planar (xy) Projection

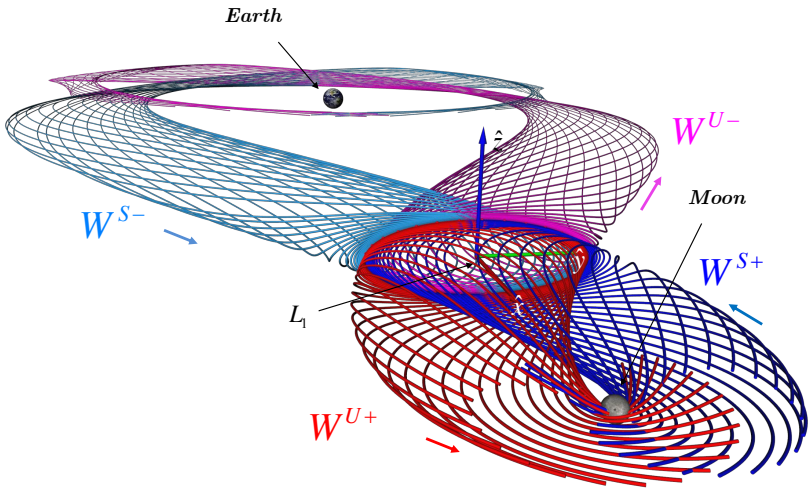

(b) Perspective View

Figure 4.5. Unstable and stable manifolds for an L_1 halo orbit originating from 30 fixed points in the Earth-Moon system $C = 3.17$.

On the Poincaré section for planar flow, invariant manifolds of planar periodic orbits behave analogously to manifolds in a discrete dynamical system [49, 61, 63]. With the discrete system defined by $\boldsymbol{\mathcal{P}}^p(\boldsymbol{x})$, a single trajectory (or streamline of the CRTBP dynamical system) is represented by a set of unconnected points on the Poincaré section. In the planar problem, the invariant manifolds of periodic orbits possess topological equivalence to the streamline-based W^U and W^S for saddle-type critical points in nonlinear flow fields [48, 49]. The saddle-type topology appears as 1D curves on the Poincaré section as the phase-space projection of the invariant manifold streamsurface as it crosses Σ. Trajectories belonging to the invariant manifold streamsurface follow predictable patterns in the area-preserving planar CRTBP, but the patterns are tied to stability characteristics. Let $\lambda_{\max}$ represent the eigenvalue of $\mathcal{M}$ with the largest magnitude, i.e., the strongest (unstable) mode. Also, let $\boldsymbol{x}_{0,U\pm}$ and $\boldsymbol{x}_{0,S\pm}$ symbolize states on Σ that coincide with $W^{U\pm}$ and $W^{S\pm}$, respectively, at some small perturbation from the p-periodic $\boldsymbol{x}^*$ on the Poincaré section. In the case where $\lambda_{\max} > 1$ (or equivalently $\nu_{SI} > 1$), the subsequent returns of the trajectory evolving from $\boldsymbol{x}_{0,U\pm}$ race away from $\boldsymbol{x}^*$ in an exponential manner as shown in Figure 4.6(a). The strength of this exponential growth (or increasing amount of Poincaré section distance) is determined by $\lambda_{\max}$. As apparent in Figure 4.6(b), the contrasting stability case for saddle-type fixed points ($\lambda_{\max} < 1$ or $\nu_{SI} < 1$) demonstrates a different pattern on the Poincaré section. The nonlinear sequence of returns originating from $\boldsymbol{x}_{0,U+}$ in Figure 4.6(b) switch from W^{U+} to W^{U-} in successive p iterates of the Poincaré map. The odd iterations jump to the opposite half manifold while the even iterations return the the original direction, mimicking an orientation reversing source for W^U [49]. Another description of this switching behavior is submitted by Wiggins as an instability that follows a half-twist Möbius strip [63]. Thus, an unstable periodic orbit with $\lambda_{\max} < -1$ (and $\nu_{SI} < -1$) is classified as a *Möbius orbit*. Note that this same flipping behavior applies to W^S for Möbius orbits when trajectories are simulated in reverse time or $\boldsymbol{P}^{-p}(\boldsymbol{x})$.

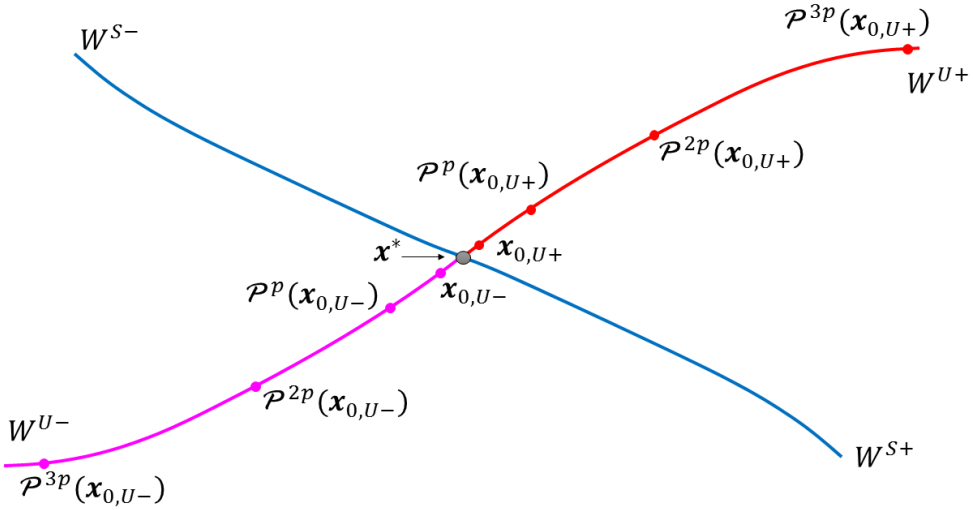

(a) W^U for $\lambda_{\max} > 0$

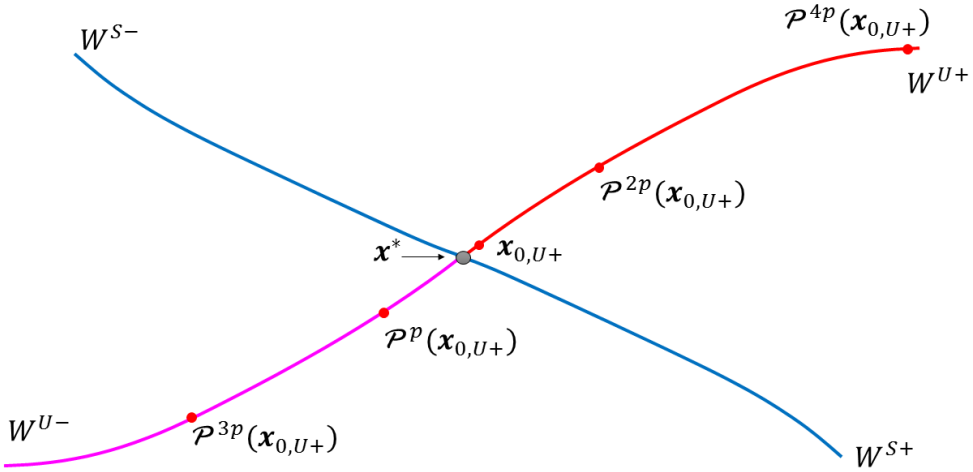

(b) W^U for $\lambda_{\max} < 0$ (Möbius orbit)

Figure 4.6. Discrete mappings of invariant manifold trajectories associated with a p-periodic saddle-type fixed point $\boldsymbol{x}^*$ on the Poincaré section [49,61].

4.4 Poincaré Map Topology

In a time-invariant, Hamiltonian system with two degrees of freedom such as the planar CRTBP, topological structures on Poincaré maps are confined to prescribed itineraries. The topology available on a Poincaré map emanates from the fixed points that may exist in a region of interest. Again, the monodromy matrix supplies a linear approximation of the behavior in the vicinity of the fixed point (or periodic orbit) that is reflected in a Poincaré section. Stable and unstable periodic orbits are also described in terms of the topology that appears on a Poincaré section. A stable periodic orbit possesses only a center subspace with no stable or unstable modes; thus, the Poincaré map of small perturbations in the vicinity of a stable periodic orbit appear as the quasi-periodic structures that encircle the fixed point. In contrast, stable and unstable subspaces exist in the vicinity of an unstable periodic orbit. Unstable fixed points present similar to a saddle-type critical point on the Poincare section (as shown previously in Figure 4.6. A plausible schematic topological skeleton of a Poincaré map with saddle-type and center-type behaviors is displayed in Figure 4.7. Quasi-periodic structures exist as closed curves on the Poincaré section that encircle the centers [49, 50]. From Kolmogoroff-Arnold-Moser (KAM) theory, a bounding trajectory, or KAM curve on the map (Figure 4.7), signifies the transition from quasi-periodic behavior to chaotic behavior [50]. Stable and unstable manifolds emerge from the saddle points indicating dynamical flow into and out of saddle-type periodic orbits, respectively [49, 50]. A pivotal element of map topology, especially for low maneuver-cost trajectory design problems, is the connection between saddle points via the unstable-to-stable manifold transition. The stable and unstable manifolds generally intersect an infinite number of times due to the chaotic tangles (the driving force of chaos) as seen in Figure 4.7, thereby making manifold tracking difficult [14, 50].

4.4.1 Invariant Tori and the Winding Number

For integrable and near-integrable Hamiltonian systems with two-degrees of freedom, considering the flow along a standard torus (or two-torus) provides an abstract interpretation of the dynamical behavior. Dynamical motion on a torus is described by the uncoupled evolution along two circles tracing out a trajectory on the outer surface [51]. The first circle,

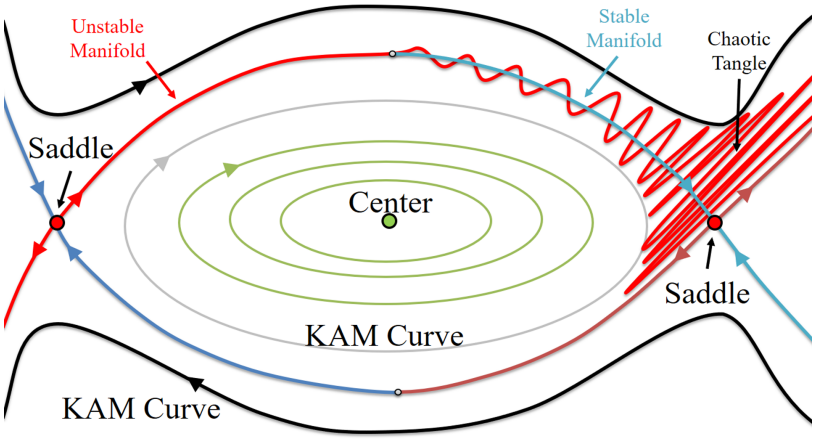

Figure 4.7. Available topological structure associated with a Poincaré map in a near-integrable dynamical system [14, 49, 50].

defined by the angle θ_1, indicates the cross-sectional evolution along the shorter poloidal dimension whereas the second circle, prescribed by the angle θ_2, represents motion along the toroidal dimension. The evolutionary history of the poloidal and toroidal angles can be plotted on a square with periodic boundary conditions such as the example appearing in Figure 4.8(a). The motion along the torus is then characterized by the ratio of the evolutionary frequencies of these two angles, namely,

$$w = \frac{\omega_1}{\omega_2}, \tag{4.19}$$

where ω_1 and ω_2 are the poloidal and toroidal frequencies, respectively. The quantity w is titled the *winding number* and represents a classification for a particular trajectory. The slope of the angular history chart in Figure 4.8(a) is simply the reciprocal of w as defined in Equation (4.19) [50, 51]. Winding numbers with exact integer ratios correspond to periodic orbits. When employing an integer number of rotations, the winding number, w, is defined as the number of poloidal rotations (q) versus the number of toroidal rotations (p), or $w = \frac{q}{p}$. Two sample periodic orbits with winding numbers $w = \frac{1}{1}$ and $w = \frac{3}{2}$ are displayed in Figure4.8(a) as green and blue trajectories, respectively. The $w = \frac{1}{1}$ orbit (green) completes a poloidal rotation for every toroidal rotation whereas the $w = \frac{3}{2}$ orbit (blue) requires 2 toroidal rotations to complete 3 poloidal rotations, indicated by the

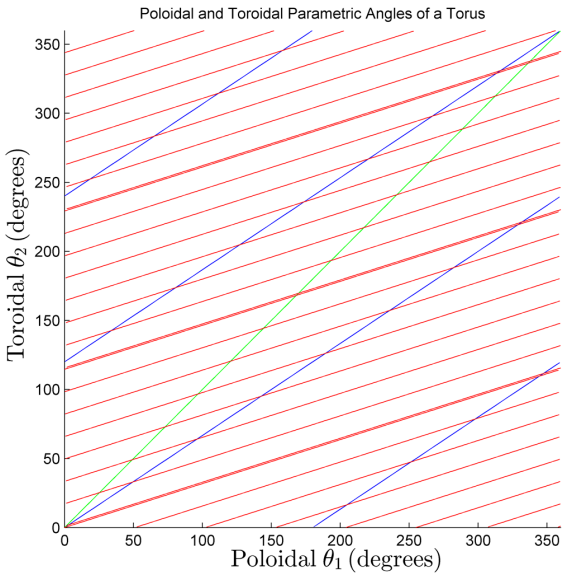

(a) Angle History

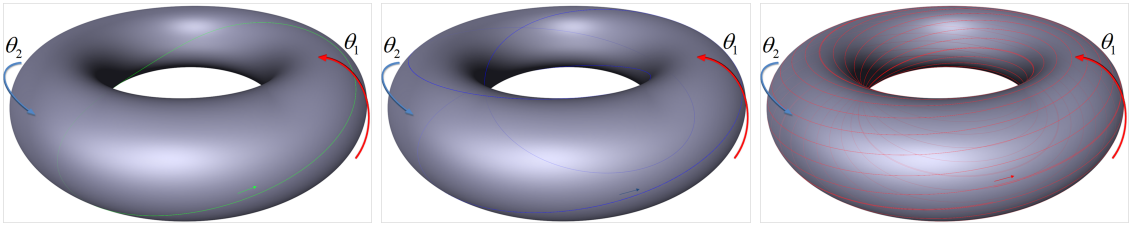

(b) $w = \frac{1}{1}$ Fixed Point (c) $w = \frac{3}{2}$ Fixed Point (d) $w = \frac{\pi}{1}$ Quasi-periodic

Figure 4.8. Dynamical behavior of motion along a torus for a $w = \frac{1}{1}$ orbit (green), a $w = \frac{3}{2}$ orbit (blue), and a $w = \frac{\pi}{1}$ quasi-periodic trajectory (red) [50, 51].

different slope in Figure 4.8(a). In contrast to periodic orbits, quasi-periodic trajectories possess irrational winding numbers. Thus, a quasi-periodic orbit such as the $w = \frac{\pi}{1}$ example (red in Fig. 4.8(a)) will never trace exactly the same path along the torus but will visit a dense portion of the torus as the trajectory evolves [51]. Near-integrable systems may also include chaos, creating structures that no longer map directly to a torus-type structure [50]. The winding number is, therefore, undefined for chaotic trajectories, but the saddle-type orbits that typically reside within the chaos still possess a valid winding number [50].

4.4.2 Heteroclinic and Homoclinic Connections

Intersections between various invariant manifolds are common within chaotic regions, forming a crucial component to Poincaré map topology and maneuver-saving spaceflight. Consider a pair of saddle-type periodic orbits, Γ_1 and Γ_2, with fixed points residing on the hyperplane Σ at $\boldsymbol{x}_1^*$ and $\boldsymbol{x}_2^*$ at mapping periods p_1 and p_2, respectively. Let the Poincaré section depiction in Figure 4.9 represent the corresponding dynamics in the vicinity of the saddle points. Note, Figure 4.9 depicts the associated invariant manifolds as 1D curves on the Poincaré section with unique coloring for each subspace ($W^U(\Gamma_1)$ as red, $W^S(\Gamma_1)$ as blue, $W^U(\Gamma_2)$ as orange, and finally $W^S(\Gamma_2)$ as black). Map locations where stable and unstable invariant manifolds intersect ($W^U(\Gamma_1) \cap W^S(\Gamma_1)$, $W^U(\Gamma_1) \cap W^S(\Gamma_2)$, $W^U(\Gamma_2) \cap W^S(\Gamma_1)$, or $W^U(\Gamma_2) \cap W^S(\Gamma_2)$) form trajectories that belong to both manifold streamsurfaces. An intersection between invariant manifolds of separate orbits is dubbed a *heteroclinic connection*, or $\mathcal{H}_c$. Based on a perfectly timed initial deviation, dynamics induce a trajectory, represented by the discrete points of $\mathcal{H}_c$, that flows from orbit Γ_i along $W^U(\Gamma_i)$ to orbit Γ_j via the asymptotic approach on $W^S(\Gamma_j)$ ($i \neq j$). The green dots in the sample dynamics of Figure 4.9 indicate heteroclinic connections between Γ_1 and Γ_2 that connect at the provided fixed points. Similarly, a *homoclinic connection*, $\mathcal{H}_o$, links an unstable manifold arc to a stable manifold arc from the same periodic orbit. Sample $\mathcal{H}_o$ trajectories are conveyed by the purple dots in Figure 4.9. A special homoclinic connection between $W^{U-}(\Gamma_1)$ and $W^{S-}(\Gamma_1)$ is also shown in Figure 4.9. Since this special $\mathcal{H}_o$ appears as a tangential intersection on Σ, every trajectory on $W^{U-}(\Gamma_1)$ flows into $W^{S-}(\Gamma_1)$, forming a *saddle loop* [49,51]. Although Figure 4.9 displays a saddle loop emanating from and returning to a single fixed point, such loops often occur between different fixed points of the same unstable orbit [50]. Saddle-loop connections actually form the KAM tori where a saddle-type orbit resides at the edge of a quasi-periodic region [50]. These KAM saddles are weakly unstable at the onset of chaos, possessing a stability index on the range $1 < |\nu_{SI}| \leq 2$. Heteroclinic and homoclinic connections are highly valuable in the context of versatile spaceflight because the underlying dynamics permits a maneuver-free transfer between saddle-type orbits. Yet, these free-flowing pathways must be derived or extracted from the dynamics in order to employ in design procedures.

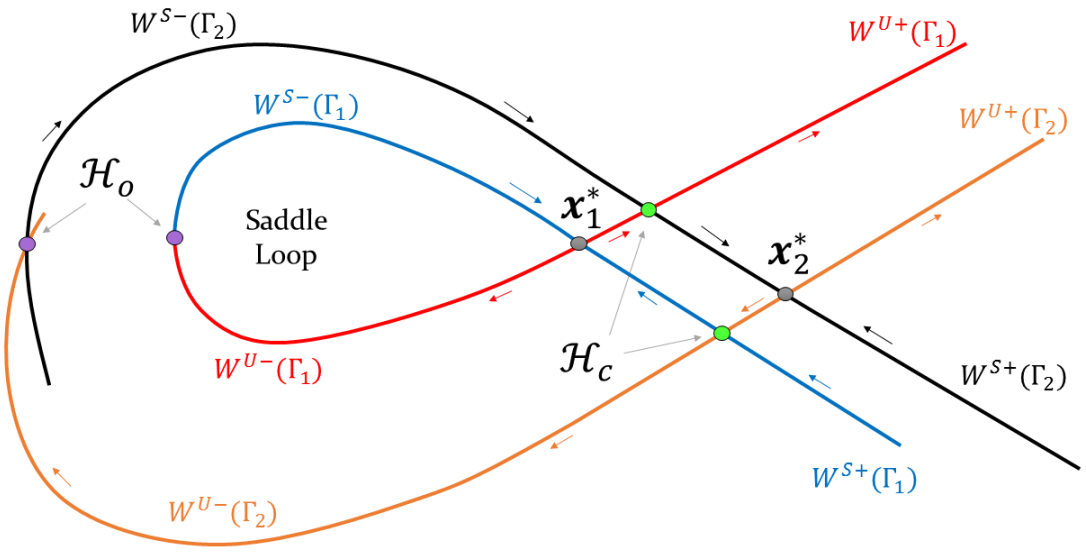

Figure 4.9. Schematic representation of homoclinic ($\mathcal{H}_o$) and heteroclinic ($\mathcal{H}_c$) connections between two unstable fixed points on a Poincaré section [49, 50].

4.4.3 Topology Extraction with Puncture Plots

In the planar CRTBP, the standard *puncture plot* approach renders a Poincaré map as a general depiction and supplies insight into the associated topology. As a sample pair of Poincaré sections, Poincaré maps are computed for the hyperplane $\Sigma : y = 0$ in different systems and displayed as puncture plots in Figure 4.10. Domains of interest in the Jupiter-Europa and Earth-Moon systems are selected arbitrarily as

$$D_{JE} = \{(x, \dot{x}) | x \in [-1.5, -1.0], \dot{x} \in [-0.5, 0.5]\}, \tag{4.20}$$

$$D_{EM} = \{(x, \dot{x}) | x \in [-0.4, 1.1], \dot{x} \in [-2.5, 2.5]\}, \tag{4.21}$$

respectively, where the range in x and $\dot{x}$ are expressed in nondimensional coordinates. (The gravitational parameters, μ_{JE} and μ_{EM}, associated with the the given systems are listed in Table 2.1.) A full state on Σ is then determined by selecting a Jacobi constant (C) value for analysis. For the puncture plots in Figure 4.10, initial states are selected randomly

throughout the domain and numerically simulated for 200 returns to the surface of section. Each initial state is assigned a unique color, and all subsequent returns from the same initial state are plotted as points with that designated color. Note, the white space bounded by the zero-velocity curves on the section represent the forbidden regions where trajectories are not allowed to evolve due to the Jacobi integral. Quasi-periodic regions are readily visible through the ordered groupings of returns from like-orbits. Trajectories that reside in chaotic regions appear with unpredictable behavior, and thus, populate a majority of the space where quasi-periodic behavior is not present. Thus, the saddle-type fixed points and the correlated stable and unstable manifolds are difficult to ascertain from the puncture plots in Figure 4.10 without additional analysis.

Extracting topology from a puncture plot representation of a Poincaré map involves several steps. Isolation of the topology is initiated by visually locating fixed points in the domain of interest, forming a set of initial guesses for a numerical corrections process. The center-type orbits are easily identified since these fixed points reside in the middle of quasi-periodic regions such as the closed curves in Figure 4.10. On the other hand, the hyperbolic saddle points hide in the chaotic sea, i.e., visual acquisition of saddle-type positions is difficult. Alternatively, a designer can locate fixed points that reside on a given Poincaré section by computing families of periodic orbits *a priori* and selecting the orbits that exist at the corresponding Jacobi constant value; however, it is impractical to generate orbit families for *all* the fixed points that appear on a section. Another key component to topology extraction is the computation of the stable and unstable manifolds associated with the saddle-type fixed points. It is standard practice in the puncture plot approach for displaying invariant manifolds on a Poincaré map to modify the DGE method to propagate numerous Poincaré map iterates [9, 64]. Unfortunately, this approach produces gaps in the manifold representation due to the divergent behavior of nearby manifold trajectories [7, 9, 10, 65]. This drawback can be mitigated by using a large number of fixed points distributed along the orbit ($> 10^5$ states) with an expensive number of mapping simulations. Overall, Poincaré map topology visualization with the puncture plot method typically requires a significant user effort beyond the initial numerical simulation.

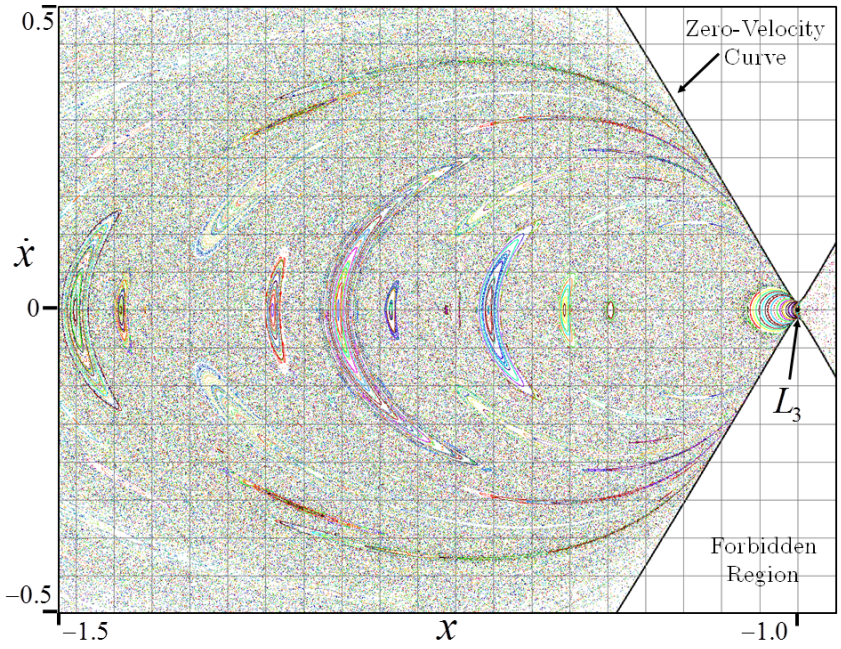

(a) Jupiter-Europa ($C = 3.00$)

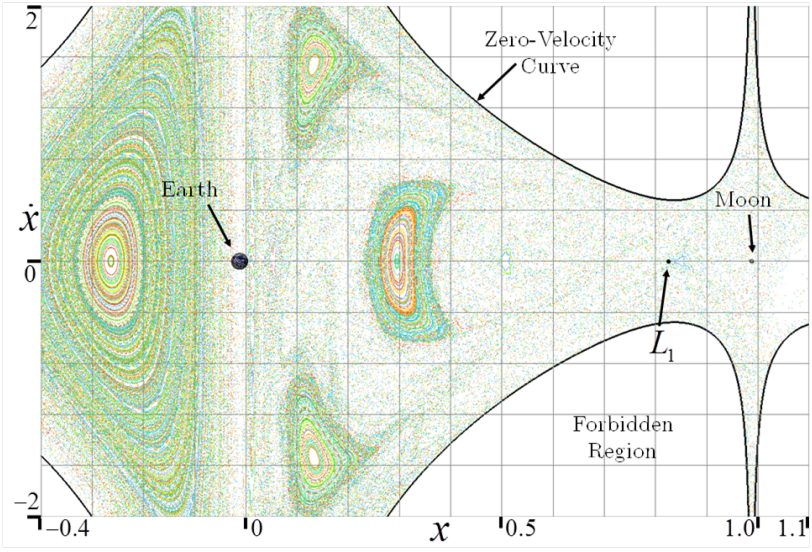

(b) Earth-Moon ($C = 2.96$)

Figure 4.10. Sample Poincaré maps for the hyperplane $\Sigma : y = 0$ in the planar CRTBP for different systems and domains visualized with the puncture plot method.

5. ENHANCING VISUALIZATION OF POINCARÉ SECTIONS

Although the puncture plot technique offers topological acuity in a system of interest, the rendering blurs the transition from quasi-periodicity to chaos and hinders localization of chaotic structure embedded in the sea of points. Texture-based techniques that utilize image-processing provide an enhanced visualization of streamlines in standard dynamical systems [66]. Since dynamical behavior on Poincaré section is topologically equivalent to a standard vector-field with saddle-type and center-type critical points [51], a texture-based visualization method is formulated for Poincaré mapping applications to create a focused image representing map structure.

5.1 Orbit Convolution

The *orbit convolution* method (OC) is employed for a texture-based depiction of the dynamics associated with a particular Poincaré map [14]. In a manner similar to the *Line Integral Convolution* method for vector field visualization (Cabral and Leedom [66]), the domain of interest for a Poincaré map is overlaid with a colored noise image, $\sigma(\boldsymbol{x})$, such that a random color (σ in RGB color coordinates from $[0,0,0]$ to $[1,1,1]$) exists at each pixel (or grid node) in an $N \times M$ image. The Poincaré map is then computed for each node in the image for n returns to the relevant surface of section. The resulting color image for a given initial state, $I(\boldsymbol{x})$, is then the average color mapping corresponding to the given number of iterations, n, of the Poincaré map, i.e.

$$I(\boldsymbol{x}) \ = \frac{1}{n}\sum_{p=0}^{n} \sigma(\boldsymbol{\mathcal{P}}^p(\boldsymbol{x})). \tag{5.1}$$

Here, p is an increasing sequence of map iterates such that $\boldsymbol{\mathcal{P}}^p(\boldsymbol{x})$ is contained in the domain of interest (i.e., there is a corresponding pixel in the input image). The resulting image identifies pixels (i.e., initial states) that reside on the same periodic or quasi-periodic orbit as a single color since the map corresponding to these states will visit the same set of colors

on the noise image. Chaotic trajectories intersect $\sigma(\boldsymbol{x})$ at seemingly random locations due to the unpredictable motion. The orbit convolution procedure reflects the chaotic behavior as a average color value that tends towards the expectation value of the colored noise–gray (or $[0.5, 0.5, 0.5]$ in RGB color coordinates) [14].

Modifications to the original orbit convolution procedure are required to adapt this approach to maps in multi-body regimes. Computing a large number of map iterations for a dense grid of initial states produces sufficient quality in a final visualization but at a high computational expense. A reduction in computational cost is achieved by replacing a large total number of orbit intersections, n, with extra convolution passes, thereby reducing the total number of numerical integrations. Let K represent the number of convolution passes applied to $I(\boldsymbol{x})$. If a convolution pass (Equation (5.1)) is expressed in terms of an operator $\mathcal{T}$, successive convolution passes generate the resulting image

$$I(\boldsymbol{x}) = \mathcal{T}^K(\boldsymbol{x}), \tag{5.2}$$

where the result of one convolution pass $(K-1)$ is used as the input to the subsequent pass (K), beginning with a noise image in the first pass $(K = 1)$. Essentially, the extended convolution is independent of the numerical propagation and, thus, trajectories are pre-computed and retained in memory for use in each subsequent convolution pass. A high-pass image filter is also employed after each convolution pass to preserve the contrast between available structures [14]. If the orbit convolution image is utilized as a rough background skeleton for the topology of the Poincaré map, the computational cost can be further mitigated by using a lower-accuracy simulation (numerical simulation with a higher error tolerance). In multi-body dynamical models, some initial states residing in an arbitrarily chosen sampling domain may reside within regions of non-real dynamical behavior (e.g., the forbidden regions in the CRTBP). It is also possible for a spacecraft trajectory to depart the primary system (i.e., the domain of interest) or for numerical sensitivities to impede the simulation of a particular initial state. Thus, a sufficient number of hyperplane intersections (n) cannot be reliably computed for some pixels. When such an event occurs, the corresponding pixels in orbit convolution images are marked as white pixels.

When applied to planar CRTBP examples, the orbit convolution method creates images with an evident distinction between quasi-periodicity and chaos. The orbit convolution scalar field for a 512×512 grid representing the domain D_{JE} is illustrated in Figure 5.1 with $n = 100$ returns and different degrees of convolution passes. The white areas in Figure 5.1 embody the forbidden regions in dynamical flow for D_{JE}. The resulting image in Figure 5.1(a) demonstrates the result of applying the color blending identified in Equation (5.1) (i.e., a solitary convolution pass). Two additional convolution passes with high-pass filtering are applied to the same set of data for enhanced clarity (Figure 5.1(b)). The resulting image efficacy is dramatically improved by utilizing multiple convolution passes even though the number of map iterates is unchanged. The gray regions in Figure 5.1(b) represent the state locations in D_{JE} that exhibit chaotic behavior as the map is propagated forward. Quasi-periodic trajectories appear in regions possessing the same non-gray color.

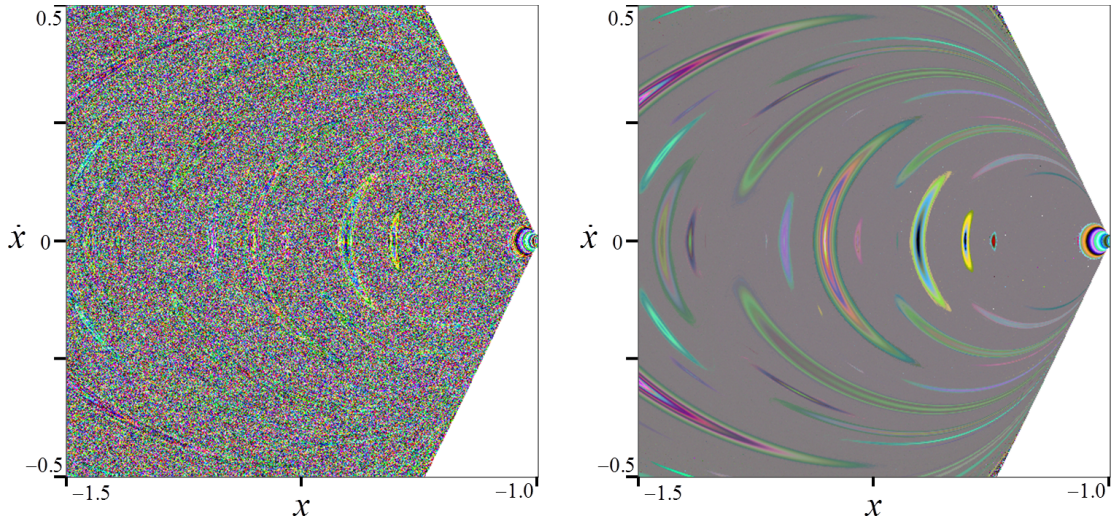

(a) $K = 1$ (b) $K = 3$

Figure 5.1. Orbit convolution visualization technique applied to a $\Sigma : y = 0$ section in the Jupiter-Europa system with parameters $n = 100$ iterates and K convolution passes.

Since the color values are randomly generated from the noise image, two distinct and separate orbital structures may display very similar colors. Fortunately, it is easy to disassociate like-colored structures as the color pattern in a given island chain remains consistent.

Orbit convolution reveals additional Poincaré section behavior in an example formulated in the Earth-Moon system. A visualization of the domain D_{EM} is portrayed in Figure 5.2 as a 1024×512 grid with $K = 3$ convolution passes. The resulting image again conveys chaotic regions in gray and regions of ordered behavior with a non-gray color. In contrast to the Jupiter-Europa example, large areas of the domain of interest in Figure 5.2 do not yield a sufficient number of map iterates in practical time, leading to a large number of white pixels between viable regions; however, these white-tagged trajectories are still a part of the chaos, and in fact, display the tendency to depart the Earth-Moon vicinity (i.e., the evolution of the simulated path does not return to the domain of interest).

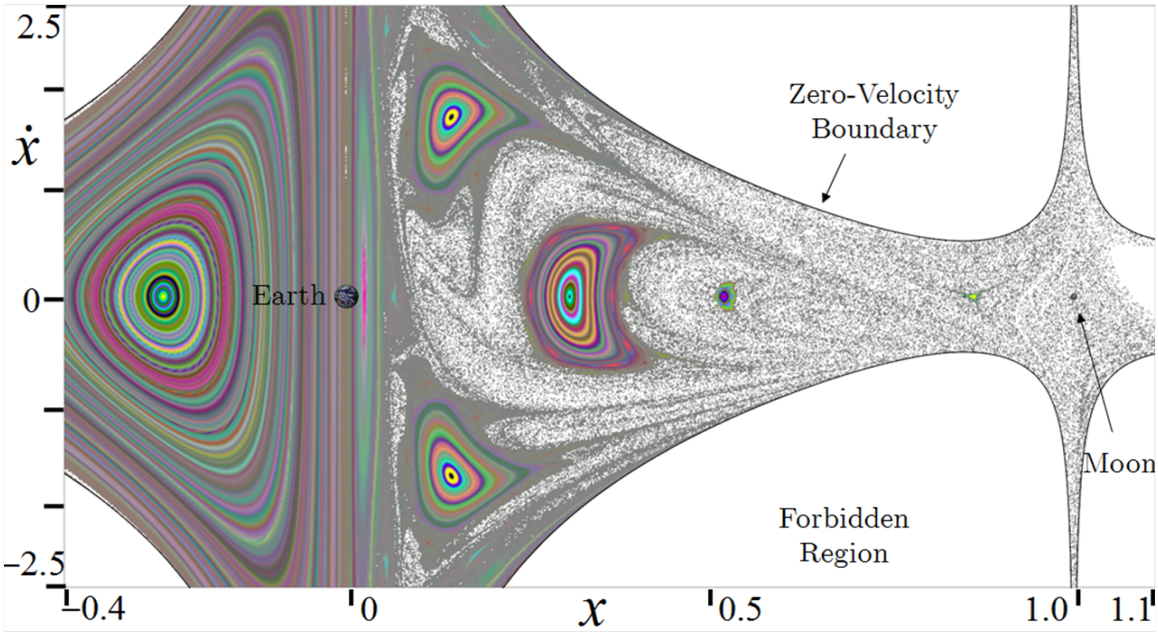

Figure 5.2. Orbit convolution visualization technique applied to the Poincaré section describing D_{EM} with parameters $C = 2.96$, $n = 100$ iterates, and $K = 3$ convolution passes.

Dynamical structures within the chaos emerge with orbit convolution imagery. In OC images like Figure 5.2, white pixels indicate trajectories that escape the given domain before n map iterates, yet gray pixels successfully complete n returns to Σ in forward time. Since stable invariant manifolds represent asymptotic approach to a periodic orbit in forward time, contrast between white and gray pixels within the chaos indicates stable invariant manifolds of some yet unknown fixed point. Thus, the OC image portrays a glimpse of

the topology associated with a given domain in the form of invariant manifold geometry. Another application of OC images is to demonstrate the effect of energy alterations on dynamical behavior. Progression of dynamical structure is highlighted in the Earth-Moon set of OC images shown in Appendix A.1 and A.2. At high C values, dynamical flow is restricted to the vicinity of the primaries with closed gateways (as stated in Chapter 2). As the L_1 gateway opens and the C value is lowered, quasi-periodic structure on the L_2 side of the Moon switches to almost purely chaotic. Further reduction in C introduces more velocity into the system and more chaotic trajectories between Earth and Moon indicated by the white pixels that become prevalent throughout the chaotic sea near $C = 3.13$. Quasi-periodic islands push closer towards Earth from lunar vicinity as C continues to drop; meanwhile, quasi-periodic islands on the L_3 of Earth appear to shed off of the larger stable region and translate away from Earth in the $-\hat{x}$ direction. Eventually, velocities are large enough (with a low Jacobi constant value of $C \approx 2.4$) that hardly any hits occur in lunar vicinity, meaning most of the trajectories in the chaos at this level escape the system. Similar behavior is demonstrated in the Saturn-Titan system within Appendix A.3, yet, the range of Jacobi constant values where flow around Titan is much smaller than the Earth-Moon system. Around $C = 2.8$, few trajectories remain in the Titan vicinity. Luckily, stable manifold structure (gray-white contrast) does appear to persist in Titan vicinity over a healthy range of Jacobi constant values within the Saturn-Titan system, possibly allowing for a variety of capture-like trajectories.

5.2 Chaos-Penalty Variant to Orbit Convolution

The orbit convolution method stores white pixels in areas where not enough mapping information is constructed, but exploiting available mapping data assists the understanding of dynamics in such areas. Recall that the term *returns* refers to the crossings of the hyperplane Σ and the actual Poincaré map iteration $\boldsymbol{\mathcal{P}}^p(\boldsymbol{x})$. The term *hits*, on the other hand, classifies returns that are also within the provided analysis domain for orbit convolution. When an insufficient number of hits is encountered, one way to still portray the achieved hits is to use gray colors in place of the missing information. Say that there are n_h hits to

the domain of interest. Also, let the color gray be represented as $I_g = [0.5, 0.5, 0.5]$. The *chaos-penalty OC* method then collects the convolution color as

$$I(\boldsymbol{x}) \ = \frac{1}{n}\left(\sum_{i=0}^{n_h} \sigma(\boldsymbol{\mathcal{P}}^{p_i}(\boldsymbol{x})) + \sum_{i=0}^{n-n_h} I_g\right) \tag{5.3}$$

when the number of hits is $n_h > 0$. Each i^{th} successful hit, or $\boldsymbol{\mathcal{P}}^{p_i}(\boldsymbol{x})$, is passed though the convolution field but missing returns are represented by blending in gray color. Since the partially completed trajectories are typically within the chaos anyway, this gray padding adds a weighting towards chaotic. If no hits are computed for a given initial state ($n_h = 0$), the resulting pixel is again set as white.

The primary application of the chaos-penalty variant of orbit convolution is for examining Poincaré sections on smaller domains within chaotic regions. These small domains possess many trajectories that only hit the given image bounds a few times. With the base version of the OC method, quasi-periodic structure appears over such smaller domains as it is quite difficult for trajectories in the chaos of multi-body dynamics to stay in close vicinity to a starting location. To demonstrate, an OC image is computed for a domain near the Distant Retrograde Orbit (DRO) which is a center-type periodic orbit that encircles the Moon in the retrograde direction [67, 68]. The nondimensional coordinate domain

$$D_{EM,DRO} = \{(x, \dot{x}) | x \in [0.8, 0.9], \dot{x} \in [-0.3, 0.31]\}, \tag{5.4}$$

encloses the DRO orbit as well as the associated quasi-periodic region. Applying the standard OC method to display the Poincaré section generates the 512×512 image in Figure 5.3(a). The invariant manifolds of the $p = 3$ saddle-type periodic orbit (at the corners of the triangular shape, called the *period-3 DRO*), form the KAM torus at the edge of the quasi-periodic region. Unfortunately, most of the surrounding area in Figure 5.3(a) is white since the chaotic trajectories depart this region. The preferable approach to examining this DRO region is to employ the chaos-penalty OC method as shown in Figure 5.3(b). Even with some trajectories never returning to this domain (white pixels), the contrast between white and gray indicates that many stable invariant manifold structures are available within this region. The large gray bands near the DRO quasi-periodic island indicate that trajec-

tories in the close vicinity to the $p = 3$ DRO actually remain for at least a few hits before departing. The added capability of chaos-penalty OC method clearly provides an in-depth look at dynamical structure even on small regions of interest.

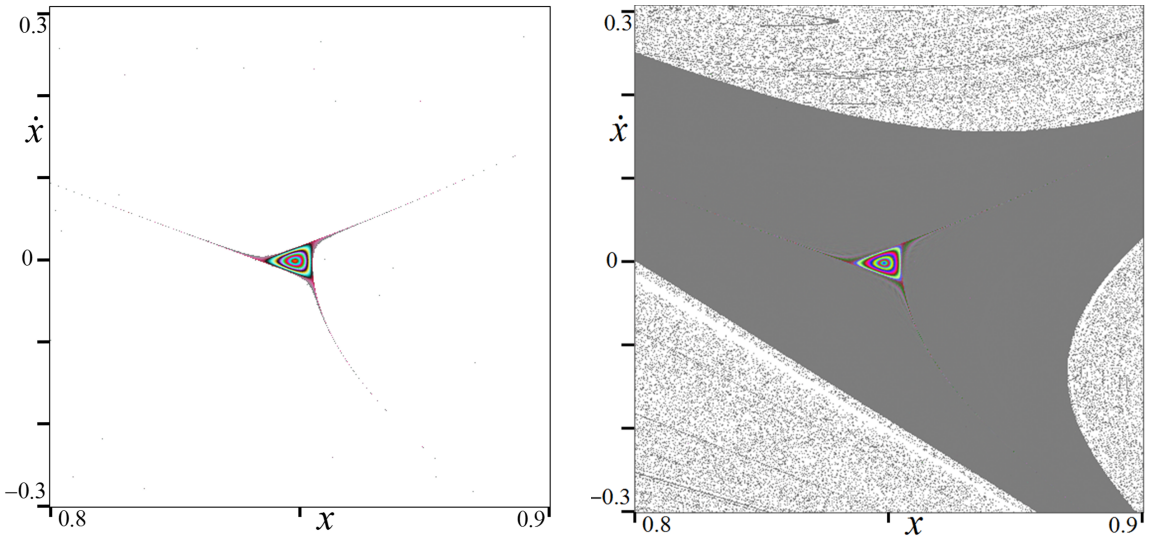

(a) Original OC

(b) OC with Chaos Penalty

Figure 5.3. Orbit convolution images representing the smaller Poincaré section domain $D_{EM,DRO}$ at $C = 2.96$ with parameters $n = 50$ iterates and $K = 4$ convolution passes.

6. INTERACTIVE STRATEGIES FOR ASTRODYNAMICS

The advancement of interactive trajectory design ideas hinges upon the interactive components of the visual analytics design process. Understanding the fundamentals of human-computer interaction leads to additional applications embedded in trajectory design procedures and, thus, introduces novel immersive design techniques tailored to astrodynamics. Immersive design procedures can greatly enhance and expedite trajectory construction that incorporates complex dynamical models where intuition is vague or absent. The following techniques are demonstrated within the CRTBP model, yet the application can be transferred easily to other dynamical systems.

6.1 Computer Graphics and Human-Computer Interaction

Understanding the basic construction of a virtual environment is rooted in the fundamentals of human-computer interaction. Graphical objects in a virtual scene are characterized by vertexes, segments, and faces placed in a world coordinate frame $(\hat{\boldsymbol{x}}, \hat{\boldsymbol{y}}, \hat{\boldsymbol{z}})$. Some graphical objects representing a possible astrodynamics scene, including vertexes and faces assembled into spheres for gravitating bodies and segments for trajectories, are depicted in Figure 6.1. The camera defines the human viewpoint of the scene via a location $(\boldsymbol{E})$ and a view direction $(\hat{\boldsymbol{c}})$. The computer screen displays the projection of the scene onto a view plane, or Σ_{VP}, that is spatially perpendicular to $\hat{\boldsymbol{c}}$ and at a specified distance from the camera (commonly known to as the near-distance) [69]. The on-screen image is then generated through rasterization (conversion of graphical data to pixels) of the scene after projection onto Σ_{VP} with screen-space coordinates $(\hat{\boldsymbol{a}}, \hat{\boldsymbol{b}})$ [69, 70].

Human-computer interaction transitions human modifications on an input device such as a keyboard, mouse, or joystick to a selection or change in the virtual environment. Device input is typically converted into an action such as the *picking action* (a mouse click, device button press, or touch over an object) or the *motion action* (movement of a pointer) [69, 70]. A common example of these actions is camera movement like panning and zooming [71].

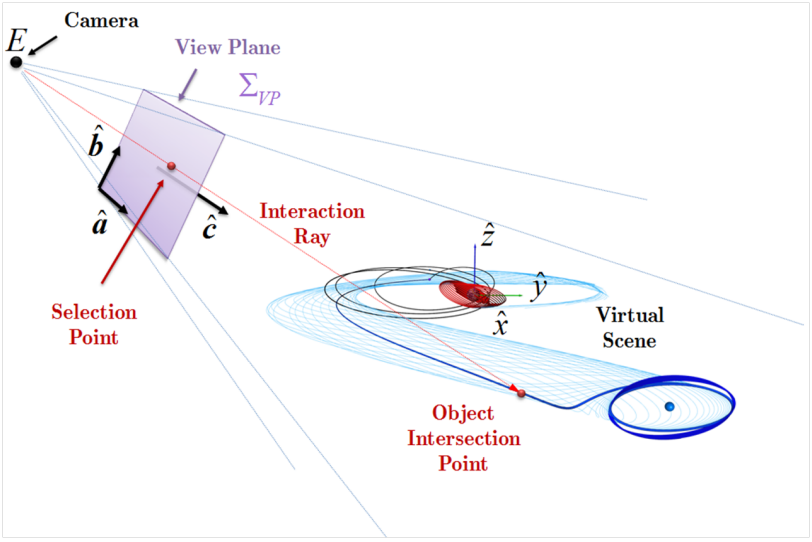

Figure 6.1. A practical viewing system with a camera at point E, a view frustum created through perspective projection, and a view plane (purple). An interaction ray is indicated by the red line (adapted from Watt [69] and Schlei [2]).

When interacting with graphical objects representing data, the selection process works in an inverse order to constructing the virtual scene. At the occurrence of a picking action instantiated by the mouse, for example, the mouse position on the screen is extracted as a 2D pixel-based coordinate on Σ_{VP}. The midpoint of that pixel originates an interaction ray (red ray in Figure 6.1) that is sent into the scene subject to the current projection system (e.g., perspective or orthographic) [69]. Intersection testing functions then locate the graphical objects that the interaction ray hits and return the objects in a front-to-back order as well as additional information about the picked objects [70].

Human-computer interaction influences the visual analytics scenario via a user-created post-process to an action, converting returned information into a change in the scene or creation of new data. A sample of a user-specified interaction protocol is demonstrated in Figure 6.1 where an arc-selection routine employs the picked line index to highlight the selected arc by increasing line thickness and emphasizing the rendered color (selection of the dark blue arc). Interaction protocols create new options to access the visual data that already exists in the scene. With the relevant trajectory data already available within the scene, human-computer interaction protocols supply the methods to manipulate that data

for desired effects instead of generating information from scratch. If on-the-fly generation of new data is required though, interaction with reference data in the form of simpler graphical objects (points, lines, planes, etc.) can be linked to numerical propagation to create trajectories. Numerous discovery, analysis, and design objectives benefit from such interactive data acquisition techniques.

6.2 Interaction with Poincaré Maps

A straightforward implementation of the picking action in astrodynamics problems frequently applies to a Poincaré section. If the Σ hyperplane exists as a physical plane in configuration space (e.g., $y = 0$), then Σ resides in the virtual world coordinates that represent xy planar trajectories. The vacant virtual world $\hat{z}$ dimension, though, can be exploited to represent a Poincaré section by overlaying a scaled version of the remaining map coordinate ($\sigma\dot{x}$ with $\Sigma : y = 0$). A simple plane object is placed in the world $\hat{x}\hat{z}$ plane to virtually represent a Poincaré section as depicted in Figure 6.2. Interacting with the Poincaré map is accomplished with a pick-selection on the representative plane.

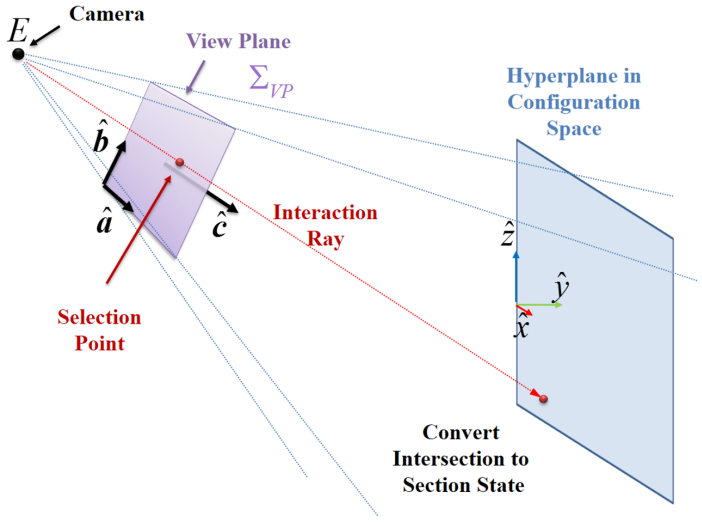

Figure 6.2. Schematic depiction of user-interaction with a hyperplane for a Poincaré section embedded within a graphical scene. The user-supplied interaction function converts the selected point that intersects the hyperplane to a state for propagation.

References to actual flow behavior are added to the hyperplane through a texture-based technique to represent the Poincaré section. The orbit convolution (OC) technique generates a texture image for a given domain on a Poincaré section where colored regions indicate periodicity or quasi-periodicity. Gray and white regions within the valid flow space display areas of chaotic motion [72]. Arbitrarily selecting a scaling factor ($\sigma = 0.16$ for $\Sigma : y = 0$), an OC image is embedded as a texture-map to the (hyper)plane object. The textured plane object itself now provides visual cues to associated flow behavior, highlighting desired effects based on selections within the hyperplane.

When the interaction ray intersects the plane (or image), the point of intersection is returned as virtual world coordinates. In turn, these picked point coordinates are easily converted to an initial state on Σ through a series of transformations. If linked to a user-created propagation process, the trajectory associated with the selected initial state on the map is instantly simulated and displayed in the scene as depicted by the single selection in Figure 6.3. A selected state on the Poincaré section is propagated instantaneously to form the green trajectory the Earth-Moon system in Figure 6.3 with the initial location indicated by black point on the Poincaré section. Other iterates of the Poincaré map for the selected trajectory are illustrated by the additional black points. Trajectories are either displayed directly in the same visualization as the OC image (as in Figure 6.3) or in a companion visualization conveying the xy projection. The colored examples in Figure 6.4 demonstrate additional selected map states with a similar propagation in a companion scene. Intermediate map states are also displayed with spatial text indicating return number. Continuous propagation of nearby points is achieved by holding the mouse button down during motion, resulting in a visual depiction of the spatial variance of the map. This Poincaré map interaction technology enables the real-time probing of Poincaré map behavior, supplying a vital asset for understanding Poincaré map behavior and topology.

The picking action within most visualization software packages is often built-in with the ability to return a ray intersection with any object that currently exists in a graphical scene. Thus, interactions with Poincaré map objects such as points that represent returns or fixed points or lines that display invariant manifold curves are readily available albeit with additional user-supplied action-output conversion. Since most graphical primitives like points and lines are stored with single precision parameters (i.e., the "float" data type), the

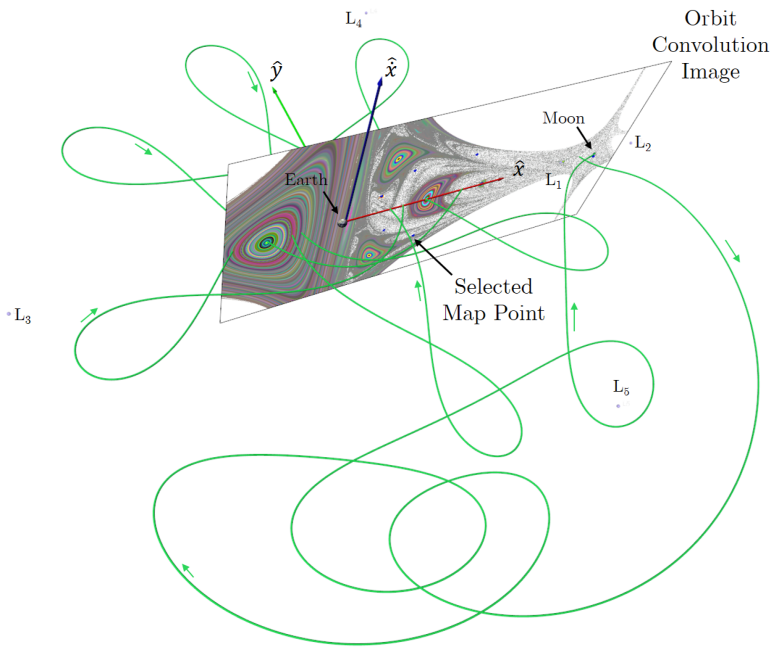

Figure 6.3. Embedding an OC image in world coordinates (where $\dot{x}$ occupies the z-axis) enables the interactive construction of Poincaré map trajectories with a picking action. The example here is in the Earth-Moon system with $C = 2.96$.

interaction with fixed points and invariant manifold objects on a map must be augmented to extract the necessary double-precision characteristics for accurate trajectory reconstruction.

6.3 Sketching Arcs

Expansion of the plane interaction concept leads to the exploration of trajectories via a sketching ability. User interaction with the plane collects position information via the intersection point whenever a motion action is registered. Collecting the string of picked points via motion callbacks results in an ordered set of guess points that resemble a trajectory, but the ordered set of points does not actually follow the true dynamics in the assumed model. Unfortunately, the only dynamical information available from the interaction includes plausible position vectors in projected order and velocity directions corresponding to approximated tangents between points. Although velocity information and time can be approximated with the drag information [71], it is not feasible to expect a user to draw

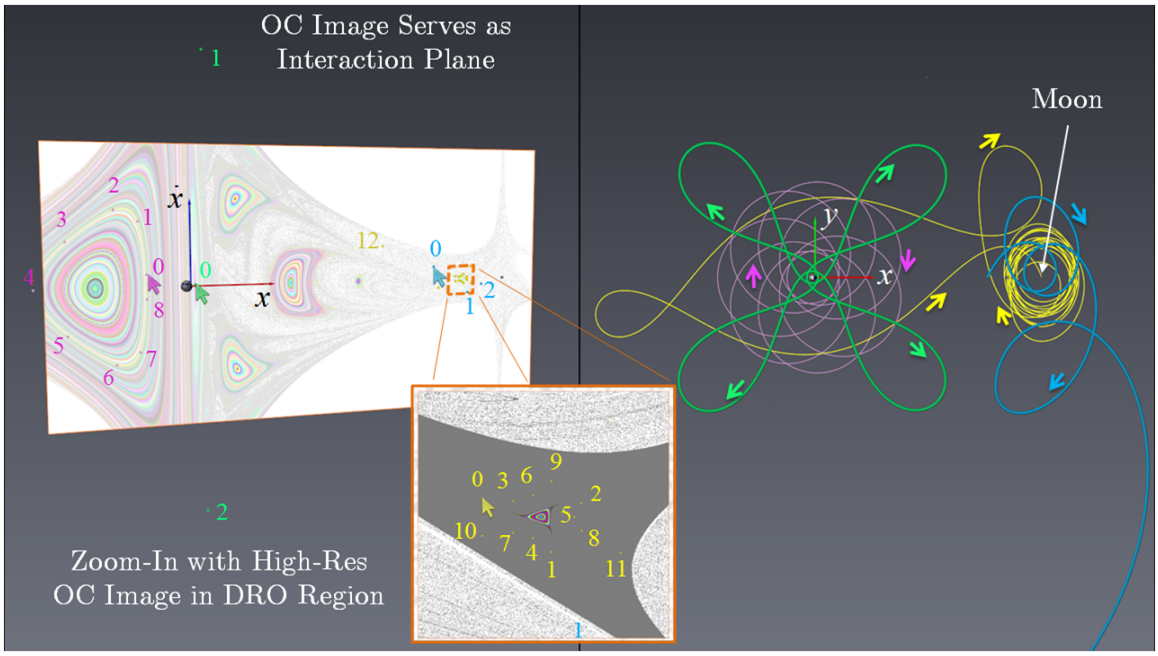

Figure 6.4. Embedding an OC image in world coordinates (where $\dot{x}$ occupies the z-axis) enables the interactive construction of Poincaré map trajectories with a picking action. Four orbits are plotted in the Earth-Moon system ($C = 2.96$) with the initial location indicated by the colored mouse pointer.

true dynamics to sufficient accuracy. Thus, the dynamics are approximated by arbitrarily selecting a Jacobi constant value, C_0, and a predicted time of flight, T_0, to generate an initial path. An initial velocity magnitude, v_0, is extracted from the Jacobi integral (Equation (2.49)) given the initial draw position $\boldsymbol{r}_0$; the velocity vector, $\boldsymbol{v}_0$, is then assigned with the corresponding tangent from the draw or $\boldsymbol{v}_0 = v_0\hat{v}_0$. The resulting initial state is then simulated in an appropriate model (e.g., CRTBP or an ephemeris model) for the predicted T_0 to complete an initial representation of the true dynamics. The sketch reflects the perceived dynamics and therefore, offers a simple way to input plausible trajectories as long as the resulting trajectory is consistent with the assumed model.

Even though a trajectory is easily formed as a drawn arc, the closest trajectory to the sketch is more beneficial for applications. The parameters C_0 and T_0 greatly impact the resulting dynamical arc with many possibilities that dissociate the sketch and actual dynamical structure. A process similar to vector-field reconstruction is then required to nu-

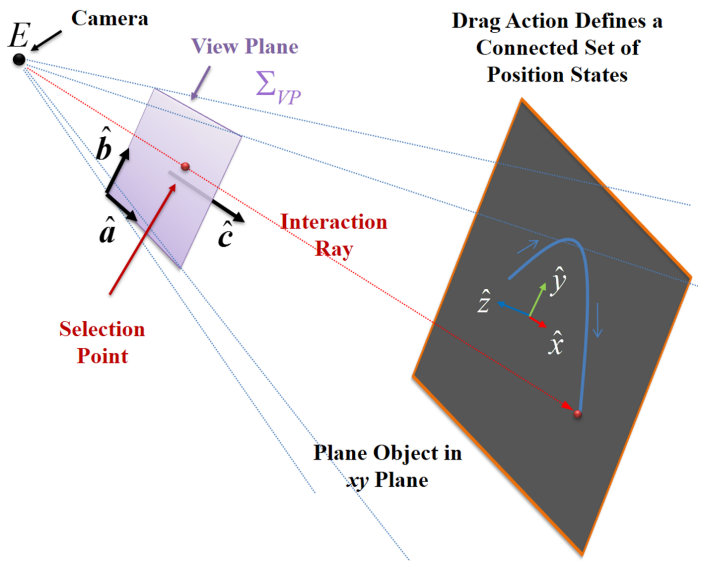

Figure 6.5. Sketching a trajectory by collecting the intersections of the interaction ray (red) with a plane object (gray, typically in xy plane) during a drag action.

merically construct the closest nearby arc possessing analogous characteristics to the sketch. Vector-field reconstruction problems are initiated with empirical data indicating a flow field and apply a model-fitting procedure to determine the best-fit differential equations governing the motion [73]. The arc reconstruction problem reverses vector-field reconstruction since the data is manipulated to accurately reflect follow the noted model.

Three techniques are formulated to convert a drawn arc into a true-dynamical path (i.e., a trajectory that satisfies the equations of motion). First, the position-matching optimization approach seeks the minimal position error between selected states along the drawn curve and a true-dynamical trajectory. Thus, an optimization problem is formed to minimize the positional difference between the points in the sketch and selected states of a nearby true-dynamical trajectory. As a subtle modification, geometry-matching optimization (or shape-matching) substitutes the variance in tangent (velocity) vectors of the drawn arc and the actual dynamics for the positional differences in position-matching, focusing the solution to preserve the geometric shape of the drawn arc. Both methods represent unconstrained nonlinear optimization problems where several solution techniques are available including a BFGS optimization routine [36]. Such formulation is quite beneficial to

an interactive design scenario as the solution techniques are computationally inexpensive compared to constrained nonlinear optimization problems (requiring Sequential Quadratic Programming or SQP or a similar technique) [36]. The ability to return a nearby arc rapidly is ideal for a virtual design setting where arcs may need to be analyzed quickly. In contrast to optimization, a variable-time multiple shooting (VTMS) method gathers positions and tangents throughout the sketch to create patch points and iteratively solves a nonlinear system of equations subject to continuity and monotonic temporal progression constraints. The VTMS solutions are generated quickly by employing a small arbitrary number of sampling points. Note that the C and T values of a constructed trajectory may vary from the input parameters C_0 and T_0 as a result of the sketch-to-trajectory conversion processes.

Applications to mission design objectives demonstrate the efficacy of the various sketch-to-trajectory construction techniques. A prime application of a sketching ability pertains to constructing known behavior without rigorously formulating an initial state. For instance, consider a scenario where a near-Earth conic is desired in a CRTBP design such as the sample path appearing in Figure 6.6(a). The simple sketch (orange in Figure 6.6(a)) reflects the supposed shape required to meet the goals in the problem. Various suitable trajectories are constructed in the general vicinity of the sketched path through interactively testing construction techniques and parameters. With the indicated parameters in Figure 6.6(a), the geometry-matching (red) and VTMS (green) techniques generate roughly the same planar conic (slightly different times-of-flight) whereas the position-matching result (blue) finds the closest trajectory to the draw that is slightly out-of-plane. In this example, the near-Earth conic is constructed quickly using merely a rough spatial appearance via the sketch. As another example, consider that a 2:1 resonant orbit is suggested (where the spacecraft completes 2 revolutions about P_1 for a single revolution of P_2), yet data about the orbit is unavailable without significant external processing. The example in Figure 6.6(b) depicts that position-matching struggles to construct the desired arc, but geometry-matching and VTMS locate a plausible solution (Figure 6.6(b)) that is not periodic but sufficient for design implementation via differential corrections. Another implementation of drawing arcs exists when no intuition about local flow behavior is available. If, for example, a single loop around the L_5 point is desired while transferring from the lunar vicinity to the L_3 vicinity, drawing the loop in a clockwise fashion (orange sketch in Figure 6.6(c)) conveys the transfer

concept. Although geometry-matching and VTMS are ineffective here, solutions are rapidly tested with position-matching (blue) to construct a valid transfer candidate. Various C_0 values are interactively employed via a value slider. The value $C_0 = 2.83481$ creates the desired L_5 loop in addition to arriving near the intended destination. The combination of all three techniques with interactive feedback to parameter choices (such as input time, Jacobi constant value, and method) prototypes a plausible solution to almost any drawn arc. In summary, the ability to draw dynamical arcs provides a simple interface for con-

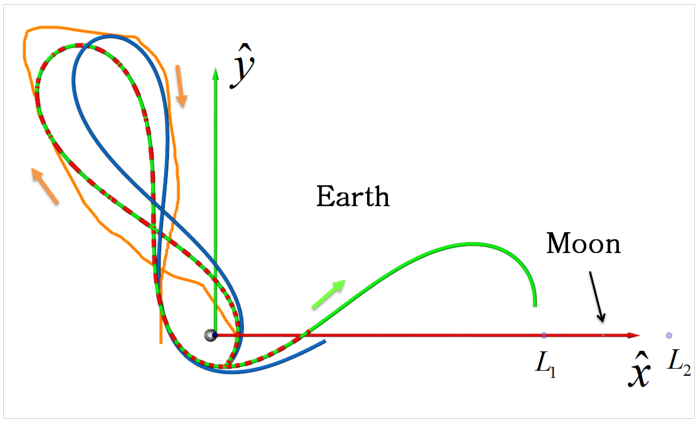

(a) Near-Earth Conic, $C_0 = 2.96$ and $T_0 = 8.65$ days

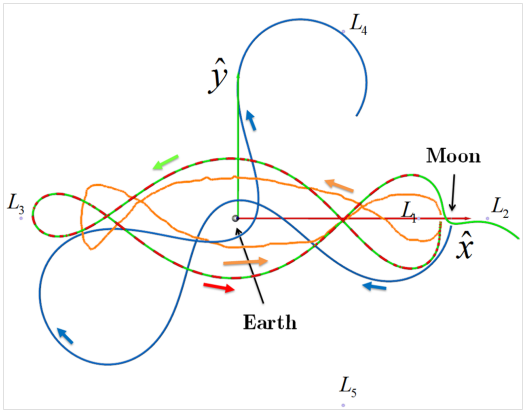

(b) Resonant Arc, $C_0 = 2.96$ and $T_0 = 24.59$ days

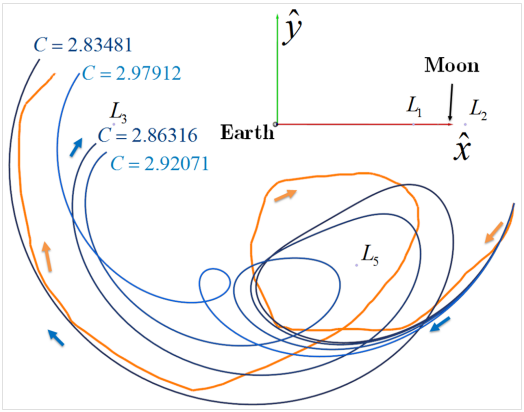

(c) L_5 Loop, C_0 (various) and $T_0 = 198.07$ days

Figure 6.6. Drawing arcs in the planar CRTBP yields plausible real-dynamics trajectories when the drawn states (orange) are used as inputs to three different numerical procedures: position-matching (blue), geometry-matching (red), or variable-time multiple shooting (green).

structing and exploring dynamical possibilities as well as assists the joint effort of scientists and trajectory designers for mission development.

6.4 Dragging Arcs

The drag action is also useful to generate or modify trajectories if applied to different data objects. Another interactive strategy is to utilize the beginning and ending nodes of a particular trajectory arc as points for manipulation. If the selection of a point (or sphere) portraying end points of a standing arc are combined with a drag action, the movement and new mouse location indicates a desired translation of the selected point. In other words, this type of drag action serves as the desire to pull the trajectory such that the intended arc satisfies starting from or hitting the new position. The translation of the pathway is then achieved through the appropriate construction of new locations and a nimble deployment of differential corrections.

The user function that identifies the new position of a dragged point on an initial trajectory employs information that forms the graphical scene. Consider a scenario where the user desires to translate the end node of a standing trajectory. The graphic depiction in Figure 6.7 demonstrates the process of displacing the end point (red) of an initial trajectory (blue) via a drag action, indicated by the yellow arrow. The end node drag action occurs in screen space (on Σ_{VP}), residing at a distance d_m away from the end node in world coordinates. If the location of the new end point is restricted to be at the same d_m distance from Σ_{VP}, then the new end point resides within an interaction plane, Σ_m, that is parallel to Σ_{VP}. The interaction plane is easily computed by defining the plane normal, $\hat{n}$, as $\hat{n} = \hat{c}$ (the camera view direction) and by ensuring that Σ_m contains the original trajectory end point. Any new location indicated in screen space after a mouse movement (drag action) is then projected into Σ_m by localizing the intersection of an interaction ray with Σ_m or via an inverse z-buffer projection (equivalent to ray intersection) [69].

A modification to the trajectory is applied via differential corrections to incorporate the newly positioned beginning or ending point. A variable-time multiple shooting (VTMS) method with fixed-position constraints at the beginning and end of the trajectory is employed to obtain a new solution arc following the drag action. The generic multiple shooting

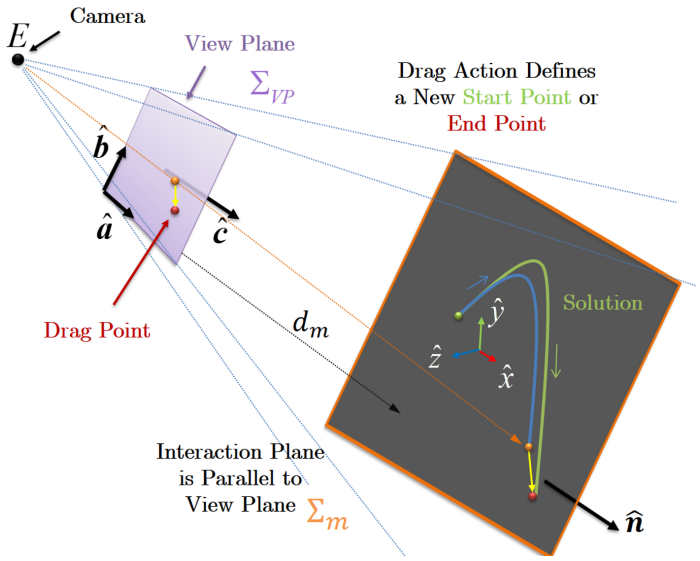

Figure 6.7. A schematic representation of dragging the end point of a standing trajectory (blue) to construct a nearby arc (green) that satisfies the translated end node (red).

method described in Section 3.6 highlights the details of the enlisted VTMS method. The detection rate of mouse movement is generally quite high in graphics engines [70,71], meaning the drag action produces small node displacements. Since the node displacement is small, the initial arc supplies a close guess to the solution, and thus, the VTMS computation executes quickly at near real-time speeds. The fast implementation of the VTMS process allows for the ability to string drag actions sequentially while continuously updating the solution. The effect is a real-time dragging capability that continuously moves arcs to new solutions until the drag action has ceased (mouse button release).

A demonstration of the arc-dragging interactive strategy highlights a potential usage case. In an Earth-Moon system design scenario, let an initial arc be the L_1 Lyapunov half-revolution at $C = 2.96$. Say that this initial arc, displayed as the blue arc in Figure 6.8, possesses a desired ending position (red), but the ideal pathway originates from another arbitrary location (green starting point) that is also in the xy plane. With the initial arc loaded into the visual scene, the camera view is placed above and parallel to the xy plane, limiting node displacement to be only within that plane. A user employs arc-dragging to simply grab and pull the initial arc to the desired point by displacing the starting node.

The drag history of the starting node in this example is indicated by an orange path in Figure 6.8 where each displacement movement executes a new VTMS solution. The result is a pathway similar to the original Lyapunov orbit shape but connects the two desired points. The drag process takes only a few seconds to find the desired solution. In a similar manner to this example, the arc-dragging technique supplies a powerful follow-on to the sketching technique; a sketch may produce a similar arc to an intended path yet arc-dragging closes the gaps.

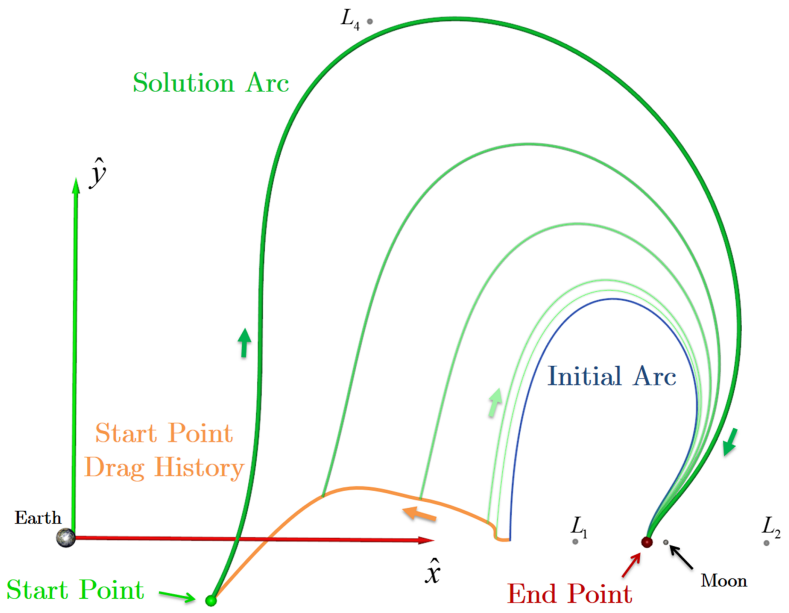

Figure 6.8. An example of arc-dragging displays the drag motion applied by the user on a starting point of an initial arc (blue) to a final position (green) through the marked intermediate steps.

The dragging functionality operates on whatever orientation the current camera portrays, so out-of-plane solutions are also simple to construct. Starting from a planar 3:1 resonant orbit in the Earth-Moon system, an example demonstration of dragging an arc out of plane appears in Figure 6.9. The xz view in Figure 6.9(a) defines the view plane, allowing for end-point dragging to create out-of-plane modifications. First, the initial point (green dot) is pulled along the black path in the xz plane, and subsequently the user then drags the ending point (red dot) along the red path. The resulting trajectory, shown as the solid green line in Figures 6.9(b) and 6.9(c), maintains a similar shape to the 3:1 resonant

orbit (the initial arc) with a twist for an out-of-plane solution. One can further pull the starting and ending nodes together just below the $\hat{x}$ axis in $-z$, forming a return to the starting position as shown in Figures 6.9(d) and 6.9(e). This new solution is very close to a periodic orbit since the transition from ending node to starting node appears seamless. Even though the drag solution in Figures 6.9(d) and 6.9(e) is not truly periodic since periodic constraints are not applied during drag operations, it does represent an excellent guess for an out-of-plane version of the 3:1 resonant periodic orbit family.

Qualitative observation of the VTMS method during the arc-dragging operation delineates solutions based on the number of applied patched points. With $k = 2$ selected patch points, the VTMS method reverts to a a variable-time single shooting algorithm; the single shooting form of arc-dragging changes the solution wildly during the drag operation as the method only employs the starting and ending nodes, creating drastic changes in time of flight and Jacobi constant versus the initial arc. On the other hand, a medium number of patch points ($k = 20$) for the VTMS method anchors the solution to the previous shape. At least a medium number of patch points are required to successfully converge initial arcs with complex shapes and high curvature. Too many points ($k = 100$), though, can be detrimental to the VTMS method as the problem becomes more stiff since the patch points move by minuscule amounts during each update step of the VTMS method (and so, many iterations are required to converge on an adequate solution). In general, a small number of patched points permits exploration for new solutions when the shape is unknown whereas a medium number of patch points transitions a desired trajectory geometry to a nearby solution.

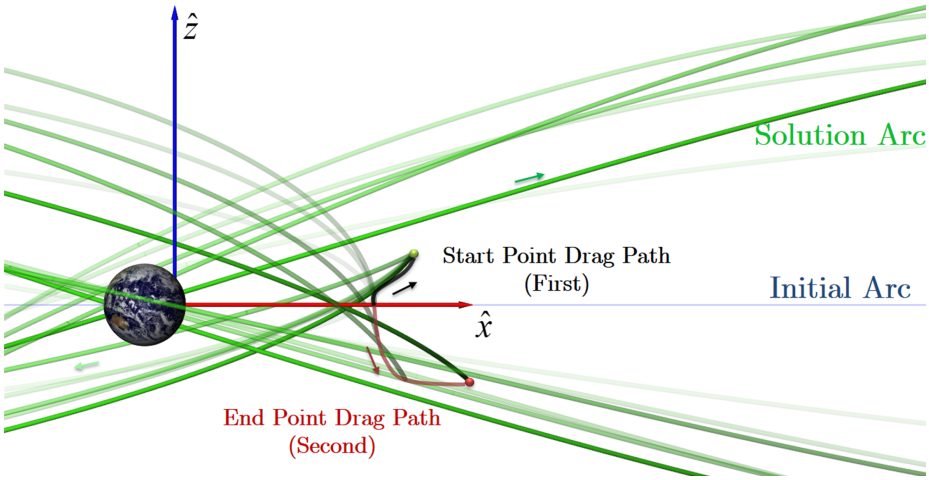

(a) Drag view (xz plane)

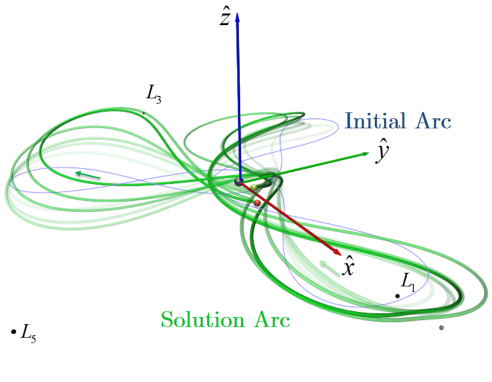

(b) Drag solutions

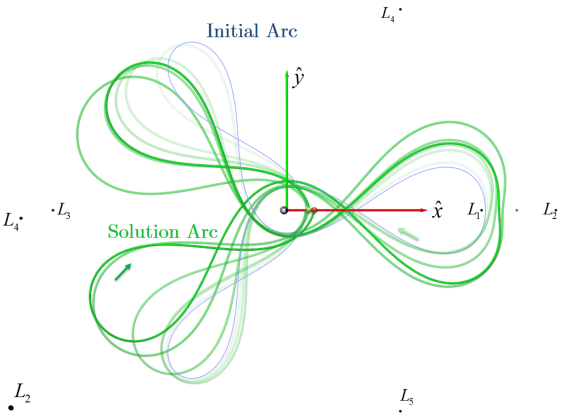

(c) Drag solutions (xy plane)

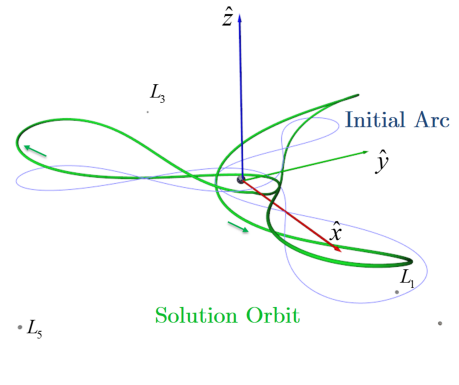

(d) Nearly periodic solution

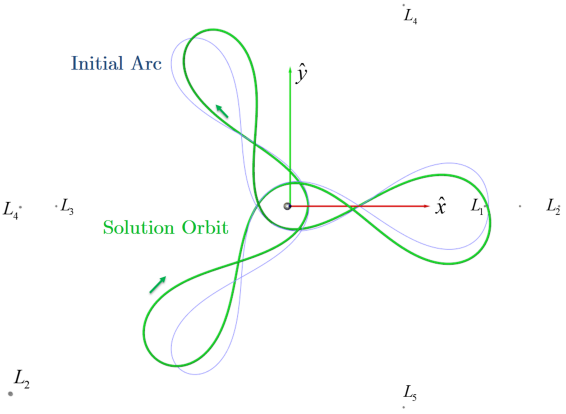

(e) Nearly periodic solution (xy plane)

Figure 6.9. Arc-dragging functionality applied to pull a planar solution in the z direction.

7. AUTONOMOUS TOPOLOGY EXTRACTION FOR POINCARÉ MAPS

Computing the periodic orbits (topology nodes) and associated invariant manifolds (topology links) in the CRTBP relies on a topology-based technique that originates from index theory. In vector fields (e.g., a simple linear flow described by $\dot{\boldsymbol{x}} = A\boldsymbol{x}$), the critical points (or nodes of the flow field at $\dot{\boldsymbol{x}} = \mathbf{0}$) can be detected by computing the rotation of the velocity traced about closed curves that surround plausible areas for critical points. The index (sometimes refereed to as circulation) is then evaluated based on the number and direction of complete velocity-vector rotations around the closed curve [51]. A critical point of the flow field exists within that closed curve if the index is non-zero, and thus, the critical point is detected through an autonomous topology-based process [51]. If the same index-based extraction can be applied to analyze data from the Poincaré section, then fixed point detection can also be accomplished. In a similar manner, the simple propagation of invariant manifolds of saddle-type critical points is transformed into a new method for constructing invariant manifolds for saddle-type periodic orbits that exclusively operates on the Poincaré section.

Since it is impractical in an interactive design setting for a user to manually compute the massive amount of topological structure available on a Poincaré section within a visual design setting, an autonomous extraction procedure that runs externally is essential. Employing an algorithm for autonomous topology extraction generates the pertinent topological features of a Poincaré map (i.e., periodic orbits and applicable invariant manifolds) with minimal user input. The details of automated topology extraction from a Poincaré map for a domain of interest are established by Tricoche et al. [14], but many adaptations are required for successful deployment in multi-body dynamical environments. The procedure for extracting topology relies on the user for an initial definition of the Poincaré section and the domain of interest. The resulting orbital structure, though, is generated through an automated orbit-detection technique that is designed to utilize parallel processing while minimizing the overall performance bottlenecks. The following phases of the

algorithm, labeled *Phase A-F*, highlight the primary components required for the Poincaré Map Autonomous Topology Extraction (PMATE) algorithm.

7.1 Phase A: Poincaré Section Definition and Initial Sampling

Minimizing map iteration compute times is achieved by assigning the appropriate numerical propagation technique to a suitable task. The most time-consuming numerical procedure for developing the Poincaré map is evaluating the Poincaré map itself through simulation and root-solving. Runge-Kutta methods with adaptive error control are preferable over predictor-corrector methods when computing a Poincaré map since Runge-Kutta methods automatically generate an interpolating polynomial between subsequent steps, rendering root-finding as a simple step [36]. The current investigation implements a Dormand-Prince fifth-order method for computing maps and the fixed point detection procedure. Assuming that the bottleneck for computation time is executing a map iteration, elements of the automated topology extraction process are tailored to minimize the total number of required mappings as well as enhance the speed of each Poincaré map computation where possible. In some phases of topology extraction, it is more desirable to form a general depiction of the behavior quickly rather than extreme accuracy; in these general behavior computations, including the orbit convolution procedure or the initial grid sampling, the error tolerances on the Dormand-Prince method are elevated to 1×10^{-8} for enhanced speed. Where more precision is needed (e.g., refining a fixed point or computing a manifold), an error tolerance of 1×10^{-12} supplies the required accuracy.

Implementation of the autonomous extraction strategy initially requires isolation of a hyperplane and a sampling grid to represent the domain of interest. The surface of section, Σ, is essential to all phases of the process and must be declared as a first step to initiate the process. In this investigation, the hyperplane $\Sigma : y = 0$ is employed exclusively, but other hyperplanes are permissible and may be more suitable for other applications. The sampling grid can possess a rather low resolution (e.g., 16×16 or 20×20); note, however, that the number of resulting orbital structures is increased as the sampling resolution increases since the Poincaré map possesses a fractal nature [14]. Orbit convolution imagery offers valuable insight into selecting a domain of interest since the contrast between possible structures

is already highlighted. Thus, topology extraction can be focused on key regions identified by orbit convolution. Poincaré maps possess fractal properties, meaning more information appears as a region of interest is narrowed [50]. Therefore, a specified maximum on the number of toroidal periods (p_{max}) confines the search for topological structures to a practical level [14]. At each node of the user-specified sampling grid, the Poincaré map is numerically simulated in parallel utilizing error tolerances that favor a general description of dynamical behavior over high accuracy (i.e., computational speed is increased by employing 10^{-8} versus 10^{-12}). The numerical simulation is executed for a relatively long duration such that the total number of map iterates, n, is sufficiently large for an accurate representation of the space ($n \in [50, 200]$ is usually sufficient).

7.2 Phase B: Node Trajectory Classification

A general sense of dynamical behavior is achieved by designating a corresponding scalar quantity at each grid node. Essentially, the classification phase determines the scalar metric as the available toroidal periods for a particular location. Classifying the behavior at each grid node allows the algorithm to operate over a smaller subset of toroidal periods rather than the entire range $[1, p_{max}]$. The subsequent steps in the automated topology extraction algorithm are comprised of operations on grid cells that collect the available toroidal periods at each grid node to run mapping computations. Reducing the operational range on the toroidal period translates to enhanced efficiency since p values that are not associated with a cell are skipped.

In an area-preserving (2D) Hamiltonian system, a good choice for a classifying parameter is the winding number since this parameter suggests a fundamental dynamical behavior and a toroidal period [14, 50]. Since the planar CRTBP is a time-invariant Hamiltonian system, periodic and quasi-periodic regions on the surface of section are confined to a two-torus and, hence, are fully described by a single winding number [8, 49–51]. Numerically evaluating this winding number requires a transformation from state space to a more appropriate set of coordinates (e.g., action-angle variables)–an excessively complex procedure for a algorithm seeking an efficient execution. As an alternative, Lichtenberg and Liebermann demonstrate that multiple winding numbers exist for Hamiltonian systems of higher dimension ($N \geq$

3) [50]. Although the planar CRTBP is a 2D Hamiltonian system, Cartesian position and velocity coordinates expressed in terms of a rotating reference frame are typically employed as the variables for dynamical modeling. Thus, a collection of winding numbers is produced utilizing only the state space coordinates to isolate plausible toroidal periods for an individual node on the grid. The computation of this collection of winding numbers is accomplished congruently with the numerical simulation via the tracking of particular angles as they rotate about the origin (i.e., the barycenter in the planar CRTBP). An angle of rotation, θ_{ab}, for Cartesian coordinates a and b is measured as the cumulative rotation that the 2D vector $\boldsymbol{r}_{ab}(t) = [a_t, b_t]^T$ traces during the numerical simulation process with the current time step indicated by t; this rotation angle is then defined as the signed angle

$$\theta_{ab} = \sum_{t=0}^{t_n} \arccos\left(\frac{\boldsymbol{r}_{ab}(t+\Delta t)\cdot\boldsymbol{r}_{ab}(t)}{\|\boldsymbol{r}_{ab}(t+\Delta t)\|\|\boldsymbol{r}_{ab}(t)\|}\right), \tag{7.1}$$

where t_n reflects the total simulation time to achieve n map iterates and Δt represents the current step size in the differential equation solver. By convention, a value such that $\theta_{ab} > 0$ identifies counter-clockwise rotation about the origin. The suitable state space coordinate combinations include x, $\dot{x}$, and $\dot{y}$, yet naturally exclude the defining coordinate of the hyperplane (y). The set of available winding numbers is then $\boldsymbol{W} = (w_{x\dot{x}}, w_{x\dot{y}}, w_{\dot{x}\dot{y}})$, where the individual ratios are computed as

$$w_{x\dot{x}} = \frac{2\pi n}{\theta_{x\dot{x}}}, \qquad w_{x\dot{y}} = \frac{2\pi n}{\theta_{x\dot{y}}}, \qquad w_{\dot{x}\dot{y}} = \frac{2\pi n}{\theta_{\dot{x}\dot{y}}}. \tag{7.2}$$

Fortunately, these rotation angles are tracked concurrently during the initial map simulation and without noticeable penalty to computational efficiency. The approximation of the winding numbers converge to the true value as $n \to \infty$ [14], but the initial sampling reaches a suitable approximation for the winding numbers within the prescribed range for n.

Classification via winding number is conveyed through the combination of puncture plots and scalar field visualizations. As an example, the computed set $\boldsymbol{W}$ is displayed as colored scalar fields mapped to a puncture plot originating from a randomly seeded set of initial states within the domain D_{EM} (Figure 7.1). Examining Figure 7.1(a), most trajectories (periodic, quasi-periodic, and chaotic) hold a winding number with the value $w_{x\dot{x}} = \frac{-1}{1}$ (in-

dicated by the greenish color), even though the orbital behavior varies significantly throughout the domain. The prevalence of the same characteristic number throughout the Poincaré section in Figure 7.1(a) is clear evidence that more than one winding number is necessary to classify which toroidal periods are representative of an arbitrary initial state. The $w_{x\dot{y}}$ number, appearing in Figure 7.1(b), supplies a strong contrast between quasi-periodic behavior (residing at the white and yellow extrema of the indicated color map) and chaotic behavior which transitions through the purple range near $w_{x\dot{y}} = 0$. The final winding number, $w_{\dot{x}\dot{y}}$ as displayed in Figure 7.1(c), completes the classification of a grid node. The appearance of $w_{\dot{x}\dot{y}}$ in Figure 7.1(c) is similar to the winding number $w_{x\dot{x}}$ (Figure 7.1(a)), but ratios within the $w_{\dot{x}\dot{y}}$ field are set apart from the $w_{x\dot{x}}$ field, meaning additional information is acquired. Although the winding number associated with chaotic initial states is undefined, motion along chaotic trajectories is influenced by nearby saddle-type fixed points. As a result, the winding numbers corresponding to chaotic initial states computed through rotation-tracking yield a classification of nearby behavior even though a "true" winding number does not exist.

Generating the classification of toroidal periods per grid node requires a conversion from the set $\boldsymbol{W}$ to a set of plausible integers that indicate the representative number of Poincaré map iterates. The winding number is often represented as a *continued fraction*, or

$$w = a_0 + 1/(a_1 + 1/(a_2 + 1/(a_3 + \ldots, \tag{7.3}$$

where the coefficients, a_j, are selected to approximate w to a specified precision [14, 74]. Computing the excited toroidal periods at a grid node from $\boldsymbol{W}$ involves converting each winding number to the nearest integer ratio. A continued fraction algorithm (such as the methodology by Shoemake [74] and Thrill [75]) is employed to compute the best rational approximation for each winding number at every grid node. This algorithm identifies the best integer ratio approximation where the highest allowable denominator is equal to p_{max}. The denominator in each winding number integer ratio represents a possible toroidal period for a fixed point within a nearby grid cell. As a sample scenario for computing toroidal periods, consider a 24×16 sampling grid mapped to the domain D_{EM} with $p_{max} = 12$. The resulting grid, as well as the set of plausible toroidal periods from the continued fraction

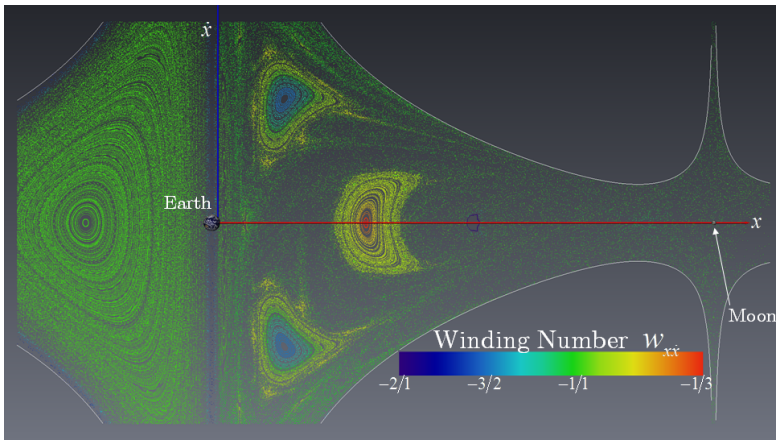

(a) $w_{x\dot{x}}$

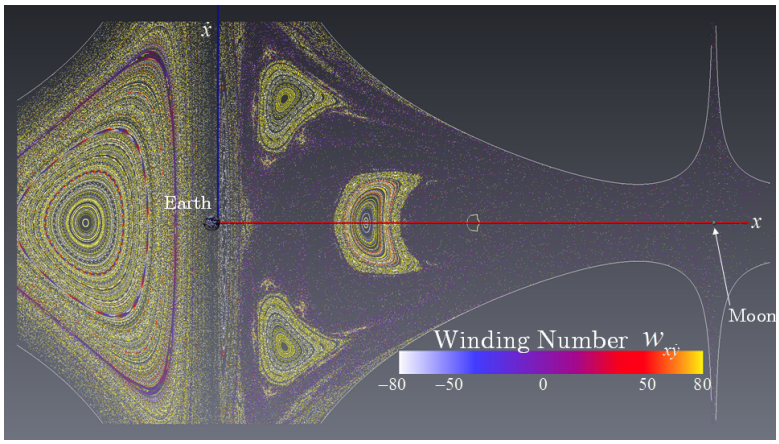

(b) $w_{x\dot{y}}$

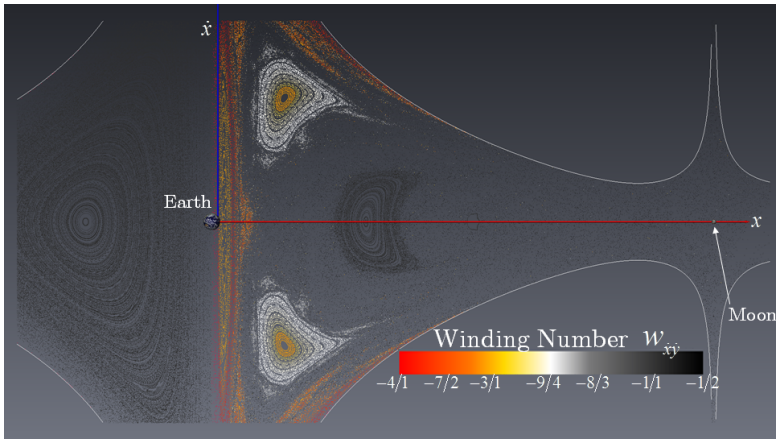

(c) $w_{\dot{x}\dot{y}}$

Figure 7.1. Classification of the Poincaré phase space using winding numbers within the Earth-Moon system domain D_{EM} computed for a set of randomly seeded initial states ($n = 200$).

algorithm, are displayed in Figure 7.2. The continued fraction algorithm yields 3 integer values at each grid node that classify the potential toroidal periods at nearby fixed points. An example set of potential toroidal periods is indicated in Figure 7.2 as the red highlighted set [1 11 1]; the 3 values indicated in the highlighted set ([1 11 1]) correspond to the denominator of each approximate integer ratio as the continued fraction algorithm is applied to the winding number set $\boldsymbol{W}$. Thus, the values 1, 11, and 1 represent the toroidal number of rotations for the winding numbers $w_{x\dot{x}}$, $w_{x\dot{y}}$, and $w_{\dot{x}\dot{y}}$, respectively. The influence of nearby fixed points is illustrated by observing grid cells that encircle a period-1 (or $p = 1$) center-type fixed point (appearing within the yellow cells in Figure 7.2). Each grid node from the yellow cells includes the value $p = 1$ as a member of the plausible set of periods, so the initial states that are close to the period-1 center-type fixed points all demonstrate dynamical behavior that is similar to the nearby center. The automated fixed point detection process examines each cell by searching for fixed points that possess a toroidal number of rotations indicated by the set of plausible toroidal periods available at each corner. Although each cell could examine up to 12 toroidal periods based on 4 grid nodes offering 3 possible values, it is common that integers in the set at a single node are repeated at all of the nodes of cell, and thus, the total number of toroidal periods examined per-cell remains much lower than the full range $[1, p_{max}]$.

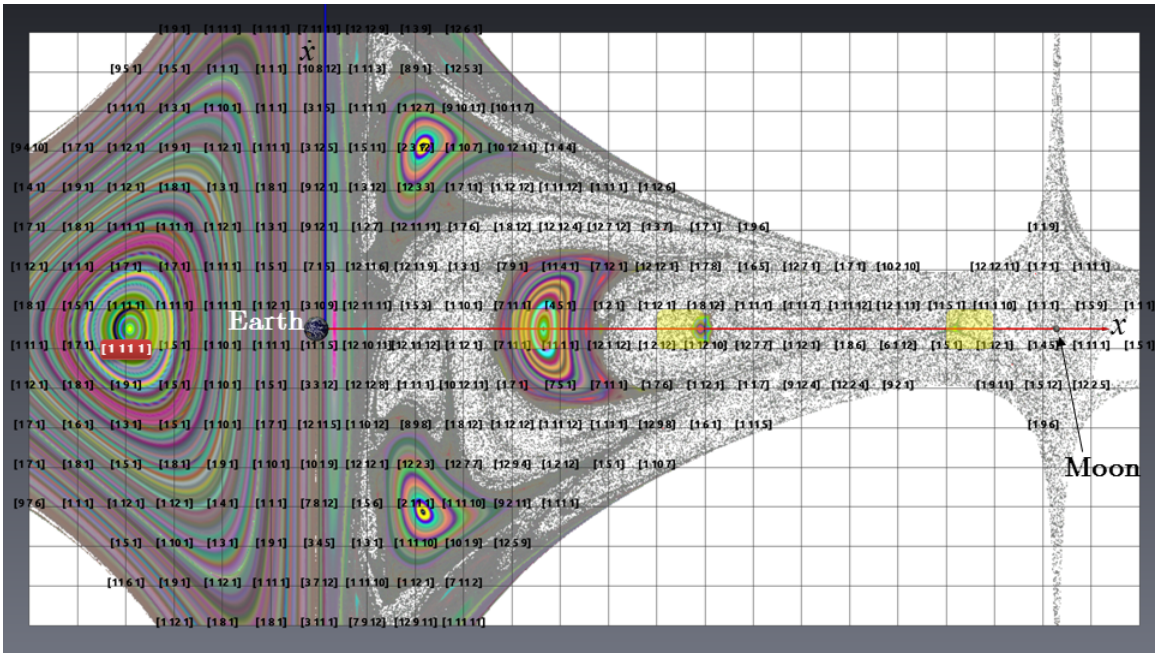

Figure 7.2. Available periods for each grid node of a sample grid (24×16) applied to the domain D_{EM} with $p_{max} = 12$. The possible periods are the denominators of the set of winding numbers, $\boldsymbol{W}$, computed with a continued fraction algorithm.

7.3 Phase C: Isolating Dynamical Areas

Employing the Poincaré index for fixed point detection in the CRTBP requires cell-size variation. Analysis cells should surround isolated fixed points since information is overlooked when more than one fixed point is encircled [51]. This suggests that small analysis cells are desired [14], but creating a dense regular grid of small analysis cells exponentially increases computational costs. It is, therefore, advantageous for the analysis grid to adapt sizes autonomously (i.e., shrink the cells only in areas where more analysis is needed). Adaptive modification of the initial analysis grid is accomplished through subdivision of analysis cells into smaller parts in conjunction with a crafted spatial data structure.

Since the winding number is a smoothly varying characteristic parameter, variance in the winding number set $\boldsymbol{W}$ is utilized to determine when to subdivide a cell. Ideally, a cell that isolates fixed points of a given period possesses a smooth convex shape in $\boldsymbol{W}$ values within the cell; therefore, the decision to subdivide a cell is based on a convex-hull concept for $\boldsymbol{W}$

values. A true convex-hull approach conforms winding number values to follow a convex surface, but a rudimentary linear-variance approach with heuristics (or a first-order convex-hull algorithm) is employed here for simplicity and streamlined computation [36]. Variance in the cell corner values is capped as the first subdivision check to ensure the dynamic behavior within the cell is similar. Let the cell corner maximal variance be denoted as

$$\Delta \boldsymbol{W}_c = \boldsymbol{W}_{max\forall c} - \boldsymbol{W}_{min\forall c}, \tag{7.4}$$

i.e., the difference between the maximum and minimum winding number values for all the corners ($c \in [1, 4]$) of an analysis cell. The first heuristic criteria is then

$$\Delta \boldsymbol{W}_c \leq \boldsymbol{\psi}_w, \tag{7.5}$$

where $\boldsymbol{\psi}_w$ represents a set of maximal range parameters specified by the user. The values of $\boldsymbol{\psi}_w$ bound the dynamic range within a cell, so smaller $\boldsymbol{\psi}_w$ parameter values yield smaller analysis cells during the subdivision process. Dynamical behavior within a cell is also examined for smoothness, indicated by the convexity of $\boldsymbol{W}$ throughout the cell. A sophisticated convex-hull approach employs a model-fitting problem that examines the convexity of a generated parametric surface [36], but a linear heuristic test for convexity is utilized in this work for computational efficiency. If $\boldsymbol{W}_i$ represents a winding number set for a Poincaré section point (with index i) inside a particular analysis cell, then all n internal points to a cell adhere to

$$\boldsymbol{W}_{min\forall c} - \boldsymbol{\epsilon}_w \odot \boldsymbol{\psi}_w \leq \boldsymbol{W}_i \leq \boldsymbol{W}_{max\forall c} + \boldsymbol{\epsilon}_w \odot \boldsymbol{\psi}_w. \tag{7.6}$$

for the linear convexity check. Note that $\boldsymbol{\epsilon}_w$ is another set of user-specified parameters, and the $\odot$ symbol represents element-by-element multiplication of vectors ($\boldsymbol{a} \odot \boldsymbol{b} = (a_1 b_1, a_2 b_2, a_3 b_3)$). Any analysis cell that fails the criteria in either Equation 7.5 or Equation 7.6 encompasses too much dynamical behavior or surrounds a spatially diverse dynamical region, and thus, such a cell is marked for subdivision.

A spatial data structure with modifications explicitly for Poincaré maps supplies the framework for an adaptive cell subdivision procedure. At a user-specified initial grid size (or grid depth $d = 0$) over a domain, the Poincaré map emanating from the initial grid is

sampled in the same manner as Phase B (Section 7.2). A standard quad-tree data structure is employed to not only associate $\boldsymbol{W}$ values at vertexes (cell corners) but also to assign spatial data inside cells. Since all Poincaré section crossings from an initial state are the same trajectory and an entire trajectory is classified by a single $\boldsymbol{W}$ set, then all subsequent p crossings, or $\boldsymbol{\mathcal{P}}^p(\boldsymbol{x})$, are also assigned the same $\boldsymbol{W}$ values. This assignment creates internal cell values that are tested as part of the subdivision criteria in Equation (7.6). When subdivision is required, cells are subdivided into 4 subcells via the quad-tree structure with internal data assigned to the corresponding quadrant within the original cell. A schematic representation of the quad-tree subdivision of a large cell (green) appears in Figure 7.3. Three subdivision depths are indicated as blue, red, and black in order of ascending depth. A 3D integer coordinate uniquely identifies an adaptive grid cell based on the lower-left vertex. The three elements of this identifying vector represent the horizontal, vertical, and depth locations, respectively. The initial analysis grid represents the zeroth depth level ($d = 0$), and each level of subdivision increments the current depth level. Upon the creation of subcells, the horizontal and vertical integers of the cell identity coordinate are multiplied by 2 as depth increases by 1 as Figure 7.3 demonstrates. A user-specified maximum depth level parameter, d_{max}, is employed to represent the total number of subdivision layers allowed. For example, a $d_{max} = 3$ specifies that an initial analysis cell at $d = 0$ can be subdivided into 4 cells per layer up to 3 times, creating up to 64 potential subcells. Cells are also subdivided if any corners reside within invalid dynamical regions.

The efficiency of the adaptive cell subdivision process is aided by a parallel implementation of a priority queue that ranks subdivision requests based on need. Cell priority is assigned based on the depth level and the severity of cell-convexity violation. First, invalid or partially invalid cells (i.e., cells possessing one or more corners outside valid flow space) are subdivided to localize the bounding region of valid flow on the Poincaré section. Invalid cells are removed from analysis when maximum depth is achieved. Next, valid cells with non-convex $\boldsymbol{W}$ sets (i.e., violating either Equation (7.5) or (7.6)) are assigned the next highest priority with lower depth levels processed ($d = 0$ or $d = 1$) before higher depth levels. The priority queue is cleared as cells reach d_{max} or as cells are classified with convex hulls with respect to $\boldsymbol{W}$. This process is repeated as batch rounds containing a small subset of all available cells (64 cells constitute a round in the current work). The adaptive cell

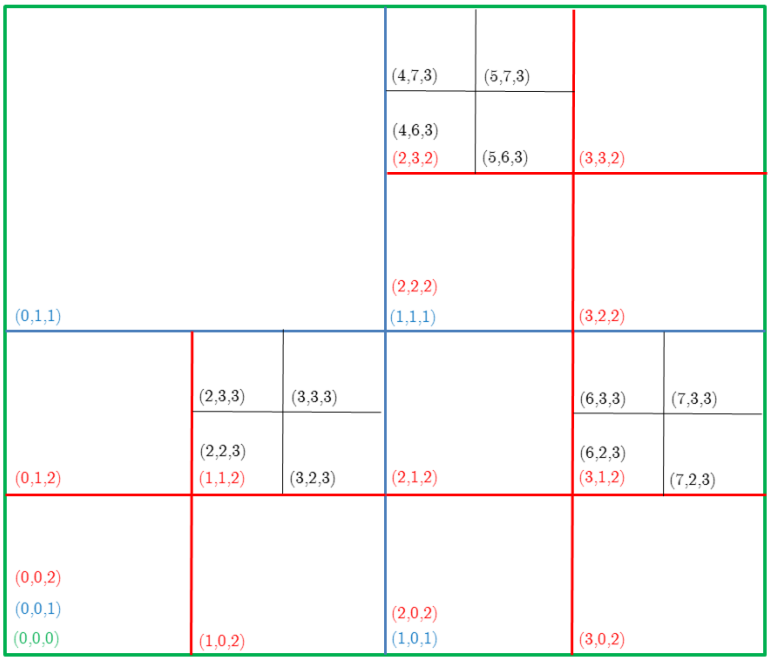

Figure 7.3. An initial grid cell (green) with adaptive cell subdivision applied to demonstrate the associated changes in cell index.

subdivision procedure is completed when all remaining valid cells are convex or at maximum depth.

Applying adaptive cell subdivision on Poincaré sections in the CRTBP indicates the advantages of the technique. An example of the adaptive cell subdivision process is applied to the domain D_{EM} to a maximum depth level $d = 3$ in Figure 7.4. An initial analysis grid (thick gray lines) is quartered at each subdivision level, resulting in smaller cells (outlined with black in Figure 7.4) throughout chaotic regions with strong behavior fluctuations. In astrodynamics, high-period fixed point island chains, especially within a quasi-periodic region, provide limited application as traversing the KAM manifold barriers imbues maneuver costs. Thus, the heuristic parameters are selected to focus computational efforts on locating saddles in chaos, leading to isolating heteroclinic connections later in the PMATE process. Note that $w_{x\dot{y}}$ acts as a chaotic indicator when the value is near zero, yet very large magnitudes of this number (approaching $\pm\infty$) actually signify the similar quasi-periodic trajectories. Therefore, the range of values is truncated at $[-1000, 1000]$ where trajecto-

ries possessing $|w_{x\dot{y}}| \geq 1000$ exhibit only quasi-periodicity. As Figure 7.4 demonstrates, employing the truncated range for $w_{x\dot{y}}$ and the heuristic parameters $\boldsymbol{\epsilon}_w = [0.5, 1.0, 0.5]$, and $\boldsymbol{\psi}_w = [1.0, 1000.0, 1.0]$ generates larger cells in quasi-periodic regions where behavior is similar and focused analysis in different chaotic regions. Cells that reside outside the valid flow region are marked as invalid (red in Figure 7.4) and removed from analysis. Also, since numerical analysis is difficult near primaries and structures computed within primaries are not of practical use for most trajectory design problems, cells that are partially inside P_1 or completely within P_2 (i.e., Earth and Moon in Figure 7.4, respectively) are voided as analysis cells.

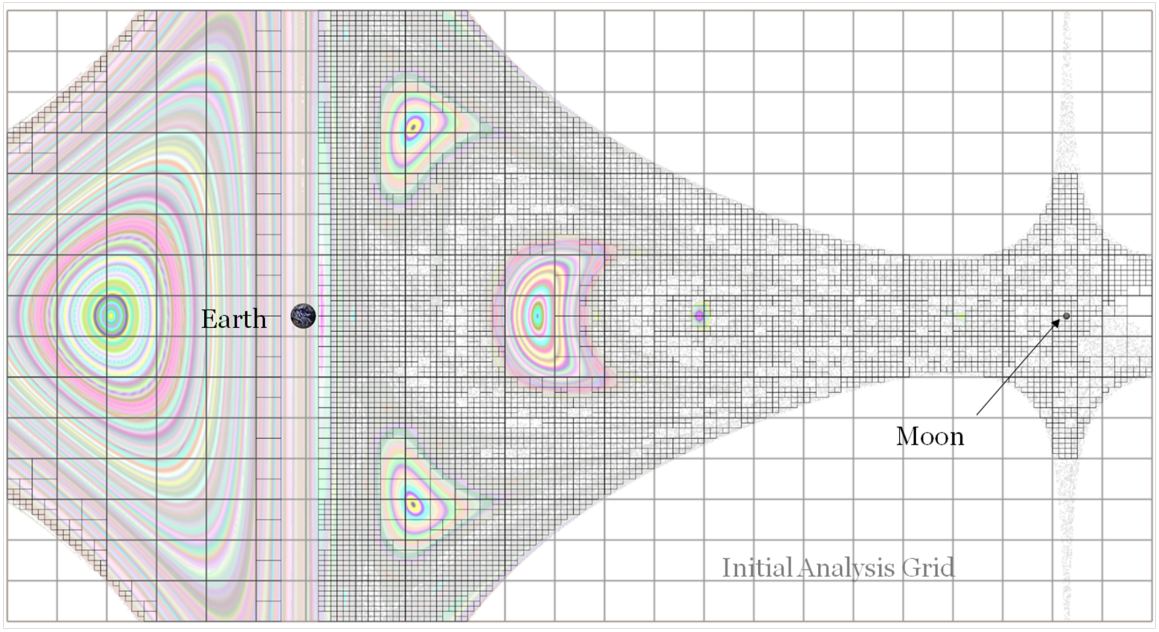

Figure 7.4. Adaptive cell subdivision based on the winding number set $\boldsymbol{W}$ applied to the domain D_{EM} with parameters $C = 2.96$ and $d_{max} = 3$.

7.4 Phase D: Periodic Orbit Detection with the Poincaré Index

The location of fixed points that likely exist within the initial sampling grid is achieved autonomously with an application of index theory on Poincaré section information. Let Γ represent a closed curve that encircles an isolated fixed point. Also, define the vector $\boldsymbol{\Delta}$ as a displacement vector between $\boldsymbol{x}$, an initial state on the surface of section, and the Poincaré map representation of that state to p iterations, or namely

$$\boldsymbol{\Delta} = \boldsymbol{\mathcal{P}}^p(\boldsymbol{x}) - \boldsymbol{x}. \tag{7.7}$$

The *Poincaré index* is then defined as the summation of the signed angles of rotation that the vector $\boldsymbol{\Delta}$ generates over Γ [49]. Let the angle α represent the orientation of $\boldsymbol{\Delta}$ with respect to the x-axis through the dot product

$$\boldsymbol{\Delta} \cdot \hat{\boldsymbol{x}} = \|\boldsymbol{\Delta}\| \cos(\alpha), \tag{7.8}$$

where α is computed as a function of the current map displacement (or $\alpha(\boldsymbol{\Delta})$). On the surface of section in the planar CRTBP, the Poincaré index, κ, is represented utilizing the coordinates existing on the section through the line integral

$$\kappa = \frac{1}{2\pi} \oint_{\Gamma} d\left(\arctan\left(\frac{d\dot{x}}{dx}\right)\right) = \frac{1}{2\pi} \oint_{\Gamma} d\alpha(\boldsymbol{\Delta}), \tag{7.9}$$

with the x and $\dot{x}$ coordinates on the section [14,49]. If the Poincaré index is non-zero, a fixed-point exists inside the closed-curve Γ, and index values of $\kappa > 0$ and $\kappa < 0$ correspond to center-type and saddle-type fixed points, respectively [49, 51]. The cell edges that comprise the initial sampling grid form the closed-curves on the surface of section within PMATE, and thus, the Poincaré index is evaluated for each possible toroidal period (p) associated with a particular cell obtained during the node classification process. Along each edge in the sampling grid for a particular p value, the map displacement vector $\boldsymbol{\Delta}$ is computed in sufficiently small increments such that the rotation of $\boldsymbol{\Delta}$ (or the change in the angle $\alpha(\boldsymbol{\Delta})$) exhibits a clear and monotonic transition. The resulting change in α tracked along an edge of a grid cell then contributes a portion of the total integral in Equation (7.9). Specifically, the Poincaré index for a cell is then the signed, counter-clockwise summation

of these partial edge-rotation contributions computed for all sides of the cell. Grid cells that return a non-zero index for a specified value of p are then processed to generate an initial guess for a fixed point in the proceeding Phase E (Section 7.5).

7.4.1 Rotation Calculation Via Adaptive Edge Subdivision

Pruning redundant computations during the evaluation of the Poincaré index assists in maintaining algorithmic efficiency. Evaluating the Poincaré index per-cell implicitly generates duplicate computations since some cells share the same edge. Thus, a per-edge computation is employed to enhance the computational speed of the detection process. Each edge is paired with the set of possible toroidal periods that must be evaluated. The rotation computation is then conducted in order of largest period to smallest period while mapping information is stored in a data cache. This temporary storage of mapping data at higher periods enables a faster retrieval of a lower period mapping if the initial map state is the same, and thus, the total number of overall mappings is reduced through accessing existing information. Each edge-rotation calculation is executed in parallel as each edge is independent.

Adaptive samples combined with an appropriate data structure assist in computing the rotation of $\mathbf{\Delta}$ along an edge. The change in orientation of the vector $\mathbf{\Delta}$ between subsequent points along an edge may exhibit an ambiguity (i.e., the direction of rotation for a 180° transition in α is unclear). For subsequent points i and $i+1$ along an edge, let the variable $\delta\alpha_i$ represent the signed change in the angle $\alpha(\mathbf{\Delta})$ between the points or,

$$\delta\alpha_i = \alpha(\mathbf{\Delta}_{i+1}) - \alpha(\mathbf{\Delta}_i) = \text{sign}(\mathbf{\Delta}_i \times \mathbf{\Delta}_{i+1}) \arccos\left(\frac{\mathbf{\Delta}_i \cdot \mathbf{\Delta}_{i+1}}{\|\mathbf{\Delta}_i\|\|\mathbf{\Delta}_{i+1}\|}\right). \tag{7.10}$$

The rotation of $\mathbf{\Delta}$ is then computed under a maximum variation cap, $\delta\alpha_{max}$, to avoid ambiguous scenarios through adaptive sampling along an edge ($\delta\alpha_{max} = 135°$ is employed in the current work). The adaptive edge structure is first formed with the two corner nodes of a cell corresponding to the desired edge. Mapping data for the indicated cell-relevant periods at the corner nodes are stored in a hash table for correlated access similar to the adaptive cell data structure in Section 7.3. As illustrated in Figure 7.5, points along the tree-like edge structure are accessed via a 2D integer coordinate that holds a point index,

i, and tree-depth level, d, as (i, d). Next, the initial edge ($d = 0$ or the green edge in Figure 7.5) is subdivided with a simple bisection to create the midpoint for the next depth level ($d = 1$ or the blue edge in Figure 7.5). The $\mathbf{\Delta}$ value associated with the edge midpoint is evaluated for the corresponding periods and inserted into the tree-like data structure. The angular constraint $\delta\alpha_i \leq \delta\alpha_{max}$ then determines if adjacent edge points (i, d) and $(i + 1, d)$ require further rotation resolution. Bisection of existing segments creates new points to smoothly track a monotonic rotation of $\mathbf{\Delta}$. The adaptive edge subdivision continues until the angle of rotation is resolved or a minimum distance between consecutive sample points is achieved. Selecting this minimum distance, or $l_{\min}$, is problem-dependent [14]. In cases where adjacent sample points along an edge that are within the distance $l_{\min}$ that also indicate an instantaneous flip in $\mathbf{\Delta}$ (or a change in α of 180°) with a small $\|\mathbf{\Delta}\|$ ($< 10^{-4}$), a fixed point may exist in close proximity to the edge. When the algorithm encounters this juxtaposition, the state along the edge is saved as a suitable guess for a fixed point to be employed later in a refinement procedure (Section 7.5). In a scenario where the rotation in $\mathbf{\Delta}$ is not monotonic or the rotation angle between subsequent points is undetermined, sensitive dynamical conditions present in the CRTBP force ambiguities to remain regardless of the $l_{\min}$ value. Such ambiguities are dubbed *discontinuities* of the $\mathbf{\Delta}$ field and cannot be resolved for Poincaré index computation without additional knowledge of the dynamics.

7.4.2 Poincaré Section Transversality

Two phenomena present in the modeling formulation contribute to the discontinuities in tracking $\mathbf{\Delta}$ around a closed curve – highly sensitive dynamics that are known to exist in the CRTBP and the definition of Σ in relation to the dynamical flow. To demonstrate these issues, the orientation of $\mathbf{\Delta}$ for $p = 1$ is computed throughout a sample cell in the EM system with $C = 2.96$ as displayed in Figure 7.6. The color in Figure 7.6(a) displays the nondimensional magnitude of the map displacement vector ($\|\mathbf{\Delta}\|$) according to the attached colorbar. This sample cell spans the $(x, \dot{x})$ nondimensional coordinates $(0.7, -0.16)$ to $(0.77, 0.16)$) and encircles the period-1 fixed point representing the Lyapunov orbit about the L_1 Lagrange point (the fixed point is roughly at $(0.728, 0.0)$). The depiction of the orientation of the various $\mathbf{\Delta}$ vectors (Figure 7.6) clearly conveys that $\mathbf{\Delta}$ can flip direction

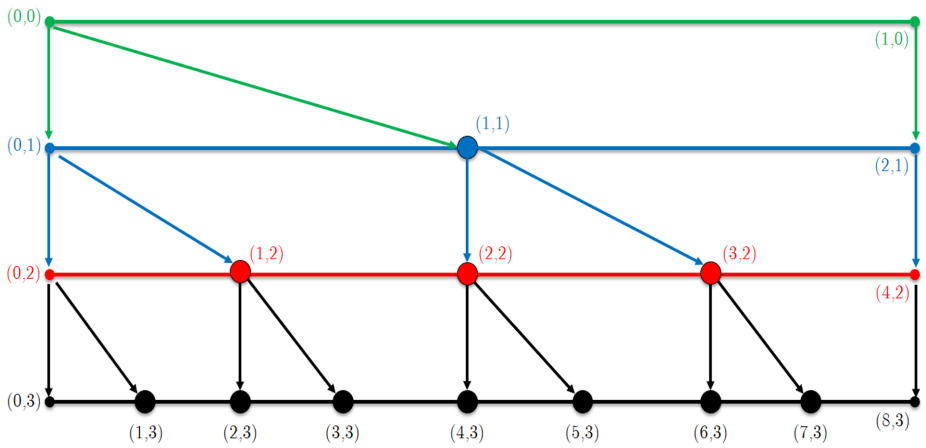

Figure 7.5. A schematic depiction of an initial edge (green) with adaptive subdivision applied to demonstrate the associated changes in point index. Each level is the same edge, but now with additional points added via the lineage indicated by the arrows.

readily along edges. Locations along an edge for which the rotation is not resolved utilizing $l_{\min} = 0.32/256$, or 256 divisions along the smaller dimension, are highlighted by orange circles in Figure 7.6. Some orange circles occur where the nearby $\|\mathbf{\Delta}\|$ values are similar (color in Figure 7.6(a)) but the orientation flips between nearby starting locations. Such behavior correlates with a propagation through a singularity such as the Moon in this example. Perhaps more prevalent are locations in this sample cell where $\|\mathbf{\Delta}\|$ is discontinuous with an abrupt angular displacement. Discontinuities in $\|\mathbf{\Delta}\|$ are examined by computing $p = 1$ trajectories in affected areas with the colored points in Figure 7.6(a) and corresponding trajectories displayed in Figure 7.6(b). Since the trajectories in Figure 7.6(b) possess returns to Σ on opposite sides of the Earth, these sample trajectories suggest that the hyperplane $\Sigma : y = 0$ is not truly transverse to the flow everywhere within this cell. Such behavior violates a fundamental definition of a Poincaré section, rendering ambiguity in the $\mathbf{\Delta}$ field as actual discontinuities on the hyperplane (not discontinuities in dynamics).

New terminology is necessary to describe Poincaré map behavior in areas ripe with discontinuities in $\mathbf{\Delta}$. As proven by Dullin and Wittek, any *configuration space* hyperplane (such as $\Sigma : y = 0$) defining a Poincaré section in a time-invariant Hamiltonian system possesses discontinuities as flow is not globally transverse to Σ [76]. The *transversality* of a

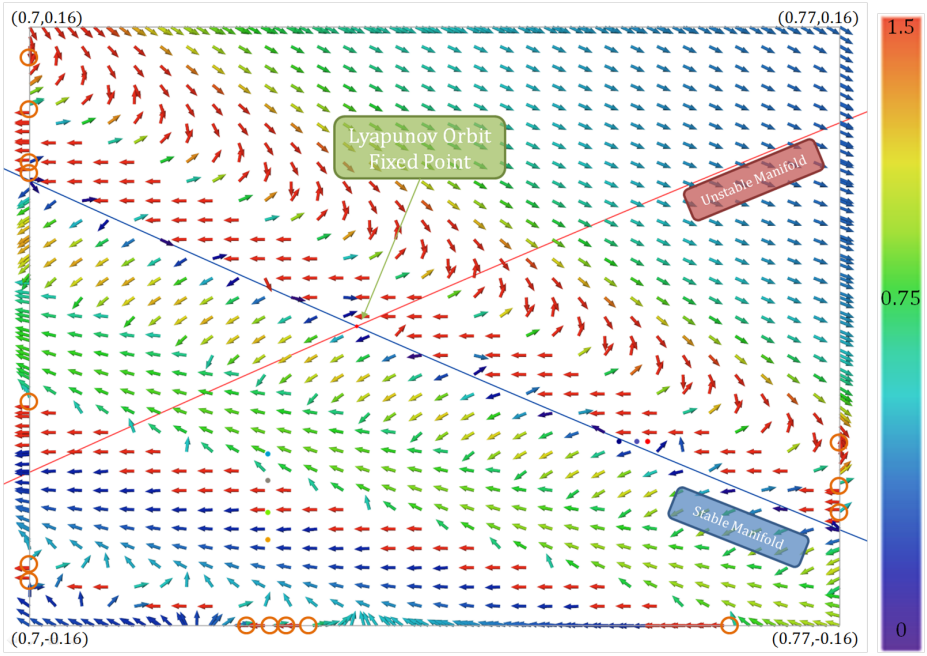

(a) Poincaré map displacement (colored by $\|\mathbf{\Delta}\|$) for $p = 1$

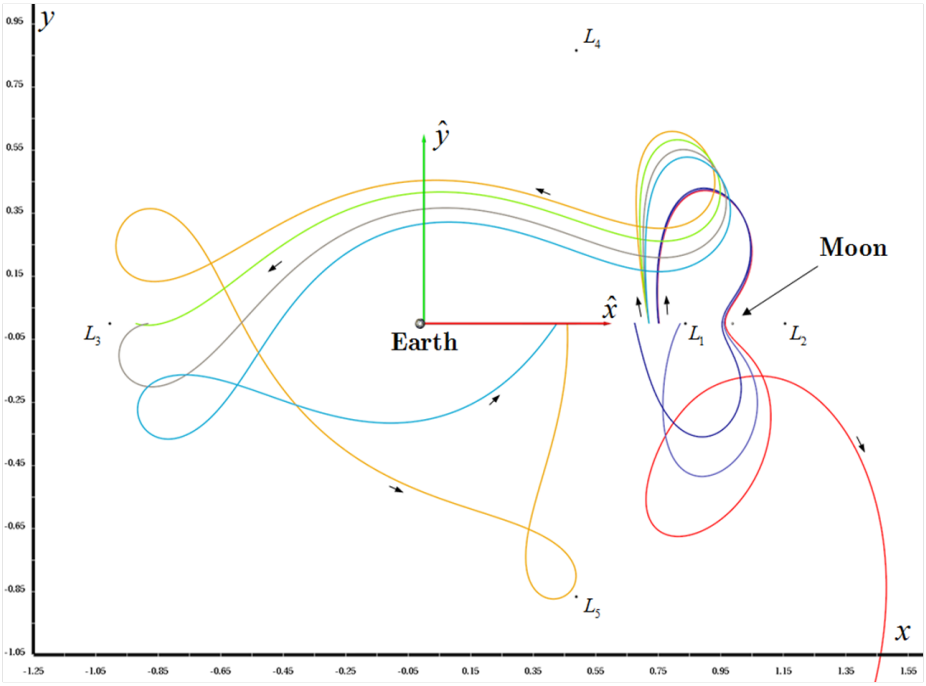

(b) Trajectories for $p = 1$ from sample points with similar color

Figure 7.6. The orientation of the map displacement vector $\mathbf{\Delta}$ evaluated with $p = 1$ for the cell ($x \in [0.7, 0.77]$, $\dot{x} \in [-0.16, 0.16]$) which encircles the L_1 Lyapunov orbit fixed point at $C = 2.96$ in the Earth-Moon system. Regions of ambiguous rotation in $\mathbf{\Delta}$ along an edge are circled in orange.

domain on Σ describes the behavior of the flow through Σ (i.e., the transverse or perpendicular flow component). An analysis cell on a Poincaré section where all the encased flow possesses a non-zero component of velocity through Σ with no discontinuities in $\mathbf{\Delta}$ at a given integer period (p) is noted as a *transverse* domain for p. A *non-transverse* domain, on the other hand, surrounds map locations where the transversality of Σ is violated. These transversality violations typically form at the occurrence of one of two specific trajectory events. First, map states resulting in a downstream velocity at p that is perfectly tangent to the section, denoted as *section tangencies*, generate discontinuities in $\mathbf{\Delta}$. A schematic example of a section tangency condition appears in Figure 7.7(a) where three arcs that reside in close proximity to one another possess a discontinuous set of returns to Σ. Section tangency conditions are also suitably dubbed *section separations* as downstream trajectories detach from Σ after a small initial state perturbation and reconnect to Σ in a separate spatial location. The second transversality violation is an exact intersection of any singularity in the model such as P_1 or P_2 crossings in CRTBP (exemplified in Figure 7.7(b)). Arcs on opposite sides of the trajectory passing directly through the singularity (or the divide-by-zero case in Equations (2.24)–(2.26)) portray the subsequent crossing of Σ at a completely different location in phase space. Note, the transversality of a domain may or may not be preserved for sequential integer periods, but singularity intersections persist for all periods over the onset of the singularity.

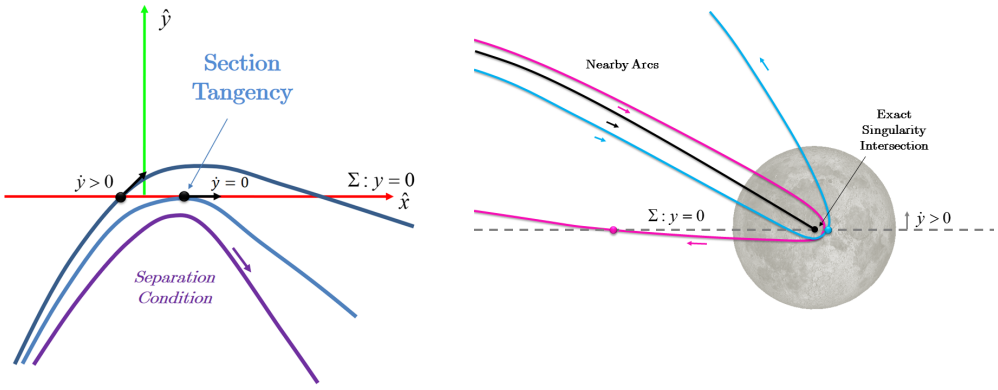

(a) Section Tangency (b) Singularity Intersection

Figure 7.7. Transversality violation types for a Poincaré section in the CRTBP.

7.4.3 Resolving the Poincaré Index

Evaluation of the Poincaré index for fixed point detection in non-transverse cells is completed by considering the behavior of $\boldsymbol{\Delta}$ in the limit approaching a transversality violation. Near singularities, the velocity of a trajectory approaches infinite magnitude as the downstream distance to the singularity decreases ($r_1, r_2 \to 0$), yet the direction of $\boldsymbol{\Delta}$ approaches $\pm\hat{x}$ in the phase space projection of the Poincaré section. Thus, the angle $\alpha(\boldsymbol{\Delta})$ has a finite limit where singularities arise in $\boldsymbol{\Delta}$ even though the value is inconsistent from different directions. The angle $\alpha(\boldsymbol{\Delta})$ also approaches a finite limit near section tangencies on Σ. It is important to note that fixed points also present discontinuities in $\alpha(\boldsymbol{\Delta})$ since $\|\boldsymbol{\Delta}\|$ drops to 0 with a roughly 180° orientation flip in $\boldsymbol{\Delta}$ on opposing sides of the fixed point. At a discontinuity point $\boldsymbol{g}$ (either a transversality violation or a fixed point) on the closed curve Γ for period p, the Poincaré index from Equation (7.9) possesses a discontinuity at $\boldsymbol{g}$. Since the limits of $\alpha(\boldsymbol{\Delta}(\boldsymbol{g}))$ exist in various directions approaching $\boldsymbol{g}$, the Poincaré index for a non-transverse cell is expressed as the summation of improper integrals

$$\kappa = \frac{1}{2\pi} \oint_{\Gamma} d\alpha(\boldsymbol{\Delta}) = \frac{1}{2\pi} \left(\int_{\boldsymbol{\gamma}_0}^{\boldsymbol{g}} d\alpha(\boldsymbol{\Delta}) + \int_{\boldsymbol{g}}^{\boldsymbol{\gamma}_0} d\alpha(\boldsymbol{\Delta}) \right), \tag{7.11}$$

where $\boldsymbol{\gamma}_0$ is a starting point along Γ ($\boldsymbol{\gamma}_0 \neq \boldsymbol{g}$). In the event of multiple transversality violations, the piecewise version of the Poincaré index in Equation (7.11) is simply expanded to evaluate the rotation in $\alpha(\boldsymbol{\Delta})$ in contiguous segments around Γ.

The same adaptive edge sampling method as discussed in Section 7.4.1 is augmented with the additional heuristics to detect transversality violations. Subsequent map states along cell edges are tested for transversality violations via a set of heuristic trials that search for fundamental differences in map information (see Section 7.4.4). The adaptive subdivision of an edge localizes the locations of $\boldsymbol{g}$ as well as generates sufficient approximations of the limiting values of $\alpha(\boldsymbol{\Delta}(\boldsymbol{g}))$. Luckily, all information required for heuristic detection is available during numerical simulation or easily retrieved from the output. The results of heuristic detection of a transversality violation are demonstrated in Figure 7.8 on an analysis cell near the sample L_1 Lyapunov fixed point ($p = 1$). Singularity intersections and section tangencies are represented as magenta and red dots, respectively, along the edges of the analysis cell. As apparent in Figure 7.8, transversality violations tend to form coherent

contours on the section domain that represent fundamental transitions between trajectory types. As long as cell edges are not aligned with such fundamental contours, it is possible to heuristically detect the two types of transversality violations and resolve the Poincaré index using a piecewise integral. Here, the parameter $l_{\min}$ also now indicates how many bisections to allow to localize $\boldsymbol{g}$. If a transversality violation is detected between adjacent states, subdivision continues until achieving a segment length lower than $l_{\min}$. Thus, the value of $l_{\min}$ presents a trade-off between computation time and analysis yield. A low $l_{\min}$ (say 10^{-8}) provides exceptional accuracy at great computational expense, yet higher values of $l_{\min}$ ($\approx 10^{-3}$) return results quickly at the expense of overlooking orbital structures. As a tractable compromise, an intermediate value of $l_{\min}$ is selected within the range $[10^{-6}, 10^{-4}]$ for all analysis hereafter (typically, a medium value of 2×10^{-5}).

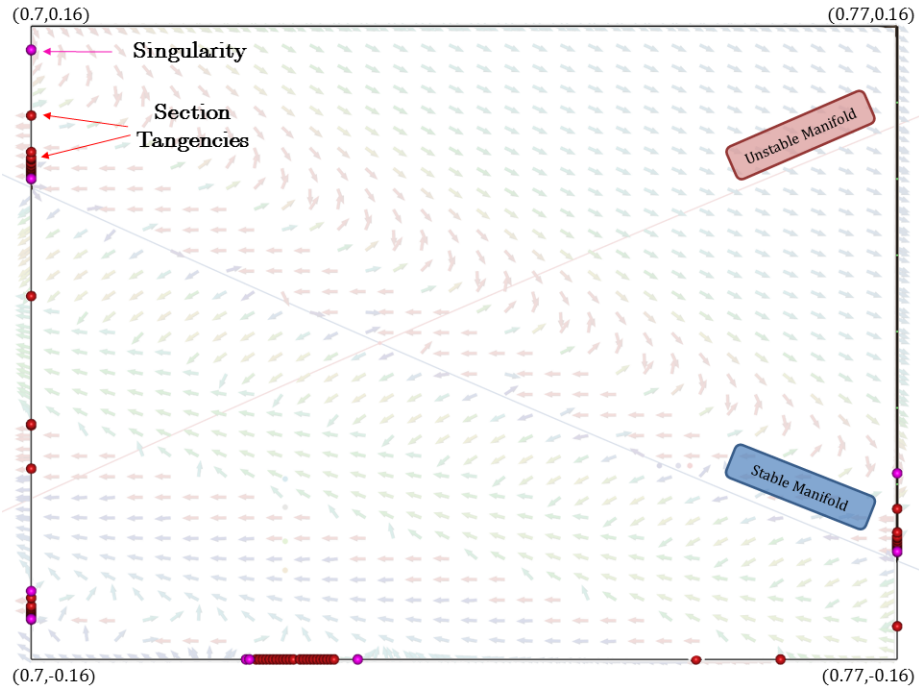

Figure 7.8. Detected transversality violations at $p = 1$ along the edges of the cell surrounding the L_1 Lyapunov fixed point at $C = 2.96$ in the Earth-Moon system. Red dots represent section tangencies whereas magenta dots locate singularity intersections.

7.4.4 Heuristic Tests for Detecting Transversality Violations

Heuristic comparison trials localize transversality violations in a Poincaré section along a line segment or edge. Such tests compare the mappings of subsequent edge points (i, d) and $(i+1, d)$ to detect if either a smooth rotation of $\alpha(\boldsymbol{\Delta})$ is achieved or if a transversality violation exists between the corresponding simulated trajectories. Let the indexed point (i, d) reside at the state location $\boldsymbol{x}_i$ with mapping $\boldsymbol{\mathcal{P}}^p(\boldsymbol{x}_i)$ and map displacement $\boldsymbol{\Delta}_i$. Empirical examination of a variety of line segments (made possible thanks to the interactive selection of Poincaré section states in Section 6.2) produces the testing order and plausible heuristic comparison values. The heuristic trials are performed in the following order:

1. *Numerical Singularity Monitor*: The first trial inspects the numerical mapping procedure for a singularity intersection. During the evaluation of $\boldsymbol{\mathcal{P}}^p(\boldsymbol{x}_i)$, a tracking object monitors for the divide-by-zero condition by examining the distances from the primaries (r_1 and r_2). Specifically, a numerical singularity is encountered when either

$$r_1^3 \leq (r^3)_{\min} \text{ or } r_2^3 \leq (r^3)_{\min}, \tag{7.12}$$

   where $(r^3)_{\min}$ represents the minimum allowable divisor in a numerical computation (a value of 10^{-20} typically suffices for $(r^3)_{\min}$).

2. *Time of Flight Comparisons*: The most reliable test to locate a violation in section transversality is to compare the respective times of flight that form the Poincaré maps. Let dt_i and dt_{i+1} represent the time of flight to complete the mappings $\boldsymbol{\mathcal{P}}^p(\boldsymbol{x}_i)$ and $\boldsymbol{\mathcal{P}}^p(\boldsymbol{x}_{i+1})$, respectively. If the absolute difference in time of flight is greater than or equal to a user-defined maximum difference δt_{abs}, or more formally

$$|dt_{i+1} - dt_i| \geq \delta t_{abs}, \tag{7.13}$$

   then a separation condition likely exists between the adjacent points. The absolute difference in time of flight may be too large for the more subtle section tangencies. Consequently, the relative differential between times of flight is also examined where

$$\frac{|dt_{i+1} - dt_i|}{|dt_i|} \geq \delta t_{rel} \tag{7.14}$$

indicates a plausible transversality violation with δt_{rel} representing a user-defined parameter.

3. *Map Displacement Tests*: As apparent in Figure 7.6, a large discontinuity in Poincaré map displacement vectors ($\boldsymbol{\Delta}$) also reveals possible transversality violations. Let $\Delta_{x,\max}$ and $\Delta_{\dot{x},\max}$ represent tolerances on the differences in map displacement coordinates. Transversality violations are suspected between adjacent points if either phase space coordinate satisfies

$$|(\boldsymbol{\Delta}_{i+1} - \boldsymbol{\Delta}_i) \cdot \hat{x}| \geq \Delta_{x,\max} \tag{7.15}$$

or

$$|(\boldsymbol{\Delta}_{i+1} - \boldsymbol{\Delta}_i) \cdot \hat{\dot{x}}| \geq \Delta_{\dot{x}\,\max}. \tag{7.16}$$

Also, the magnitude of $\boldsymbol{\Delta}$ should stay consistent for the transversality assumption to hold (violations occur at any abrupt change in color in Figure 7.6). A transversality violation exists if the corresponding magnitudes of $\boldsymbol{\Delta}$ differ too greatly, i.e.,

$$\|\boldsymbol{\Delta}_{i+1}\| - \|\boldsymbol{\Delta}_i\| \geq \delta\Delta_{\max} \tag{7.17}$$

where $\delta\Delta_{\max}$ is a user-specified tolerance. Note, the trial in Equation (7.17) only applies when at least one map displacement has a smaller magnitude, so either $\|\boldsymbol{\Delta}_i\| < 0.5$ or $\|\boldsymbol{\Delta}_{i+1}\| < 0.5$ must be true to implement the $\|\boldsymbol{\Delta}\|$ trial.

4. *Map Coordinate Tests*: The state coordinates of the Poincaré map can also be useful to determine discontinuities. One might assume that searching for $\dot{y} = 0$ (the section tangency condition) is fruitful, but it is actually quite difficult to detect this condition with heuristics as all values of $\dot{y}$ at $\boldsymbol{\mathcal{P}}^p(\boldsymbol{x})$ are positive (by definition of Σ). On the other hand, sign changes in other map coordinates do indicate plausible transversality violations. Define the new scalar quantities $\mathcal{P}^p_x(\boldsymbol{x}_i)$ and $\mathcal{P}^p_{\dot{x}}(\boldsymbol{x}_i)$ as

$$\mathcal{P}^p_x(\boldsymbol{x}_i) = \boldsymbol{\mathcal{P}}^p(\boldsymbol{x}_i) \cdot \hat{x}, \tag{7.18}$$

$$\mathcal{P}^p_{\dot{x}}(\boldsymbol{x}_i) = \boldsymbol{\mathcal{P}}^p(\boldsymbol{x}_i) \cdot \hat{\dot{x}}, \tag{7.19}$$

accordingly. Also, define $\delta\mathcal{P}_x$ and $\delta\mathcal{P}_{\dot{x}}$ as user-tolerances for the change in x and $\dot{x}$ map coordinates, respectively. The x section coordinate shows separation conditions if

$$\mathcal{P}_x^p(\boldsymbol{x}_{i+1})\mathcal{P}_x^p(\boldsymbol{x}_i) < 0 \text{ and } |\mathcal{P}_x^p(\boldsymbol{x}_{i+1}) - \mathcal{P}_x^p(\boldsymbol{x}_i)| \geq \delta\mathcal{P}_x. \tag{7.20}$$

Similarly, a transversality violation is detected with the $\dot{x}$ section coordinate when the inequalities

$$\mathcal{P}_{\dot{x}}^p(\boldsymbol{x}_{i+1})\mathcal{P}_{\dot{x}}^p(\boldsymbol{x}_i) < 0 \text{ and } |\mathcal{P}_{\dot{x}}^p(\boldsymbol{x}_{i+1}) - \mathcal{P}_{\dot{x}}^p(\boldsymbol{x}_i)| \geq \delta\mathcal{P}_{\dot{x}} \tag{7.21}$$

are true. Typically, $\delta\mathcal{P}_{\dot{x}}$ is larger than $\delta\mathcal{P}_x$ since the $\dot{x}$ coordinate stretches significantly more than x, especially near a singularity.

5. *Heuristic Singularity Intersection Tests*: Since a precise starting state is necessary to trigger the numerical divide-by-zero condition (Equation (7.12)), many singularity intersections remain undetected without additional heuristics. As shown in Figure 7.7(b), trajectories on either side of the terminating arc possess Poincaré map states on opposite sides of the primary. This fact is exploited by testing for a sign change in map coordinates with the origin translated to the primary. Set the new x coordinate quantities $s_{1,i}$ and $s_{2,i}$ for point (i, d) as distances relative to the problem singularities P_1 and P_2 through

$$s_{1,i} = \mathcal{P}_x^p(\boldsymbol{x}_i) + \mu \tag{7.22}$$

$$s_{2,i} = \mathcal{P}_x^p(\boldsymbol{x}_i) - 1 + \mu, \tag{7.23}$$

respectively. Also, let CA_j symbolize the minimum distance to singularity position P_j, i.e., closest approach distance which considers the whole mapped trajectory. A trajectory is defined to be near singularity j if CA_j is smaller than a user-defined safe distance from the singularity, δCA_j (usually greater than or equal to the body

radius). If either state $\boldsymbol{x}_i$ or $\boldsymbol{x}_{i+1}$ produces a mapped trajectory that is within the safe distance of singularity j, then sign changes in modified map coordinates via

$$(s_{j,i})(s_{j,i+1}) < 0 \tag{7.24}$$

$$\mathcal{P}^p_{\dot{x}}(\boldsymbol{x}_i)\mathcal{P}^p_{\dot{x}}(\boldsymbol{x}_{i+1}) < 0 \tag{7.25}$$

indicate a singularity intersection somewhere between the adjacent initial points. A trial for a singularity crossing that is always checked, even when $CA_j > \delta CA_j$, examines if adjacent initial points produce trajectories in close proximity to a primary yet on opposite sides. When the conditions

$$(s_{j,i})(s_{j,i+1}) < 0 \quad \text{and} \quad |s_{j,i}| + |s_{j,i+1}| \leq \delta s_{\max} \tag{7.26}$$

are true with the user-defined parameter $\delta s_{\max}$, a crossing of singularity j is heuristically detected between (i, d) and $(i + 1, d)$ as well.

6. *Stable Manifold Crossing Test*: Some $\boldsymbol{\Delta}$ rotation calculations along edges are unable to resolve based on nearby topology as opposed to a transversality violation. Such an unresolved ambiguity typically occurs where the stable and unstable invariant subspaces of a nearby saddle-type fixed point are in close proximity to each other and intersect the affected edge. Topologically, the influential saddle appears with a stretched "x" pattern featuring a small horizontal or vertical angle. The ambiguity resides roughly at the point where the edge crosses the stable manifold (W^s) of the influential saddle. The trial here first waits until $\delta\alpha_i$ remains unresolved to $l_{\min}$ resolution. If all of the preceding tests indicate that no transversality violation exists between (i, d) and $(i + 1, d)$, then the midpoint of $\boldsymbol{x}_i$ and $\boldsymbol{x}_{i+1}$ (or $\boldsymbol{x}_m$) and the corresponding map displacement $\boldsymbol{\Delta}_m = \boldsymbol{\Delta}(\boldsymbol{x}_m)$ are computed. With $\delta\Delta_{Ws}$ as a user-defined heuristic parameter, a stable manifold crossing is detected when

$$\|\boldsymbol{\Delta}_i\| \leq \delta\Delta_{Ws} \text{ and } \|\boldsymbol{\Delta}_{i+1}\| \leq \delta\Delta_{Ws} \text{ and } \|\boldsymbol{\Delta}_m\| \leq \delta\Delta_{Ws}. \tag{7.27}$$

Unlike transversality violations, this stable manifold crossing event generates a continuous rotation of $\boldsymbol{\Delta}$ even though the monotonic change happens in a compact spatial area. Since this is a known rotation, the value of $\delta\alpha_i$ is evaluated as

$$\delta\alpha_i = (\alpha(\boldsymbol{\Delta}_m) - \alpha(\boldsymbol{\Delta}_i)) + (\alpha(\boldsymbol{\Delta}_{i+1}) - \alpha(\boldsymbol{\Delta}_m)) \tag{7.28}$$

which employs the midpoint to smooth out the ambiguity in $\boldsymbol{\Delta}$ rotation.

A summary of the recommended heuristic parameters and suggested values is provided in Table 7.1. Anything else not detected by the provided trials is labeled an unknown type of transversality violation. Unknown cases are treated the same as standard $\boldsymbol{g}$ points during the piecewise evaluation of the Poincaré index in Equation (7.11).

Parameter	Value	Brief Description
$(r^3)_{\min}$	10^{-20}	Minimum allowable divisor (numerical)
δt_{rel}	0.15	Maximum relative variation in time of flight
δt_{abs}	2.0	Maximum absolute variation in time of flight
$\Delta_{x,\max}$	0.2	Maximum change in map displacement x coordinate
$\Delta_{\dot{x},\max}$	2.0	Maximum change in map displacement $\dot{x}$ coordinate
$\delta\Delta_{\max}$	0.5	Maximum differential in $\|\boldsymbol{\Delta}\|$ values
$\delta\mathcal{P}_x$	1.0	Maximum differential in mapping x coordinate
$\delta\mathcal{P}_{\dot{x}}$	1.0	Maximum differential in mapping $\dot{x}$ coordinate
δCA_1	0.0166*	Minimum safe distance from singularity P_1
δCA_2	0.0045*	Minimum safe distance from singularity P_2
$\delta s_{\max}$	0.2	Maximum summed distance from singularity
$\delta\Delta_{Ws}$	0.1	Maximum $\|\boldsymbol{\Delta}\|$ value to indicate W^s crossing

Table 7.1 User-defined parameters and suggested nondimensional values employed during heuristic detection of transversality violations on $\Sigma : y = 0$ in the CRTBP. *Indicated value is based on the Earth-Moon system but should change for other systems.

7.5 Phase E: Fixed Point Refinement

The fixed points are computed to finer precision utilizing selected analysis cells resulting from the detection phase as input. The computation process as described by Tricoche et al. [14] is reinforced with shooting schemes to accommodate the sensitive dynamics associated with corrections procedures in multi-body problems. Also, intelligent processing exploits topological behavior and convergence basins to generate robust initial guesses for fixed points.

7.5.1 Refinement Methods

The numerical refinement procedures employed in this work isolate a set of design variables that are iteratively modified to meet constraints that apply to periodic orbits. note that the detected fixed points from Phase D are not necessarily symmetric about Σ, so an asymmetric scheme is enlisted. Two approaches–variable-time single shooting and variable-time multiple shooting methods–are employed in a similar fashion to the generic multiple shooting method for targeting periodic orbits in Section 3.5. The fixed point refinement methods are tailored to enforce a starting condition on Σ and constrain the Jacobi constant to a desired value without enforcing symmetry. Generating the appropriate initial guess for a fixed point is discussed in Section 7.5.3, but for now, assume that an initial guess for a fixed point is provided as input for the refinement procedure as the phase space coordinate $(x_0, \dot{x}_0)$ for a given p iterates of the Poincaré section.

Single Shooting Method for Fixed Point Refinement

The free-variable vector for the single shooting fixed point refinement method is comprised of information from the given phase space coordinates. The approximated fixed point coordinates $(x_0, \dot{x}_0)$ for a given p are converted to the initial state $\boldsymbol{x}_0^0$ employing the definition of Σ and the desired Jacobi constant, C_D. The superscript value, or j, refers to the

iteration number in the solution process, so $j = 0$ symbolizes the initial guess. Free-variables for the single shooting problem for finding fixed points are setup as

$$\boldsymbol{X}^j = \left\{ \begin{array}{c} \boldsymbol{x}_0^j \\ T^j \end{array} \right\}, \tag{7.29}$$

with dimension $N + 1$ (N is the dimension of the state vector, and $N = 6$ in the CRTBP). The variable T^j represents the orbital (time) period. Evolving $\boldsymbol{x}_0^0$ through $\boldsymbol{\mathcal{P}}^p(\boldsymbol{x}_0^0)$ sets T^0 as the accumulated simulation time at the p^{th} crossing of Σ. The superscripts on $\boldsymbol{X}^j$ components (such as $\boldsymbol{x}_0^j$ and T^j) are omitted from component entries henceforth for clarity.

The true fixed point location is determined by guaranteeing condition for a periodic orbit that are consistent with Poincaré section parameters. As demonstrated by Figure 7.9, fixed point refinement employing single shooting propagates an initial state ($\boldsymbol{x}_0$) forward for time T and evaluates periodicity conditions at the end of the simulation, signified by $\boldsymbol{x}_0(\boldsymbol{x}_0, T)$. After adjusting the initial state for a subsequent iterations based on constraints, the process is repeated until constraints satisfy a specified error tolerance (namely, $\|\boldsymbol{F}(\boldsymbol{X}^*)\| < \epsilon$ with $\epsilon = 10^{-8}$ for this investigation). The initial state is restricted to possess the specified Jacobi constant value for analysis, or C_D as defined by the user, through the constraint equation

$$C(\boldsymbol{x}_0) - C_D = 0, \tag{7.30}$$

where $C(\boldsymbol{x}_0)$ is simply the Jacobi integral evaluated at the initial state, or

$$C(\boldsymbol{x}_0) = 2\Upsilon(\boldsymbol{x}_0) - (\dot{x}_0^2 + \dot{y}_0^2 + \dot{z}_0^2). \tag{7.31}$$

The pseudo-potential function, $\Upsilon(\boldsymbol{x}_0)$, is strictly position dependent (Equation (2.30)). To enforce periodicity, the initial state must propagate back to itself over the time period T. Constraining *all* N components of the final state $\boldsymbol{x}_0(\boldsymbol{x}_0, T)$, however, over-constrains the problem since $\boldsymbol{x}_0(\boldsymbol{x}_0, T)$ is already partially constrained with the Jacobi constant (Equation (7.30)). Thus, periodicity is enforced via

$$\tilde{\boldsymbol{x}}_0(\boldsymbol{x}_0, T) - \tilde{\boldsymbol{x}}_0 = 0. \tag{7.32}$$

Note that $\tilde{\boldsymbol{x}}_0$ represents a partial state vector where the transverse component of velocity ($\dot{y}$) is excluded ($N-1$ elements). Since $\boldsymbol{x}_0$ is required to start on the Poincaré section in future analysis, another constraint is added to restrict that the initial state resides on the specified hyperplane, Σ, via the hyperplane equation or

$$D_{\Sigma}(\boldsymbol{x}_0) = y_0 = 0. \tag{7.33}$$

Summarizing, the constraint vector, $\boldsymbol{F}(\boldsymbol{X})$, for the single shooting fixed point refinement method appears as

$$\boldsymbol{F}(\boldsymbol{X}^j) = \left\{ \begin{array}{c} \tilde{\boldsymbol{x}}_0(\boldsymbol{x}_0, T) - \tilde{\boldsymbol{x}}_0 \\ D_{\Sigma}(\boldsymbol{x}_0) \\ C(\boldsymbol{x}_0) - C_D \end{array} \right\}. \tag{7.34}$$

Constraints are evaluated by simulating the initial state $\boldsymbol{x}_0$ for the proposed time period T as opposed to an implicit Poincaré map evaluation that may over-constrain solution movement. The matrix

$$D\boldsymbol{F}(\boldsymbol{X}^j) = \left[\begin{array}{cc} \tilde{\Phi}_0 - \tilde{I} & \dot{\tilde{\boldsymbol{x}}}_0(\boldsymbol{x}_0, T) \\ \Psi & 0 \end{array} \right], \tag{7.35}$$

stands as the analytical Jacobian matrix for the single shooting process with dimension $(N+1) \times (N+1)$. The Newtonian update formula (Equation (3.24)) is employed since the problem possesses an equal number of constraints and free-variables ($n = m$). The submatrix

$$\tilde{\Phi}_0 = \frac{\partial \tilde{\boldsymbol{x}}_0(\boldsymbol{x}_0, T)}{\partial \boldsymbol{x}_0} \tag{7.36}$$

represents the STM (or $\Phi_0(T, 0)$) with the row correlated with $\dot{y}_0$ removed. Similarly, the indicated special submatrix $\tilde{I}$ is a modified identity matrix also with the appropriate row removed. The special submartrix Ψ represents the analytical derivatives

$$\Psi = \left[\begin{array}{c} \frac{\partial D_{\Sigma}(\boldsymbol{x}_0)}{\partial \boldsymbol{x}_0} \\ \frac{\partial C(\boldsymbol{x}_0)}{\partial \boldsymbol{x}_0} \end{array} \right] = \left[\begin{array}{cccccc} 0 & 1 & 0 & 0 & 0 & 0 \\ 2\Upsilon_x(\boldsymbol{x}_0) & 2\Upsilon_y(\boldsymbol{x}_0) & 2\Upsilon_z(\boldsymbol{x}_0) & -2\dot{x}_0 & -2\dot{y}_0 & -2\dot{z}_0 \end{array} \right], \tag{7.37}$$

for the remaining constraints on the initial state. To assist with the corrections process, the STM is propagated concurrently with any given state vector.

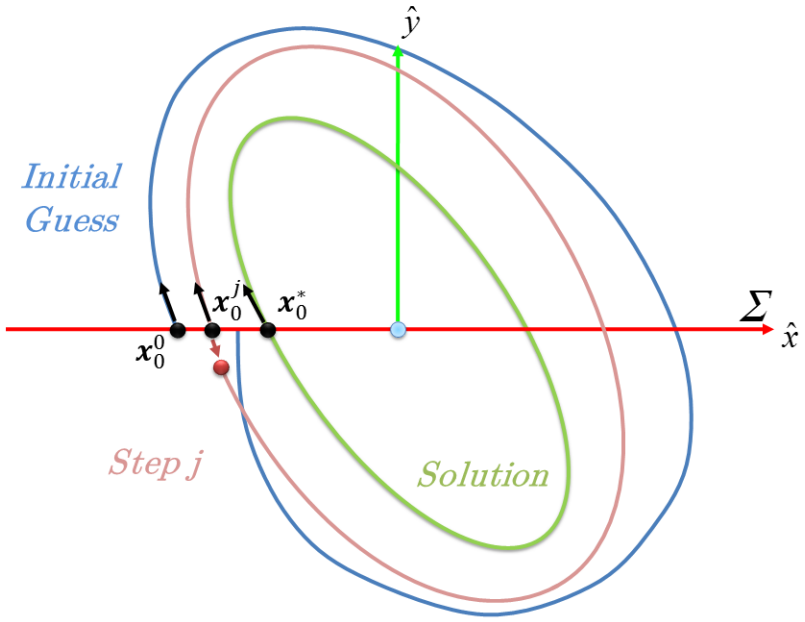

Figure 7.9. Schematic depiction of the single shooting method applied for fixed point refinement for a $p = 1$ fixed point guess $\boldsymbol{x}_0$.

Multiple Shooting Method for Fixed Point Refinement

The multiple shooting version of fixed point refinement separates the single shooting segment to form the problem definition. The design-variable vector, $\boldsymbol{X}^j$, requires the user to specify the number of patch points between successive iterates, k_p, such that trajectory segments from the simulation of a particular solution step (j) are split into $k = pk_p$ patch points with $k-1$ trajectory segments. The state vectors corresponding to the k patch points and the orbital (time) period, T, are collected to form the design-variable vector as

$$\boldsymbol{X}^j = \left\{ \begin{array}{c} \boldsymbol{x}_0 \\ \boldsymbol{x}_1 \\ \vdots \\ \boldsymbol{x}_{k-1} \\ T \end{array} \right\}, \tag{7.38}$$

where the dimension of $\boldsymbol{X}^j$ is $Nk+1$. For the initial guess vector $\boldsymbol{X}^0$, the values $\boldsymbol{x}_0$ and T are populated with a simulation of the detected guess state. The remaining $k-1$ state entries in $\boldsymbol{X}^0$ are sampled from the propagated evolution at equal time intervals of T/k. An illustration of the segments and patch points for a $p=1$ analysis appears in Figure 7.10. The blue initial guess is a continuous evolution with displacement only existing between the initial state and the final return to the section whereas the desired periodic solution (green) is continuous throughout the evolution of $\boldsymbol{\mathcal{P}}^p(\boldsymbol{x}_0^*)$. Intermediate steps in the solution process, such as the red arcs indicating the j^{th} step, may possess discrepancies between patch points, which are highlighted through the numerical simulation of a patch point over a specified time interval. The notation $\boldsymbol{x}_1(\boldsymbol{x}_0, T/k)$ indicates the final state from the propagation of $\boldsymbol{x}_0$ through simulation time T/k. The number of patch points per Poincaré map iterate, or k_p, influences convergence properties; the value $k_p=5$ provides reasonable convergence for many cases and is employed in the current work.

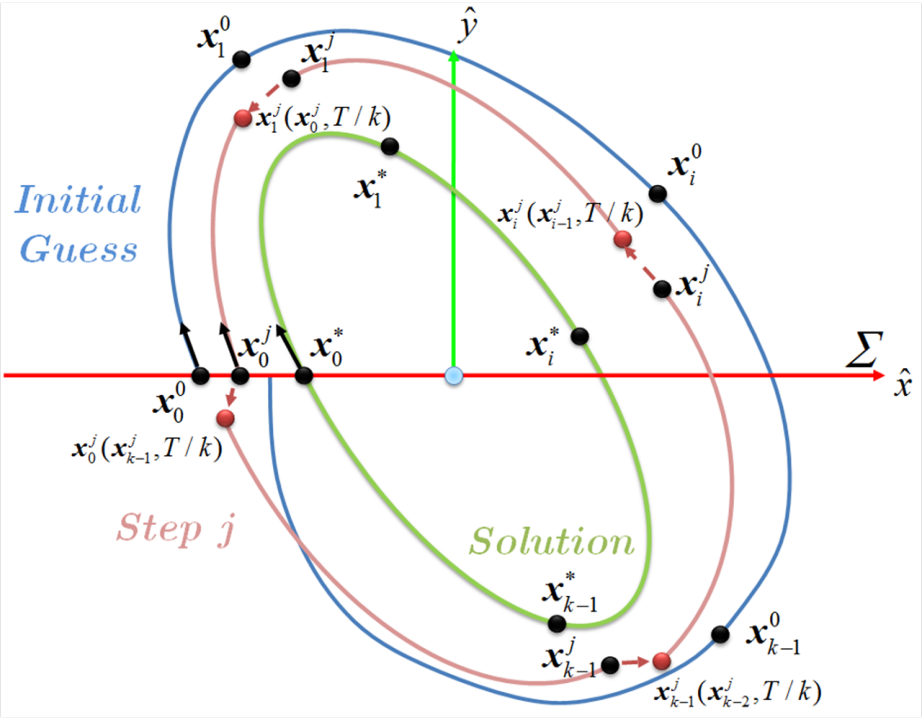

Figure 7.10. Schematic diagram of the fixed point refinement procedure employing a multiple shooting approach with k patch points given a $p=1$ initial guess.

The constraints for fixed point refinement are augmented with segmentation when employing the multiple shooting method. Periodic orbit conditions now also include constraints to enforce continuity between segments. Thus, $N(k-1)$ constraints enforce continuity at the patch points, and $N-1$ constraints ensure the periodicity conditions, i.e., that the propagation of the $k-1$ state for the time period T/k matches the initial state through

$$\tilde{\boldsymbol{x}}_0(\boldsymbol{x}_{k-1}, T/k) - \tilde{\boldsymbol{x}}_0 = 0. \tag{7.39}$$

The same Jacobi constant and section definition constraints (Equations (7.30) and (7.33), respectively) are also applied to the initial state in the same manner as single shooting. Overall, the multiple shooting constraint vector, $\boldsymbol{F}(\boldsymbol{X}^j)$, incorporates the patch point continuity constraints and all additional constraints for iteration j in the form

$$\boldsymbol{F}(\boldsymbol{X}^j) = \left\{ \begin{array}{c} \boldsymbol{x}_1(\boldsymbol{x}_0, T/k) - \boldsymbol{x}_1 \\ \boldsymbol{x}_2(\boldsymbol{x}_1, T/k) - \boldsymbol{x}_2 \\ \vdots \\ \boldsymbol{x}_{k-1}(\boldsymbol{x}_{k-2}, T/k) - \boldsymbol{x}_{k-1} \\ \tilde{\boldsymbol{x}}_0(\boldsymbol{x}_{k-1}, T/k) - \tilde{\boldsymbol{x}}_0 \\ D_\Sigma(\boldsymbol{x}_0) \\ C(\boldsymbol{x}_0) - C_D \end{array} \right\}. \tag{7.40}$$

Note, the first $N(k-1)$ entries of $\boldsymbol{F}(\boldsymbol{X}^j)$ represent the continuity conditions applied to the patch points. Since the formulation employs $Nk+1$ design variables to uphold $Nk+1$ constraints, the refinement procedure utilizes the Newtonian update formula (Equation (3.24)). Analytical expressions are available for the Jacobian matrix via

$$D\boldsymbol{F}(\boldsymbol{X}) = \begin{bmatrix} \frac{\partial \boldsymbol{x}_1(\boldsymbol{x}_0, T/k)}{\partial \boldsymbol{x}_0} & -I & & & \frac{\dot{\boldsymbol{x}}_1(\boldsymbol{x}_0, T/k)}{k} \\ & \frac{\partial \boldsymbol{x}_2(\boldsymbol{x}_1, T/k)}{\partial \boldsymbol{x}_1} & -I & & \frac{\dot{\boldsymbol{x}}_2(\boldsymbol{x}_1, T/k)}{k} \\ & & \ddots & \ddots & \vdots \\ -\tilde{I} & & & \frac{\partial \tilde{\boldsymbol{x}}_0(\boldsymbol{x}_{k-1}, T/k)}{\partial \boldsymbol{x}_{k-1}} & \frac{\dot{\tilde{\boldsymbol{x}}}_0(\boldsymbol{x}_{k-1}, T/k)}{k} \\ \Psi & & & & \end{bmatrix}, \tag{7.41}$$

with $\tilde{I}$ and Ψ (Equation (7.37)) representing the same special submatrices as the single shooting fixed point refinement method. The missing entries in the $D\boldsymbol{F}(\boldsymbol{X})$ matrix are zero elements. Entries in the last column of $D\boldsymbol{F}(\boldsymbol{X})$ are evaluated as the state derivatives at the end of the specified numerical simulation multiplied by a constant $(1/k)$.

7.5.2 Applying a Sequence of Periodic Orbit Targeting Algorithms

Although both single shooting and multiple shooting are moderately successful for finding fixed points, each differential corrections technique possesses varying convergence properties. To demonstrate, consider states on Σ in the vicinity of the L_1 Lyapunov orbit as initial guesses for finding the known $p = 1$ periodic orbit. As shown in Figure 7.11, areas where many initial states converge on the L_1 Lyapunov orbit with the single shooting are highlighted red, and convergent section states for multiple shooting are shown in green. These areas approximate the *basin of convergence* assigned to the shooting schemes considering states emanating from Σ. Also, the larger blue convergence basin in Figure 7.11 is also demonstrated for a quasi-Newton version of the variable-time single shooting method (see Section 3.7). Knowledge of convergence basin geometry is unavailable *a priori* for an arbitrary fixed point since the fixed points are unknown beforehand; therefore, differential corrections procedures are executed systematically in a predefined sequence to inflate the overall fixed point refinement convergence basin. The sequential set starts with single shooting refinement, and then, transitions to the variable-time multiple shooting method in the event of single shooting divergence. If neither process succeeds, the quasi-Newton single shooting method is then attempted last. Even though the quasi-Newton approach appears to have the largest basin of convergence, the quasi-Newton method requires far more computational time with many more function evaluations to complete the line search [36]. Hence, single shooting and multiple shooting are attempted first for computational efficiency. Expanding the fixed point refinement process to a systematic set of targeting methods increases the overall convergence basin and strengthens the ability to refine fixed point guesses.

Ordering and pre-screening the fixed point refinement computations leads to an efficient parallel execution. Some guesses are repeated at higher periods within the same cell. Note, a $p = 1$ orbit is also a fixed point for every period up to p_{max}, fixed points at $p = 2$ are also

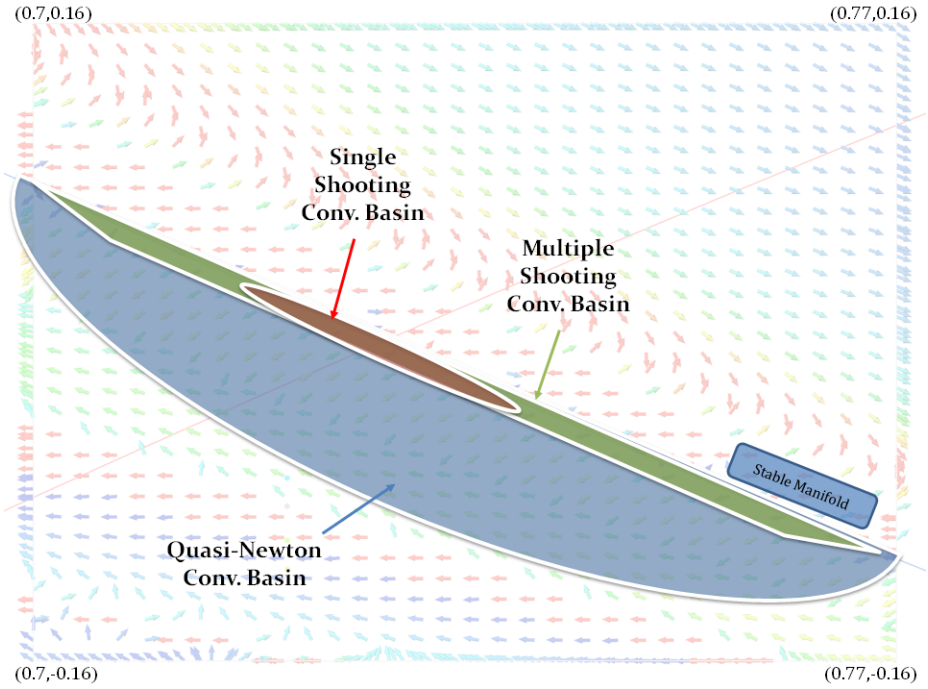

Figure 7.11. Approximate convergence basins employing states in phase space near the L_1 Lyapunov fixed point in the Earth-Moon system ($C = 2.96$).

fixed points for $p = 4, 6, 8, \ldots, p_{max}$, and so on. To initiate guess screening, the guess states are first sorted with ascending periods. Then, PMATE discards the higher period multiples of the same guess states (if the guesses are at the same state to a magnitude differential less than 10^{-3}). After the high-period pre-screening, each fixed point refinement process is conducted an independent computation. Thus, each sequential solution procedure is executed in parallel on individual computation threads. Fixed point guesses are processed in order of descending period as high-period orbits are often more computationally challenging to process with longer orbital time periods and higher sensitivities. The high-to-low period processing order balances thread workload as the hardest computations are attacked first.

7.5.3 Determining the Initial Guess for Fixed Points

Although employing several differential corrections procedures in succession helps overall robustness of the refinement process, the refinement result is still heavily contingent on the

initial guess. Some fixed point guesses come from the evaluation of the Poincaré index with refined sampling along edges (Section 7.4.1), yet most detected fixed points exist inside the analysis cells with non-zero Poincaré indexes. Within such analysis cells, guesses are generated naively via searching for the minimum $\|\boldsymbol{\Delta}\|$ for the indicated p throughout a small subgrid of initial map states within the cell. For a robust initial guess, the guess state on the section should reside within the blended convergence basin of the corrections set for the fixed point of interest. The subgrid, though, is typically very coarse (e.g., 4×4) to limit map calls, causing states from the subgrid to commonly reside outside the thin convergence basins. Thus, the naive subgrid search misses robust initial guesses but initiates the honing of improved fixed point guess locations.

Since map information is already available in the form of the coarse search grid, fitting that map data to a simple saddle-type flow field model offers an alternative initial guess point. The forward map displacement vectors form a flow field for model-fitting ($\boldsymbol{\Delta}(\boldsymbol{x})$), but the map tangent vector, $\boldsymbol{\eta}(\boldsymbol{x})$, defined as

$$\boldsymbol{\eta}(\boldsymbol{x}) = \boldsymbol{\mathcal{P}}^{p}(\boldsymbol{x}) - \boldsymbol{\mathcal{P}}^{-p}(\boldsymbol{x}), \tag{7.42}$$

represents a low-pass filter on the discrete Poincaré map process, and thus, another flow field to consider. In the $\boldsymbol{\Delta}(\boldsymbol{x})$ field, Lyapunov's Theorem dictates that mode strength persists as reciprocal pairings, meaning the unstable mode dominates topological behavior [50, 51]. The enlistment of $\boldsymbol{\eta}(\boldsymbol{x})$ roughly equalizes the strength of the stable and unstable modes, bypassing the mode strength issues present in the $\boldsymbol{\Delta}(\boldsymbol{x})$ field. The thick, transparent arrows in Figure 7.12 display the $\boldsymbol{\eta}(\boldsymbol{x})$ field near the indicated $p = 3$ saddle-type fixed point as topologically similar to a linear flow field saddle. Thus, a linear dynamical model as well as a simple quadratic extension are implemented as the approximated fitting models. If $\boldsymbol{\zeta} = \boldsymbol{x} - \boldsymbol{s}$ serves as the dynamical state of the model on the section with $\boldsymbol{s}$ representing the saddle-type fixed point location, then the quadratic model is formed as

$$\dot{\boldsymbol{\zeta}} = A_s\boldsymbol{\zeta} + \tfrac{1}{2}\boldsymbol{\zeta}^T\underline{Q}\boldsymbol{\zeta}. \tag{7.43}$$

Note, A_s is a 2×2 matrix, and $\underline{Q}$ is a $2 \times 2 \times 2$ tensor where $\underline{Q} = 0$ in the linear model. A Levenberg-Marquardt optimization process is applied to minimize the difference between

the model $\dot{\boldsymbol{\zeta}}(\boldsymbol{x})$ in Equation 7.43 and known data (i.e., the $\boldsymbol{\eta}(\boldsymbol{x})$ field or the normalized $\hat{\boldsymbol{\eta}}(\boldsymbol{x})$ field to remove variances in magnitude) [36]. The optimization result is a set of coefficients, or $\boldsymbol{s}$, A_s, and $\underline{Q}$, that describe the field and return the approximate saddle location ($\boldsymbol{s}$). The solution from the optimization routine is anisotropic with respect to the initial coefficients, so it is important to seed the initial value for the models appropriately. The saddle structure near a fixed point, shown as the blue (stable) and red (unstable) manifold lines in Figure 7.12, typically appears as an "x" pattern on Σ in the planar CRTBP. Levying the known saddle pattern forms the initial coefficient values as

$$\boldsymbol{s} = \left\{ \begin{array}{c} x_{center} \\ \dot{x}_{center} \end{array} \right\}, \text{ and } A_s = \left[\begin{array}{cc} 0 & 2 \\ 2 & 0 \end{array} \right], \tag{7.44}$$

where $\boldsymbol{s}$ is initially set at the center of the cell, and the eigenvectors of A_s correlate with the appropriate saddle pattern. The solution from the linear model (black in Figure 7.12) is utilized as the initial value for the quadratic model (magenta). As apparent in Figure 7.12, the critical points of the various models reflect the approximate location of the saddle-type fixed point more closely than any of the cell subgrid points with the quadratic fit yielding the best results in the example case. Since the Levenberg-Marquardt solution is generated fairly quickly (less than a second), all three models are employed to help find the best fixed point guess.

Unfortunately, it is impossible to employ the model-fitting guess generation strategy in a non-transverse analysis cell due to the discontinuities in the map tangent vector. A new strategy for non-transverse cells is gleaned from observing the approximate basins of convergence in the vicinity of the L_1 Lyapunov fixed point on Σ. Apparent in Figure 7.11, the expanded convergence basin aligns with the stable manifold associated with the L_1 Lyapunov fixed point ($p = 1$). An ancillary fact is that the lowest $\|\boldsymbol{\Delta}\|$ values also correlate with the stable manifold, explaining why the convergence basins of the various differential corrections methods are closely related to the stable manifold structure (see Figures 7.6(a) and 7.11). In non-transverse cells, therefore, the sampling subgrid within the cell is modified to examine states along lines adjoining the minimal $\|\boldsymbol{\Delta}\|$ locations of each cell edge. Since manifold structure is generally not known before the refinement process, sampling occurs on all 6 possible lines that connect the 4 local minimums in $\|\boldsymbol{\Delta}\|$ belonging to each cell

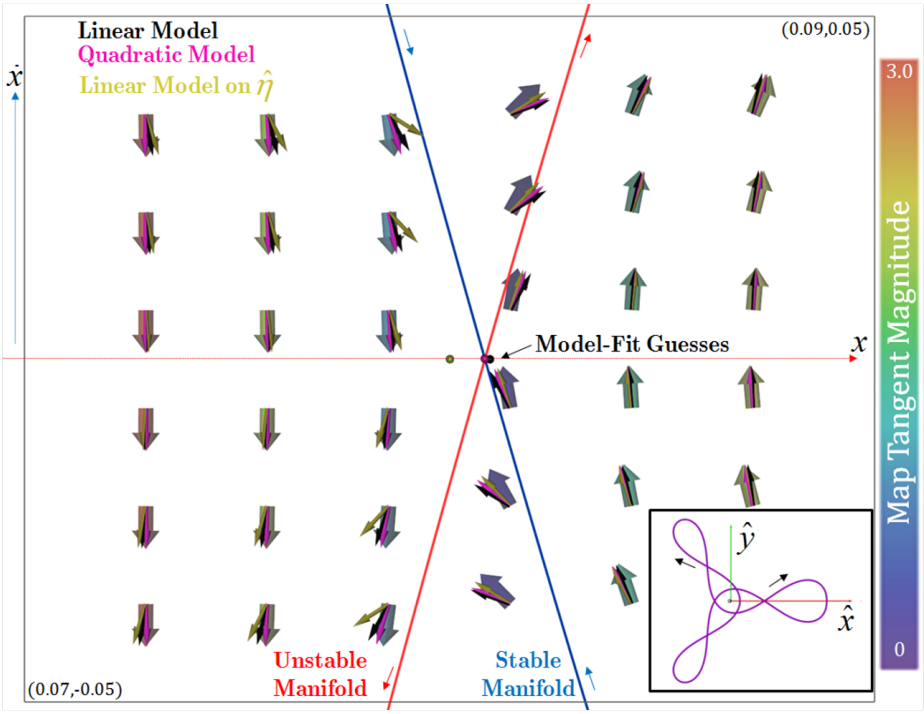

Figure 7.12. The $\boldsymbol{\eta}(\boldsymbol{x})$ field and saddle model fitting techniques for generating initial guesses for transverse Poincaré section analysis cells.

edge with the intent that a single line will closely resemble the sought-after stable manifold structure. An example of the modified sampling grid appears in Figure 7.13 with green dots along the modified sampling lines (black) representing the new possible guesses. Note, one of the sampling lines in Figure 7.13 closely aligns with the stable manifold of the L_1 Lyapunov orbit. The initial map state resulting in the smallest $\|\boldsymbol{\Delta}\|$ overall is then chosen as the fixed-point guess for that cell.

7.5.4 Filtering Fixed Point Results

Multiples of the same periodic orbits commonly result from the refinement procedure and must be reduced through a filtering process. Duplicate fixed points may appear by refining different initial guesses, especially repeats of the same periodic orbit through detecting various fixed points of said orbit at separate map locations. In fact, it is often advantageous to test these duplicates during refinement because some fixed points possess

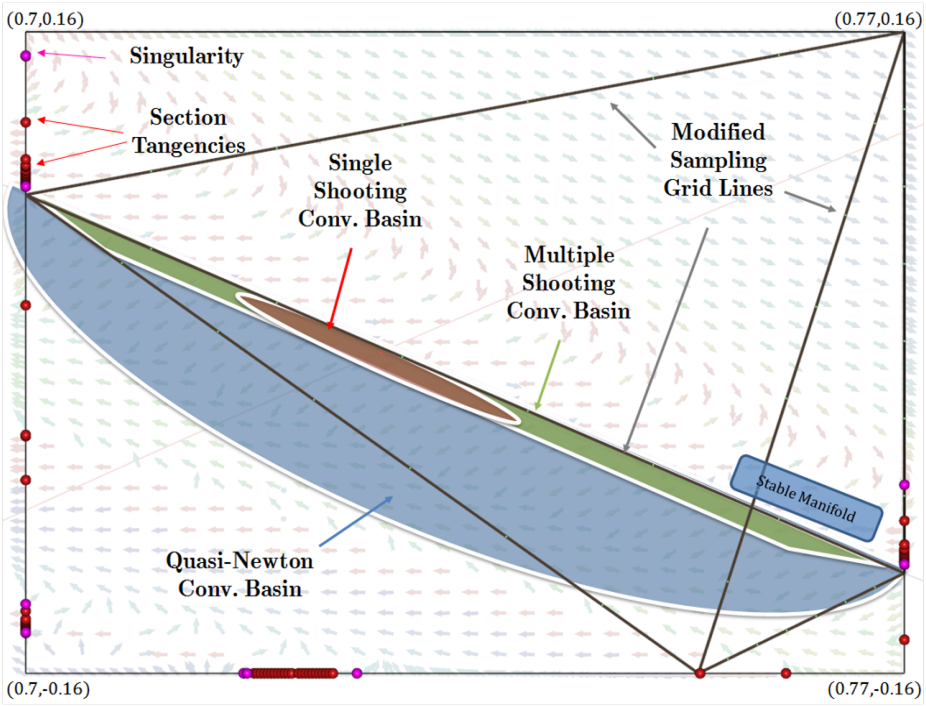

Figure 7.13. Initial guesses generation strategy for fixed points in non-transverse Poincaré section analysis cells that favors convergence within the sequence of differential corrections procedures.

more amenable convergence basins than others of the same orbit based on local Poincaré map behavior. Many asymmetric periodic orbits exist in the planar CRTBP and should appear with a correlated paired orbit via the symmetry properties of the CRTBP. Both asymmetric members of the pair, though, may not always be located through the detection or refinement phases. The filtering process, therefore, initiates with orbit classification as symmetric or asymmetric by examining the return set for states along the x-axis or symmetric pairings across the x-axis on the Poincaré section. The mirrored counterpart to any identified asymmetric orbit is added to the list of computed fixed points, possibly adding additional copies of detected orbits. Removing duplicates, pre-existing or newly generated, is then the next step to filtering fixed point results. Again, higher period multiples to lower period counterparts are filtered out by testing if states are equivalent to a specified tolerance in a similar manner to pre-screening. The tolerance here, however, is more stringent at 5×10^{-6}. After reducing to the lowest possible integer period, fixed point filtering is

concluded by removing duplicate periodic orbits. Periodic orbits with equivalent p values are compared at each crossing to detect if map states are equivalent (again, to tolerance 5×10^{-6}), and repeated orbits are discarded if equivalent map states are located. After the filtering process, the resulting set of fixed points contains a set of unique periodic orbits with all symmetric pairings included.

7.6 Phase F: Invariant Manifold Extraction

After the initial guesses are refined to periodic orbits and appropriately filtered, the resulting fixed points are classified based on stability. The full-period STM (or monodromy matrix $\mathcal{M}$ in Equation (4.7)) is employed to classify the orbital stability characteristics through the standard eigenvalue analysis [9, 49]. If $\lambda_{\max}$ represents the monodromy matrix eigenvalue with maximum magnitude, then a periodic orbit with $|\lambda_{\max}| > 1$ is classified as a saddle-type (unstable) fixed point [49]. All other computed fixed points are classified as centers. Additional data is also collected for fixed points, including ν_{SI} and $\nu_{z,SI}$ from the trace of $\mathcal{M}$ (Equations (4.12) and (4.13)) and the appropriate eigenvectors for saddle points. Since $\mathcal{M}$ is an unsymmetric matrix and the sensitivities in certain systems (e.g., ST or SEnc) create vast scaling differences, the eigenvector computation may fail if $|\lambda_{\max}|$ is very large ($> 10^5$) [36]. When such a failure is encountered, manifold extraction is skipped for that periodic orbit.

For the saddle-type fixed points, the stable and unstable manifolds are computed in the final stage of the PMATE algorithm. The DGE method for manifold construction (Section 4.3) is easily converted to output a puncture plot on the intended hyperplane Σ; however, the exponential growth behavior of invariant manifolds exacerbates the Poincaré map distance between the discrete set of trajectories in phase space [7, 61, 65]. Thus, manifolds are located in PMATE by employing an alternative approach to the standard DGE method for astrodynamics. Ideally, the 1D invariant manifold curves of saddle-type periodic orbits are constructed exclusively on the Poincaré section with adaptive resolution to deliver more information where structure is rapidly varying. The *ManBVP algorithm*, offered by England et al., is one such adaptive method that builds manifolds on the surface of section by solving a successive sequence of two-point boundary value problems (or

TPBVPs) that enforce that newest point of the 1D manifold curve continues a prescribed level smoothness and detail [13]. Like several other manifold generation algorithms [59], the England et al. method embeds adaptive refinement measures to add more manifold arcs (Poincaré section states) as exponential spreading is encountered [13]. Unfortunately, the ManBVP algorithm does not accommodate Poincaré section transversality violations as Poincaré map discontinuities are not considered [13]. Thus, an offshoot algorithm is constructed for PMATE with the explicit purpose of invariant manifold extraction within the CRTBP. This offshoot algorithm, termed the *ManCurve algorithm*, employs the manifold construction assumptions on smoothness and detail of the ManBVP algorithm but replaces the TPBVP solution step with a refinement procedure that accommodates transversality violations in the Poincaré section (similar to the resolved Poincaré index computation during Phase D in Section 7.4.3).

7.6.1 Manifold Extraction with Curve-Refinement

Several definitions are outlined to describe the relevant quantities pertaining to invariant manifolds and the application of curve-refinement procedures. First, let the vector state $\boldsymbol{\phi}_i$ represent an invariant manifold state, either W^S or W^U, on the 1D curve projection existing on the Poincaré section. For clarity, this notation for manifold states on a Poincaré section stands apart from the STM, denoted with an uppercase Φ_i or $\Phi_i(t, 0)$. A key assumption to both the ManBVP and ManCurve algorithms is that states along the manifold are computed at sufficiently close intervals such that all states along the linear segment connecting existing states are also members of the same 1D manifold curve on the Poincaré section. Following that assumption, mapping states sampled from linear segments joining existing states creates new manifold states to advance a manifold of interest. For an arbitrary manifold, the sampled state $\boldsymbol{x}_w(\tau)$ on a linear segment w is computed from the existing adjacent states $\boldsymbol{\phi}_i$ and $\boldsymbol{\phi}_{i+1}$ that form segment w through

$$\boldsymbol{x}_w(\tau) = (1 - \tau)\boldsymbol{\phi}_i + \tau\boldsymbol{\phi}_{i+1}, \tag{7.45}$$

where τ represents the linear sampling parameter ($\tau \in [0, 1]$). A depiction of manifold states and a linearly interpolated state $\boldsymbol{x}_w$ at τ are represented in Figure 7.14. The state $\boldsymbol{x}_w(\tau)$ is

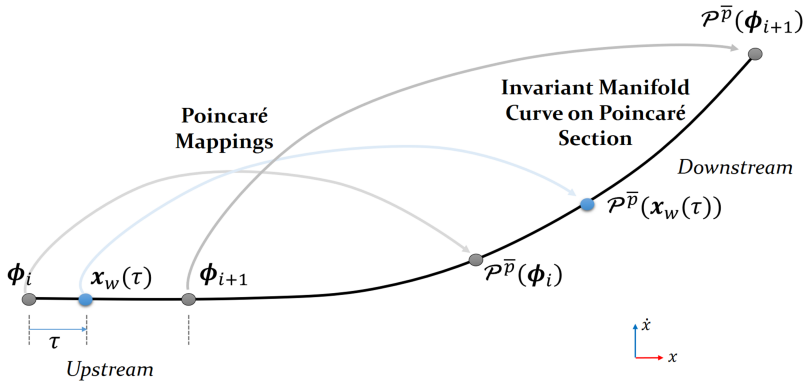

Figure 7.14. Schematic of a 1D invariant manifold curve on the Poincaré section.

then a member of the existing, or *upstream*, portion of the invariant manifold. *Downstream*, or new, members of an invariant manifold are computed by computing the Poincaré map of upstream states with an appropriate number of iterates. Mapping iterates must consider the invariant manifold behavior, and specifically, Möbius orbits (periodic orbits with $|\lambda_{\max}| < 0$) are assigned a doubled period. Therefore, the Poincaré map iteration number for invariant manifolds, labeled $\overline{p}$, is set through the conditional

$$\overline{p} = \begin{cases} 2p & \text{if } \lambda_{\max} < 0 \text{ for } W^U, \\ -2p & \text{if } \lambda_{\max} < 0 \text{ for } W^S, \\ p & \text{if } \lambda_{\max} > 0 \text{ for } W^U, \\ -p & \text{if } \lambda_{\max} > 0 \text{ for } W^S. \end{cases} \tag{7.46}$$

Assuming the upstream segment $\overline{\boldsymbol{\phi}_i \boldsymbol{\phi}_{i+1}}$ approximates the manifold between states, new downstream states of the manifold are generated by mapping a linearly interpolated state, or $\boldsymbol{x}_w(\tau)$, from the upstream interval through $\boldsymbol{\mathcal{P}}^{\overline{p}}(\boldsymbol{x}_w(\tau))$. Note that the terms upstream and downstream refer to the universal mapping direction for both stable and unstable manifolds. As highlighted by Table 7.2, mapping states downstream along the manifold generates new states following the time-advancement definition of a particular manifold (i.e., forward-time for W^U and reverse-time for W^S).

The manifold generation algorithm for PMATE combines curve-refinement procedures with the discrete nature of the Poincaré section. With saddle-type critical points of a

Manifold	Symbol	Iterates	Upstream	Downstream
Stable	W^S	$-p$ or $-2p$	Forward ($t > 0$)	Backward ($t < 0$)
Unstable	W^U	p or $2p$	Backward ($t < 0$)	Forward ($t > 0$)

Table 7.2 Definition of upstream and downstream directions along the 1D invariant manifold curves as seen through the Poincaré map projection of the associated streamsurfaces.

vector-field, streamlines representing invariant manifolds are produced by propagating an appropriately perturbed state from the critical point through the dynamical system [51,61]. Since the Poincaré section conveys the projection of invariant manifold streamsurfaces, simple propagation of a state perturbed from a fixed point does not deliver the representation of the entire manifold. Yet, the streamline generation idea can be applied if a group of states along the perturbation direction are evolved simultaneously. The term *advection* represents the act of transporting a group of trajectories belonging to a given invariant manifold to subsequent downstream Poincaré map iterates. *Advecting* a manifold, therefore, is the act of mapping a contiguous portion of the invariant manifold streamsurface (such as a segment on the Poincaré section) to a downstream set. Let an upstream segment of an invariant manifold, or $\overline{\boldsymbol{\phi}_i\boldsymbol{\phi}_{i+1}}$, be referred to as the *working segment*, denoted with the symbol w. In the ManCurve algorithm, the working segment is adaptively subdivided with an adaptive edge data structure in a very similar manner to computing the Poincaré index (Section 7.4). States along the working edge currently residing in the adaptive edge representation are mapped downstream through $\boldsymbol{\mathcal{P}}^{\overline{p}}(\boldsymbol{x}_w(\tau))$. When adjacent downstream states emanating from the working segment fail curve-refinement initiatives (see Section 7.6.3), a simple bisection procedure adds the midpoint of the corresponding upstream states to the adaptive edge structure. Once an upstream segment has subdivided to form a sufficiently smooth downstream curve or to a minimal distance on the working segment ($u_{\min}$), the constructed downstream states and smooth segments are added to the depiction of the invariant manifold. Then, manifold propagation advances to the next upstream segment to continue processing new downstream manifold segments. ManCurve uses the same assumptions as the ManBVP algorithm but subdivides the working segment while simultaneously checking for Poincaré map discontinuities in downstream section states; thus, the

ManCurve algorithm accommodates manifold generation through transversality violations while maintaining curve-refinement criteria.

A schematic demonstration of manifold construction via adaptive edge data structures and curve-refinement highlights the ManCurve procedures for various saddle-type fixed points. For now, assume that the appropriate initial on-section step is selected to form the first segment, identified as Segment 0 ($w = 0$). (The process for computing Segment 0 is discussed later in Section 7.6.2.) Segment 0 is comprised of the first points on the manifold of interest: $\boldsymbol{\phi}_0$ (or the originating fixed point $\boldsymbol{x}^*$) and $\boldsymbol{\phi}_1$ which exemplifies the initial on-section step. Any new working segment is initialized with the corresponding midpoint, $\boldsymbol{x}_{mw} = \boldsymbol{x}_w(\tau = 0.5)$, in the adaptive edge structure as to provide at least one depth level in the evaluation of downstream curve-smoothness and transversality tests. In addition, the Poincaré map of the working segment end point (or $\boldsymbol{\mathcal{P}}^{\overline{p}}(\boldsymbol{\phi}_1)$ for Segment 0) and the working segment midpoint (or $\boldsymbol{\mathcal{P}}^{\overline{p}}(\boldsymbol{x}_{m0})$ for Segment 0) are also computed. A schematic demonstration of the first segment and its accordingly mapped downstream points appears in Figure 7.15. If the new downstream states (mapped from the working segment) constitute a disjointed or jagged 1D (on-section) curve representation of the manifold through linear segments, then the working segment is subdivided further to spawn additional downstream manifold points. Otherwise, the new downstream points are accepted as additional parts of the invariant manifold, and the newly formed segments are stored for implementation as future working segments. In the sample case of Segment 0 in Figure 7.15, only the midpoint mapping is required to form the new points $\boldsymbol{\phi}_2$ and $\boldsymbol{\phi}_3$. The ManCurve algorithm then transitions to next working segment, i.e., Segment 1 that joins $\boldsymbol{\phi}_1$ and $\boldsymbol{\phi}_2$. While processing the subsequent working segment, however, a second subdivision round is required to produce sufficient downstream smoothness and advect the invariant manifold curve, generating the red downstream mapping points $\boldsymbol{\phi}_4$, $\boldsymbol{\phi}_5$, $\boldsymbol{\phi}_6$, and $\boldsymbol{\phi}_7$. This advection procedure (evaluating the downstream mappings of a group of states sampled from a working segment) constructs the full 1D curve representing the invariant manifold by progressing through subsequent working segments until certain stopping conditions are encountered (discussed in Section 7.6.4).

Special care in manifold construction is applied to unstable periodic orbits that slowly depart a fixed point in the downstream direction. Manifolds that comprise the KAM bound-

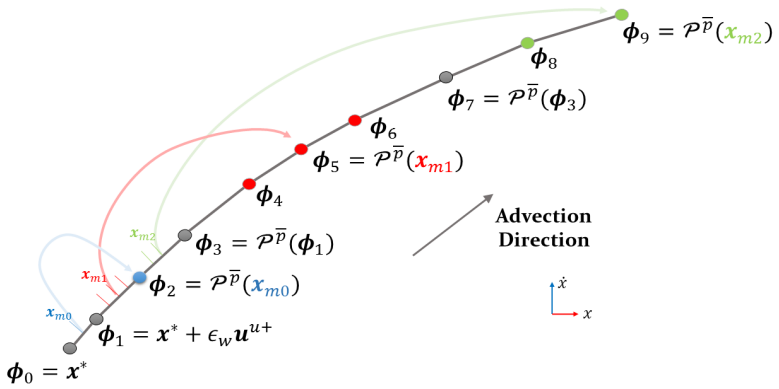

Figure 7.15. Schematic depiction of manifold advection with curve-refinement for standard invariant manifolds on the Poincaré section.

aries of quasi-periodic regions demonstrate this slow downstream departure pattern, indicating a seemingly weak instability. Note that *weak-strength manifolds* are then so termed due to the exceptionally slow approach to or departure from the originating saddle-type periodic orbit. On weak-strength manifolds, the exponential downstream growth rate is stunted due to the smaller characteristic multiplier magnitude; therefore, *weak-strength saddles* are set as periodic orbits with $|\lambda_{\max}| < 50$ since manifolds of such periodic orbits require several Poincaré map iterates to overcome slow asymptotic downstream departure (i.e., downstream manifold advection). Recall that one level of subdivision is always employed during advection by testing the working segment midpoint and the correlated mapping. Accepting the mapping of the working segment midpoint of a weak-strength saddle, though, creates a downstream segment that is smaller than the working segment. Compounding this effect through subsequent working segments slows the overall generation of the manifold with unnecessary states. Ergo, the midpoint of the working segment is still mapped to check criteria, but the advection process for weak-strength saddles is expedited by omitting the midpoint mapping if the downstream curve is smooth regardless. Figure 7.16 demonstrates the advection of weak-strength manifolds. As shown by the blue, red, and green midpoints in Figure 7.16, the working segment midpoint mappings for the first 3 segments do not contribute to the advected curve growth. The purple midpoint on Segment 3, however, is necessary to construct a downstream smooth curve between $\boldsymbol{\phi}_4$ and the downstream

mapping $\boldsymbol{\mathcal{P}}^{\overline{p}}(\boldsymbol{\phi}_4)$, and hence, employed for advection. Once a subdivision is encountered on working segments of weak-strength manifolds, the advection procedure returns to normal operation (i.e., accepting midpoint mappings) since sufficient asymptotic growth has resumed.

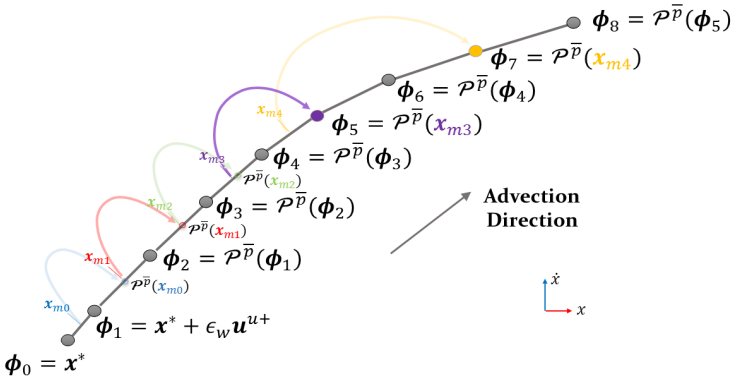

Figure 7.16. Demonstration of manifold advection on the Poincaré section via curve-refinement with weak-strength manifolds ($|\lambda_{\max}| < 50$).

Transversality violations are also integrated into invariant manifold advection with curve-refinement procedures. The heuristics for detecting transversality violations in Section 7.4 for Poincaré index evaluation are reapplied for adaptive edge data structures on working segments alongside the curve-refinement criteria. If a downstream transversality violation is detected between subsequent working segment states, then the working segment is bisected on that interval. Subdivision continues until subsequent working segment points are within a user-prescribed minimal distance apart ($u_{\min}$). Note that the distance $u_{\min}$ can also be expressed as a minimal difference in τ between subsequent upstream states on the working segment, or $\Delta\tau_{\min}$. The subdivision of a working segment that encapsulates a downstream transversality violation is depicted in Figure 7.17 where downstream mappings are color-coded by the working segment initial state. Here, a downstream transversality violation exists between $\boldsymbol{\phi}_i$ and the midpoint $\boldsymbol{x}_{mw}$, and subdivision of the adaptive edge structure representing the working segment localizes the separation condition when the linear parameter differential is below $\Delta\tau_{\min}$. New downstream segments are constructed as usual, but ManCurve purposefully skips the segment through the separation condition as

this is a known downstream discontinuity in the Poincaré section based on heuristic detection. After advecting a working segment to create a group of new downstream segments for the invariant manifold curve, ManCurve advances to the next viable working segment in the existing set of manifold segments.

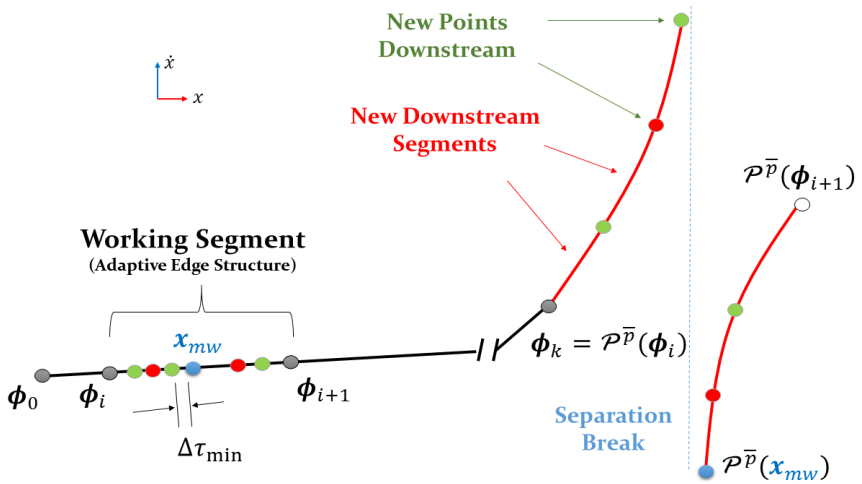

Figure 7.17. Generating new downstream manifold points and segments through a transversality violation on the Poincaré section with PMATE.

7.6.2 Seeding an Invariant Manifold on the Poincaré Section

Empirically defined functions based on stability information seed the initial segments for invariant manifold curves by evaluating on-section step directions and distances. The eigenvalues of the monodromy matrix describe the stability characteristics of a periodic orbit, and the corresponding eigenvectors provide a linearly approximated basis for the global invariant manifolds. Thus, a small step away from a fixed point along an appropriate eigenvector direction approximates an initial state on the invariant manifold; yet, the step along the eigenvector creates a perturbation in all N dimensions of the problem ($N = 4$ in the planar CRTBP). Unfortunately, the ManCurve algorithm for PMATE requires a perturbation on the Poincaré section to begin manifold advection, and direct projection of the eigenvector onto the hyperplane Σ yields a vector that inadequately characterizes the on-section manifold curve. Consider the example of the ND step from a fixed point ($\boldsymbol{x}^*$ defined on the hyperplane Σ) onto the eigenvector $\boldsymbol{\nu}^{S+}$ as demonstrated below in Figure 7.18. The nondimensional step distance in N-space, or ϵ_N, is arbitrarily set as 10^{-9} to generate a universally small step onto invariant manifolds for all periodic orbits. In PMATE, the expression $\boldsymbol{x}^* \pm \epsilon_N \boldsymbol{\nu}^{U/S}$ locates the initial state of the associated invariant manifold as a translation from a fixed point on Σ in ND. The on-section normalized representation of the same invariant manifold space, defined as $\boldsymbol{u}^{U/S}$, is then created by propagating $\boldsymbol{x}^* \pm \epsilon_N \boldsymbol{\nu}^{U/S}$ to the nearest crossing of Σas indicated by Figure 7.18. Note that the propagation direction may be either forward or backward in time depending on the step relationship with Σ. For $\Sigma : y = 0$, the value of y in the ND step state determines the appropriate simulation direction (forward time for $y < 0$ and reverse time for $y > 0$). Now, $\boldsymbol{u}^{U/S}$ represents the correct eigenvector projection onto section coordinates (e.g., $(x, \dot{x})$ for $\Sigma : y = 0$). The advection algorithm computes initial steps by employing only the projected coordinates of $\boldsymbol{u}^{U/S}$ with the appropriate Jacobi constant value thereby enforcing that the invariant manifold is actually at the *exact* C value as the base periodic orbit. (Note that the DGE method, discussed in Section 4.3, generates manifold arcs at a similar Jacobi constant but never truly at the same C value as the periodic orbit.) The schematic in Figure 7.18 demonstrates the process of creating the on-map eigenvector, $\boldsymbol{u}^{S\pm}$, but the process is similar for both $\boldsymbol{u}^U$ and $\boldsymbol{u}^S$.

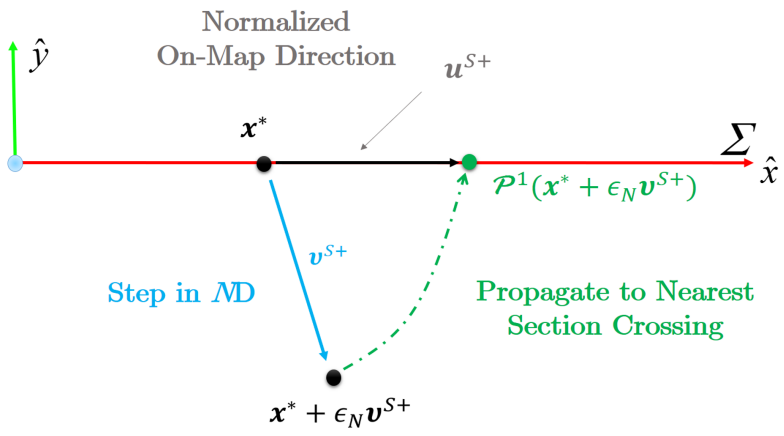

Figure 7.18. Construction of the normalized on-section eigenvector $\boldsymbol{u}^{S+}$ representing the invariant manifold W^S basis on the Poincaré section.

With the on-section eigenvector $\boldsymbol{u}^{U/S}$ located, the ManCurve algorithm for PMATE begins by taking an initial step onto this on-section projection through an empirically defined function to determine the appropriate step size. Normally, a small step is desired such that the linear approximation is valid; small steps are exceedingly important for strong saddle-type periodic orbits with large stability indexes. Yet, small steps onto manifolds emanating from periodic orbits with small $\lambda_{\max}$ (i.e., weak-strength saddles) propagate very slowly downstream because of the exceptionally weak exponential growth rate away from fixed points. So for weak-strength saddles, it is vital to take the largest step possible to circumvent slow downstream growth. Thus, the step size should be proportional to the strength of the saddle under analysis. Let ϵ_w represent the nondimensional step distance onto $\boldsymbol{u}^{U/S}$ to compute the first point of a manifold (i.e., $\boldsymbol{\phi}_1 = \boldsymbol{\phi}_0 \pm \epsilon_w \boldsymbol{u}^{U/S}$). Note that ϵ_w and ϵ_N are completely different quantities. The step ϵ_w is formulated as a function of the largest Lyapunov exponent, $\lambda_{\max}$, and the system of interest determined by μ. This adaptive step function is constructed in a piecewise fashion through the expression

$$\epsilon_w(\mu, \lambda_{\max}) = \begin{cases} a_\mu \left(1 - \exp\left(2\frac{150-\lambda_{\max}}{1-\lambda_{\max}}\right)\right) + b_\mu & \text{if } \lambda_{\max} \leq 150 \\ c_\mu \left(1 - \exp\left(\frac{150-\lambda_{\max}}{200}\right)\right) + d_\mu & \text{otherwise} \end{cases} \tag{7.47}$$

where the coefficients a_μ, b_μ, c_μ, and d_μ are determined by the current μ value. Let z_μ stand as a scalar function of the Earth-Moon and Saturn-Enceladus gravity parameters (μ_{EM} and μ_{SEnc}, respectively) through

$$z_\mu = \frac{\ln(\mu) - \ln(\mu_{EM})}{\ln(\mu_{SEnc}) - \ln(\mu_{EM})}. \tag{7.48}$$

The coefficients are derived empirically for a given μ with the interpolation set

$$a_\mu = (a_1 - a_0)z_\mu + a_0 \tag{7.49}$$

$$b_\mu = (b_1 - b_0)z_\mu + b_0 \tag{7.50}$$

$$c_\mu = (c_1 - c_0)z_\mu + c_0 \tag{7.51}$$

$$d_\mu = (d_1 - d_0)z_\mu + d_0 \tag{7.52}$$

where a_i, b_i, c_i, and d_i are constants listed in Table 7.3. The adaptive step function in Equation (7.47) defines a larger map perturbation for weak saddles and smaller map perturbations for stronger saddles. In addition, Equation (7.47) takes the system of interest into account to scale analysis for smaller regions of interest such as near Enceladus vicinity in the Saturn-Enceladus system versus broader stretching manifolds in the Earth-Moon problem.

System	Coeff.	Value (NonDim)
EM	a_0	4.99×10^{-5}
	b_0	1.00×10^{-7}
	c_0	-0.99×10^{-7}
	d_0	1.00×10^{-7}
SEnc	a_1	1.999×10^{-5}
	b_1	1.00×10^{-8}
	c_1	-0.99×10^{-8}
	d_1	1.00×10^{-8}

Table 7.3 Coefficient values for the manifold initial step function in Equation (7.47).

7.6.3 Curve-Refinement Criteria

Testing conditions on downstream invariant manifold states ensure the construction of a smooth 1D curve on the Poincaré section baring known discontinuities. Based on the same testing criteria proposed by England et al. [13], curve-refinement tests compare two subsequent downstream points $\boldsymbol{\phi}_k$ and $\boldsymbol{\phi}_{k+1}$ that are also labeled as points A and B for convenience. Smoothness criteria is also determined through the geometric arrangement of segment $\overline{AB}$ and an adjacent segment. The downstream testing segment and adjacent segments formed by states $\boldsymbol{\phi}_{k-1}$ and $\boldsymbol{\phi}_{k+2}$ (labeled as points C and D, respectively) are displayed with relevant smoothness parameters in Figure 7.19. Curve-refinement heuristic tests determine if downstream manifold segment $\overline{AB}$ (or the testing segment) is classified as sufficiently smooth compared to adjacent downstream segments. The following criteria utilize segment lengths and angles between segments to signify if upstream subdivision is required for enhanced refinement:

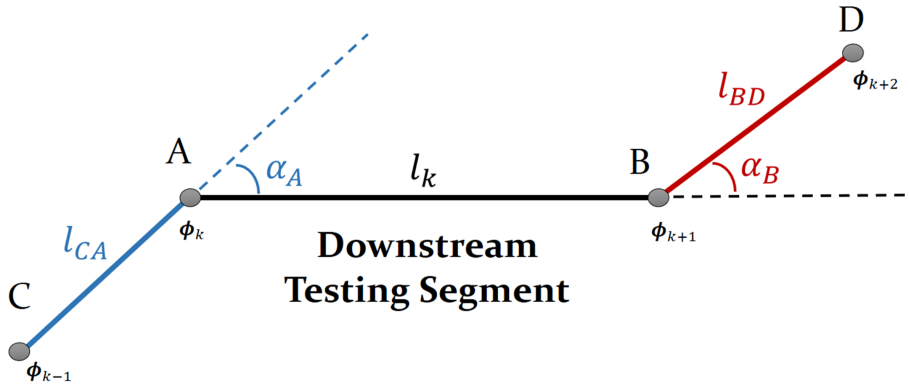

Figure 7.19. A downstream manifold testing segment $\overline{\boldsymbol{\phi}_k\boldsymbol{\phi}_{k+1}}$ and the neighboring segments. Angles and distances determine if the testing segment forms a smooth 1D curve with neighboring segments during curve-refinement.

1. *Downstream Separation* Let the on-section distance between points A and B be represented by l_k as shown in Figure 7.19. If A and B are too close together considering the heuristic minimum map distance parameter $\Delta_{\min}$ through the test

$$l_k \leq \Delta_{\min}, \tag{7.53}$$

then the manifold segment is considered smooth to prevent any unnecessary subdivision while generating points along a very sharp turn. Downstream points must also be close enough together, i.e., satisfying

$$l_k \leq \Delta_{\max} \tag{7.54}$$

where $\Delta_{\max}$ is a maximal distance parameter supplied by the user. Suggested values of $\Delta_{\min}$ and $\Delta_{\max}$ for various CRTBP appear in Table 7.4. Since velocity tends to approach infinity near primary locations in the CRTBP, it is recommended to only apply the maximal separation condition within a limited $\dot{x}$ bounds (such as ± 3.2 km/s).

2. *Valid Neighbors* The remaining curve-refinement tests require a valid neighboring segment to determine smoothness criteria. First, the adjacent segment must not surround a downstream transversality violation since a known discontinuity resides along such a segment. PMATE is also unable to use the neighboring segment if it vastly differs in length compared to $\overline{AB}$. Whether utilizing the previous downstream segment $\overline{AC}$ or the next downstream segment $\overline{BD}$, the relative segment length comparison

$$\frac{|l_k - l_{AC}|}{l_{AC}} < 10^3 \text{ or } \frac{|l_k - l_{BD}|}{l_{BD}} < 10^3 \tag{7.55}$$

must hold. If an adjacent segment fails Equation (7.55) or possesses a downstream transversality violation, the offending segment is marked as invalid. The preceding segment $\overline{AC}$ is typically attempted first within the ManCurve algorithm. When $\overline{AC}$ is invalid, the proceeding segment $\overline{BD}$ is then examined for validity in curve-refinement testing. If both $\overline{AC}$ and $\overline{BD}$ are invalid, subdivision is forced on the working segment.

3. *Angle Smoothness* Keeping the angle between segments small prevents a jagged depiction of the invariant manifold curve on the Poincaré section. The angle between adjacent segments (α_A or α_B depending on the employed adjacent segment as shown in Figure 7.19) is simply computed via a dot product. The angular constraint

$$\alpha_A \leq \alpha_{\max} \text{ or } \alpha_B \leq \alpha_{\max} \tag{7.56}$$

limits the angle between adjacent segments to a maximum angle parameter $\alpha_{\max}$. If the angle is too big, subdivision occurs on the working segment in order to generate more downstream manifold points to reduce the values of α_A and α_B.

4. *Arc Length Separation* The final refinement criteria confines the generation of points with respect to the curvature of the 1D streamsurface projection on the Poincaré section [13]. The arc length combines the length of a segment and the angular deviation with respect to a neighboring segment. The constraints on downstream manifold arc length are signified by

$$(l_k \alpha_A) \leq (\Delta\alpha)_{\max} \text{ or } (l_k \alpha_B) \leq (\Delta\alpha)_{\max} \tag{7.57}$$

where the parameter $(\Delta\alpha)_{\max}$ is specified by the user. The arc length distance constraint safeguards ManCurve from employing an invalid working segment where interpolation produces erroneous approximations of manifold points [13, 14].

Suggested values for the heuristic parameters in various systems are listed in Table 7.4. Note that curve smoothness cannot be evaluated if a transversality violation is detected between *both* $\overline{CA}$ and $\overline{BD}$; if such a case occurs, subdivision is automatically triggered on the working segment unless already at the minimum parameter separation $\Delta\tau_{\min}$.

7.6.4 Stopping Criteria

The ending conditions for manifold generation via curve-refinement employ the previous methods in topology extraction but are also adapted to dynamical behavior of invariant manifolds in the CRTBP. The global 1D invariant manifold advection method by England

et al. (ManBVP) halts only when a total accumulated arc length is achieved [13]. Although this single stopping condition suffices for demonstration purposes in a general autonomous system, large arc lengths are collected on manifold asymptotes near singularities in the CRTBP model, making manifold advection quit long before gathering a broad sampling of arc possibilities emanating from the entire periodic orbit. The investigation by Tricoche et al. highlights that generated manifolds encounter other saddle points in the same island chain (i.e., saddle loops) and are detected as part of that investigation [14]. Saddle-loops are prevalent in the CRTBP, especially at KAM boundaries, and so, a saddle-loop exit condition must also be incorporated for PMATE. Describing the global spread of a manifold is also an important factor for trajectory planning. Advection procedures should continue until some measure of global manifold population is accomplished. Thus, three stopping criteria for the ManCurve algorithm are formulated from these studies with the addition of an adaptive data structure for processing downstream advection.

The first stopping criteria tracks a practical measure for spacecraft trajectory planning via an adaptive number of returns for all invariant manifold arcs emanating from a given orbit. The ManCurve algorithm essentially grows downstream segments from an upstream segment, creating a parent-child relationship between upstream and downstream segments. The spawning of child segments from a parent segment represents a transition of depth level, d_w, in an interconnected tree of manifold segments. The ManCurve method advects the initial segment (Segment 0 at $d_w = 0$) to generate new downstream segments all at $\overline{p}$ map iterates from the initial segment. These new downstream segments exist at an incremented tree depth, or $d_w = 1$, indicating that segments at $d_w = 1$ describe the overall spread of Segment 0 for $\overline{p}$ map iterations. The downstream global progression of Segment 0 is completed by advecting all segments at a current depth to the next thereby portraying the entire spread of the initial segment downstream. ManCurve then caps the studied manifold progression by continuing the advection procedure until a specified maximum tree depth $d_{w,\max} = 5$. The resulting invariant manifold representation then encompasses the total downstream spread of the initial segment for a practical propagation length ($d_{w,\max} \cdot \overline{p}$ map iterates).

The event of a massive subdivision triggers the second stopping condition. Since PMATE considers the entire spread of downstream segments, an upstream segment with numerous

refinement steps overloads data structures and computation time as the downstream mappings disperse on the Poincaré section. If an upstream segment spawns over 1000 new segments (chosen arbitrarily), then ManCurve has captured a sufficient depiction of invariant manifold behavior and is prompted to exit even if not at maximum depth. This prevents the exponential growth of advection executions while still delivering a rich description of an invariant manifold projection on the Poincaré section.

The final stopping condition observes simultaneous advection of manifolds from the same periodic orbit for the detection of saddle-loops. Saddle-loops are present throughout the dynamical regime, and it is important to locate such structures to prohibit saddle advection through known linkages. Newly-generated downstream segments from both the stable and unstable manifolds of the *same periodic orbit* (as in all the fixed points of the orbit) are compared to detect if a tangential segment crossing exists. This is easily implemented through simple line-segment intersection testing procedures [77, 78]. Line-segment intersection testing identifies a saddle-loop condition if a pair of stable and unstable manifold segments are either

1. Collinear with overlap,
2. Intersecting with a small incidence angle ($< 3^\circ$),
3. Parallel with a small Poincaré section (or phase space) distance between segments ($< 10^{-6}$ nondimensional map-coordinate distance),
4. Not intersecting but with a small angle between segments ($< 3^\circ$) and a small Poincaré section (or phase space) distance between segments ($< 10^{-6}$ nondimensional map-coordinate distance).

These conditions address numerical difficulty characterizing manifold segment intersections at double precision where differences between the true nonlinear manifold and the linear initial seeding perpetuate downstream [61, 78]. Note, invariant manifolds in the CRTBP rarely trigger the saddle-loop stopping condition outside of the KAM boundaries.

7.6.5 Efficiency and Screening Computations

The algorithm execution for manifold extraction is purposefully crafted to enhance overall computational efficiency. Every fixed point of a periodic orbit submits 4 manifolds for advection, representing the 2 step directions for both W^U and W^S. Each manifold advection procedure is executed simultaneously. The bottleneck of the entire ManCurve algorithm, though, resides with the computational effort exerted with Poincaré map calls, so it is important to formulate the execution setup to exploit the independent nature of Poincaré mappings. Upstream segments generate a set of mappings for each round of subdivision. These map calls are gathered as tasks for an overall job queue alongside mapping calls submitted by all other advection processes. Computation threads then evaluate the mappings in parallel and return simulation results for refinement testing once all mappings for the current round are complete. This tasking queue ensures parallel analysis for all mapping calls and expedites the overall execution of manifold extraction. The mirror theorem–providing symmetry in problems like the CRTBP–can be employed to limit the number of computations, but the mirror image of an invariant manifold for asymmetric periodic orbits across the x-axis is not associated with the same periodic orbit. In fact, the mirror image of manifolds from asymmetric orbits commute to the symmetric partner orbit, which can be complicated to track within fixed point and manifold data structures. Another difficulty with applying the mirror theorem directly is that the resulting curves are not always consistent between stable and unstable manifolds due to numerical sensitivities and heuristic testing values. Thus, the mirror theorem is not applied directly in this investigation yet should be considered for future development. Another way to accelerate the extraction of manifolds is to pre-screen for potentially impractical structures for spaceflight, i.e., periodic orbits with exceptionally high instabilities. A threshold cutoff is established on stability index magnitude at $|\nu_{SI}| > 10^6$ for manifold extraction. In addition, more screening (or a lower $|\nu_{SI}|$ cutoff) reduces the overall workload required by PMATE and is often implemented in practice. Suggested thresholds are listed in Table 7.4. As a cautionary remark, the adaptive nature of manifold advection via curve refinement garners an enormous amount of map calls even with the suggested sifting procedures. Consequently, manifold extraction

in PMATE is implemented as a stand-alone program with the autonomously extracted fixed points of earlier PMATE phases as input.

Although the parameters $l_{\min}$ (from cell edges) and $u_{\min}$ (regulating upstream manifold segment subdivisions) are fundamentally equivalent, a lower bound is necessary for $u_{\min}$ as a transfer stipulation for realistic spaceflight. Error in real-world devices such as sensors and engines translate into limitations on state acquisition and deliverable maneuvers; if a particular transfer requires that the position and velocity match a desired state to 10^{-6} m and 10^{-6} m/s, for example, that trajectory is not necessarily flight worthy as many instruments cannot deliver that level of accuracy [79, 80]. Spacecraft state determination outside of low Earth orbits is limited to an accuracy of 3 km for position and 0.1 mm/s for velocity based on measurement error of standard capabilities [81]. Also, higher-fidelity modeling with more realistic effects perturbs trajectories that utilize exceptionally sensitive dynamical structures. Therefore, manifold trajectories that require high-accuracy are screened out by selecting an appropriate $u_{\min}$ at 2×10^{-5} (nondimensional map displacement) for the Earth-Moon system, which is equivalent to 2.05 cm/s for velocity and 7.69 km for position. This $u_{\min}$ value adds a buffer for perturbations caused by higher-fidelity models and disallows the evaluation of arcs that need unattainable accuracy. Moreover, the value of $u_{\min}$ changes based on the CRTBP system considered because of different characteristic parameters, and thus, different $u_{\min}$ quantities are employed for similar accuracy limitations in smaller μ-value systems such as the ST and SEnc systems. The linear parameter form of $u_{\min}$, or $\Delta\tau_{\min}$, is computed as an adaptive measure based on the current working segment by utilizing the current segment length, l_w, as

$$\Delta\tau_{\min} = u_{\min}/l_w. \tag{7.58}$$

Such an expression uniquely determines a maximal level of subdivision for an arbitrary working segment. A $\Delta\tau_{\min} > 1$ indicates that only the initial midpoint subdivision of a segment is evaluated. Drastically changing dynamics in the near vicinity of a fixed point may cause the inability to resolve downstream curve smoothness while subdividing the first few working segments employing the adaptive $\Delta\tau_{\min}$ parameter. If such difficulty arises, the troublesome segment is restarted with a *fixed* $\Delta\tau_{\min} = 0.01$ to encourage early generation of

new segments and then reverted back to Equation (7.58) when PMATE finishes advecting the problematic upstream segment.

System	$u_{\min}$	$\Delta_{\min}$	$\Delta_{\max}$	$\alpha_{\max}$	$(\Delta\alpha)_{\max}$	$\lvert\nu_{SI}\rvert_{\max}$
EM	2×10^{-5}	1×10^{-5}	0.1	0.3 (17.2°)	0.001	2.5×10^{3}
ST	4×10^{-6}	1×10^{-6}	0.05	0.1 (5.7°)	0.001	2.5×10^{3}
SEnc	1×10^{-6}	1×10^{-6}	0.05	0.1 (5.7°)	0.001	5.0×10^{3}

Table 7.4 Heuristic parameters employed for invariant manifold advection in the indicated CRTBP systems. Phase space displacement values are listed in nondimensional units.

8. INTERACTIVE DESIGN FOUNDATION EMPLOYING POINCARÉ MAP TOPOLOGY

Autonomous Poincaré map topology extraction delivers the base-level data describing the dynamical framework in the CRTBP, but capabilities to interact with map topology data provide access to the natural pathways of the system. The format of invariant manifold advection encourages arc reconstruction by user selection and even the interactive definition of map-based maneuvers for transfer design.

8.1 Selecting Fixed Points

Propagation and display of the periodic orbit associated with a particular fixed point is often useful during design construction. With the data extracted from PMATE, a single data object stores each sequence of fixed points that comprise a periodic orbit as well as associated information such as integer period (p), time-period (T), the eigenvalues and eigenvectors of the monodromy matrix, and stability indexes. Fixed points are typically visualized on the Poincaré section within a graphical scene as simple circular markers or spheres that are either colored by stability type (e.g., green for stable and red for unstable) or with a single color representing the same periodic orbit. Selecting a fixed point and extracting the associated periodic orbit works much like map interaction; if the mouse pointer enters a fixed point graphical object (determined by ray cast intersection tests), the fixed point is immediately converted to a state and propagated to render a display of the periodic orbit within the scene. Unfortunately, employing the fixed point graphical object location or the picked point creates an unreliable starting state for propagation. Graphics primitives and other scene objects (including scene intersection retrieval with rays) are typically all represented as single precision values to conserve memory during scene construction [69,70]. This is a reasonable downgrade in precision because two objects that are only displaced by a double precision difference are virtually indistinguishable without a significantly zoomed visualization [69]. Propagating an initial state to form a periodic orbit, however, requires

more digits of precision for the initial state components than single precision delivers. Thus, a simple hash table (key-value pairing) is employed that links the index of the graphical objects representing fixed points (the key) to the actual fixed point within the PMATE data structure (the value). When selection occurs in the scene, the appropriate double precision initial state is derived by evaluating the appropriate data structure index through the hash table.

8.2 Extracting Discrete Arcs on Invariant Manifolds

Design practices exploiting Poincaré map topology require the ability to reconstruct any arbitrarily selected arc from the autonomously extracted invariant manifolds. Invariant manifold arc extraction seeks to either reconstruct the *upstream* pathway to a current selection point or the downstream pathway beyond the selection state. Constructing the downstream destination of a selection point is simply a downstream simulation of the selected point (i.e., forward-time for W^U and reverse-time for W^S). Upstream propagation, on the other hand, defines how the trajectory progresses from the base periodic orbit downstream to arrive at the selected manifold state. In either case, a discrete arc at a user-selected invariant manifold state on the Poincaré section is extracted by first isolating which manifold and segment correlates with an intended mouse-intersection location from the visualization. Recall that PMATE employs the ManCurve algorithm to construct invariant manifolds as 1D curve representations on the Poincaré section. The 1D invariant manifold curves are then represented as linear segments connecting adjacent map states ($\boldsymbol{\phi}_i$). As stated in Sections 6.2 and 8.1, utilizing the Poincaré map interaction tool to select manifold states is ineffective since the returned state is a single precision representation like the intersected graphics primitives. Extraction of the double precision selection state enlists a hash table in a very similar fashion to fixed point selection in Section 8.1. As illustrated in Figure 8.1, the selection of a Poincaré section location of either the stable or unstable invariant manifold returns a picked point at the interaction ray intersection and a line segment pertaining to the manifold graphical object. A line index identifies the particular selected line, and the particular line segment selected is identified by a part index that describes the line segment location in the set of segments comprising the graphical

line. The hash table matches line-part index pairs to a manifold index representing each advected 1D manifold curve and a manifold segment index for the selected segment within the Poincaré map topology skeleton data set. Converting the line segment selection within the visualization to a manifold-segment index pairing then identifies the source manifold and the originating periodic orbit for additional arc-extraction procedures.

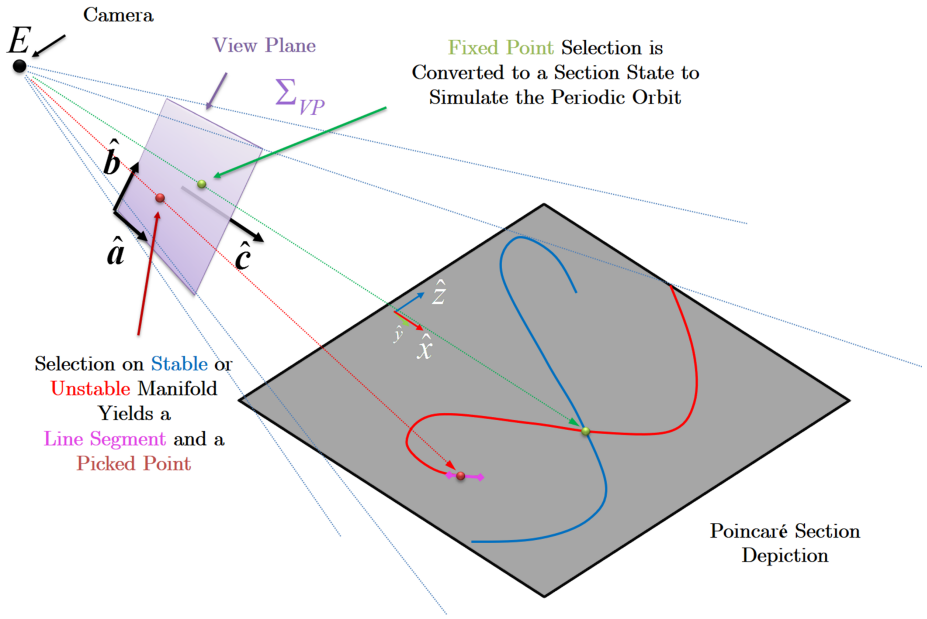

Figure 8.1. Schematic of selecting fixed points or invariant manifolds from PMATE data on a Poincaré section within a visual environment.

Extraction of a selected arc continues by determining the state along the selected invariant manifold segment. Let the user-selected manifold segment be represented as Segment c with $\boldsymbol{x}_{pp}$ symbolizing the picked point state on the Poincaré section. The manifold states $\boldsymbol{\phi}_k$ and $\boldsymbol{\phi}_{k+1}$ represent the end points of Segment c (and compute the vector $\boldsymbol{c} = \boldsymbol{\phi}_{k+1} - \boldsymbol{\phi}_k$)as shown by the schematic of manifold point selection in Figure 8.2. The desired arc for selection intersects the Poincaré section at the state $\boldsymbol{x}_c$. Again, linear parametrization defines points along a manifold segment in a similar manner to the manifold advection algorithm in Equation (7.45), so $\boldsymbol{x}_c$ occurs at a linear sampling distance u between $\boldsymbol{\phi}_k$ and $\boldsymbol{\phi}_{k+1}$ with $u \in [0, 1]$. Due to the employed numerical precision for the graphical interface, it is possible that the returned picked point $\boldsymbol{x}_{pp}$ is slightly off of the intended Segment c (shown as the exaggerated distance between the purple point and the red segment in Figure 8.2). Pre-

venting such a case during the definition of $\boldsymbol{x}_c$, the picked point is projected onto Segment c to form the vector $\boldsymbol{\zeta}$ (orange vector in Figure 8.2) through the expression

$$\boldsymbol{\zeta} = ((\boldsymbol{x}_{pp} - \boldsymbol{\phi}_k) \cdot \boldsymbol{c}) \frac{\boldsymbol{c}}{\|\boldsymbol{c}\|}. \tag{8.1}$$

The user-specified selection state on the manifold now follows

$$\boldsymbol{x}_c(u) = \boldsymbol{\phi}_k + \boldsymbol{\zeta} = (1-u)\boldsymbol{\phi}_k + u\boldsymbol{\phi}_{k+1}. \tag{8.2}$$

One can compute the value of the linear parameter u by rearranging Equation 8.2 or through the simple ratio

$$u = \frac{\|\boldsymbol{\zeta}\|}{\|\boldsymbol{c}\|}. \tag{8.3}$$

The projection of the picked point onto the selected manifold segment culminates in the definition of the section state $\boldsymbol{x}_c(u)$ for arc simulation.

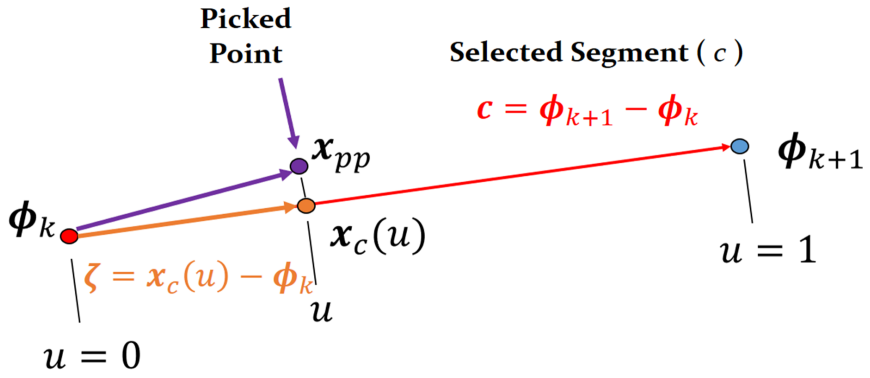

Figure 8.2. The picked point, $\boldsymbol{x}_{pp}$, and the resulting extraction state ($\boldsymbol{x}_c(u)$) along a selected manifold segment.

Even with the user-selected invariant manifold state, additional adjustments are necessary to reproduce the arc pertaining to the upstream pathway of the selected state. Constructing the downstream destination is actually a straightforward downstream simulation of $\boldsymbol{x}_c(u)$ (i.e., forward-time for W^U and reverse-time for W^S). Conversely, propagation of the extracted state $\boldsymbol{x}_c(u)$ upstream (i.e., forward-time for W^S and reverse-time for W^U) often fails because of the flow-dividing nature of the invariant manifolds [20]. Both W^S and

W^U represent a ridge separating local upstream flow behavior. Such a ridge is analogous to the summits of a mountain range; a slight deviation off the ridge produces a rapid departure away from the invariant manifold curve during an upstream propagation, similar to sliding down the mountain side [20, 82]. The user-selected projection $\boldsymbol{x}_c(u)$ is computed with numerically defined states along the invariant manifold, so numerical errors (roundoff and truncation) may induce a subtle deviation leading to an exponential departure from the true invariant manifold through upstream propagation. As an illustration, the forward mapping employed to generate the $\boldsymbol{\Delta}$ field in Figures 7.6(a) and 7.8 also represents the upstream mapping direction for the stable manifold. Note that all the $\boldsymbol{\Delta}$ vectors in the near vicinity of the stable manifold point away from the stable manifold itself, simulating the slide down the invariant manifold ridges during upstream propagation.

Upstream manifold arc reconstruction circumvents the challenges associated with propagating supposed manifold arcs upstream with a clever data structure format resulting from the manifold advection procedure. The ManCurve algorithm (Section 7.6) advects states sampled from an upstream manifold segment to create a group of new downstream segments through the Poincaré map; such a transaction inherently links upstream segments as the parents of spawned downstream segments (or child segments). This parent-child relationship of invariant manifold segments via the Poincaré map allows for the organization of segment data into a *manifold segment tree*. To illustrate, sample manifold segments near the start of the advection procedure are arranged as a staircase schematic indicating depth levels (d_w) as shown in Figure 8.3; each step down symbolizes the downstream progression to the next group of segments at after $\overline{p}$ map iterates. As shown by Figure 8.3, states sam-

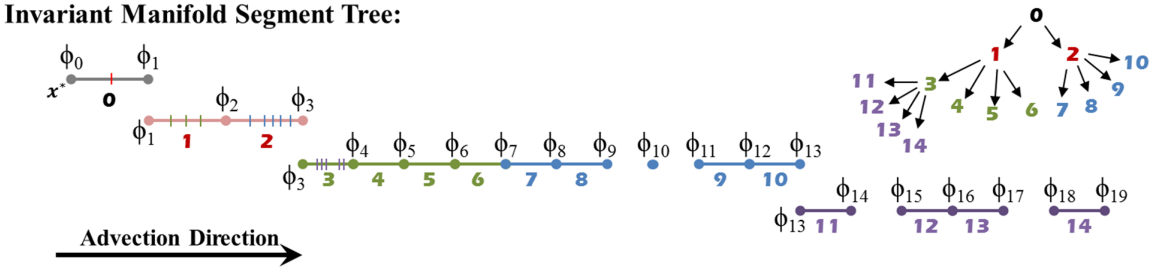

Figure 8.3. As the invariant manifolds are progressed via curve-refinement, the spawning of new manifold segments generates a tree structure that can be employed for accessing data.

pled from gray Segment 0 map downstream to form Segments 1 and 2 (red), subdivision on Segment 1 creates the green Segments 3-6, sampling from Segment 2 spawns the blue Segments 7-10, advecting Segment 3 initiates the next depth level with the purple Segments 11-14, and so forth. This generation behavior is outlined by the node tree diagram also included in Figure 8.3.

The manifold segment tree links an arbitrarily selected manifold state ($\boldsymbol{x}_c(u)$) on a known manifold segment back to the initial manifold segment (Segment 0 or the root segment) to trace out the upstream arc. The relationship between a user-selected child segment (c) and the corresponding parent segment, entitled Segment w, is conveyed in Figure 8.4. The linear parameter τ signifies a linearly sampled state on the parent segment, and the values τ_0 and τ_1 locate the Segment w states $\boldsymbol{x}_w(\tau_0)$ and $\boldsymbol{x}_w(\tau_1)$, respectively. The mappings of $\boldsymbol{x}_w(\tau_0)$ and $\boldsymbol{x}_w(\tau_1)$ are previously employed by manifold advection procedures to produce the endpoints of Segment c. Since the user-selected point $\boldsymbol{x}_c(u)$ resides between , a corresponding initial state exists on the parent segment between $\boldsymbol{x}_w(\tau_0)$ and $\boldsymbol{x}_w(\tau_1)$ that maps downstream to $\boldsymbol{x}_c(u)$. Let $\boldsymbol{x}_w(\tau_u)$ represent the upstream mapping of $\boldsymbol{x}_c(u)$, or namely

$$\mathcal{P}^{\overline{p}}(\boldsymbol{x}_w(\tau_u)) = \boldsymbol{x}_c(u), \tag{8.4}$$

such that the linear parameter τ_u locates $\boldsymbol{x}_w(\tau_u)$ on Segment w ($\tau_0 \leq \tau_u \leq \tau_1$). If the parent τ value, or source value, is stored with every manifold point, then the source linear parameter of $\boldsymbol{x}_c(u)$ is easily interpolated through

$$\tau_u = (1-u)\tau_0 + u\tau_1. \tag{8.5}$$

The upstream mapping of the user-selected state $\boldsymbol{x}_c(u)$ is then extracted for a single tree-depth level ($-\overline{p}$ iterates) by linear interpolation as well, i.e.,

$$\boldsymbol{x}_w(\tau_u) = (1-u)\boldsymbol{x}_w(\tau_0) + u\boldsymbol{x}_w(\tau_1). \tag{8.6}$$

This expression backtracks $\boldsymbol{x}_c(u)$ to an upstream node *without* numerical simulation. Reconstructing the full set of upstream nodes to Segment 0 is completed by compounding the procedure, i.e., traversing the manifold segment tree back to the root node by recur-

sively applying Equation 8.6. Thus, the upstream pathway is now formed by the upstream nodes *without* propagation, which is extremely powerful for interactive analysis since tree-traversal operations combined with linear interpolation occur at real-time speeds. A similar procedure can also be implemented to reconstruct iterates downstream of a selection if downstream nodes exist in the manifold segment tree. If the entire upstream trajectory from the fixed point to the user-selected point is required, the downstream mappings (e.g., $\mathcal{P}^{\overline{p}}(\boldsymbol{x}_w(\tau_u))$) supply a reliable numerical simulation to return the intermediate trajectory states between the parent and child manifold segments as such downstream simulations are employed during the construction of the 1D invariant manifold curves. The complete upstream arc is reconstructed by numerically simulating each upstream node to the subsequent downstream level. Propagation in this manner essentially resets the accumulated deviation from the manifold every $\overline{p}$ iterates; any discontinuities in the extracted arc are easily fixed with differential corrections when necessary. Note that it is assumed the root segment is small enough that tracing the upstream history back to Segment 0 is essentially equivalent to reaching the periodic orbit at the originating fixed point $\boldsymbol{\phi}_0$.

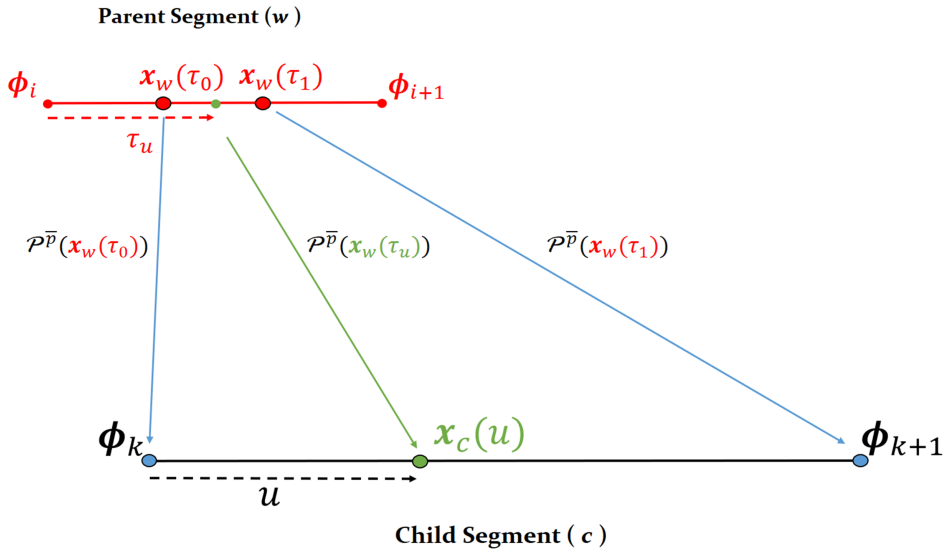

Figure 8.4. Tracing the upstream history of a child segment to a parent segment along the invariant manifold data tree.

8.2.1 Tracking Relevant Quantities

The invariant manifold tree used to organize the manifold information is also deployed to evaluate different data products along the 1D invariant manifold curve. Quantities that are relevant to a design of interest including closest approach to a singularity and time of flight are already considered during the advection algorithm to heuristically test for transversality violations; storing this germane design data at the invariant manifold states within the manifold segment tree permits the quick retrieval of transfer information without actually evaluating the entire manifold trajectory through propagation. For example, the closest approach distance to singularity $s = 1, 2$, represented as $CA_{s,w}(\tau)$ for a downstream propagation from Segment w, is a tracked quantity during the ManCurve algorithm. At a user-selected state $\boldsymbol{x}_c(u)$, the closest approach distance pertaining to the mapping $\mathcal{P}^{\overline{p}}(\boldsymbol{x}_w(\tau_u))$ (ending at $\boldsymbol{x}_c(u)$) is approximated through

$$CA_{s,w}(\tau_u) = (1-u)CA_{s,w}(\tau_0) + uCA_{s,w}(\tau_1). \tag{8.7}$$

The minimum CA_s for the entire upstream arc of $\boldsymbol{x}_c(u)$ is recursively evaluated through

$$CA_s(\boldsymbol{x}_c(u)) = \min_{i=c\mapsto 0} CA_{s,i}(\tau_u) \tag{8.8}$$

where i symbolizes each depth level as the tree is traversed back to the root segment. In a similar manner, the time of flight for the upstream arc, or Δt, associated with the user-selection is approximated as the sum Poincaré mappings at each depth level. Let $\Delta t_w(\tau)$ represent the flight time required to complete the Poincaré mapping $\mathcal{P}^{\overline{p}}(\boldsymbol{x}_w(\tau))$ that maps a state from a parent Segment w to child Segment c state $\boldsymbol{x}_c(u)$. Each parent-to-child flight duration is approximated via

$$\Delta t_w(\tau_u) = (1-u)\Delta t_w(\tau_0) + u\Delta t_w(\tau_1), \tag{8.9}$$

and the overall flight time is summed by traversing the depth layers up to the top of the manifold tree, or

$$\Delta t(\boldsymbol{x}_c(u)) = \sum_{i=c\mapsto 0} \Delta t_w(\tau_u). \tag{8.10}$$

Tracked information greatly assists the interactive design process exploiting Poincaré map topology as designers examine the trade space of available arcs for a minimal transfer flight time or for invalid transfers that get too close to a celestial body. The ability to track data within the manifold segment tree adds to the interactive visual analytics design platform as invariant manifolds can now be colored with germane design quantities or perhaps even filtered out of the visualization based on design constraints.

8.2.2 Interactive Definition of Heteroclinic and Homoclinic Connections

With the capability to reconstruct an upstream arc from an arbitrary manifold state, the extraction of heteroclinic ($\mathcal{H}_c$) and homoclinic ($\mathcal{H}_o$) connections is now a trivial matter. If the interaction ray intersects *both* a stable and an unstable invariant manifold, the selection point then represents a discrete trajectory connection between the two manifold types as well as a natural pathway between the two base periodic orbits. For clarity, the selection point is typically colored green when a hover detects a $\mathcal{H}_c$ or $\mathcal{H}_o$. Time of flight between for the whole connection is collected as the summed contribution of the two arcs back upstream to Segment 0 without propagation. The approximated time of flight for a selected transfer can be easily shown as text next to the green connection point. Numerous free-connection possibilities exist between saddle-type orbits, but the ability to examine data allows a designer to quickly evaluate the trade space for a superior option. Recall, the flight time obtained through tree-traversal is only an estimated time of flight based on interpolated data, yet a true transfer time for the selected $\mathcal{H}_c$ or $\mathcal{H}_o$ is derived by reconstructing the full upstream trajectories for the associated W^U and W^S selection points.

8.2.3 Defining Practical Arrival (or Departure) Points

A practical entrance point (or departure point) is established for manifold arcs and connections. With upstream arc reconstruction, tracing a user-selected manifold arc closer to the root segment generates a geometry that appears like many revolutions of the periodic orbit. Due to the asymptotic nature of invariant manifolds with respect to the base periodic orbit, upstream arcs near the highest segments in the manifold segment tree are *not* revolu-

tions of the periodic orbit by definition; however, the upstream portions do closely resemble the periodic orbit. Even though the spacecraft is still on the invariant manifold in transit, the asymptotic approach path closely mimics the intended periodic orbit such that operations and scientific measurements may start long before reaching the manifold termination segment (Segment 0 upstream). For this investigation, the arrival (or departure) condition of an extracted invariant manifold arc is set via an arbitrary positional threshold from a manifold arc state that is geometrically similar to the base periodic orbit. Let the 6D state $\boldsymbol{y}_w(t_j)$ represent a state on a user-selected invariant manifold arc at time t_j with $\boldsymbol{r}_w(t_j)$ and $\boldsymbol{v}_w(t_j)$ symbolizing the position and velocity vectors, respectively. Also, define $\boldsymbol{y}_o$ as a state on the base periodic orbit for said manifold at periodic orbit time t_i with respective position vector $\boldsymbol{r}_o(t_i)$ and velocity vector $\boldsymbol{v}_o(t_i)$. A geometrically similar point to $\boldsymbol{y}_w(t_j)$ is labeled $\tilde{\boldsymbol{y}}_o$ occurring at the base periodic orbit time $\tilde{t}$ that is a function of t_j. Again, $\tilde{\boldsymbol{y}}_o(t_j)$ possesses the respective position and velocity vectors $\tilde{\boldsymbol{r}}_o(t_j)$ and $\tilde{\boldsymbol{v}}_o(t_j)$, respectively. The geometrically similar point to manifold arc state $\boldsymbol{y}_w(t_j)$ resides at the periodic orbit state where the tangent vectors of the two trajectories are the most similar; in other words, the geometric match to a manifold state at time t_j is at the periodic orbit state yielding the minimum cross product magnitude

$$\min_{t_i} \|\hat{v}_w(t_j) \times \hat{v}_o(t_i)\| \Rightarrow \tilde{t} \tag{8.11}$$

where $\hat{v}_w(t_j)$ and $\hat{v}_o(t_i)$ represent the unit velocity directions at the selected manifold state and orbit state, respectively. Note that $\tilde{t}$ is a function of t_j and is determined by employing Equation (8.11) for every point on the user-selected manifold arc. The practical arrival (or departure) location is then determined as the manifold arc state that surpasses a threshold distance (or the parameter δ_W) away from the geometrically similar point on the base periodic orbit. In algorithm form, this point is computed by looping through manifold arc time (t_j) starting from the end of an approach arc or from the beginning of a departure arc to find the first zero-crossing of the position threshold function

$$f(\boldsymbol{y}_w(t_j)) = \|\boldsymbol{r}_w(t_j) - \tilde{\boldsymbol{r}}_o(t_j)\| - \delta_W, \tag{8.12}$$

comparing the positional difference between a manifold state and the correlated geometrically similar point on the periodic orbit. Thus, the orbit arrival (or departure) point for an invariant manifold arc is achieved when the downstream manifold position surpasses the distance δ_W away from the closest position on the corresponding periodic orbit. Geometric similarity considers the entire numerically simulated pathway, so this practical orbit arrival (or departure) process should only be applied after a design is crafted. In the Earth-Moon system, the value of δ_W is selected as 8000 km for weak-strength manifolds and 1000 km otherwise. Different CRTBP systems require adjustments to δ_W to accommodate the modified dynamics.

8.3 Applying Maneuvers from a Map-Based Perspective

The area-preserving nature of the CRTBP grants access to ΔV-free connections ($\mathcal{H}_c$ and $\mathcal{H}_o$) within chaotic regions; however, the area-preserving property also bounds dynamical areas such as quasi-periodic islands and bounded chaos near saddle-center island chains, preventing the existence of natural pathways to transition a spacecraft through such areas. A maneuver (ΔV) is the only control available for a spacecraft to connect to such regions. On the Poincaré section, maneuvers are classified into two primary types. *Map-preserving maneuvers* maintain the Jacobi constant value through the maneuver, creating an instantaneous transition in $\dot{x}$ as depicted in by the vertical black arrow at $C = 3.20$ in Figure 8.5. *Transitioning maneuvers*, on the other hand, simultaneously apply an alteration to the Jacobi constant value and a translation of the vertical ($\dot{x}$) location in phase space, resulting in a 3D translation in the Poincaré map coordinate space or (x,$\dot{x}$,C) space. A sample transitioning maneuver also appears in Figure 8.5 with a translation in both the $\dot{x}$ and C directions. With a rich understanding of Poincaré map topology, a design case defines a map-based maneuver by simply applying a change in the $\dot{x}$ coordinate (or $\Delta\dot{x}$) on the Poincaré section; a ΔC is also necessary to describe transitioning maneuvers. Both types of map-based maneuvers can be defined through interactions within the virtual environment, but it is important to study where maneuvers are most effective on the Poincaré section.

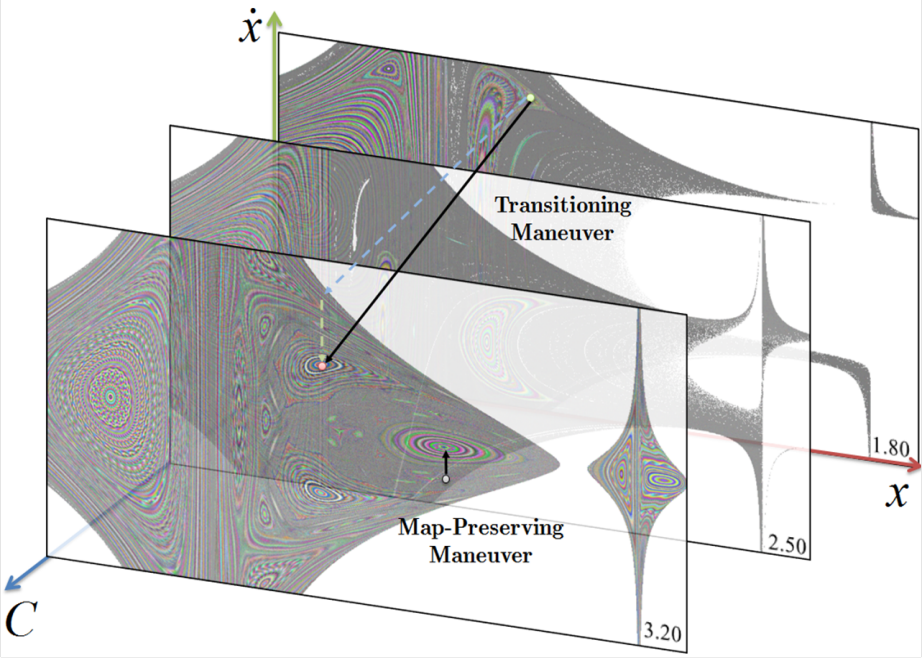

Figure 8.5. Map-preserving maneuvers versus transitioning maneuvers displayed with respect to various Jacobi constant levels on the Poincaré section phase space.

8.3.1 Map-Preserving Maneuvers

With an input $\Delta\dot{x}$, the total ΔV includes a counter $\Delta\dot{y}$ for map-preserving maneuvers. Let a map-preserving maneuver transition the 6D state $\boldsymbol{x}_0$ to the 6D state $\boldsymbol{x}_1$, assuming both states are on the hyperplane $\Sigma : y = 0$. The corresponding Jacobi constants are labeled C_0 and C_1, respectively. The map-preserving maneuver enforces $C_1 = C_0$ (and $\Delta C = C_1 - C_0 = 0$). Expanding the equivalent Jacobi constant values with the Jacobi integral yields

$$2\Upsilon(x_1, y_1, z_1) - v_1^2 = 2\Upsilon(x_0, y_0, z_0) - v_0^2. \tag{8.13}$$

Assume that the positions for $\boldsymbol{x}_1$ and $\boldsymbol{x}_0$ are the same at the impulsive maneuver and that the maneuver, ΔV, is split into components $\Delta\dot{x}$ and $\Delta\dot{y}$ ($\Delta\dot{z} = 0$ for planar analysis) with $\Delta V = \sqrt{\Delta\dot{y}^2 + \Delta\dot{x}^2}$. The map-preserving maneuver then equates the square of velocities, or

$$\dot{x}_0^2 + \dot{y}_0^2 = (\dot{x}_0 + \Delta\dot{x})^2 + (\dot{y}_0 + \Delta\dot{y})^2. \tag{8.14}$$

In the design case, the value of $\Delta\dot{x}$ is selected to translate geometry to a new map location, and as a result, the value of $\Delta\dot{y}$ is determined to maintain the Jacobi constant through the quadratic root of Equation (8.14). Therefore, the expression

$$\Delta\dot{y} = -\dot{y}_0 \pm \sqrt{\dot{y}_0^2 - \Delta\dot{x}^2 - 2\dot{x}_0\Delta\dot{x}} \tag{8.15}$$

computes the necessary counter-velocity to maintain C_0 post-maneuver. The sign of the second term is selected to minimize $|\Delta\dot{y}|$, concurrently minimizing the overall ΔV. From Equation (8.15), it is clear that small $\Delta\dot{x}$ values translate to the smallest total maneuvers, so the ideal locations to perform maneuvers are where structures align in the position coordinates yet are separated by small vertical distances corresponding to the velocity dimension. As another note, the $\dot{x}_0$ value also plays a role in the overall map-preserving maneuver cost; applying maneuvers near $\dot{x}_0 = 0$, or the $\hat{x}$ axis, reduces added requirements on $\Delta\dot{y}$.

The total ΔV for map-preserving maneuvers is demonstrated at different phase space locations with a scalar field visualization on the Poincaré section. The image appearing in Figure 8.6 indicates the required overall ΔV to accomplish a desired $\Delta\dot{x} = -102.5$ m/s ($\Delta\dot{x} = -0.1$ in nondimensional velocity) with a map-preserving maneuver. Areas in blue represent a total map-preserving maneuver that possesses a similar magnitude to the designed $\Delta\dot{x}$ where as red regions indicate that the overall maneuver to perform the desired map-based translation is at least double the prescribed $\Delta\dot{x}$. Note that the zero-velocity boundaries prevent all valid flow areas from achieving the desired $\Delta\dot{x}$. On the $\Sigma : y = 0$ map, vertical pinching (in the $\dot{x}$ dimension) of dynamical structures within the chaos are typically easier to reach with small map-preserving maneuvers such as the blue chaotic area near the L_1 gateway in Figure 8.6. Thus, maneuvers perpendicular to the velocity direction, i.e., a $\Delta\dot{x}$ applied to states along the $\hat{x}$ axis of the Poincaré section, can provide a significant geometric change in chaotic areas. Although Figure 8.6 conveys that map-preserving maneuvers near the zero-velocity curves may be sub-optimal for low-cost design, many invariant manifold structures bunch up near the zero-velocity boundaries (with exceptionally small vertical displacement on the Poincaré section). A trade study is recommended for any given design scenario to examine the optimal combination of manifold

arc location with vertical translation on the Poincaré section ($\Delta\dot{x}$ component) to minimize the overall maneuver.

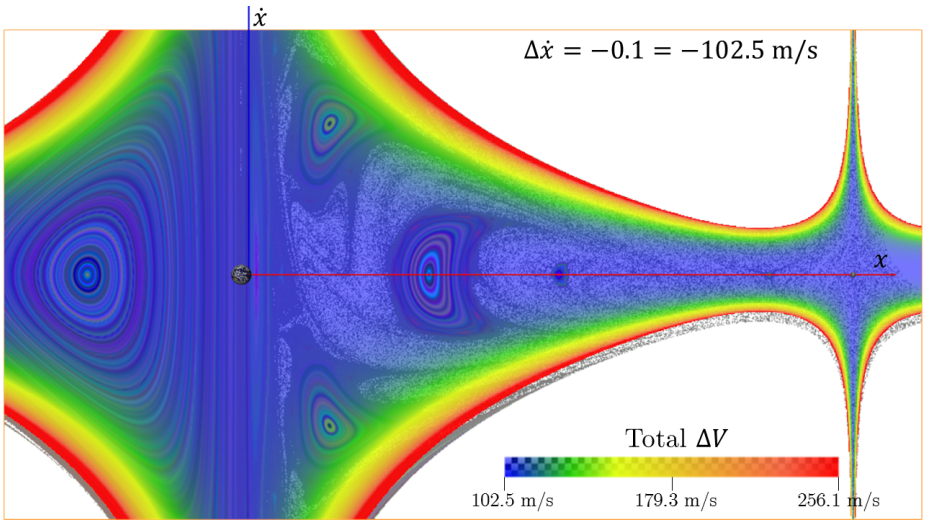

Figure 8.6. The total ΔV necessary to accomplish $\Delta\dot{x} = -0.1 = 102.5$ m/s for a map-preserving maneuver in the Earth-Moon system at $C_0 = 2.96$ for the domain D_{EM}.

8.3.2 Transitioning Maneuvers

The user-specified $\Delta\dot{x}$ and ΔC uniquely determine the total ΔV for a map-based transitioning maneuver at an arbitrary state on the Poincaré section. Again, the map-based maneuver here transitions a spacecraft from state $\boldsymbol{x}_0$ to state $\boldsymbol{x}_1$ residing at the same position on $\Sigma : y = 0$ except the Jacobi constant values shift by $\Delta C = C_1 - C_0$. The Jacobi integral comparison now appears as

$$2\Upsilon(x_1, y_1, z_1) - v_1^2 = 2\Upsilon(x_0, y_0, z_0) - v_0^2 + \Delta C \tag{8.16}$$

since $C_1 = C_0 + \Delta C$. Expanding in a similar manner as the map-preserving maneuver analysis, the required $\Delta\dot{y}$ to achieve a specified $\Delta\dot{x}$ and ΔC follows

$$\Delta\dot{y} = -\dot{y}_0 \pm \sqrt{\dot{y}_0^2 - \Delta\dot{x}^2 - 2\dot{x}_0\Delta\dot{x} - \Delta C}, \tag{8.17}$$

where the sign of the final term in Equation 8.17 is selected as the option that minimizes $|\Delta\dot{y}|$ and the overall maneuver. Much like map-preserving maneuvers, Equation (8.17) indicates that transitioning maneuvers are also dependent on the initial $\dot{x}_0$, alluding that such maneuvers are minimized when $\dot{x}_0 = 0$. Yet, the ΔC value may be significantly large enough to create additional analysis.

Additional constraints may be placed on the maneuver components $\Delta\dot{x}$ and $\Delta\dot{y}$ to formulate specific types of transitioning maneuvers. One such type is a tangential maneuver that directly modifies the velocity magnitude rather than individual components (or $v_0 + \Delta V = v_1$). With tangential maneuvers, a theoretical minimum ΔV exists to perform a change from one Jacobi constant value to another in the CRTBP. The minimal maneuver, or ΔV_{min}, to achieve the transition $\Delta C = C_1 - C_0$ is derived by applying the tangential change in velocity as $v_1 = v_0 + \Delta V_{\text{min}}$, translating to the Jacobi integral relationship

$$2\Upsilon(x_1, y_1, z_1) - (v_0 + \Delta V_{\text{min}})^2 = 2\Upsilon(x_0, y_0, z_0) - v_0^2 + \Delta C. \tag{8.18}$$

Assuming $\boldsymbol{x}_0$ and $\boldsymbol{x}_1$ are at the same position, the minimal maneuver then equates to

$$\Delta V_{\text{min}} = -v_0 \pm \sqrt{v_0^2 - \Delta C}. \tag{8.19}$$

The minimal tangential maneuver to perform ΔC hinges on the initial speed as a very large v_0 can offset the ΔC value to create small ΔV_{min} values. A scalar field visualization of ΔV_{min} to deliver a given ΔC conveys where the most effective energy-change locations exist on a Poincaré section. In the Earth-Moon system with $C_0 = 2.96$, the minimum tangential maneuver for a $\Delta C = -0.3$ is plotted a scalar field on the Poincaré section as shown in Figure 8.7. The white areas in Figure 8.7 require only a very small maneuver to achieve the desired ΔC. On the other hand, the red and yellow areas indicate a much more substantial ΔV_{min} albeit not terribly large at ≈ 300 m/s. The scalar field visualization in Figure 8.7 signifies that the areas around the L_1, L_2, and even L_3 gateways are not the ideal locations to change energy level, but maneuvers in close proximity to the primaries effectively modify the Jacobi constant value due to the inherent high speed.

A general principle in the two-body problem, called the Oberth effect, applies when considering map-based transitioning maneuvers. The Oberth effect states that the optimal

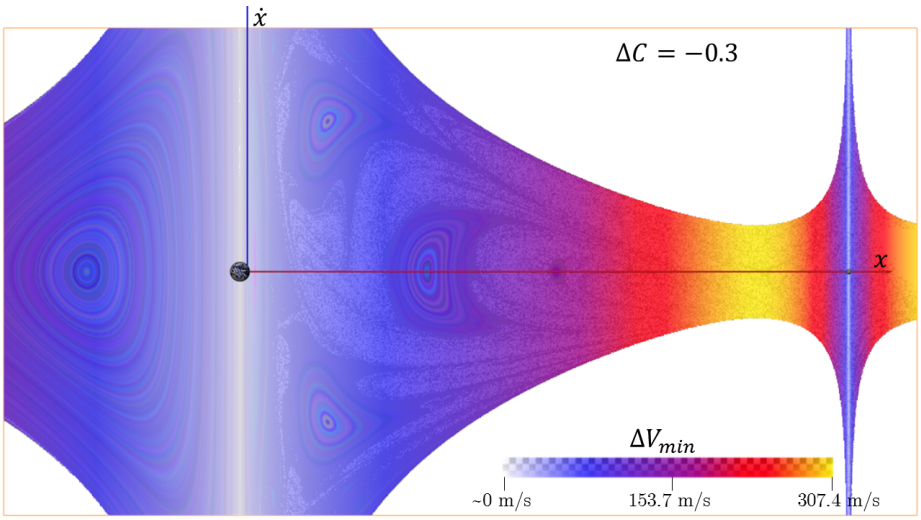

Figure 8.7. The minimum maneuver, or ΔV_{min}, to accomplish a $\Delta C = -0.3$ at various locations throughout the domain D_{EM} in the Earth-Moon system ($C_0 = 2.96$).

location for a maneuver to achieve the greatest change in (two-body) orbital energy occurs when the kinetic energy is maximized (i.e., at periapsis where the orbital velocity is maximized) [30, 31]. The Oberth effect is commonly exploited during interplanetary trajectories during a powered flyby of a body providing a gravitational assist [30]. A CRTBP equivalent to the Oberth effect is easily devised via the scalar field visualization of ΔV_{min} on the Poincaré section (namely Figure 8.7). The optimal maneuver locations to modify the Jacobi constant (or orbital energy in essence) reside at close proximities at either primary; in fact, the required ΔV_{min} reduces as the maneuver is performed closer to the primary. An additional axiom applies to the Oberth effect in the CRTBP. Consider a desired $\Delta C = -0.8$ with $C_0 = 2.96$ in the Earth-Moon system plus an added requirement of $\Delta\dot{x} = 0.01 = 10.25$ m/s on $\Sigma : y = 0$. A scalar field depiction of the necessary ΔV to deliver such a scenario is portrayed on the Poincaré section in Figure 8.8. The result again conveys that the optimal maneuver locations are close to the primaries, but expanding the observed region outward to encapsulate behavior far beyond L_2 and L_3 indicates that another viable region for effective ΔC maneuvers exists. As shown by the blueish regions at the extent of the visualization in Figure 8.8, the cost to change the Earth-Moon system Jacobi constant diminishes at far distances from both primaries.

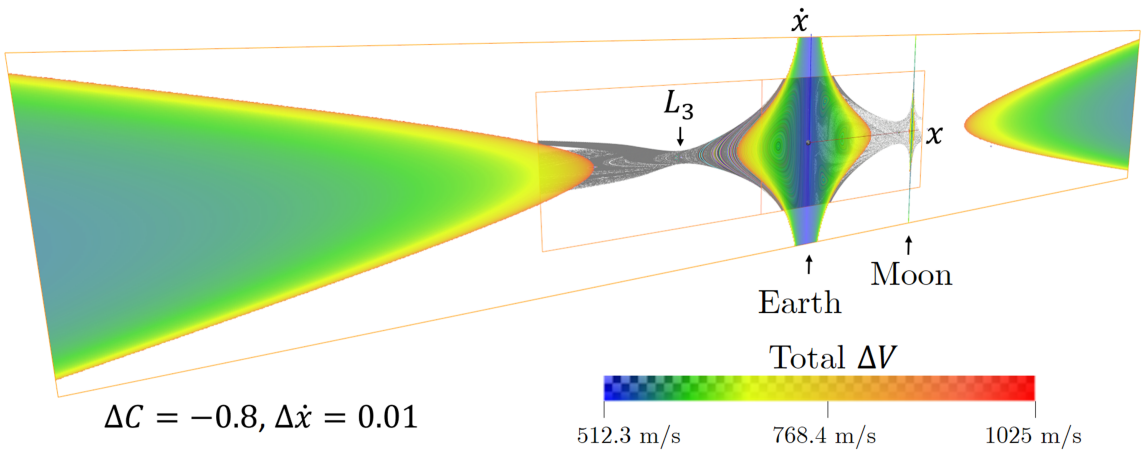

Figure 8.8. The required maneuver to accomplish a $\Delta C = -0.8$ from $C_0 = 2.96$ in addition to a $\Delta\dot{x} = 0.01 = 10.25$ m/s translation on the Poincaré section of $\Sigma : y = 0$ in the Earth-Moon system. The domain for visualization is quite far at $\{(x, \dot{x})|x \in [-4, 4], \dot{x} \in [-4, 4]\}$, reaching a distance of 1.537×10^6 km from Earth in x and 4.098 km/s in $\dot{x}$.

8.4 Topology-Based Design Construction

Poincaré map topology provides a catalog of design options that are extended into a spacecraft trajectory design paradigm for versatile spaceflight applications. Periodic orbits (fixed points) and any other provided initial states represent *design nodes*. Connections between design nodes, or *design links*, represent natural and artificial bridges between states and periodic orbits. A topology-based design perspective molds preliminary design construction to operate exclusively on the Poincaré section employing the catalog of options provided by rich topology extraction resulting from PMATE. Considering a topology-based design paradigm, the design links include map-based maneuvers (both map-preserving and transitioning) along with interactively selected invariant manifold arcs and natural connections available with the dynamics ($\mathcal{H}_c$ and $\mathcal{H}_o$).

Interactive strategies featuring Poincaré map topology aide in the construction map-based maneuvers, leading to a straightforward framework for design. Starting with a selected design node denoted $\boldsymbol{x}_0$ on the Poincaré section, a pathway to a particular periodic orbit of interest is forged by defining the map-preserving maneuver to a nearby stable manifold arc as long as the W^S structure overlaps the position x_0 correlated with the design

node. The definition of such a map-based maneuver is accomplished interactively by merely restricting stable manifold selections on the Poincaré section to be on the vertical line (or the *maneuver line*) at the appropriate x_0 location in phase space. Within the graphical scene, the interactively defined maneuver is depicted with just a simple vector connecting $\boldsymbol{x}_0$ to the stable manifold selection point. Note that the actual required ΔV for the interactively defined map-based maneuver can be displayed immediately adjacent to the maneuver vector, creating interactive feedback of maneuver cost. This interactive maneuver definition technique is easily adaptable to define design links between unstable periodic orbits that do not connect naturally with a heteroclinic connection. In such a case, the topology-based interactive design paradigm links an unstable manifold arc of the source saddle-type orbit to a stable manifold arc of the destination saddle-type orbit with a map-preserving maneuver as demonstrated in the schematic scenario of Figure 8.9. A user selects an unstable manifold location on the Poincaré section to start the design link, instantly restricting the next selection to reside along the maneuver line at the initial W^U selection point. A drag action next searches for a stable manifold of the destination orbit along the maneuver line. Note that multiple destination orbits can be considered by simply continuing the drag to a different stable manifold structure. The full pathway is finalized at the end of the drag action (button release) on a stable manifold selection point, defining the map-preserving maneuver and the asymptotic approach arc to the destination orbit. These *augmented heteroclinic connections*, or links between unstable and stable manifold structures abridged with a map-preserving maneuver, patch discontinuities in velocity on the Poincaré section. Consequently, augmented $\mathcal{H}_c$ provide links over quasi-periodic regions and bounded chaos, shortcuts through exceptionally long natural connections, and even corrective pathways to return a spacecraft back to a periodic orbit for station keeping.

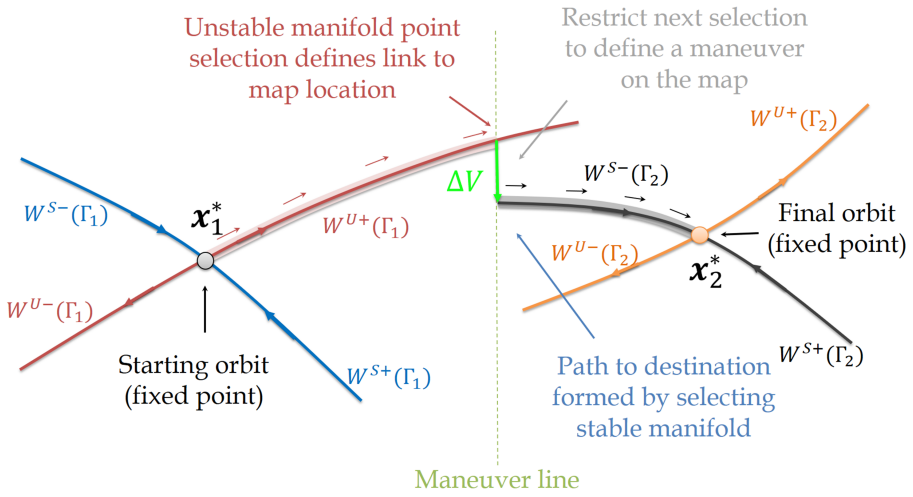

Figure 8.9. Topology-based design methodology for an interactive definition of an augmented heteroclinic connection.

9. POINCARÉ MAP TOPOLOGY APPLICATION IN PRELIMINARY MULTI-BODY TRAJECTORY DESIGN PROBLEMS

Spacecraft trajectory design applications significantly benefit from the Poincaré map information resulting from PMATE executions for the planar CRTBP in conjunction with the proposed interactive design framework. The autonomously extracted periodic orbits and the associated invariant manifolds supply the rich dynamical knowledge base that is vital for a versatile spaceflight design platform. Interactive selection of arcs and design node links from PMATE data broadens the design possibilities with new options and the ability to quickly examine trade-space decisions.

9.1 Analysis of Novel Periodic Orbits from PMATE

Periodic orbits are computed autonomously by executing PMATE Phases A-E for a selected hyperplane (e.g., $\Sigma : y = 0$) and system of interest with user-specified domains. Demonstrations of the autonomously extracted periodic orbits here include the Earth-Moon and Saturn-Titan systems. The PMATE fixed point extraction protocol easily locates common periodic orbits that are found through conventional lower-fidelity and bifurcation analysis (such as members of the Lyapunov and resonant orbit families). In addition, many novel periodic orbits appear from PMATE fixed point extraction that are, in general, difficult to discover with traditional analysis. For the following examples in various systems, PMATE analysis parameters are set as the values suggested in Chapter 7 unless otherwise stated. All analysis grids undergo adaptive cell subdivision with $d_{\max} = 3$. Also, orbit convolution imagery accompanies PMATE fixed point data to ascertain local dynamical behavior.

9.1.1 Earth-Moon System

The first application of PMATE fixed point extraction is attempted in the Earth-Moon system with a bounded flow regime. At a Jacobi constant level of $C = 3.2$, the closed L_1

and L_2 gateways prohibit flow between the primaries, yet chaos is still present. Thus, the initial PMATE fixed point extraction is applied to the EM $C = 3.2$ system on the standard domain D_{EM} (corresponding to the parameters of Trial 0 in Table 9.1). The resulting extraction, displayed in Figure 9.1, conveys solid acquisition of saddles and centers grouped in island chains and clustering of saddle-type fixed points within the limited chaotic regions. The example periodic orbits in Figure 9.1 are displayed in the xy plane (x-axis in red, y-axis in green). In Figure 9.1 and subsequent images of PMATE fixed point extraction, all fixed points with the same color originate from the same periodic orbit; however, visual distinction between similar colors is difficult. It is recommended to analyze fixed points with the interactive selection capability discussed in Section 8.1. At $C = 3.2$, transversality violations are actually somewhat rare within the analysis domain since all the chaos is bounded, making autonomous fixed point extraction relatively straightforward with seldom subdivision during Poincaré index computation.

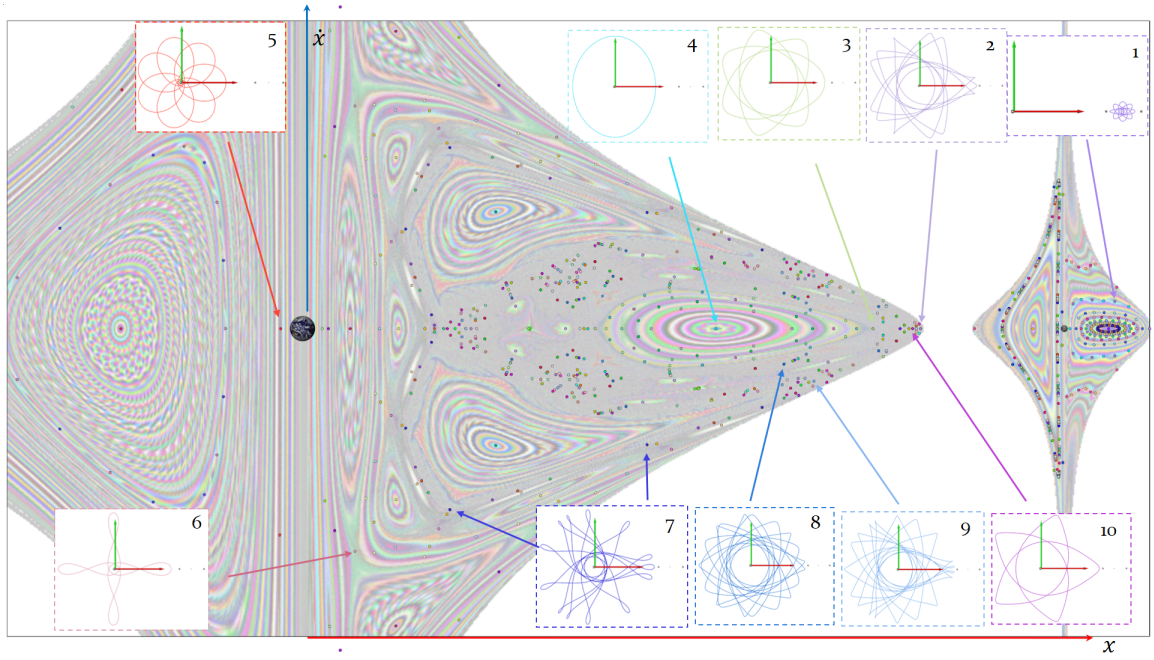

Figure 9.1. Autonomously extracted fixed points and selected periodic orbits resulting from PMATE on the Poincaré section $\Sigma : y = 0$ in the Earth-Moon system at $C = 3.2$.

A more complex yet beneficial application of PMATE fixed point extraction resides at an energy level where chaos exists throughout the planar flow space. The Earth-Moon system Jacobi constant level of $C = 2.96$ permits trajectories everywhere in the xy plane since the zero-velocity surfaces are detached from the xy plane. Broader sampling parameters are applied over a larger analysis domain as signified by Trial 1 in Table 9.1. This execution generates a set of fixed points throughout D_{EM} with sparse behavior capture near lunar vicinity; therefore, more refined extraction is applied for domains near the Moon where fixed points eluded the first extraction trial. These areas include both the $\pm x$ side of the Moon and the vicinity around the DRO orbit (quasi-periodic island near the Moon) as shown by Trials 2, 3, and 4 in Table 9.1. As shown by Figure 9.2, the resulting fixed points from the PMATE analysis runs for $C = 2.96$ in the EM system are numerous, arriving at a total of 1450 distinct periodic orbits all at the same Jacobi constant value.

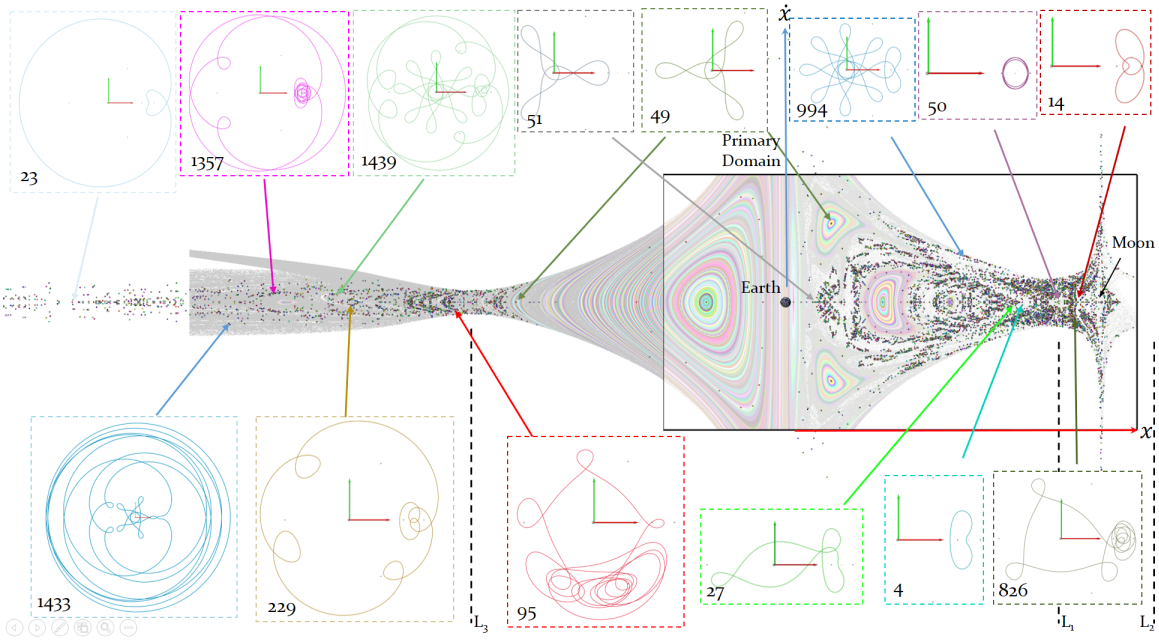

Figure 9.2. A Poincaré section displaying the fixed points available at $C = 2.96$ in the Earth-Moon system. This is the collective result of autonomous fixed point extraction with PMATE for the trials in Table 9.1.

Trial	C	Domain (nondim)	Resolution	$l_{\min}$	$p_{\max}$
0	3.2	D_{EM} (Equation (4.21))	24×16	$8{\times}10^{-5}$	12
1	2.96	D_{EM} (Equation (4.21))	24×16	$8{\times}10^{-5}$	12
2	2.96	$\{(x, \dot{x}) \vert x \in [0.9, 1.0], \dot{x} \in [-1.5, 1.5]\}$	8×8	$2{\times}10^{-5}$	12
3	2.96	$\{(x, \dot{x}) \vert x \in [0.78, 0.92], \dot{x} \in [-0.4, 0.4]\}$	8×8	$2{\times}10^{-5}$	6
4	2.96	$\{(x, \dot{x}) \vert x \in [0.9925, 1.08], \dot{x} \in [-0.2, 0.2]\}$	6×6	$2{\times}10^{-5}$	4

Table 9.1 Parameters for PMATE executions in the Earth-Moon system for collecting a broad dynamical behavior sample.

A periodic orbit sorting algorithm is applied to uniquely identify each orbit with an orbit index since many of the orbits generated from PMATE do not currently have orbit family designations. This periodic sort first orders periodic orbits by integer period. Stability then represents the next layer of sorting criteria: first centers, then saddles sorted by lowest $|\nu_{SI}|$ to highest $|\nu_{SI}|$. If any other saddles or centers are at equal positions in the sort, then the final sorting criterion places the lowest $(x, \dot{x})$ coordinates for the initial fixed point of the orbits before higher $(x, \dot{x})$ coordinates. Each orbit is subsequently assigned an identification number corresponding to the sorted set rankings. A complete tabulation of these 1450 periodic orbits for $C = 2.96$ is available in Appendix B with data reflecting orbit properties including time-period, ν_{SI}, $\nu_{z,SI}$, and the p Poincaré map iterates to Σ. The orbit identification numbers (or Orbit ID) are listed on the sample orbits appearing in Figure 9.2. These designations are only employed for the Earth-Moon $C = 2.96$ PMATE results for easy reference during sample design scenarios.

The resulting fixed points from PMATE trials in the Earth-Moon $C = 2.96$ system indicate many novel saddle-type periodic orbits. As shown by Figure 9.2, several periodic orbits are commonly known such as Orbit 4 (the L_1 Lyapunov), Orbit 23 (1:2 resonant orbit), Orbit 49 (stable 3:2 resonant orbit), Orbit 51 (unstable 3:2 resonant orbit), and Orbit 50 (the $p = 3$ unstable DRO) [54, 68, 83]. Several orbits, though, exhibit transiting behavior between the interior and exterior regions (such as Orbit 1433) and DRO vicinity to exterior or interior (Orbits 229, 826, and 1357). Yet others like Orbit 1439 visit all the aforementioned regions, perhaps making such orbits potentially useful for transfer design. More extracted periodic orbits are displayed on the enlarged Poincaré section depictions in Figure 9.3. Recall that PMATE analysis is only evaluated within the primary analysis

domain D_{EM} on the $\Sigma : y = 0$ Poincaré section (as per Table 9.1). Yet, an abundant number of unstable periodic orbits that cross this Poincaré section travel to L_3, L_4, and L_5 vicinities. Clearly, PMATE delivers a vivid dynamical understanding for the Poincaré section of interest.

9.1.2 Saturn-Titan System

Fixed point extraction with PMATE demonstrates independence on a CRTBP gravitational parameter with an application in the Saturn-Titan system. Employing a similar primary analysis domain to D_{EM} with supporting refined domains as indicated in Table 9.2, PMATE discovers 845 distinct periodic orbits ranging up to period $p = 12$ at $C = 3.00$ in Saturn-Titan system. The resulting periodic orbits, displayed on the Poincaré section in Figure 9.4, encompass the more traditional orbits and several periodic paths that transition between various regions. Orbits in the vicinity of the DRO (Figure 9.4(b)) may hover around Titan, transit to the interior or exterior, or visit multiple areas of phase space up to a limit in the interior. The crossing locations of the inner-moon orbits are also indicated in Figure 9.4(a). At this particular energy level, saddle-type periodic orbits reside in fairly close proximity to the listed interior Saturnian moons, but manifold extraction is necessary to determine if any low-cost transfers from either the Saturn-Titan exterior or Titan vicinity to such orbits exist.

Trial	C	Domain (nondim)	Resolution	$l_{\min}$	$p_{\max}$
0	3.00	$\{(x,\dot{x})\|x \in [-0.4, 1.1], \dot{x} \in [-2.5, 2.5]\}$	24×16	$8{\times}10^{-5}$	12
1	3.00	$\{(x,\dot{x})\|x \in [0.9323, 0.9855], \dot{x} \in [-0.1355, 0.1355]\}$	8×8	$2{\times}10^{-5}$	6
2	3.00	$\{(x,\dot{x})\|x \in [0.98, 1.05], \dot{x} \in [-0.225, 0.225]\}$	10×10	$2{\times}10^{-5}$	6

Table 9.2 Parameters for PMATE executions in the Saturn-Titan system for collecting a broad dynamical behavior sample.

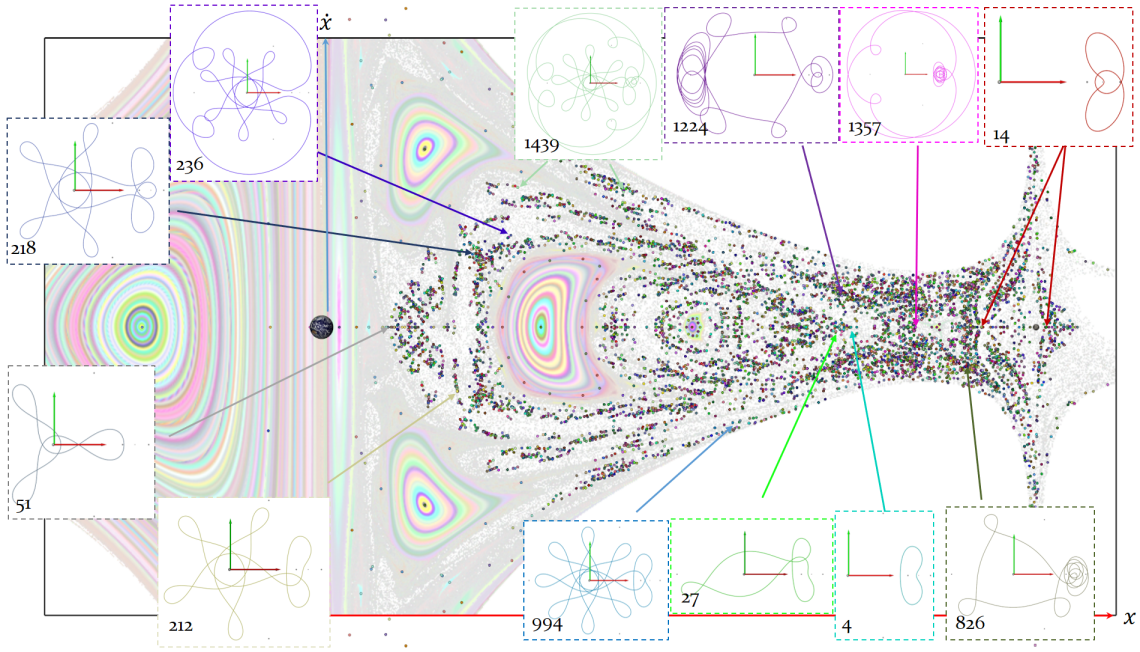

(a) Primary analysis domain D_{EM}

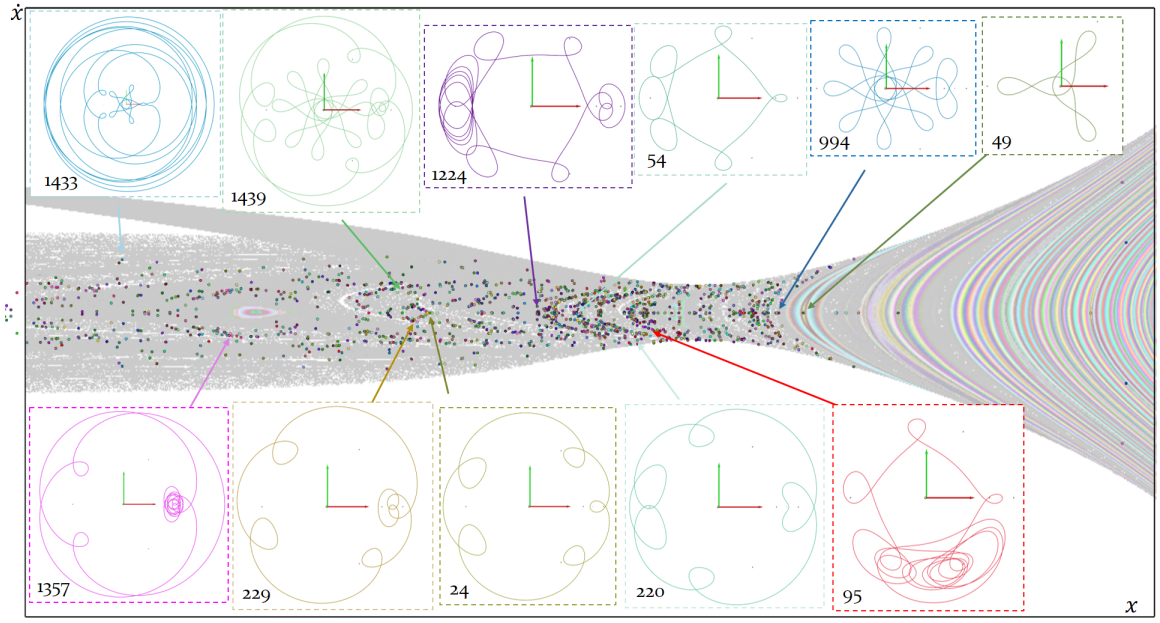

(b) Area near L_3

Figure 9.3. A sample of periodic orbits computed autonomously from PMATE fixed point extraction trials for the Earth-Moon system at $C = 2.96$.

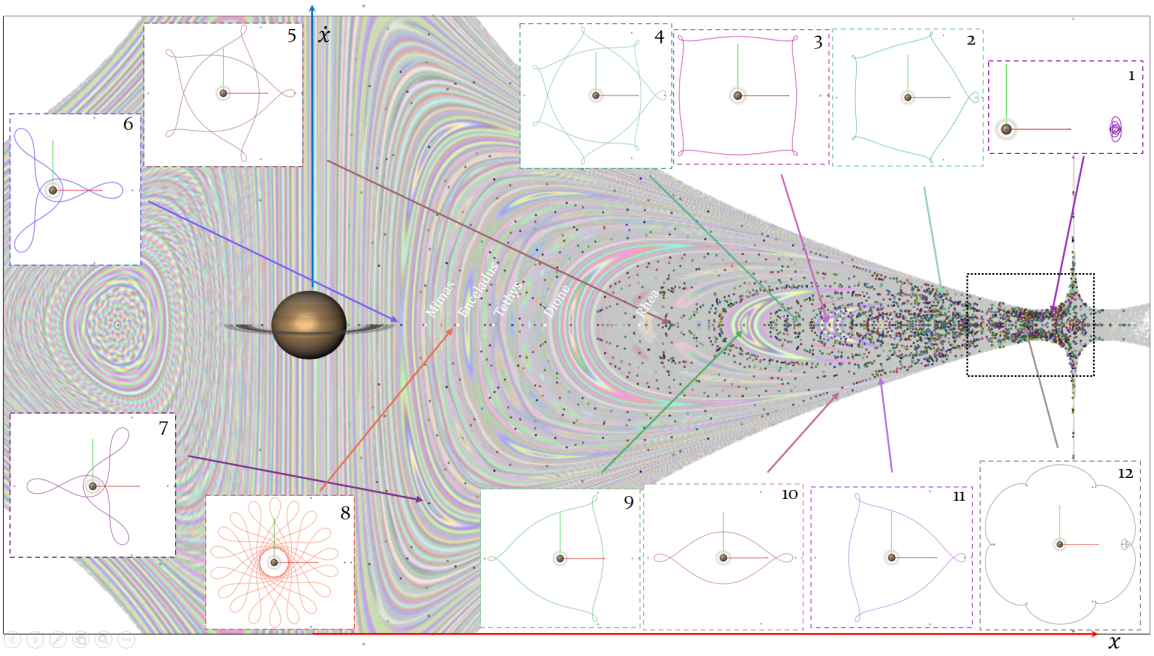

(a) Primary analysis domain

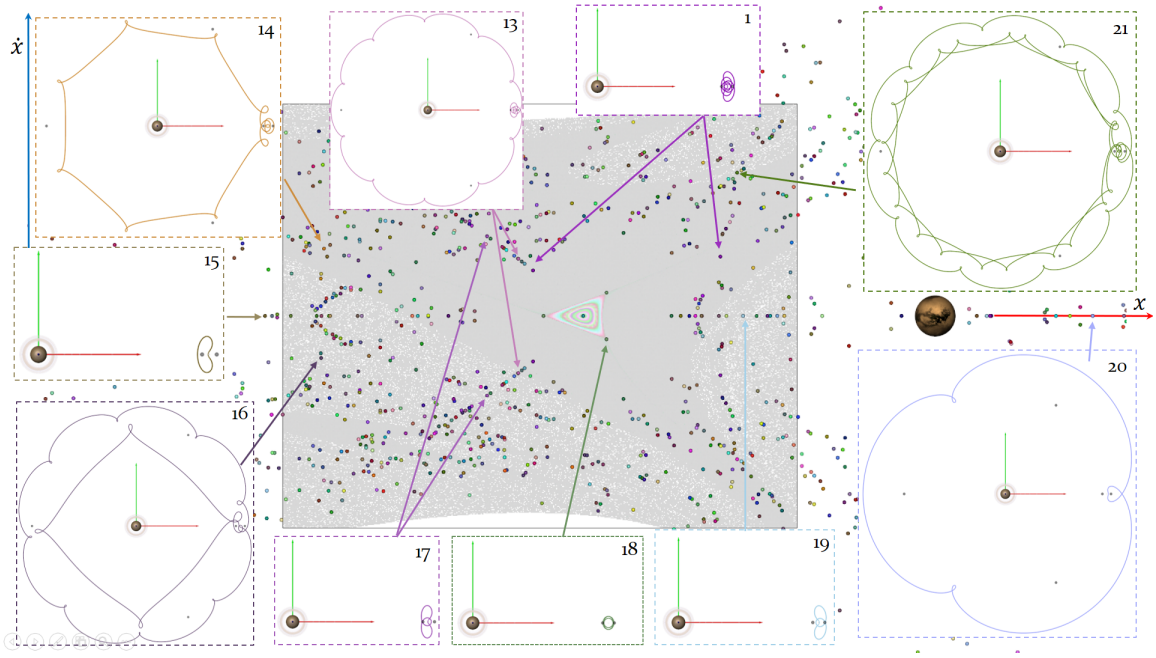

(b) Area near DRO

Figure 9.4. A Poincaré section displaying the fixed points available at $C = 3.00$ in the Saturn-Titan system. The periodic orbits here are the collective result of autonomous fixed point extraction with PMATE for the trials in Table 9.2.

9.2 The Poincaré Map Topology Skeleton

With fixed points extracted, the complete Poincaré map topology structure, often termed the *Poincaré map topology skeleton*, is evaluated next with the autonomous invariant manifold extraction algorithm (PMATE Phase F in Section 7.6). Note, the computation of invariant manifolds is a computationally costly procedure that is separated from fixed point extraction for easier implementation. The manifold advection algorithm first extracts the invariant manifolds in the Earth-Moon system on the fixed points extracted at $C = 3.2$. The large-scale topology extraction result appears in Figure 9.5 with unstable manifolds (W^U) and stable manifolds (W^S) colored in red and blue, respectively. The representation of invariant manifolds materializes throughout the chaotic areas at $C = 3.2$, thoroughly filling in the phase space areas between quasi-periodic islands. PMATE seems adept at conveying saddle-center island chains except on some islands near the Moon. The struggle with manifolds near the Moon here is attributed to numerical sensitivity and building numerical error during simulation as trajectories at those locations pass exceptionally close to the singularity multiple times before returning the $\overline{p}$ iterate. As with fixed point extraction, advecting invariant manifolds for the Earth-Moon $C = 3.2$ system is actually not as challenging as other Jacobi constant values since fewer hyperplane transversality violations are encountered. In fact, this manifold set is processed without stability index pre-screening and still completes the advection procedure faster than systems with open gateways. Yet, some challenges in describing the Poincaré map topology skeleton are still observed with a close-up representation (Figure 9.5(b)). Artifact segments shortcut some tight bends in both manifold types, but these are merely caused by non-strict curve-refinement parameters. Chaotic tangles, on the other hand, strongly influence the generation of invariant manifolds, especially as a manifold is advected towards the origin fixed point of the opposing stability type. As evident by the tri-lobe structure in Figure 9.5(b), it is unclear if the computed structure is a pure saddle-loop (a completely connected tri-petal flower) or if the chaotic tangle oscillations in the manifold are the true projection of the invariant manifold streamsurface. Nevertheless, the computed topology skeleton is still an applicable representation of manifold behavior for application in design practices.

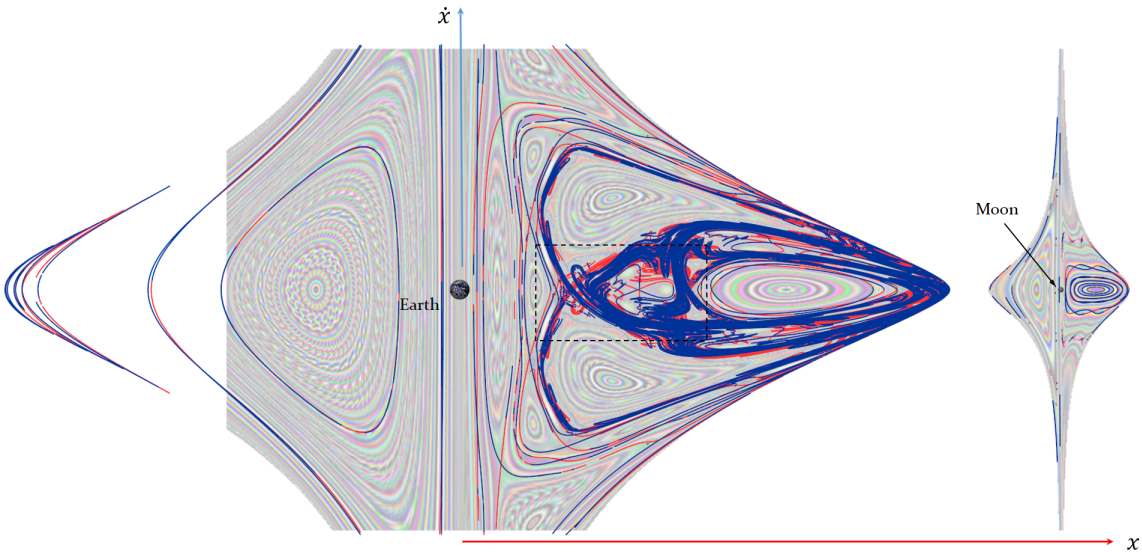

(a) Primary analysis domain D_{EM}

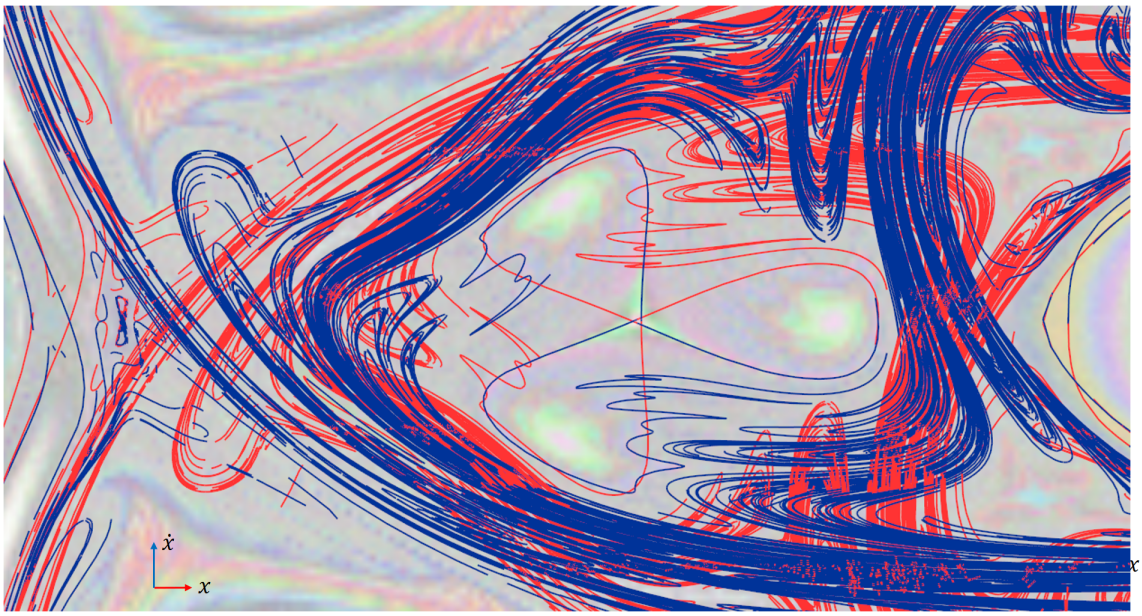

(b) Zoom-in on indicate domain

Figure 9.5. The Poincaré map topology skeleton (W^U in red and W^S in blue) computed with the PMATE manifold extraction algorithm in the Earth-Moon system within the domain D_{EM} at $C = 3.2$.

The Poincaré map topology skeleton is next extracted on a Poincaré section with open gateways. At $C = 2.96$ in the Earth-Moon system, advection produces a depiction of both stable (blue) and unstable (red) manifolds for the exceptionally large number of extracted periodic orbits as shown in Figure 9.6. Individual stable and unstable manifold skeletons appear in Figures 9.7(a) and 9.7(b), respectively. Limits on base orbit stability index ($|\nu_{SI}| \leq 2500$) screen considered fixed points to reduce overall computation during the advection procedure, cutting the number of saddle-type orbits included by over half. Even with a limited range on ν_{SI}, the advected set of manifolds populate almost the entire chaotic region. As shown by the W^S portrait in Figure 9.7(a), the only areas within the chaotic sea lacking information about stable manifolds are associated with trajectories that escape the entire Earth-Moon system (i.e., white pixels in the OC image). Knowing this highly detailed stable manifold structure, a spacecraft in almost any location within the applicable chaotic sea can reach a stable manifold of some fixed point with a small ΔV (that is, as long as the phase state is not in the large escape region to the $+\hat{x}$ side of the Moon). This rich understanding of the available flow is exceptionally beneficial to versatile spaceflight applications as the nearby structures to almost any Poincaré section state are revealed.

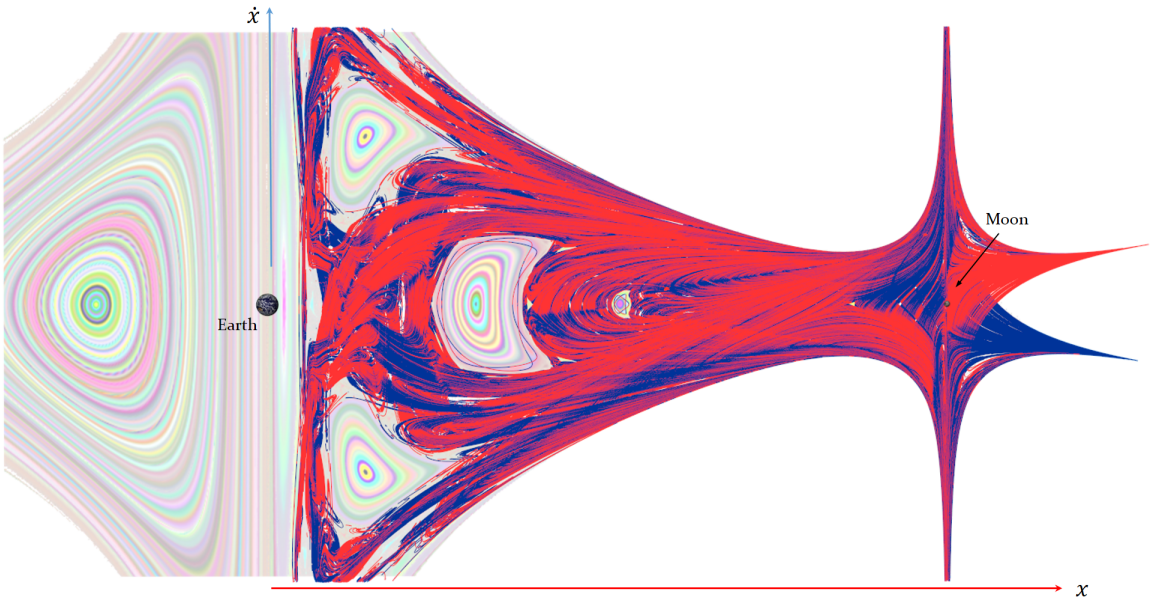

Figure 9.6. The Poincaré map topology skeleton (W^U in red and W^S in blue) computed with PMATE in the Earth-Moon system at $C = 2.96$.

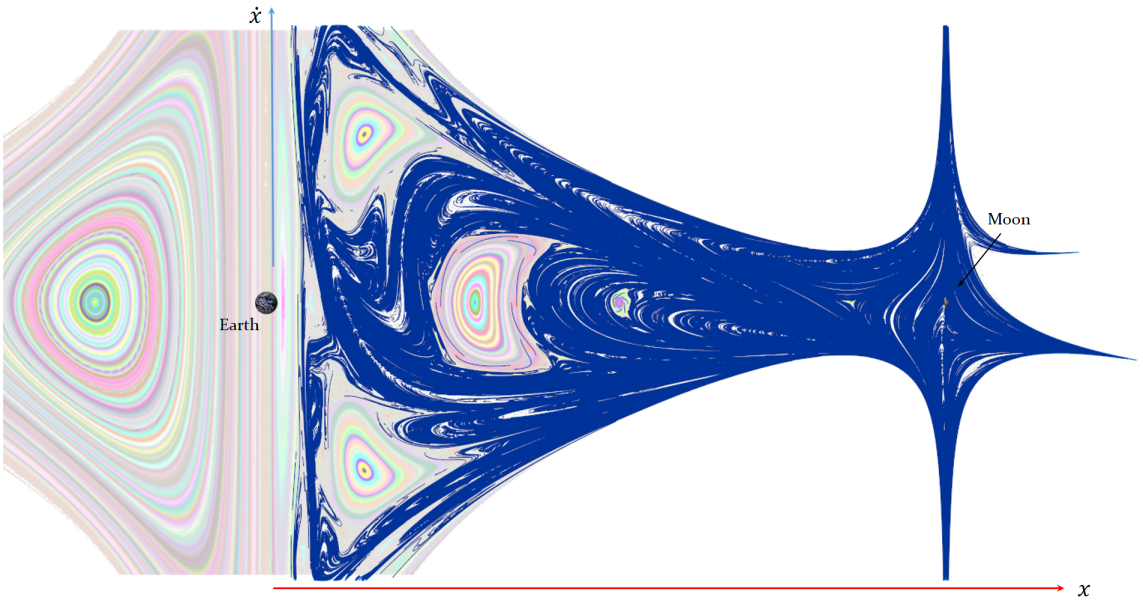

(a) Stable manifolds

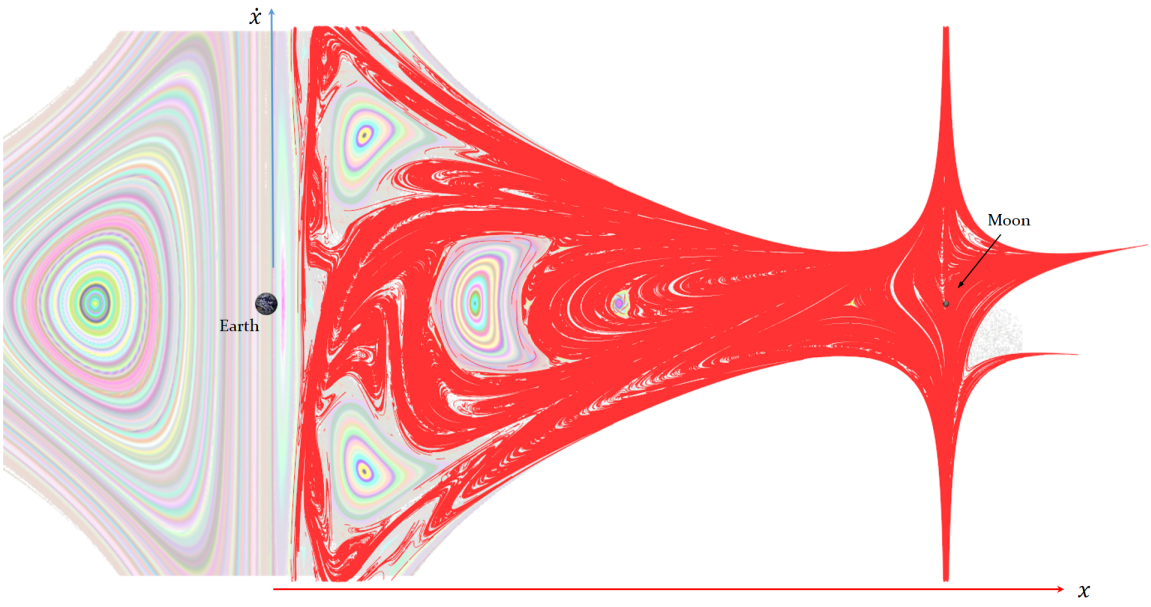

(b) Unstable manifolds

Figure 9.7. Stable and unstable manifolds on the Earth-Moon system domain D_{EM} at $C = 2.96$.

In the Saturn-Titan system, the manifold advection algorithm from PMATE portrays a similar description of the Poincaré map topology skeleton as the Earth-Moon $C = 2.96$ system with open gateways. Invariant manifolds are displayed in the Saturn-Titan system at $C = 3.00$ below in Figure 9.8. Again, limits on considered periodic orbits via stability index prevent overloading PMATE with extra and tedious advection. A depiction of stable manifolds and fixed points in Titan-vicinity appears in Figure 9.8(b). Once more, the invariant manifolds generated from PMATE create a comprehensive skeleton in the chaotic zones. Structure near Titan is particularly dense, offering many options for heteroclinic or low-ΔV transitions between structures. The inner moons Mimas, Enceladus, Tethys, Rhea, and Dione are also added to Figure 9.8 as white dots at the approximate x locations of their respective orbits. Clearly, Rhea and Dione are accessible at this energy level with a multitude of invariant manifold structure of the Saturn-Titan system intersecting the indicated positions. Yet, the other interior moons are only accessible with a saddle in bounded chaos, meaning a substantial maneuver ($\Delta V > 500$ m/s) is necessary for a spacecraft to cross over the multiple layers of bounded dynamics. Saddle-center island chains outline the dynamical boundaries of the problem towards the inner moons like Tethys and Enceladus and could be useful for design practices. The natural dynamics pathway to the inner moons, however, should employ the gravity fields of other moons like Rhea and Dione to assist a spacecraft over the regions of bounded dynamics in the Saturn-Titan system. Without an effective means to blend CRTBP systems, patched-conic design techniques such as V_∞-leveraging remain the staple for designing a transfer path to the interior moons [15–18]. Still, the Poincaré map topology skeleton in the CRTBP provides alternative pathways to initialize or finalize a moon-tour trajectory.

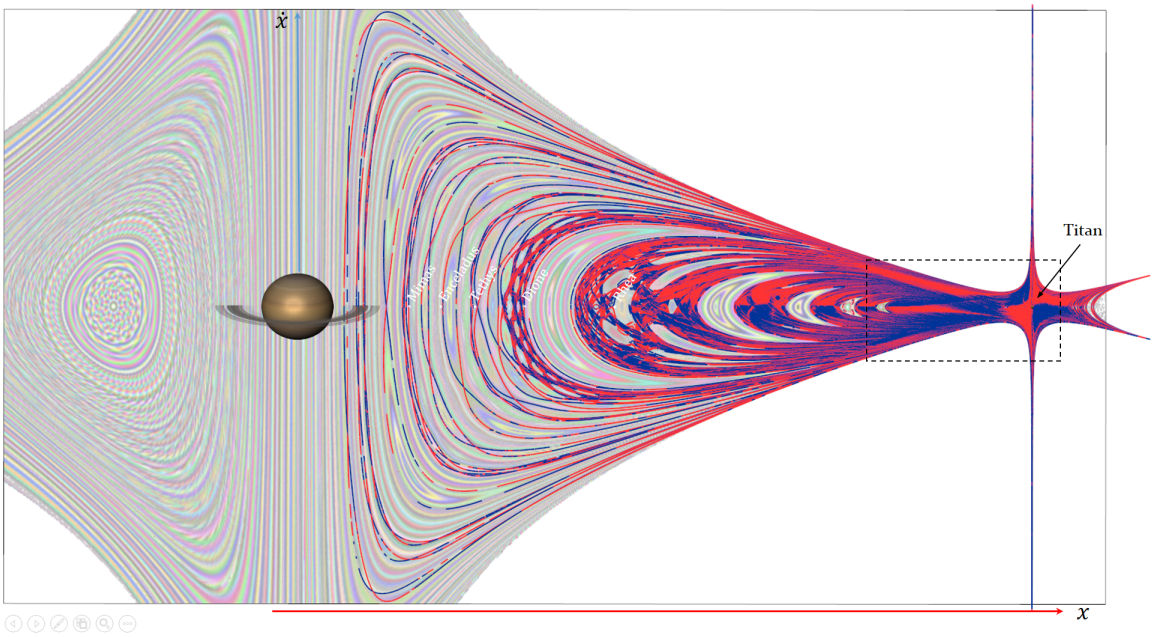

(a) Primary analysis domain

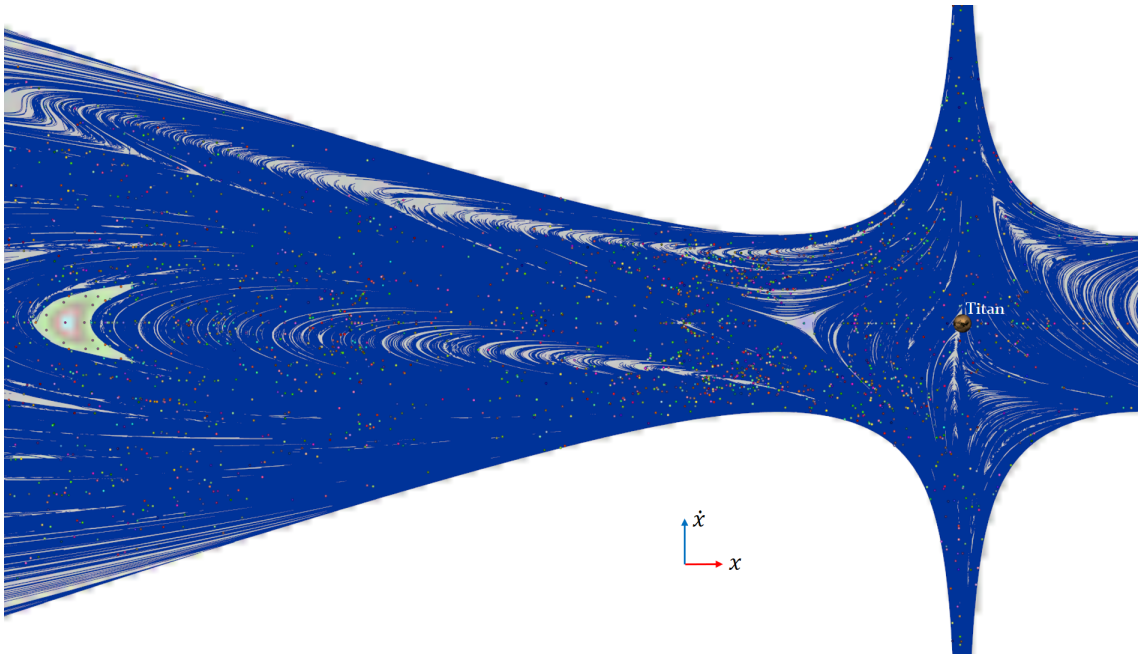

(b) Stable manifolds and fixed points near Titan

Figure 9.8. The Poincaré map topology skeleton (W^U in red and W^S in blue) computed with the PMATE manifold extraction algorithm in the Saturn-Titan system at $C = 3.00$.

9.3 Design Elements of Poincaré Map Topology in the Earth-Moon System

Manifold arc selection presents as a key tool for design construction with Poincaré map topology. Consider a the smaller topology skeleton subset that includes just the invariant manifolds of the L_1 Lyapunov (Orbit 4 in Appendix B) and the $p = 3$ unstable DRO (Orbit 50 in Appendix B). The subsample of manifolds appears on the Poincaré section as in Figure 9.9 with the W^S and W^U pair colored with black and crimson for the L_1 Lyapunov and with blue and red for the $p = 3$ DRO, respectively. A L_1 Lyapunov stable manifold arc (black) and a $p = 3$ DRO stable manifold arc (blue) are selected at the indicated locations on the Poincaré section (Figure 9.9(a)) that originate in the interior region. Both resulting arcs (shown in the rotating frame in Figure 9.9(b) and in the inertial frame in Figure 9.9(c)) demonstrate an elliptical orbit around the Earth before a second passage where the CRTBP dynamics shift the trajectories towards asymptotic approach of the respective orbits. The time of flight of the transfer trajectory considers the propagation time from the initial selection point until the geometric similarity condition between the manifold and desired orbit (see Section 8.2.3). The black arc enters the L_1 Lyapunov orbit at the practical arrival condition after 38.10 days whereas the blue arc practically arrives in the $p = 3$ DRO after 88.14 days. Clearly, the arc selection capability enhances quick design construction by readily incorporating many ballistic capture trajectories.

The same L_1 Lyapunov and $p = 3$ DRO invariant manifolds extend far beyond the L_3 point, providing another set of approach and departure possibilities. In the zoomed out Poincaré section view of Figure 9.10(a), many of the $p = 3$ DRO and the L_1 Lyapunov manifolds span a vast space in the exterior region towards the $-\hat{x}$ direction. Again, stable manifold arcs are selected, generating the representations in Figures 9.10(b) and 9.10(c). The $p = 3$ DRO W^S selection resides at $x = -8.57 = 3.18 \times 10^6$ km away from the Earth-Moon barycenter and arrives to the base after 109.91 days. The selected state of the L_1 Lyapunov W^S occurs at $x = -4.56 = 1.75 \times 10^6$ km and enters orbit after 106.36 days. Both of these exterior stable manifold arcs originate sufficiently far away from the Earth-Moon system such that the solar gravity is non-negligible, but manifold selection in the exterior indicates possible transition locations between patched CRTBP systems.

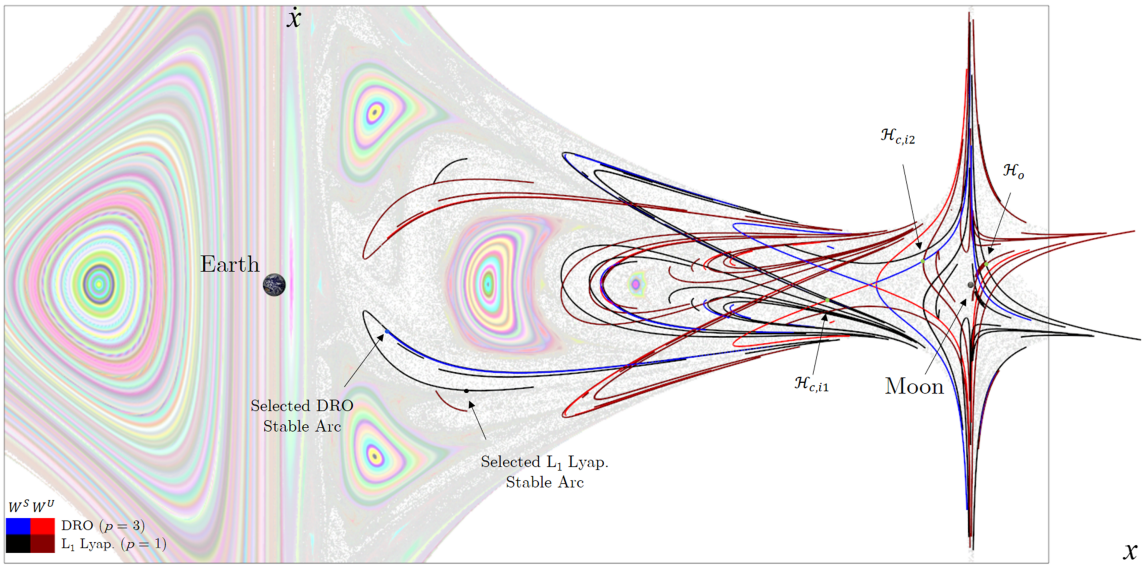

(a) Manifolds of the L_1 Lyapunov and $p = 3$ DRO periodic orbits

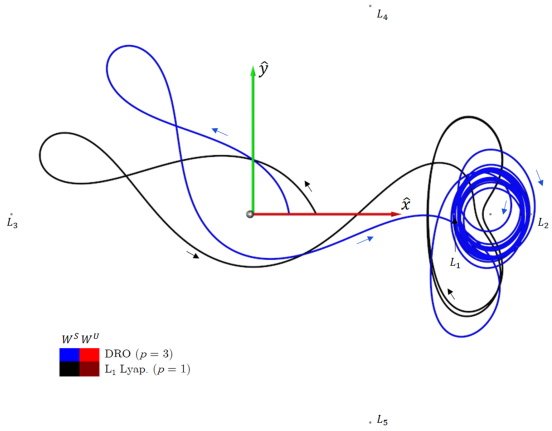

(b) Selected arcs (rotating frame)

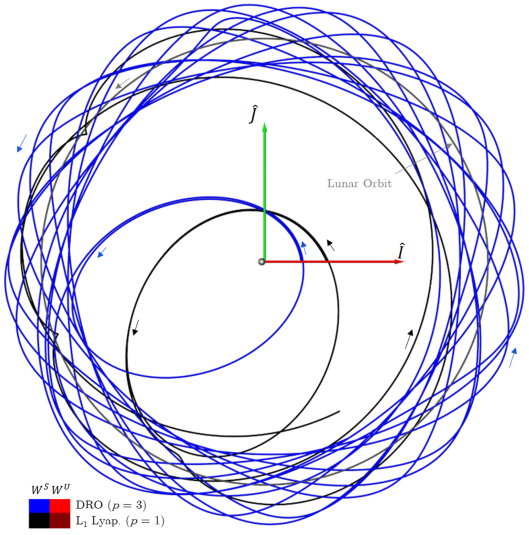

(c) Selected arcs (inertial frame)

Figure 9.9. Invariant manifolds for the L_1 Lyapunov and $p = 3$ DRO saddle-type orbits extracted with PMATE in the Earth-Moon system ($C = 2.96$). Selected stable manifold arcs are displayed in the rotating (b) and inertial (c) frames.

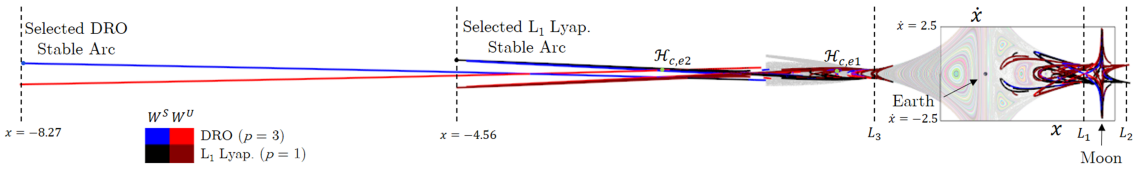

(a) Manifolds of the L_1 Lyapunov and $p = 3$ DRO periodic orbits

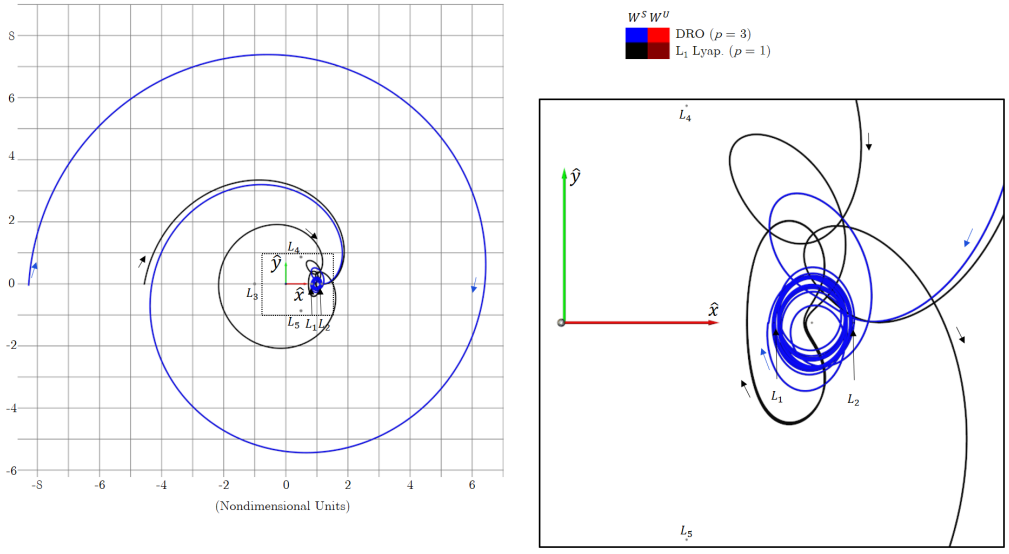

(b) Selected arcs (rotating frame)

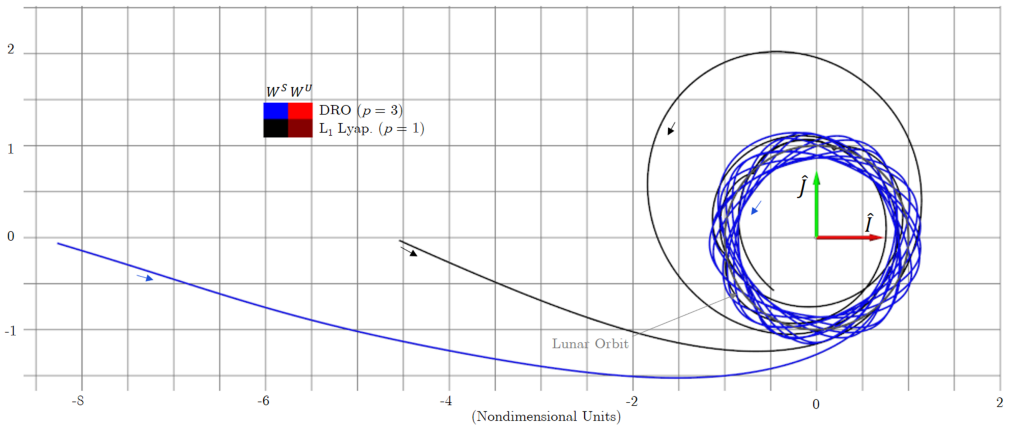

(c) Selected arcs (inertial frame)

Figure 9.10. Invariant manifolds in the exterior region for the L_1 Lyapunov and $p = 3$ DRO saddle-type orbits extracted with PMATE in the Earth-Moon system ($C = 2.96$).

9.3.1 Non-planar Considerations

All of the analysis for Poincaré sections in this investigation is restricted to the planar CRTBP model to permit area-preserving analysis on 2D Poincaré sections. The full spatial problem, however, requires 4D Poincaré sections, garnering more advanced topology. Yet, the arc-dragging capability provides an exceptionally valuable tool to construct out-of-plane versions of planar solutions crafted with interactive arc extraction, especially from orbits with $|\nu_{z,SI}| \leq 1$. Employing the camera view of Figure 9.11(a), a $p = 3$ DRO W^S arc (the same arc as Figure 9.9(c)) is pulled out-of-plane by merely dragging the end point (red) up. Note that the out-of-plane drag condition is possible since $\nu_{z,SI} = -0.38$ for the $p = 3$ DRO. The resulting structure (thick blue arc shown in Figure 9.11) is a trajectory mimicking the original capture arc but with a z amplitude of roughly 3450 km. Thus, it is evident that similar non-planar solutions can be derived from planar trajectories and design elements extracted from Poincaré map topology.

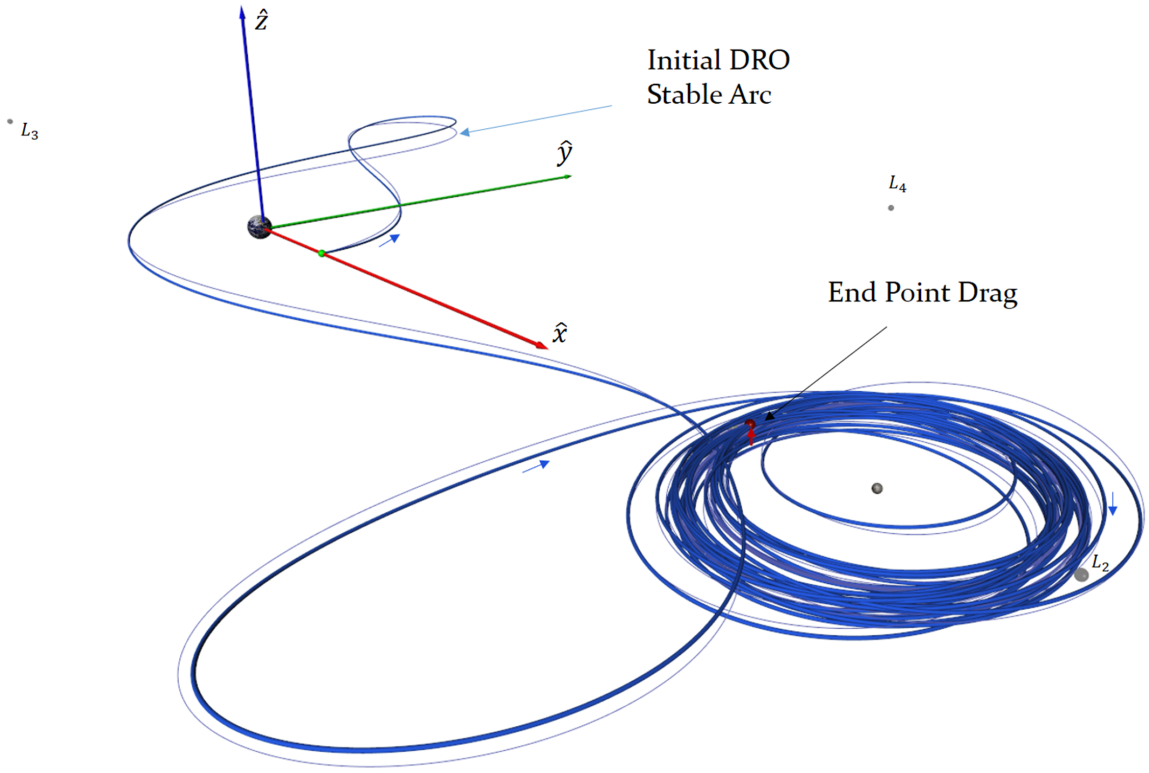

(a) Drag view

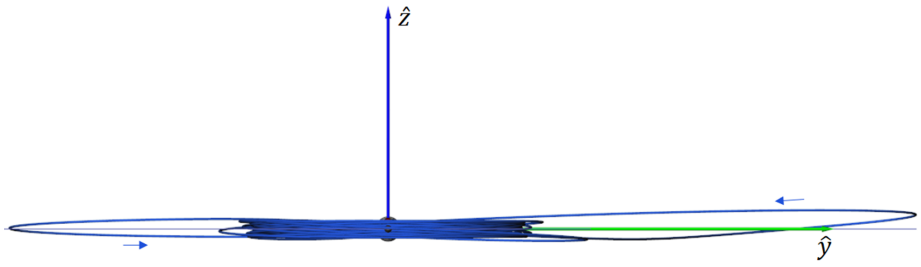

(b) yz view

Figure 9.11. The resulting out-of-plane trajectory (thick blue arc) after dragging the end point of a planar $p = 3$ DRO stable manifold arc out of the xy plane employing the camera view in (a).

9.3.2 Sample Connections Between Saddle-type Orbits

Heteroclinic and homoclinic connections between the L_1 Lyapunov orbit and the $p = 3$ DRO are quite simple to extract from Poincaré map topology with manifold selection capabilities. Any intersection of stable and unstable manifolds , so a multitude of options exist to exploit natural dynamics to transfer between the two orbits. Also apparent in Figures 9.9(a) and 9.10(a) are green points that signify selected heteroclinic connections between the $p = 3$ DRO and L_1 Lyapunov orbit in the interior region ($\mathcal{H}_{c,i1}$ and $\mathcal{H}_{c,i1}$) and the exterior region ($\mathcal{H}_{c,i1}$ and $\mathcal{H}_{c,i1}$). A homoclinic connection for the L_1 Lyapunov orbit also appears in Figure 9.9(a) as the point $\mathcal{H}_o$ at the intersection of a crimson W^U and a black W^S. Each connection is selected by simply hovering over the point of intersection between the corresponding stable and unstable manifolds. The chosen interior connection arcs are displayed in Figure 9.12 while the exterior connections appear in Figure 9.13. The simplicity of formulating free-flowing connections between unstable periodic orbits assists designers in evaluating different trade studies to align timing possibilities.

Additional connections are also easy to formulate between a wide variety of periodic orbits. Three sample connections are demonstrated with various periodic orbits in the Earth-Moon system at $C = 2.96$ to demonstrate the simple selection of heteroclinic connections. The first sample connection transports a spacecraft from a 2:1 resonant orbit (Orbit 53 in Appendix B) to the $p = 3$ DRO. Again, the procedure to extract the connection initiates by plotting the invariant manifolds associated with both periodic orbits on the Poincaré section such as the section image shown in Figure 9.14. The stable and unstable manifolds correlated with the 2:1 resonant arc appear as the dark gray and pink curves, respectively. Any intersection between pink segments and blue segments (representing W^S of the $p = 3$ DRO) is a potential connection achieving the desired transfer; a single $\mathcal{H}_c$ option is selected at the green point and demonstrated in Figure 9.14(b). The manifolds of some orbits such as the 2:1 resonant orbit and the $p = 3$ DRO, spread over a wide area within the chaotic regions. In general, periodic orbits with more invariant manifold dispersion are more ideal to implement as intermediate orbits since they possess broad access throughout the Poincaré section and flow space. Such orbits are, therefore, central to transfer possibilities and designs with a variety of links to many other orbits through heteroclinic connections. Another

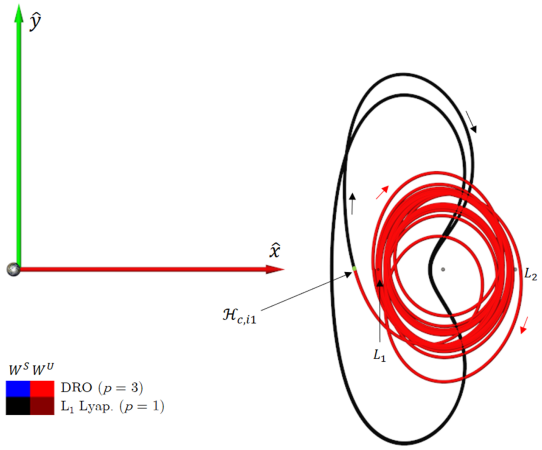

(a) $\mathcal{H}_{c,i1}$ ($\Delta t = 159.56$ days)

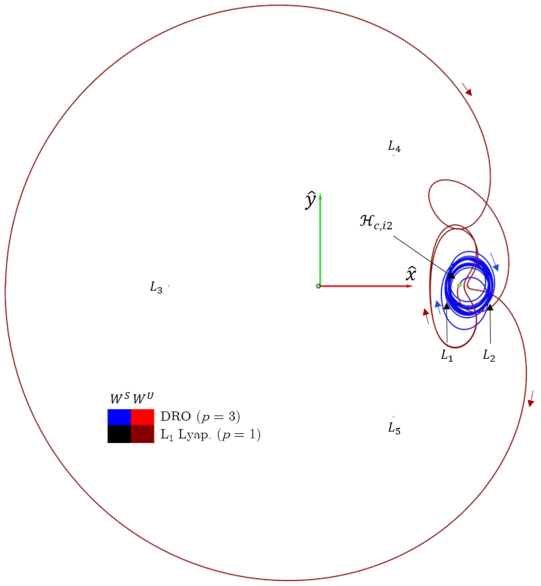

(b) $\mathcal{H}_{c,i2}$ ($\Delta t = 142.83$ days)

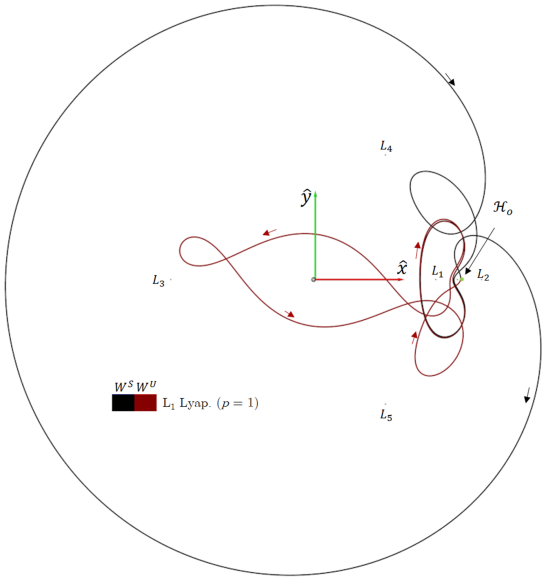

(c) L_1 Lyapunov $\mathcal{H}_o$ ($\Delta t = 142.99$ days)

Figure 9.12. Maneuver-free connections between the L_1 Lyapunov orbit and the $p = 3$ DRO constructed through interactive selection of manifold intersection states as indicated in Figure 9.9(a).

transfer is demonstrated starting at the $p = 3$ DRO and departing to the rather exotic Orbit 207 that visits L_3 and L_4 vicinities while also closely approaching the Moon several times.

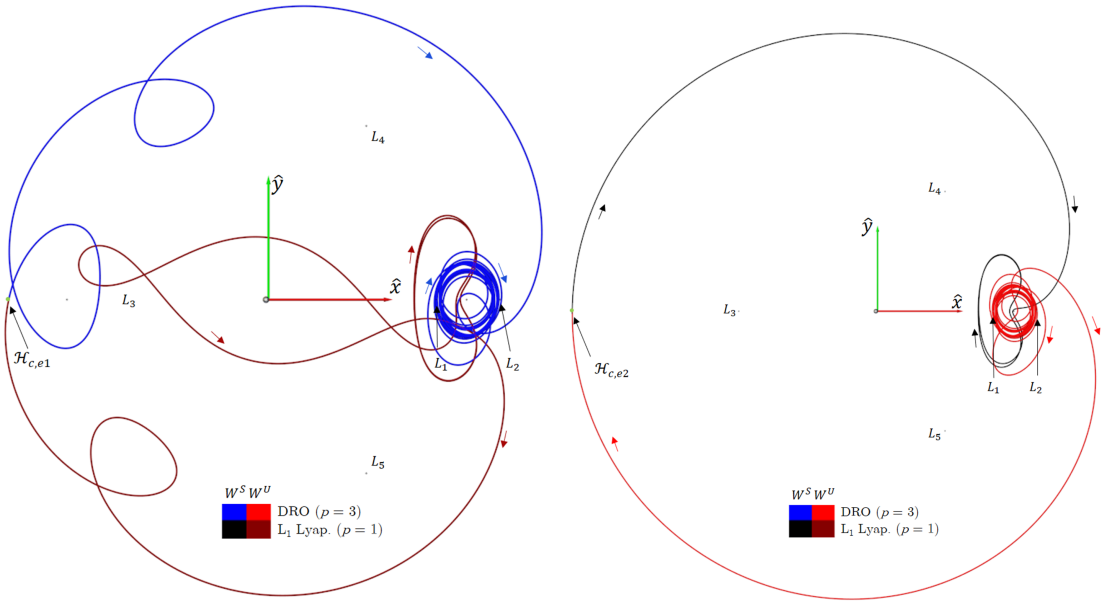

(a) $\mathcal{H}_{c,e1}$ ($\Delta t = 219.38$ days) (b) $\mathcal{H}_{c,e2}$ ($\Delta t = 128.83$ days)

Figure 9.13. Maneuver-free connections between the L_1 Lyapunov orbit and the $p = 3$ DRO constructed through interactive selection of manifold intersection states as indicated in Figure 9.10(a).

The invariant manifold curves for Orbit 207 (displayed in Figure 9.15 with indigo and tan colors) indicate that a lot of Poincaré section locations naturally flow into this orbit with the large dispersion of stable manifolds. A transfer from the $p = 3$ DRO to Orbit 207 is represented by any red-indigo intersection, and a selected option (green dot) is extracted to demonstrate a transfer possibility as shown in Figure 9.15(b). Another orbit with transfer centrality behavior is the 5:2 unstable resonant orbit (or Orbit 179). The manifolds of Orbit 179 (appearing with purple for W^S and yellow for W^U in Figure 9.16) are paired with Orbit 383 (W^S as steel and W^U as orange) to design a final heteroclinic transfer. The selected transfer from Orbit 179 to Orbit 383 (Figure 9.16(b)) demonstrates that PMATE data provides a way to link orbits that start in completely different regions. The richness of PMATE manifold information combined with the the ability to construct heteroclinic connections with ease highlights essential orbits for use as intermediate transfer candidates with a high degree of transfer centrality as indicated through manifold dispersion.

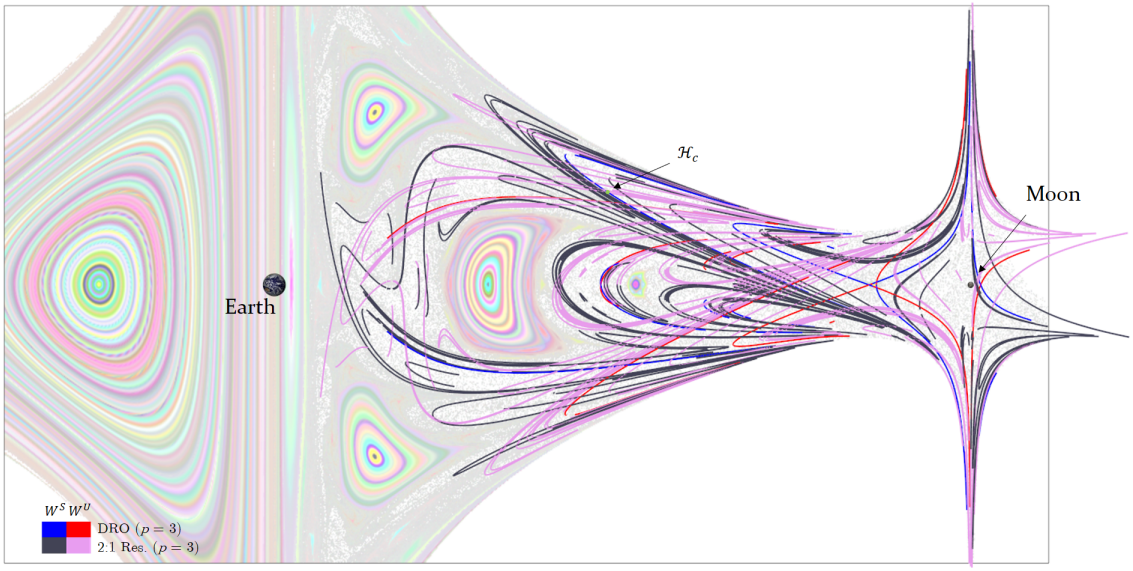

(a) Manifolds for the $p = 3$ DRO and 2:1 resonant orbit

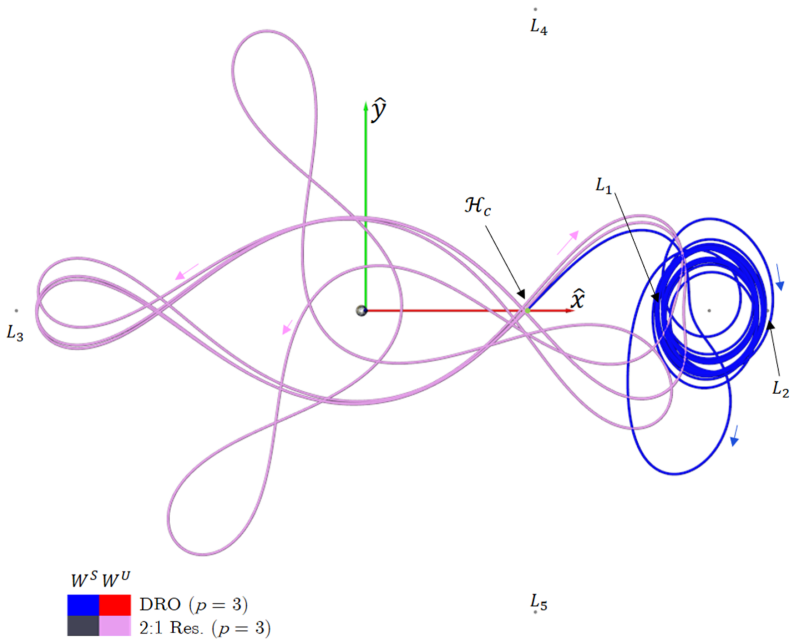

(b) $\mathcal{H}_c$: 2:1 resonant orbit to $p = 3$ DRO ($\Delta t = 197.22$ days)

Figure 9.14. Invariant manifolds for the 2:1 resonant orbit (Orbit 53) and $p = 3$ DRO extracted with PMATE and a selected heteroclinic connection in the Earth-Moon system ($C = 2.96$).

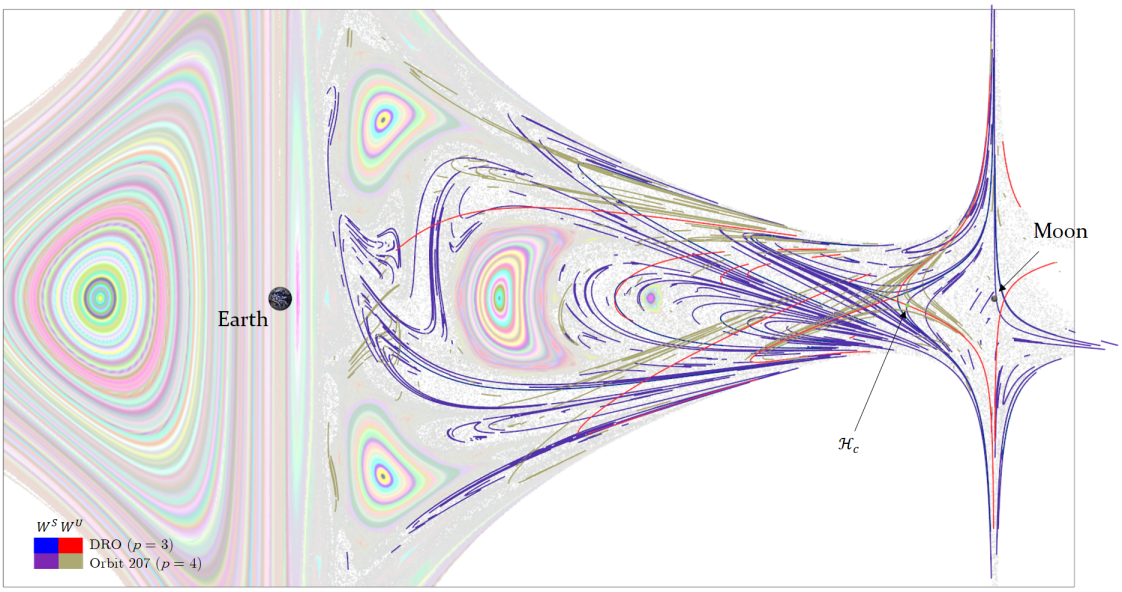

(a) Manifolds for the $p = 3$ DRO and Orbit 207

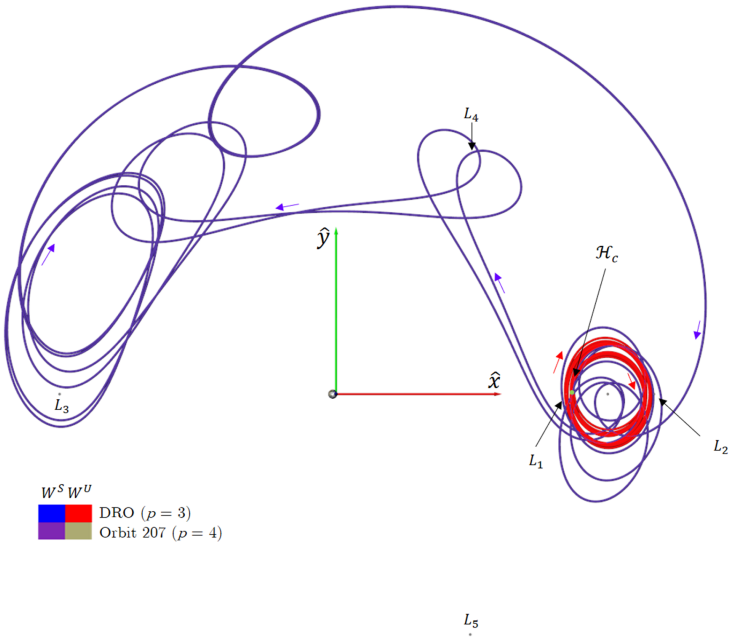

(b) $\mathcal{H}_c$: $p = 3$ DRO to Orbit 207 ($\Delta t = 197.22$ days)

Figure 9.15. Invariant manifolds for the $p = 3$ DRO and Orbit 207 extracted with PMATE and a selected heteroclinic connection in the Earth-Moon system ($C = 2.96$).

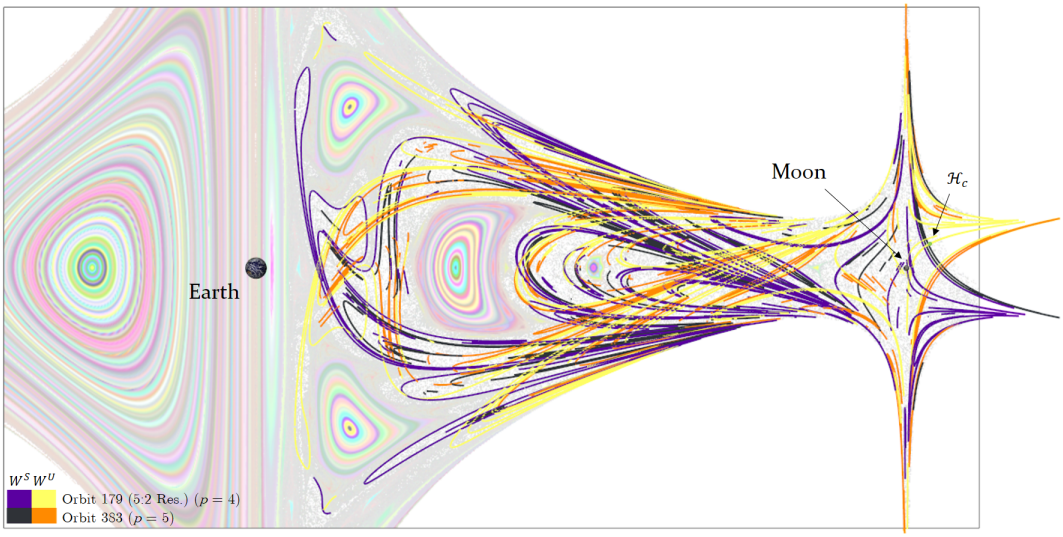

(a) Manifolds for Orbits 179 and 383

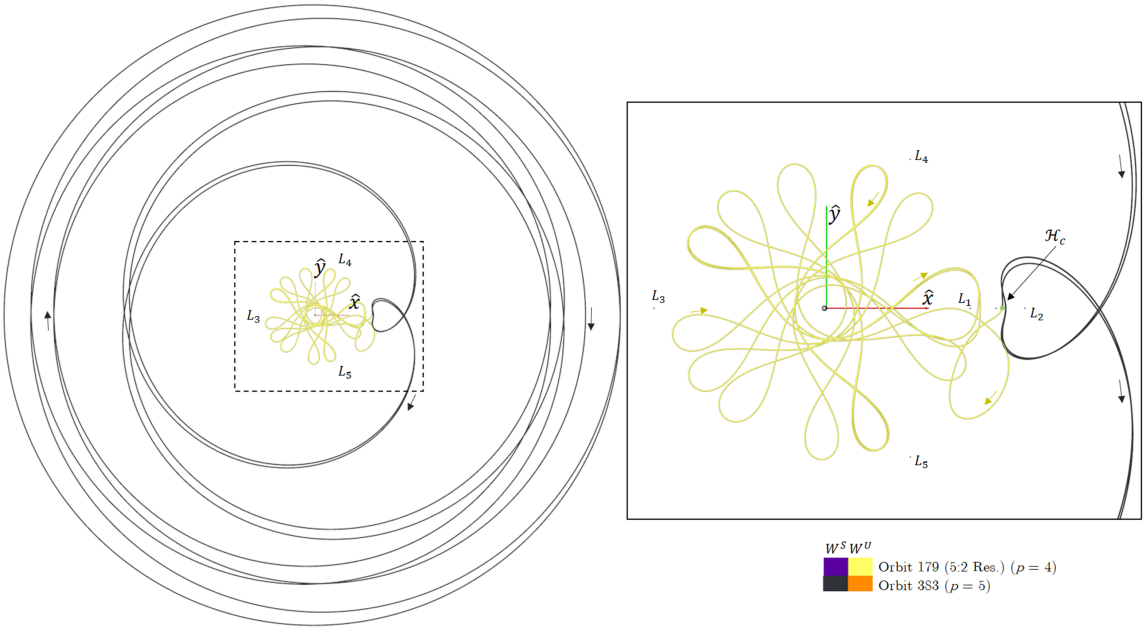

(b) $\mathcal{H}_c$: Orbit 179 to Orbit 383 ($\Delta t = 567.99$ days)

Figure 9.16. Invariant manifolds for Orbit 179 and Orbit 383 extracted with PMATE and a selected heteroclinic connection in the Earth-Moon system ($C = 2.96$).

9.4 Example of a LEO-to-Orbit Design Scenario

The novel design capabilities supplied by interactive design strategies featuring Poincaré map topology data grant a designer full access to the natural pathways of the CRTBP model. One example design scenario that exemplifies the new capabilities is the design of a pathway from a low-Earth orbit (LEO) to an arbitrary periodic orbit in the Earth-Moon system. In this scenario, the destination orbit is selected as the $p = 3$ DRO since the $p = 3$ DRO manifolds possesses no direct intersection with LEO structures (as shown by Figure 9.9(a)). The goal of the design is to construct transfers with the minimum ΔV requirements possible regardless of lengthy flight times. Such a mission constraint is typical of either a robotic science or communication mission and could even apply to heavy-lift modules for station construction if a manned station resides in the DRO vicinity. Since Poincaré map topology is already extracted for $C = 2.96$, the target destination is arbitrarily set as the same $p = 3$ DRO appearing in Section 9.3.

The first step of the design is to examine how to leave LEO to head towards the DRO region. Note that no currently extracted dynamical structure passes near a LEO altitude (less than 300 km), so the orbit convolution imagery at $C = 2.96$ is examined for potential orbital structure near the LEO or intersecting Earth. As shown by the OC image in Figure 9.17, a vertically thing quasi-periodic region resides on the $+x$ side of Earth. Although the middle of this region is a center-type periodic orbit (Orbit 48 also known as a stable 4:1 resonant orbit), the edges pinch in the $\pm\dot{x}$ directions, indicating that Orbit 48 exists in a saddle-center island chain with a yet unknown saddle that is similar to Orbit 48. Since the desired saddle-type periodic orbit possesses returns slightly outside the PMATE analysis domain, Poincaré map interaction combined with fixed point refinement isolates the desired saddle, designated Orbit 48* because it is the unstable form of the 4:1 resonance in Orbit 48. PMATE advects the invariant manifolds for Orbit 48* as the black stable manifolds and crimson unstable manifolds in Figure 9.17(a) where portions of the stable manifold of Orbit 48* reach LEO altitudes and even dip within the Earth, too. A stable manifold selection within the Earth, as shown in Figure 9.17(a), creates a potential transfer arc that forms a few LEO departure options. As shown with the CRTBP form of the Oberth effect (Section 8.3.2), it is best to change Jacobi constant from LEO to this arc as close to Earth

as possible. The location along the selected stable manifold arc that is closest to Earth while not intersecting is chosen as the LEO departure point, occurring at an altitude of 271.49 km and shown in Figure 9.17(c). Here, the theoretical minimum maneuver to reach the any orbit at $C = 2.96$ is $\Delta V_{\text{min}} = 3083.07$ m/s. The initial LEO departure burn, or ΔV_1 as displayed in Figure 9.17(c), is roughly the same as the theoretical minimum with $\Delta V_1 = 3083.11$ m/s to enter the stable manifold arc. In this saddle configuration, lunar gravity tugs the initial arc up towards the periapse altitude of the unstable 4:1 resonant orbit at roughly 2000 km even though the initial altitude is 271.49 km. Thus, the departure from LEO with ΔV_1 to a W^S arc of Orbit 48* forms the first leg of the transfer to the $p = 3$ DRO. As an aside, the Earth impact just prior to the selected LEO departure condition if Figure 9.17(c) could actually be deployed as a launch state to directly enter the stable manifold structure of Orbit 48* instead of departing from LEO.

The next step in the design process is to depart the unstable 4:1 resonant orbit towards the $p = 3$ DRO. Unfortunately, the unstable manifold of Orbit 48* never directly intersects any of the invariant manifolds extracted with PMATE because this orbit sits in a region of bounded chaos, and so, a bridge over the dynamical boundary is forged by employing a map preserving maneuver that connects W^U of Orbit 48* to a stable manifold arc of a potential transfer orbit. Several saddle-type fixed points are potential transfer candidates with returns near the Earth or Orbit 48*. Transfer candidates are tabulated with the other orbits relevant to this design scenario in Table 9.3. The invariant manifolds for the various transfer candidates are extracted and portrayed on the Poincaré section with distinct colors for each W^S and W^U (displayed in Figure 9.18). No direct intersections between the crimson W^U of Orbit 48* and any of the indicated stable manifolds exist, but two areas on the Poincaré section – shown as the encircled transfer zones in Figure 9.18 – indicate small vertical discrepancies where a $\Delta\dot{x}$ between manifold structures can produce a small map-preserving maneuver to achieve the desired link.

The transfer zones highlighted in Figure 9.18 are then examined with interactive topology-based design tools for the smallest map-preserving maneuver. An infinite number of configurations exist initially as every displayed Poincaré section state is a discrete arc, but versatile spaceflight design with Poincaré map topology evaluates multiple augmented $\mathcal{H}_c$ options quickly without propagation of actual arcs to localize an area that possesses the

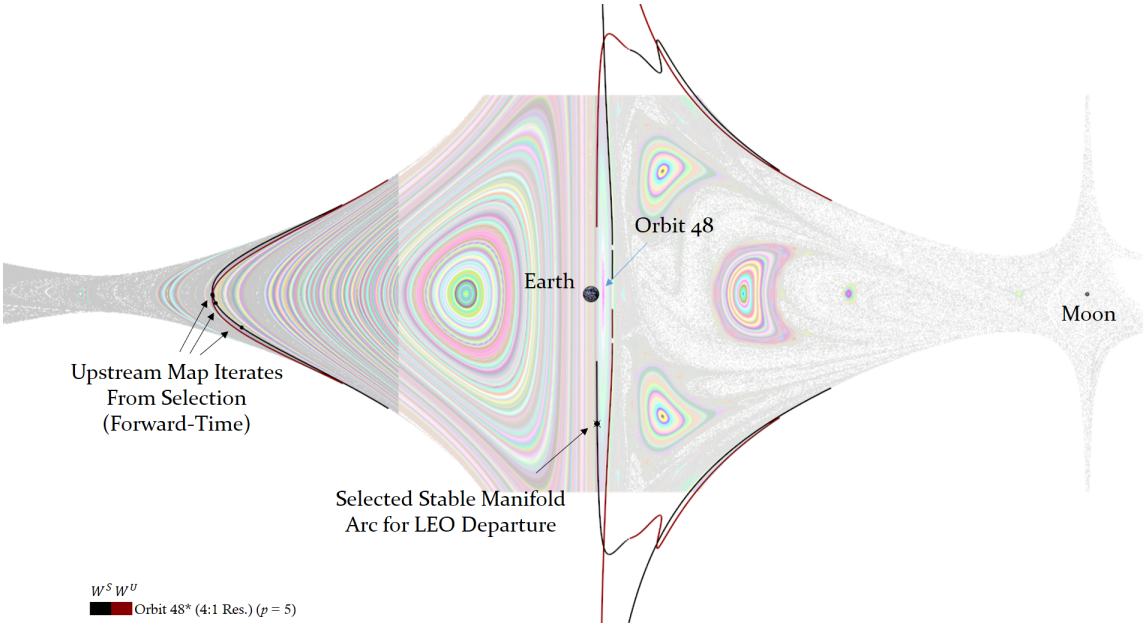

(a) Manifolds for Orbit 48* and selected W^S arc

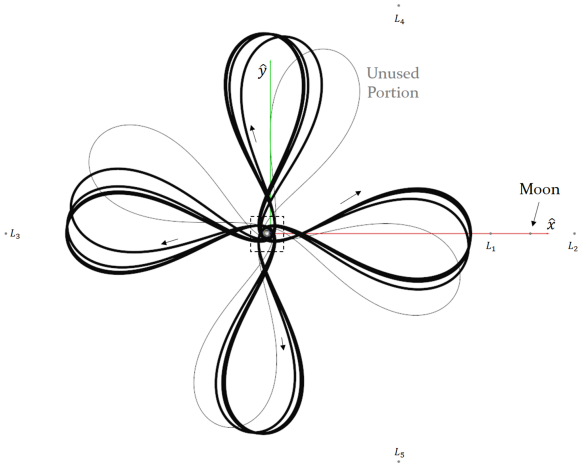

(b) Selected W^S arc

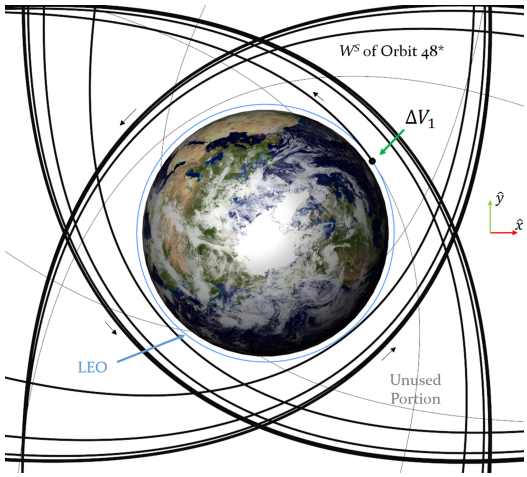

(c) Selected W^S arc and LEO departure

Figure 9.17. Departure from a LEO onto a nearby stable manifold arc at $C = 2.96$ in the Earth-Moon system.

ID	Parameters	Orbit (Map)	Orbit (xy)
48	$p = 3C$ $T = 27.32$ $\nu_{SI} = 7.08e-01$ $\nu_{z,SI} = 1.00$	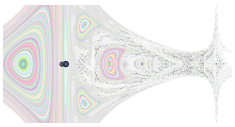	
48*	$p = 5S$ $T = 27.30$ $\nu_{SI} = 1.97e-00$ $\nu_{z,SI} = 0.97$	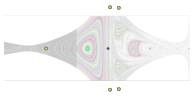	
50	$p = 3S$ $T = 30.23$ $\nu_{SI} = 1.06e+00$ $\nu_{z,SI} = -0.38$	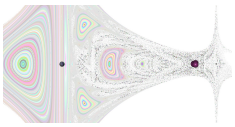	
51	$p = 3S$ $T = 27.58$ $\nu_{SI} = 8.46e+00$ $\nu_{z,SI} = 0.60$	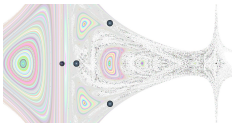	
53	$p = 3S$ $T = 27.93$ $\nu_{SI} = 7.38e+01$ $\nu_{z,SI} = -0.99$	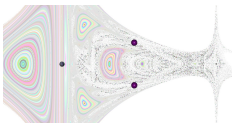	
179	$p = 4S$ $T = 55.06$ $\nu_{SI} = 4.58e+01$ $\nu_{z,SI} = -0.22$	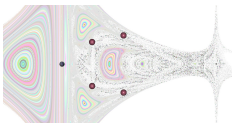	
577	$p = 6S$ $T = 54.72$ $\nu_{SI} = 3.79e+00$ $\nu_{z,SI} = 0.86$	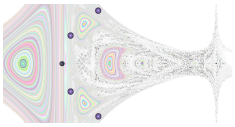	
1063	$p = 9S$ $T = 82.20$ $\nu_{SI} = -3.86e+00$ $\nu_{z,SI} = 0.60$	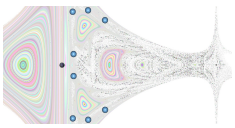	
1386	$p = 12S$ $T = 109.76$ $\nu_{SI} = -5.26e+01$ $\nu_{z,SI} = -0.19$	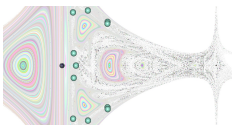	

Table 9.3 Relevant fixed points for a LEO to $p = 3$ DRO (Orbit 50) design scenario extracted with PMATE from $\Sigma : y = 0$ in the Earth-Moon system at $C = 2.96$ (T listed in days).

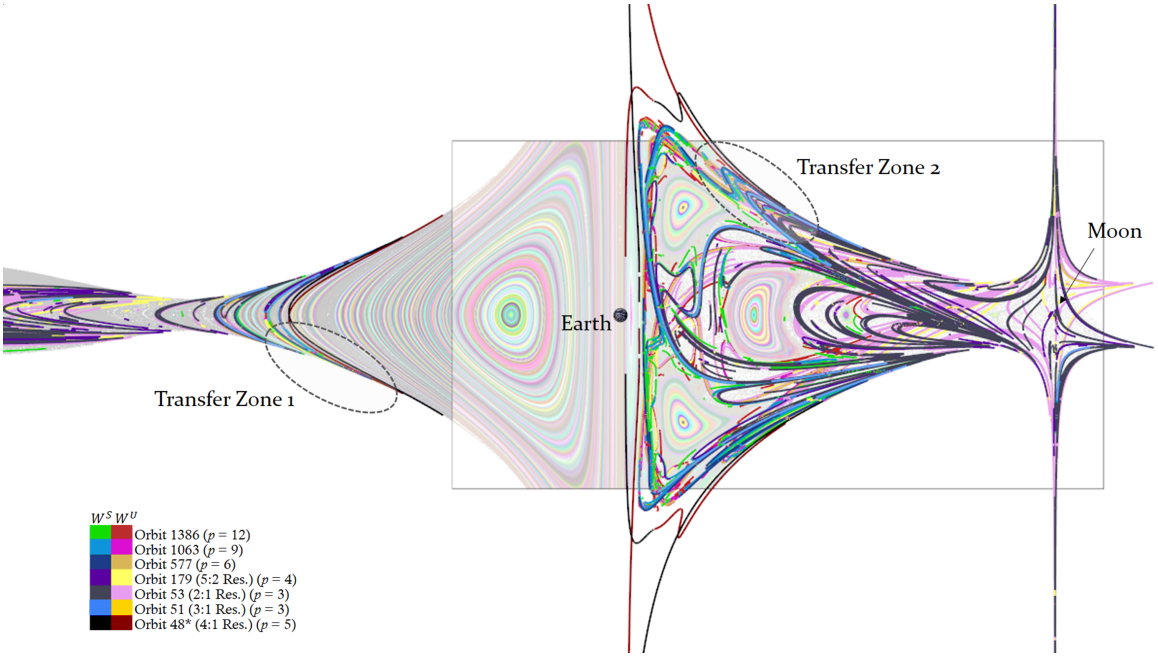

Figure 9.18. The invariant manifolds of saddle-type periodic orbits that are near the unstable manifolds of Orbit 48* and also intersect the $p = 3$ DRO stable manifolds.

cheapest ΔV options. This rapid trade study is demonstrated by the examination of Transfer Zone 1 in Figure 9.19(a) and Transfer Zone 2 in Figure 9.19(b). A click on the crimson W^U of Orbit 48* sets an x position on the Poincaré map and a downward drag to a W^S structure forms the augmented $\mathcal{H}_c$ and associated information. The ΔV requirements for the whole maneuver is displayed adjacent to the interactively design transfer option (the $\Delta\dot{x}$ is also conveyed through the bracketed value). Since most of the options require a design that translates towards the zero-velocity curve on the section, the overall ΔV for these transfer possibilities is typically much larger than the vertical map translation. As a result, the cheapest ΔV options are typically either with very little $\Delta\dot{x}$ or where the destined stable manifold sits sufficiently away from the zero-velocity boundary on the surface of section. The interactive selection trade study finds the cheapest ΔV option for an augmented $\mathcal{H}_c$ at the termination point of the connected Orbit 48* W^U curve in Transfer Zone 2, registered as the red selection with $\Delta V = 53.54$ m/s in Figure 9.19(b). This transfer option connects a W^U arc originating from Orbit 48* to a W^S arc of Orbit 1386 as shown by the associated

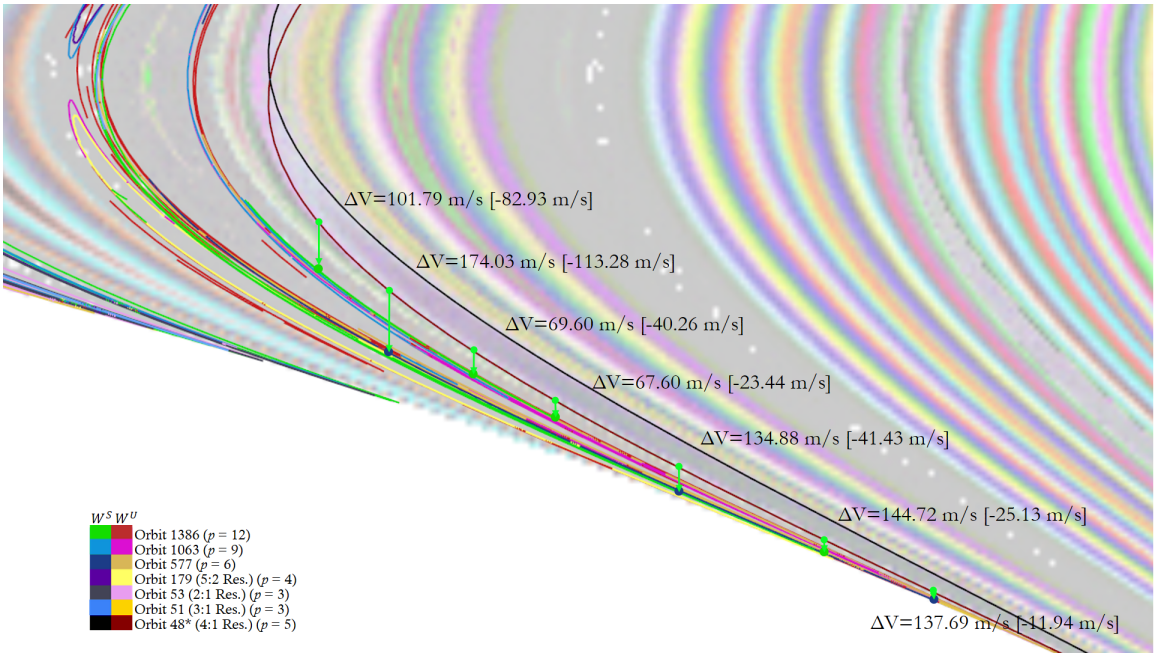

(a) Transfer Zone 1 Options

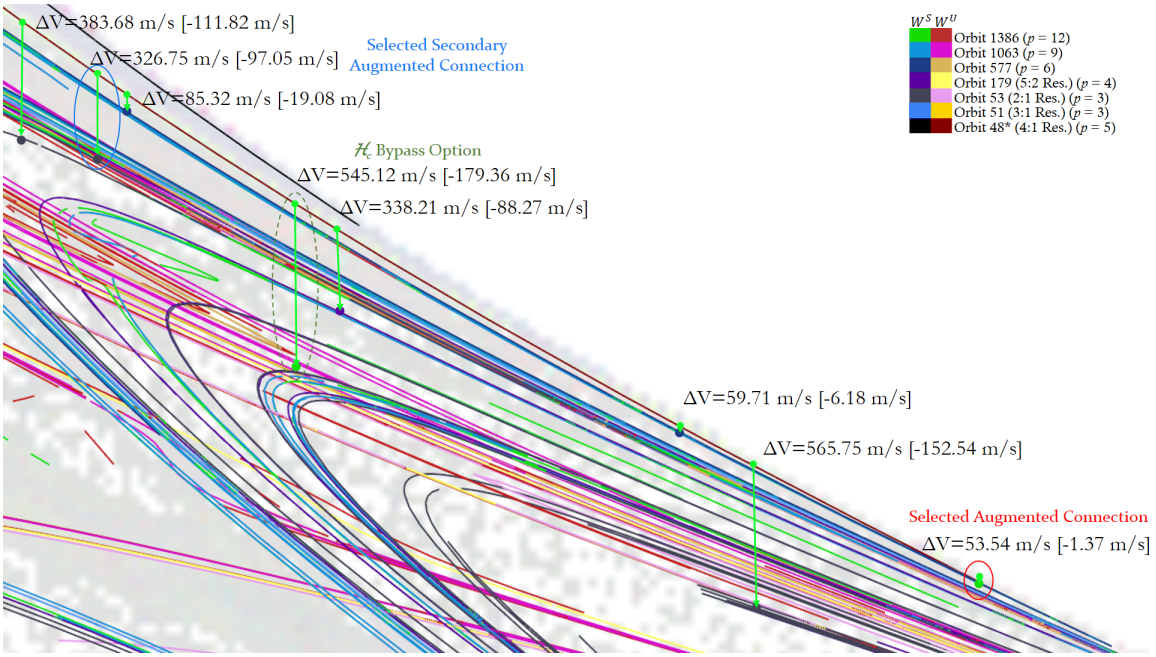

(b) Transfer Zone 2 Options

Figure 9.19. Trade studies on various augmented $\mathcal{H}_c$ in possible transfer zones from Orbit 48* W^U to W^S of intermediate transfer orbits. Bracketed velocities represent vertical translation on the Poincaré section ($\Delta\dot{x}$).

trajectories of the design option in Figure 9.20. Note that the transfer maneuver (ΔV_2) occurs on the x-axis (as per Σ), and the maneuver mainly points in the $\hat{y}$ direction.

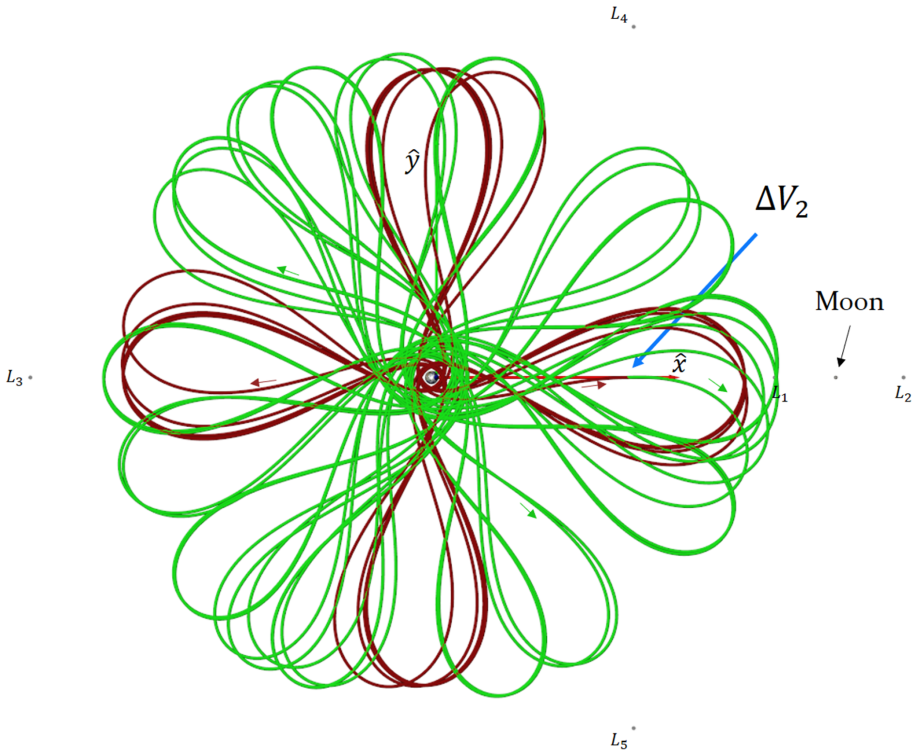

Figure 9.20. An augmented $\mathcal{H}_c$ bridging the unstable manifold of Orbit 48* (crimson) to the stable manifold of Orbit 1386 (green) by employing a map-preserving maneuver at the Σ crossing at ΔV_2 ($\Delta t = 602.20$ days).

With an augmented connection formed from Orbit 48* to Orbit 1386, the last leg of this design scenario is to define a $\mathcal{H}_c$ from Orbit 1386 to $p = 3$ DRO to exploit natural dynamics to arrive at the transfer destination. As shown in Section 9.3.2, a selection of any overlapping segments of Orbit 1386 W^U and W^S of the $p = 3$ DRO suffices as a possible heteroclinic connection. Invariant manifolds of Orbit 1386 and the $p = 3$ DRO are interlaced in Figure 9.21 with a selected connection indicated in Figure 9.21(b). The selected $\mathcal{H}_c$ merely represents one of many heteroclinic connection options; other $\mathcal{H}_c$ options could possess a shorter flight duration with less time in Earth-vicinity, indicating that another trade study should be considered.

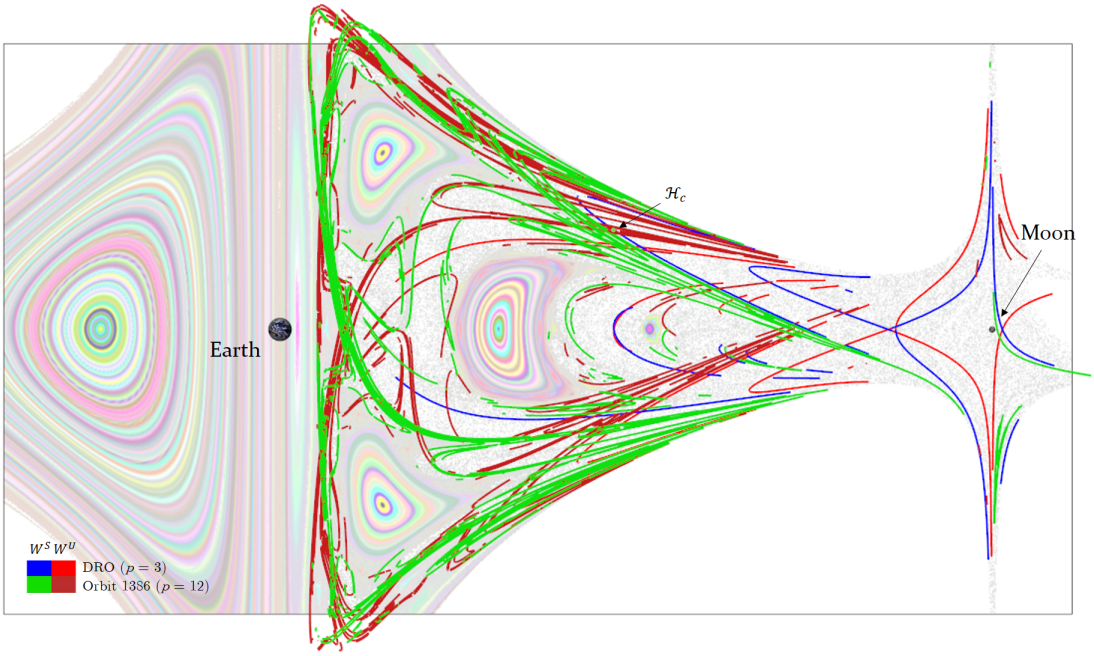

(a) Manifolds for Orbit 1386 and the $p = 3$ DRO

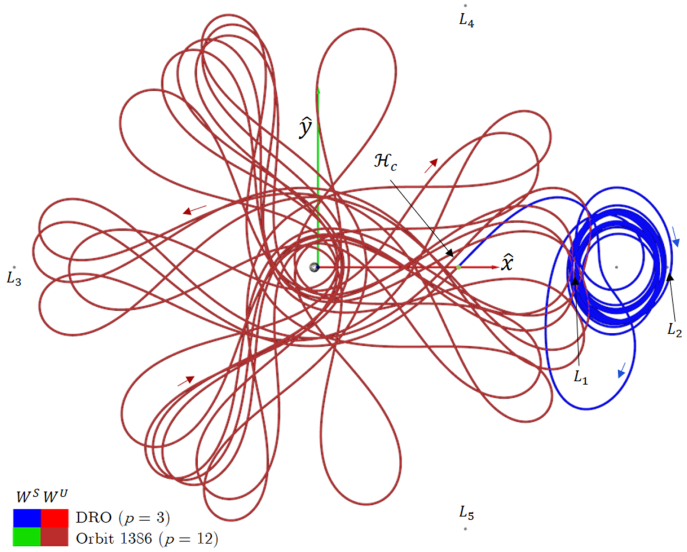

(b) H_c : Orbit 1386 to $p = 3$ DRO ($\Delta t = 342.82$ days)

Figure 9.21. Invariant manifolds for Orbit 1386 and the $p = 3$ DRO extracted with PMATE and a selected heteroclinic connection in the Earth-Moon system ($C = 2.96$).

The LEO-to-orbit preliminary planning scenario exploiting Poincaré map topology concludes with an analysis of the constructed design. A listing of the events of the design mission from LEO to the $p = 3$ DRO is available in Table 9.4 with a maneuver summary in Table 9.5. Arcs relevant to this constructed design after the arrival in Orbit 48* appear in Figure 9.22, including some loitering in intermediate periodic orbits for manifold arrival to departure realignment. The total ΔV for the entire design is only 53.58 m/s more than theoretical minimum (ΔV_{min}), resulting in a ΔV savings of ≈ 350 m/s over similar designs [83]. The total time of flight, however, is substantial at 3.02 years (1102.92 days) even with, but that is expected when letting the natural dynamics transition the spacecraft. Note that the transit time to the $p = 3$ DRO is listed as the time of flight to the practical arrival condition. The main contribution to time of flight is the long wait to naturally transition through an intermediate saddle structure such as Orbits 48* and 1386. This includes the flight time to asymptotically approach the intermediate structure along W^S, loiter in the orbit for a partial revolution, and asymptotically depart via W^U, at least based on the current design methodology. Thus, it makes sense that a much longer time of flight is required for the constant tugging of the lunar gravity to gradually pull the spacecraft to the intended destination.

Epoch	Event	Δt	ΔV (m/s)
0.0	Start in LEO ($h = 271.49$ km)		
0.0	ΔV_1 : LEO to W^S arc of 4:1 res. orbit (48*)		3083.11
0.0	Arc: Transit on W^S of 4:1 res. orbit (48*)	139.15	
139.15	Arc : Loiter in 4:1 res. orbit (48*) for partial rev.	10.23	
149.38	Arc : Aug. $\mathcal{H}_c$ transit on W^U of 4:1 res. orbit (48*)	165.94	
315.31	ΔV_2: Aug. $\mathcal{H}_c$ maneuver to W^S of Orbit 1386		53.54
315.31	Arc : Aug. $\mathcal{H}_c$ coast on W^S of Orbit 1386	436.26	
751.57	Arc : Loiter in Orbit 1386 for partial rev.	8.53	
760.10	Arc : $\mathcal{H}_c$ Coast on W^U of Orbit 1386	265.03	
1025.11	Arc : $\mathcal{H}_c$ Coast on W^S of $p = 3$ DRO	77.81	
1102.92	Arrival at $p = 3$ DRO (practical)		
	Totals	**1102.92**	**3136.65**

Table 9.4 Epochs and flight duration for the LEO to $p = 3$ DRO transit design constructed with Poincaré map topology. (Epoch and Δt are listed in days.)

Name	ΔV_x (m/s)	ΔV_y (m/s)	ΔV_z (m/s)	Epoch	ΔV (m/s)
ΔV_1	−1736.92	2547.29	0.0	0.00	3083.11
ΔV_2	−1.37	53.52	0.0	315.31	53.54
ΔV_{Total}					3136.65

Table 9.5 Summary of maneuvers in rotating frame coordinates for the LEO to $p = 3$ DRO design constructed with Poincaré map topology. (Epoch listed in days.)

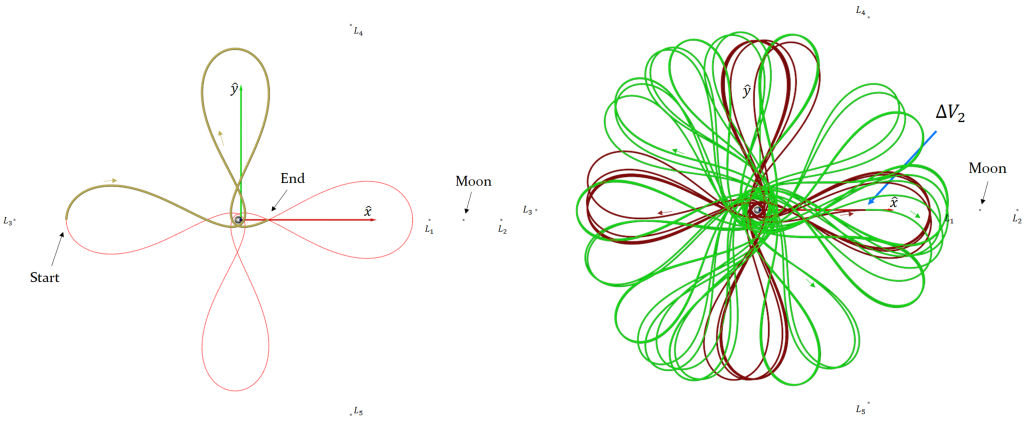

(a) Loiter (gold) in Orbit 48* ($\Delta t = 10.23$ days) (b) Augmented $\mathcal{H}_c$ from Orbit 48* to Orbit 1386 ($\Delta t = 602.20$ days)

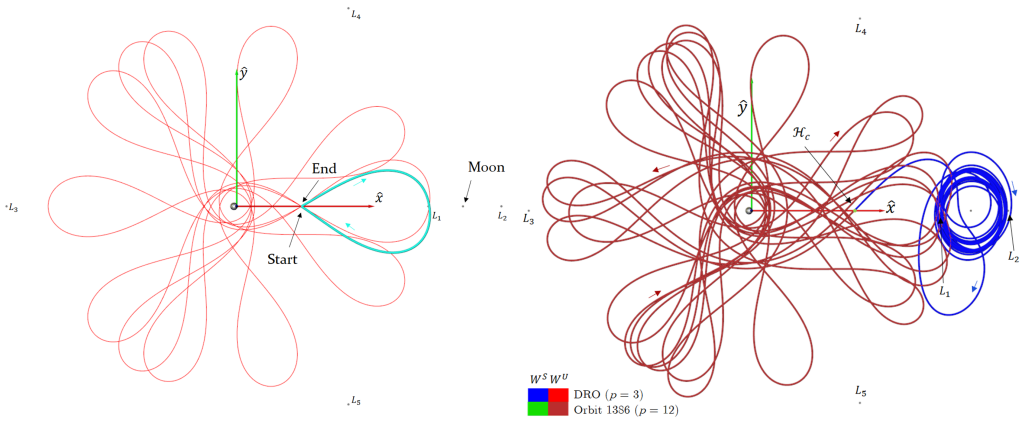

(c) Loiter (cyan) in Orbit 1386 ($\Delta t = 8.53$ days) (d) $\mathcal{H}_c$: Orbit 1386 to $p = 3$ DRO ($\Delta t = 342.82$ days)

Figure 9.22. Transfer arcs of the LEO to $p = 3$ DRO design listed in Table 9.4.

An option to reduce the time of flight is to jump from W^U of Orbit 48* directly into a computed heteroclinic connection. For example, a spacecraft could bypass the full $\mathcal{H}_c$ connecting Orbit 1386 to the $p = 3$ DRO by performing a map-preserving maneuver from Orbit 48* W^U to a sub-iterate of the intended connection. Examining the W^U arc of Orbit1386 for a Poincaré map iterate in close proximity to the W^U curve of Orbit 48*, the 14^{th} from the start of $\mathcal{H}_c$ in Figure 9.21(b) resides nearby ($\Delta\dot{x} = -179.36$ m/s) as indicated by the encircled green $\mathcal{H}_c$ bypass option in Figure 9.19(b). The caveat to this particular $\mathcal{H}_c$ bypass design is that the bridging maneuver also incurs a large $\Delta\dot{y}$, bringing the total $\Delta V_2 = 545.12$ m/s. The time-of-flight, though, is significantly reduced compared to the original design since this option bypasses the W^S arc of Orbit 1386, the loiter in Orbit 1386, and approximately half of the $\mathcal{H}_c$ W^U arc of Orbit 1386. The resulting mission itinerary for this $\mathcal{H}_c$ bypass (Table 9.6) conveys the total flight time as 1.45 years for the spacecraft to reach the practical $p = 3$ DRO arrival condition.

Epoch	Event	Δt	ΔV (m/s)
0.0	Start in LEO ($h = 271.49$ km)		
0.0	ΔV_1 : LEO to W^S arc of 4:1 Res. orbit (48*)		3083.11
0.0	Arc: Transit on W^S of 4:1 res. orbit (48*)	139.15	
139.15	Arc : Loiter in 4:1 res. orbit (48*) for partial rev.	10.23	
149.38	Arc : Coast on W^U of 4:1 res. orbit (48*)	165.46	
314.84	ΔV_2: Jump to $\mathcal{H}_c$ on W^U of Orbit 1386		545.12
314.84	Arc : Transit on partial $\mathcal{H}_c$ on W^U of Orbit 1386	136.34	
450.91	Arc : $\mathcal{H}_c$ Coast on W^S of $p = 3$ DRO	77.81	
528.72	Arrival at $p = 3$ DRO (practical)		
	Totals	**528.72**	**3628.23**

Table 9.6 Epochs and flight duration for the LEO to $p = 3$ DRO transit design that directly connects to a heteroclinic connection with the $p = 3$ DRO. (Epoch and Δt are listed in days.)

An alternative geometry influenced by stronger saddle behavior presents another option to reduced the time of flight in a LEO to $p = 3$ DRO design. The 2:1 resonant orbit (Orbit 53) possesses a slightly higher stability index than Orbit 1386 and is still in the same Poincaré section vicinity as the previous design (i.e., in Transfer Zone 2). The larger saddle strength of Orbit 53 provides faster approach and departure times while transiting the augmented and heteroclinic connections because the characteristic multiplier ($\lambda_{\max}$)

Name	ΔV_x (m/s)	ΔV_y (m/s)	ΔV_z (m/s)	Epoch	ΔV (m/s)
ΔV_1	−1736.92	2547.29	0.0	0.00	3083.11
ΔV_2	−179.36	514.77	0.0	314.84	545.12
ΔV_{Total}					3628.23

Table 9.7 Summary of maneuvers in rotating frame coordinates for the LEO to $p = 3$ DRO design that directly connects to a heteroclinic connection with the $p = 3$ DRO. (Epoch listed in days.)

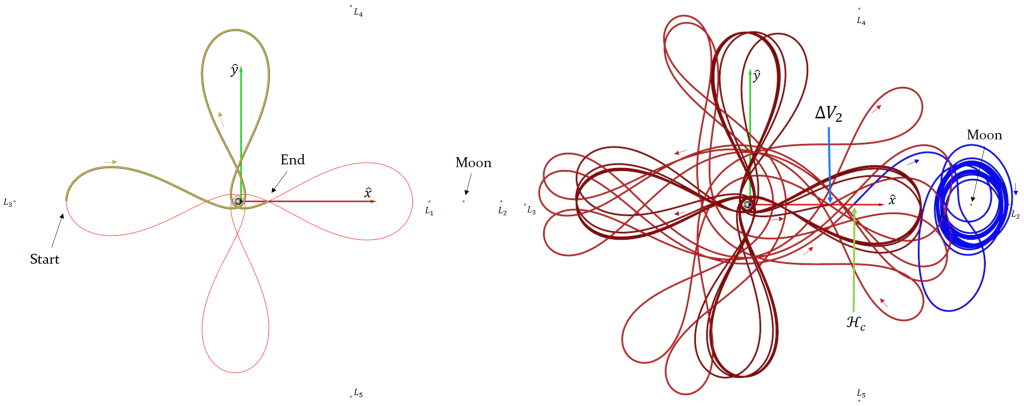

(a) Loiter (gold) in Orbit 48* ($\Delta t = 10.23$ days) (b) Augmented $\mathcal{H}_c$ bypass ($\Delta t = 379.61$ days)

Figure 9.23. Transfer arcs of the LEO to $p = 3$ DRO design employing an $\mathcal{H}_c$ bypass as listed in Table 9.6.

yields more intense attraction and repulsion. The LEO to $p = 3$ DRO design is constructed in a similar manner as before but with the 2:1 resonant arc standing as the intermediate transfer orbit between the W^U of Orbit 48* and the W^S of the $p = 3$ DRO. The topology-based design selection is interactively selected from the blue secondary option in Transfer Zone 2 (Figure 9.19(b)). The heteroclinic connection previously devised in Figure 9.14 is employed to transition from the 2:1 resonant orbit to the destination. Unfortunately, a heteroclinic bypass option is not available here as the selected $\mathcal{H}_c$ between the 2:1 resonant orbit and the $p = 3$ DRO does not offer any Poincaré map iterates in the vicinity of an Orbit 48* W^U branch for practical design considerations. The preliminary design arcs for this secondary option are displayed in Figure 9.24 with the flight itinerary described by Tables 9.8 and 9.9. This secondary design requires a total maneuver budget of 326.79 m/s over the theoretical minimum with a total time of flight of 1.75 years. Although the

flight duration for this secondary design is diminished with only a small increase in ΔV requirements over the minimal ΔV design, alternative LEO-to-DRO pathways exist that modify the Jacobi constant for transfer arcs to shorten flight duration while only slightly increasing the total ΔV. For example, three-impulse transfer sequences to reach the DRO vicinity offered by previous studies possess similar ΔV budgets (around 400 m/s after the initial LEO departure impulse) and complete the trip in under a few weeks instead of a few years [68,83]. Pathways designed solely with Poincaré map topology at a single energy level, therefore, are only recommended for missions where time-of-flight is not a design driver.

Epoch	Event	Δt	ΔV (m/s)
0.0	Start in LEO ($h = 271.49$ km)		
0.0	ΔV_1 : LEO to W^S arc of 4:1 Res. orbit (48*)		3083.11
0.0	Arc: Transit on W^S of 4:1 res. orbit (48*)	139.15	
139.15	Arc : Loiter in 4:1 res. orbit (48*)for partial rev.	10.23	
149.38	Arc : Aug. $\mathcal{H}_c$ transit on W^U of 4:1 res. orbit (48*)	165.29	
314.67	ΔV_2: Aug. $\mathcal{H}_c$ maneuver to W^S of 2:1 res. orbit		326.75
314.67	Arc : Aug. $\mathcal{H}_c$ coast on W^S of 2:1 res. orbit	108.34	
423.01	Arc : Loiter in 2:1 res. orbit for partial rev.	20.17	
443.18	Arc : $\mathcal{H}_c$ Coast on W^U of 2:1 res. orbit	119.41	
562.59	Arc : $\mathcal{H}_c$ Coast on W^S of $p = 3$ DRO	77.81	
640.40	Arrival at $p = 3$ DRO (practical)		
	Totals	**640.40**	**3409.86**

Table 9.8 Epochs and flight duration for the LEO to $p = 3$ DRO transit design employing the 2:1 resonant orbit. (Epoch and Δt are listed in days.)

Name	ΔV_x (m/s)	ΔV_y (m/s)	ΔV_z (m/s)	Epoch	ΔV (m/s)
ΔV_1	−1736.92	2547.29	0.0	0.00	3083.11
ΔV_2	−97.05	312.01	0.0	314.67	326.75
ΔV_{Total}					3409.86

Table 9.9 Summary of maneuvers in rotating frame coordinates for the LEO to $p = 3$ DRO design employing the 2:1 resonant orbit. (Epoch listed in days.)

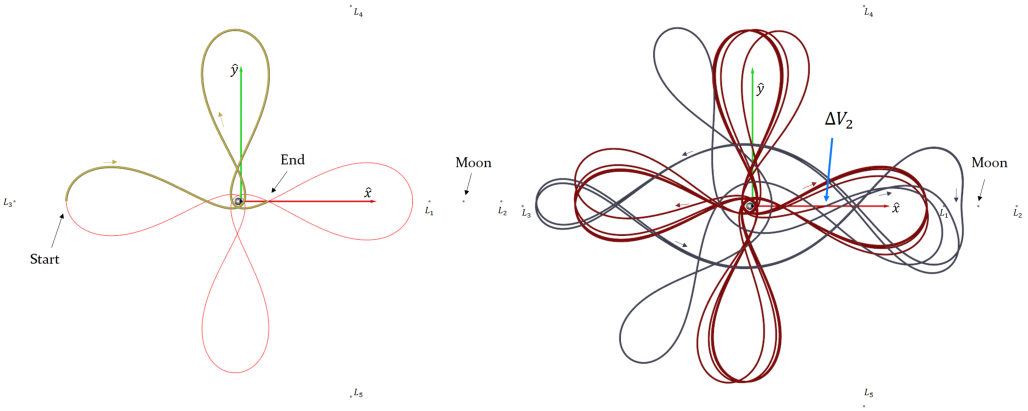

(a) Loiter (gold) in Orbit 48* ($\Delta t = 10.23$ days) (b) Augmented $\mathcal{H}_c$ from Orbit 48* to Orbit 53 ($\Delta t = 273.63$ days)

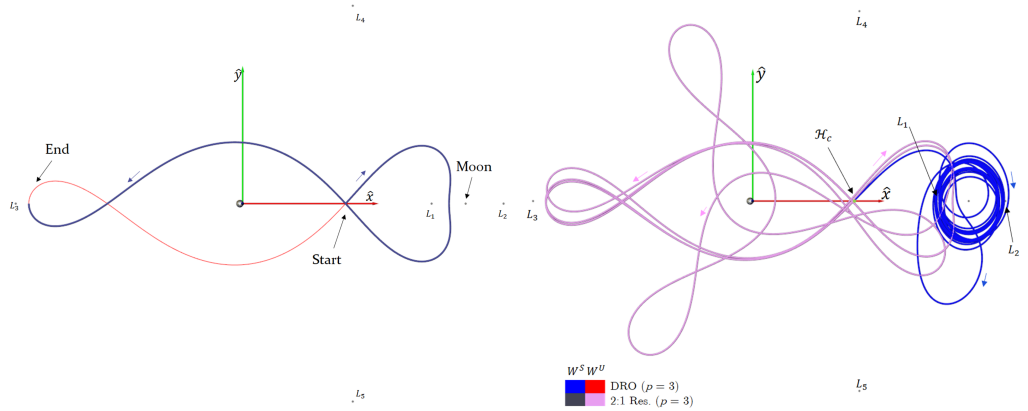

(c) Loiter (blue) in Orbit 53 ($\Delta t = 20.17$ days) (d) $\mathcal{H}_c$: Orbit 53 to $p = 3$ DRO ($\Delta t = 197.22$ days)

Figure 9.24. Transfer arcs of the secondary LEO to $p = 3$ DRO design listed in Table 9.8.

9.5 Versatility Scenario

A scenario where an adaptation to a spacecraft destination is sought illustrates the application of extracted Poincaré map topology to a versatile design paradigm. Assume that a spacecraft with a small amount of remaining fuel is on an undesirable trajectory leaving the Earth-Moon system, creating a desire to reroute the spacecraft to a new destination. Such a scenario is indicative of either a cube satellite that is dropped off from a larger spacecraft or a vehicle at the end of a primary mission. The current Poincaré map state of the undesired effect is $(x, \dot{x}) = (0.8455137, -0.1859837)$ in nondimensional rotating frame coordinates on $\Sigma : y = 0$ at $C = 2.96$ (chosen arbitrarily). The future path, displayed as the red arc in Figure 9.25, performs a pair of lunar flybys before departing Earth-Moon vicinity. In this scenario, the primary mission constraint is to simply avert the spacecraft

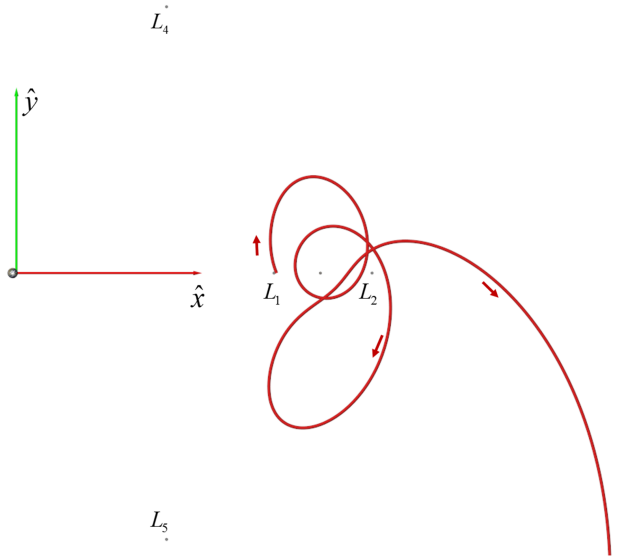

Figure 9.25. Spacecraft trajectory if no maneuver is applied in a versatile design platform scenario with an undesirable escape out of the Earth-Moon system ($C = 2.96$).

from escaping Earth-Moon vicinity subject to available spacecraft resources, namely a ΔV budget arbitrarily set at $\Delta V \leq 20$ m/s.

The rerouting maneuver is designed by examining the nearby stable manifolds on the Poincaré section resulting from PMATE trials (mainly the stable manifolds from Figure 9.7(a)). The maneuver budget constraint is portrayed visually as a green bounding

box surrounding the current map state (red) on the Poincaré section in Figure 9.26. Translation on the Poincaré section via a map-preserving maneuver is restricted to the indicated vertical maneuver line. The collection of stable manifolds from Figure 9.7(a) are also added to Figure 9.26 to observe what dynamical structures reside in close proximity to the current state. Each stable manifold projection is displayed with a unique bluish hue to signify different base orbits. The wealth of nearby stable manifold structure permits a redirection of the spacecraft to a new destination. Interactive map-based design links a map state to a stable manifold extraction point via a map-preserving maneuver along the indicated vertical displacement line. A user quickly examines multiple design options by hovering the mouse over various stable manifolds to observe potential new destination orbits and the ΔV requirements. Figure 9.26 also displays some selected stable manifold arcs within the limited resource budget with the necessary ΔV (and $\Delta\dot{x}$ in brackets). Stable manifold arcs that impact the Moon are indicated by the gray bands, but several impact-safe structures exist within reach of the current state. Possible new destinations include Orbits 71 and 331 visiting the interior region. Exterior region options are also available with Orbits 25, 72, 74, and 383. The spacecraft could even potentially depart towards L_4 or L_5 structures with Orbits 16 and 206, respectively, with still over half of the resources available for additional maneuvers later. More destinations are also possible even within this small region as only invariant manifolds of periodic orbits that possess $|\nu_{SI}| \leq 2500$ are depicted. As demonstrated here, thorough knowledge of the stable manifolds enables the quick correction of a deviation from an intended path or the adaptation of the design to a new destination.

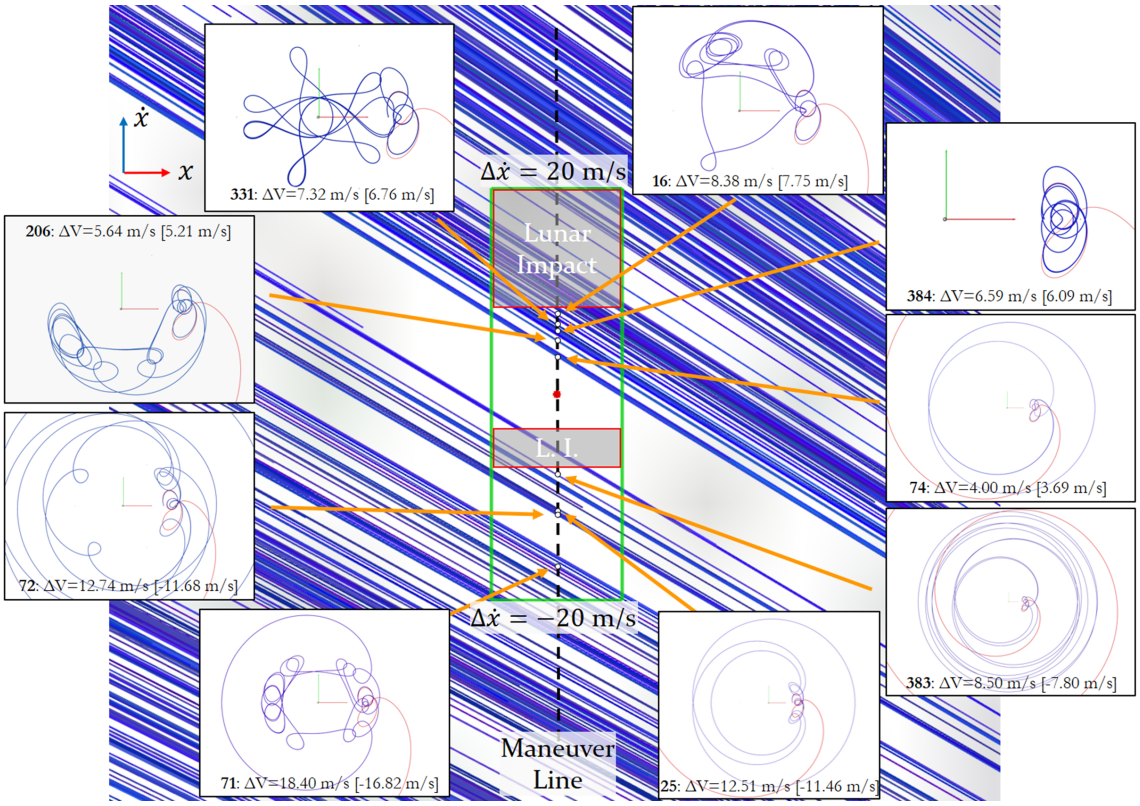

Figure 9.26. A Poincaré section displaying a current trajectory map state (red dot producing the red arc) and possible nearby stable invariant manifolds that are reachable with a $\Delta V \leq 20$ m/s (indicated with green bounding box) employing a map-preserving maneuver in the Earth-Moon system ($C = 2.96$).

9.6 Access to Enceladus

A popular topic in astrodynamics research and development is the determination of a low-ΔV pathway to an orbit about Enceladus. A tantalizing prospect for saving ΔVin an Enceladus endgame pathway is the application of a ballistic capture trajectory that exploits stable invariant manifolds, culminating with natural dynamics depositing a spacecraft into a close orbit around Enceladus. The interactive Poincaré map topology design framework (i.e., PMATE and the associated interactive visual design tools offered by this investigation) delivers the ability to construct such a ballistic trajectory even without detailed knowledge of the Saturn-Enceladus system beforehand.

First, a suitable energy level that permits ballistic capture is sought by utilizing orbit convolution predictions in vicinity of Enceladus. The gravitational influence of Enceladus in the Saturn-Enceladus multi-body system is quite diminished versus the lunar influence in the Earth-Moon system (μ_{SEnc} is 5 orders of magnitude smaller than μ_{EM}). Yet, similar multi-body dynamical structure exists in close proximity to Enceladus that can be exploited in a manner analogous to the Earth-Moon system. The $p = 3$ DRO, for example, resides significantly closer to Enceladus in the Saturn-Enceladus system versus the similar counterpart in the Earth-Moon system. Orbit convolution is, therefore, applied on several domains and Jacobi constant values to locate a suitable DRO structure that is close to Enceladus while possessing safe transfer possibilities. A Jacobi constant value of $C = 2.999995$ demonstrates the desired conditions for the DRO structure as shown by the OC image in Figure 9.27. The whole range of this OC image spreads 1904 km by 0.379 km/s, so the $p = 3$ DRO at this energy level resides at an Enceladus altitude of approximately 600 km. This is exceptionally close to Enceladus considering the characteristic length in the Saturn-Enceladus system (238,042 km). It may be possible to move any computed structure in this vicinity closer to Enceladus by subtly increasing the Jacobi constant, moving the DRO structure in the $+\hat{x}$ direction on the Poincaré section.

The development of a ballistic capture condition continues by analyzing the behavior of fixed points and invariant manifolds in the Enceladus vicinity and beyond. PMATE is employed to extract fixed points throughout the Saturn-Enceladus system. Fixed point extraction trials, indicated in Table 9.10, are guided to grasp a detailed collection of periodic

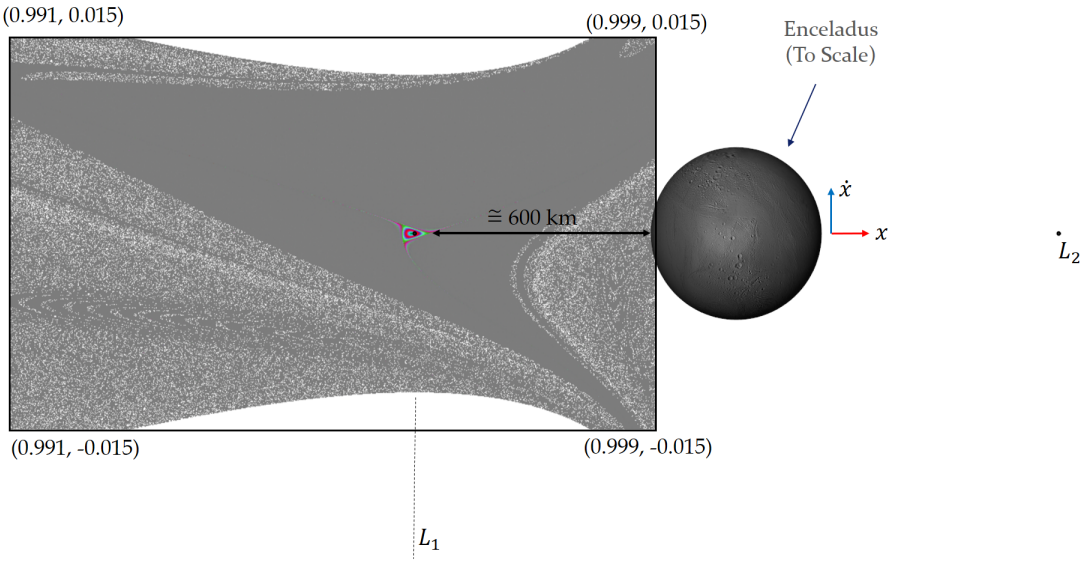

Figure 9.27. Orbit convolution image of a Poincaré section for $\Sigma : y = 0$ in the vicinity of Enceladus in the Saturn-Enceladus system at $C = 2.999995$.

orbits near Enceladus and periodic orbits that visit both Enceladus vicinity and L_3 vicinity. The invariant manifolds are then generated with the advection protocol in PMATE for the $p = 3$ DRO and a small subset of unstable periodic orbits that possess Poincaré section iterates near Enceladus and L_3. As shown by the Poincaré section depictions in Figure 9.28, the unstable $p = 3$ DRO stable manifold subspace (light blue segments) demonstrates many appropriate asymptotic approach arcs without Enceladus intersections. Also, several intersections exist between the $p = 3$ DRO stable manifold and various unstable manifolds of other orbits (red in Figure 9.28), meaning multiple transfer options are available.

The $p = 3$ DRO invariant manifolds also intersect the Poincaré section in the vicinity of L_3. Orbit convolution imagery is combined with computed fixed points and the $p = 3$ DRO invariant manifolds to generate Figure 9.29(a). The red and blue manifolds of Figure 9.28 permeate the chaotic regions in the L_3 vicinity as well but are removed from the representation in Figure 9.29(a) for clarity. A particular location along the $p = 3$ DRO stable manifold is interactively to produce the trajectory represented in Figure 9.29(b). As conveyed through the close-up view around Enceladus in Figure 9.29(b), this selected W^S

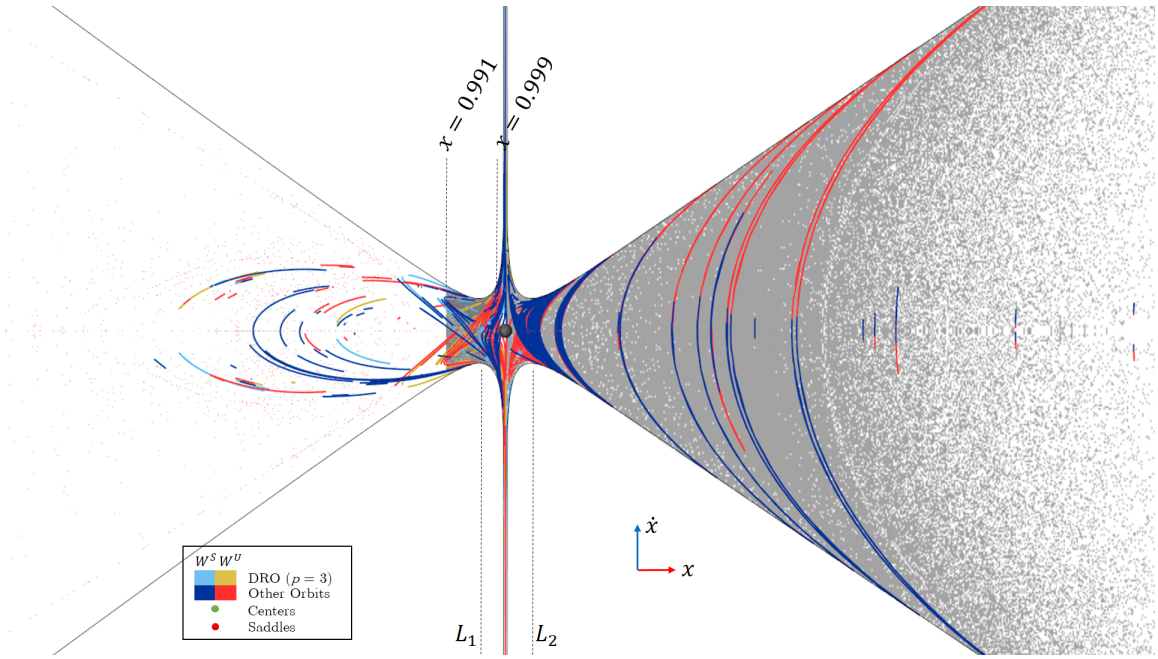

(a) Chaotic regions near Enceladus

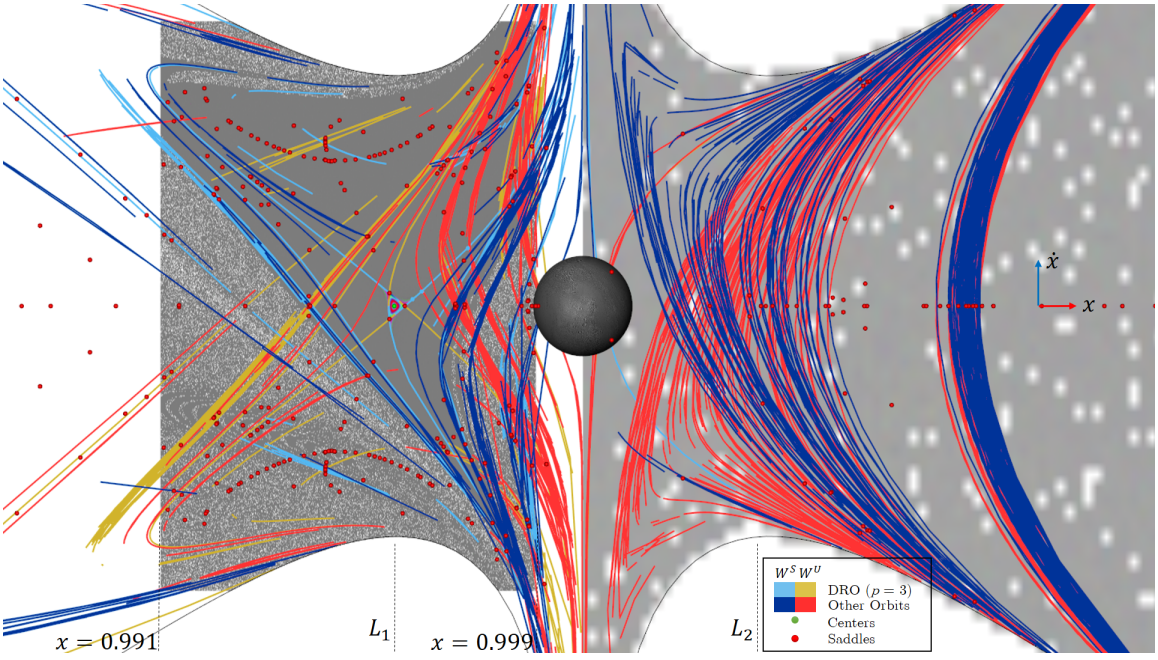

(b) Zoom-in on Enceladus area

Figure 9.28. Fixed points and invariant manifolds extracted with PMATE from the Saturn-Enceladus system at $C = 2.999995$. The selected manifolds are advected from a smaller subset of periodic orbits with Poincaré section crossings in both Enceladus vicinity and near L_3. The vertical dimension is scaled by a factor of 2.5 for enhanced detail.

Trial	Domain (nondim)	Resolution	$l_{\min}$	$p_{\max}$
0	$\{(x,\dot{x})\|x\in[0.8,1.2],\dot{x}\in[-1.0,1.0]\}$	16×16	8×10^{-5}	12
1	$\{(x,\dot{x})\|x\in[-3.5,-1.01],\dot{x}\in[-2.5,2.5]\}$	24×24	8×10^{-5}	12
2	$\{(x,\dot{x})\|x\in[-1.10,-1.0],\dot{x}\in[-0.05,0.05]\}$	16×16	8×10^{-5}	12
3	$\{(x,\dot{x})\|x\in[1.0,1.10],\dot{x}\in[-0.168,0.168]\}$	24×24	2×10^{-5}	8
4	$\{(x,\dot{x})\|x\in[0.96,1.01],\dot{x}\in[-0.06,0.06]\}$	8×8	6×10^{-5}	8
5	$\{(x,\dot{x})\|x\in[0.991,0.999],\dot{x}\in[-0.015,0.015]\}$	12×8	2×10^{-5}	6
6	$\{(x,\dot{x})\|x\in[1.0,1.02],\dot{x}\in[-0.015,0.015]\}$	20×10	2×10^{-5}	6

Table 9.10 Parameters for PMATE executions in the Saturn-Enceladus system at $C = 2.999995$ focusing on dynamics near Enceladus and L_3 vicinity.

arc performs one and a half revolutions around Saturn before one of the inward reaching loops lines up with an Enceladus close passage to then asymptotically approach the $p = 3$ DRO, making $p = 3$ DRO stable manifold structure ideal for constructing ballistic capture arcs. Many additional locations within the indicated zone in Figure 9.29(a) highlight where ballistic capture in the Saturn-Enceladus system is possible. The size of this ballistic capture zone on the Poincaré section in Figure 9.29(a) is somewhat misleading, however, as the orbit convolution image is only 2380 km by 0.379 km/s in dimensional units. Most ballistic capture trajectories and the nearby periodic orbits within this zone possess a similar perturbed circular-orbit structure around Saturn in the rotating frame.

Next, an expanded area beyond L_3 is examined in the Saturn-Enceladus system to comprehend how to bridge the exterior regions to ballistic capture conditions. The orbit convolution image in Figure 9.30 demonstrates the dynamical influence of Enceladus at a much broader region of the exterior to the Saturn-Enceladus system (this zone stretches 595,105 km beyond L_3 and 13.635 km/s between the gray dashed lines). The ballistic capture zone resides inside the tiny black box near L_3, meaning it may be difficult to enter ballistic capture conditions since they reside in a very small region. Figure 9.30 demonstrates a few selected orbits throughout the exterior region and the respective relationship with Saturn and Enceladus (marked with an E in Figure 9.30). Trajectories near the ballistic capture zone again appear as perturbed circular structures in the rotating frame, but other trajectories throughout the stretched quasi-periodic bands show various forms of resonance with Enceladus. All the quasi-periodic colored bands of the OC image are surrounded by an orange exterior KAM curve before the onset of chaotic areas. This exterior KAM

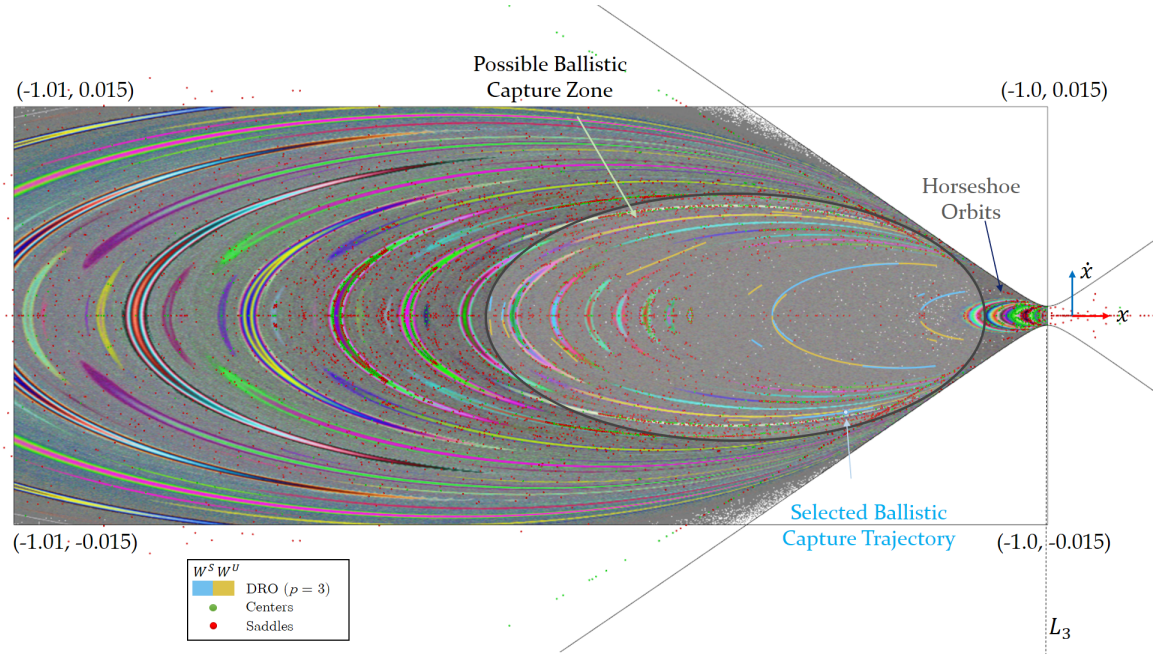

(a) Poincaré section near L_3

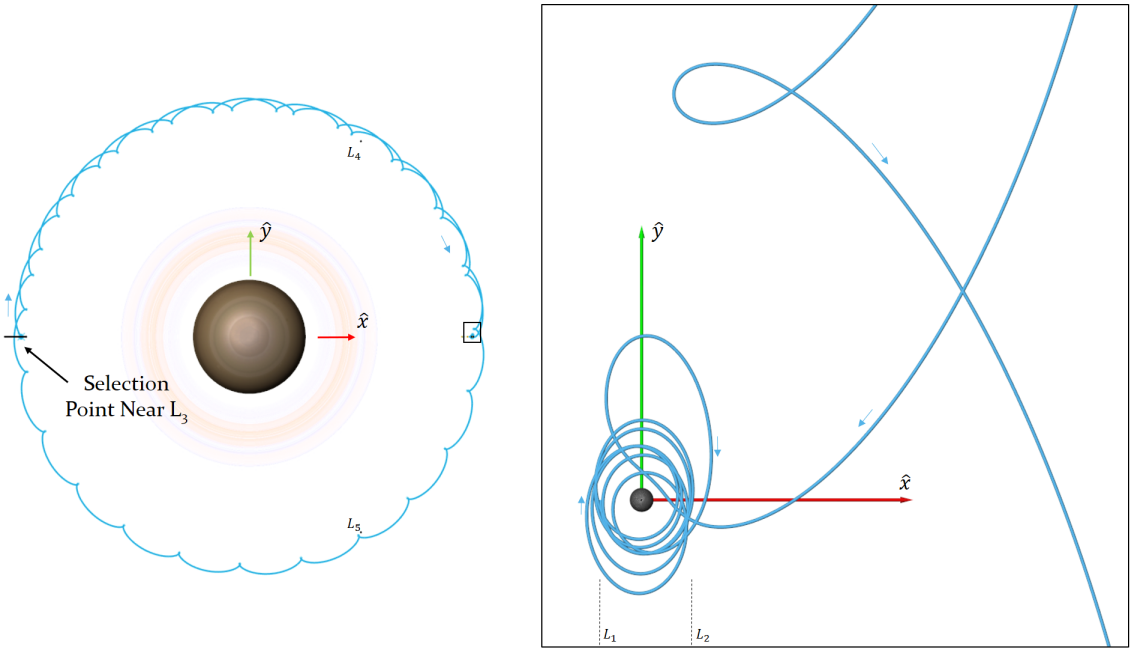

(b) Selected capture arc ($p = 3$ DRO W^S)

Figure 9.29. A plausible region for ballistic capture indicated on a Poincaré section with nearby $p = 3$ DRO manifolds in the Saturn-Enceladus system at $C = 2.999995$.

curve represents a dynamical barrier preventing a purely ballistic pathway that starts at the exterior region (say at Titan) and traverses multiple manifold links to arrive in an Enceladus capture trajectory. Unfortunately, these quasi-periodic bands and the exterior KAM boundary persist for many Jacobi constant values (if not all) as indicated by the set of orbit convolution images for the Saturn-Enceladus system in Appendix A.4. A few insulated pockets of instability exist as bounded chaos within the exterior KAM bounding curve, but a spacecraft approaching Enceladus must break through the bounding quasi-periodic areas with either maneuvers (which are very costly since the bounding curves spread 13.635 km/s in $\dot{x}$ alone) or gravity assists from the other moons of the system. The orbit locations of other Saturnian moons are indicated in Figure 9.30 by red positional markers at the appropriate distance from Saturn. With the close proximity to the moons Rhea, Dione, and Thethys, moon-tour design tools such as V_∞-leveraging are required to transition a spacecraft from exterior locations around Rhea to reach the ballistic capture zone for Enceladus [15–18]. It is unknown if this barrier presents a similar dynamical boundary in the full spatial problem, but many orbits within the exterior KAM boundary possess stable $\nu_{z,SI}$ values, alluding that an out-of-plane version of the exterior KAM boundary exists.

Interactive design with Poincaré map topology constructs the final piece of the endgame problem (ballistic capture trajectories), but Poincaré map topology also presents a format to leave Enceladus vicinity. Although observing Enceladus at close proximity is highly desired, a mission to Enceladus also requires that the spacecraft cannot impact Enceladus based on environmental and planetary protection standards. As such, a spacecraft in orbit about Enceladus is required to depart Enceladus vicinity at the end of the mission. Poincaré map topology offers potential ballistic ejection pathways as the reverse procedure to ballistic capture, namely choosing unstable manifold arcs versus stable manifold arcs. A designer simply selects an unstable arc of the $p = 3$ DRO to the L_3 vicinity within a representation like Figure 9.29(a) to initiate the safe departure. A pathway out of the ballistic capture region towards Tethys or Dione can be constructed with augmented or natural connections. The design can then be subsequently furthered via a V_∞-leveraging procedure to lift the spacecraft to a desired disposal condition such as an impact with an inactive Saturnian moon.

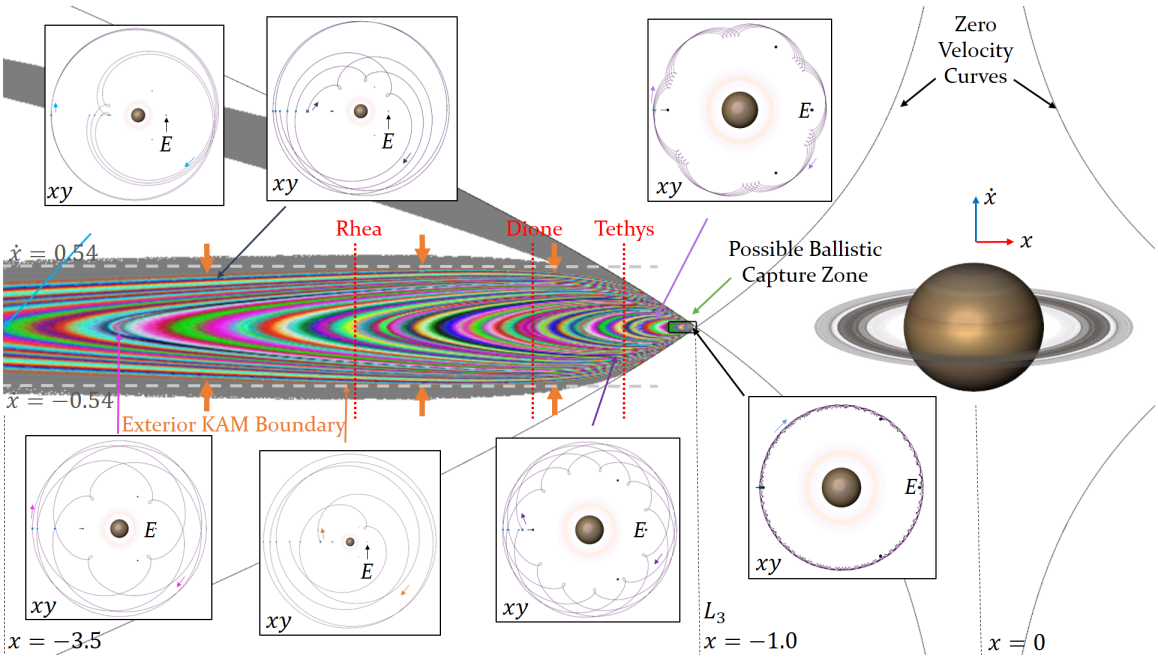

Figure 9.30. Orbit convolution image of a Poincaré section for $\Sigma : y = 0$ beyond the L_3 point in the $-x$ direction in the Saturn-Enceladus system at $C = 2.999995$.

10. SUMMARY AND RECOMMENDATIONS

Poincaré map topology and the associated interactive design strategies establish an innovated adaptation of the trajectory planning paradigm for multi-body dynamics. Spacecraft trajectory designers can employ the interactive capability of arc extraction from invariant manifolds to construct ballistic capture conditions and exploit natural pathways between periodic orbits. Versatile spaceflight operations within multi-body regimes is now fully accessible with the wealth of dynamical knowledge provided by the autonomous extraction of Poincaré map topology.

10.1 Summary

The application of Poincaré maps in astrodynamics problems is improved over the *de facto* puncture plot technique. The texture-based orbit convolution method enhances the visualization of Poincaré sections, constructing a lucid depiction of dynamical behavior. Autonomous Poincaré map topology extraction presented through the PMATE algorithm detects many novel periodic orbits in the CRTBP without relying on *a priori* solutions. Moreover, the invariant manifold curves on the Poincaré section are extracted with the PMATE algorithm to reveal the dense Poincaré map topology skeleton. The rich detail of Poincaré map topology extraction permits the interactive definition of maneuvers for corrective purposes or modifications to intended spacecraft destinations, fulfilling versatile spaceflight objectives.

Interactive design capabilities unlock the rapid construction of complex design itineraries as well as the potential ΔV-savings offered through the exploitation of chaotic dynamics in multi-body regimes. The arc-drawing and arc-dragging strategies promote trajectory construction and modification without the dependency on initial states. Interaction with Poincaré map topology data constructs invariant manifold arcs but also the ΔV-free transfer options between any two arbitrary unstable periodic orbits. Maneuvers can also be defined with an interactive vertical translation on the Poincaré section, creating augmented

connections that bridge unconnected arcs. The immersive construction of map-based maneuvers operates without numerical propagation, permitting a user to quickly analyze the trade space for a minimal ΔV transfer pathway assuming time-of-flight is not a primary concern. Yet, flight time may also be incorporated during trade analysis through graphical visualization of data during the interactive design process.

The example design scenarios presented in this investigation highlight the valuable applications of interactive design strategies that feature Poincaré map topology. Credited to the dense description of nearby stable invariant manifolds, versatile spaceflight is demonstrated with an adaptive destination change on a limited ΔV budget; knowing what structures are in the near phase-space vicinity benefits trajectory planning in extended mission and end-of-life scenarios with a multitude of possible pathway options governed by natural dynamics. Also, the LEO-to-orbit design scenario conveys the interactive method to construct low-cost transfers that culminate in a total ΔV budget only slightly above the minimum for energy-level alterations. Poincaré map topology also greatly assists moon-tour design applications by offering ballistic-capture target states for patched conic design tools (e.g., V_∞-leveraging). In addition, low-cost departure from science orbits is available from Poincaré map topology through natural pathways to either end a mission or continue to a new destination.

10.2 Recommendations for Future Work

The dragging tool for the interactive manipulation of preliminary arcs presented in this investigation should be studied for many additional applications. Considering an impact scenario, one might be able to simply drag a marker along the surface of a body to simultaneously adjust the intended impact site and the targeting maneuver. This same end-target drag philosophy could also be applied to a patched-conic B-plane flyby scenario where flyby geometry is adjusted in real-time by dragging the B-plane target point for a desired effect. Continuing along the preliminary design application, one could also expand the dragging idea to modify the velocity vectors associated with the beginning and ending states of an arc. With simple vector graphical objects to representing velocity orientation and magnitude, a designer could rotate velocity vectors by dragging them around a spherical direction

indicator and even scale velocity with the scroll wheel. Such user action interactively redefines the velocity state at the given node, creating the ability to bend an arc instead of just simply mobilizing endpoints.

Although PMATE is quite successful at autonomously extracting Poincaré map topology in the CRTBP, many avenues exist for improving computational efficiency and expanding the usage potential. First and foremost, the large number of parallel numerical simulations required by PMATE create the perfect application for GPU processing to achieve computation speedup as long as an effective double precision adaptive step-size numerical solver is available. The ideal application of Poincaré map topology in astrodynamics, though, is autonomous extraction in the full spatial CRTBP. As demonstrated in this investigation, some structure in the planar model is stable with respect to z perturbations, and thus, persists in the out-of-plane case. Yet, the Poincaré section in the full CRTBP occupies 4D space, significantly complicating the autonomous extraction process. The provided classification via winding number, fixed point refinement, and invariant manifold advection procedures can be extended to higher dimensional problems in a straightforward manner (fixed point refinement is already conducted in 6D but with $z = \dot{z} = 0$). Currently, though, no method exists for computing the Poincaré index over a 4D analysis voxel (the equivalent 4D cell). A comprehensive study on computing the 4D Poincaré index and a topological understanding of higher-dimensional saddle behavior is required for PMATE application in the full spatial CRTBP.

Additional design processes could enhance the application of Poincaré map topology towards general trajectory construction scenarios. A detrimental characteristic of employing natural pathways in space missions is the long flight durations to materialize the ΔV-free connections. Dynamics in the near vicinity of a saddle, however, can be incorporated to pass through an intermediate transfer orbit without actually entering the periodic orbit itself – a process known as a *saddle transit*. In a similar manner to streamlines near a saddle-type critical point of a vector field, the saddle transit starts with a small step off of the approaching W^S that will pass near to saddle-type orbit and departs along a similar small deviation to W^U. Overall, the flight time is conserved since the full asymptotic approach and departure arcs are bypassed while still maintaining a very similar transfer pathway. Unfortunately, no general (nor autonomous) approach to construct an efficient saddle transit exists for an

arbitrary intermediate transfer orbit, so the formulation of suitable saddle transit for time-of-flight reduction is offered as an area of interest for future investigation. Another layer to design capabilities with Poincaré map topology is to examine the relationship of topology across various C levels. Transitioning maneuvers to alter Jacobi constant values can drastically change the transfer landscape, offering shorter flight durations or connections between structures that are less expensive than the map-preserving equivalent. Note that maneuvers in the presented topology-based design examples are currently restricted to the chosen hyperplane $\Sigma : y = 0$. Observing the available flow from different surfaces of section modifies the local geometry, making some transfers more favorable than the equivalent transfer on the $\Sigma : y = 0$ section.

Finally, the detailed information linking fixed points and invariant manifolds transitions spacecraft trajectory design problems into the realm of combinatorial optimization. Far too many transfer options are offered by the Poincaré map topology skeleton for a sole designer to isolate the best combination of links between design nodes that achieves a particular mission requirement. The invariant manifold tree data structure generated by PMATE, however, holds germane trajectory design information and again allows for the quick analysis of transfer options without numerical simulation. Thus, links between periodic orbits can be autonomously evaluated including both $\mathcal{H}_c$ and augmented $\mathcal{H}_c$ options, creating a link cost from design node to design node. Link costs consider multiple trajectory design objectives such as time of flight and ΔV budget as weighted by the user. Route-finding protocols then determine the sequences of nodes and links through the design space by that minimize the transfer cost formed by fixed points, invariant manifold arcs, and map-preserving maneuvers. In essence, the rich dynamical framework supplied by Poincaré map topology represents the database of available transfers, and route-finding algorithms can employ this database to locate the best transfer combination based on design-specific metrics.